Elements for modeling pedestrian movement

from theory to application and back

Mohcine Chraibi

IAS Series
Band / Volume 60
ISBN 978-3-95806-757-8

Mitglied der Helmholtz-Gemeinschaft

JÜLICH
Forschungszentrum

Schriften des Forschungszentrums Jülich
IAS Series Band / Volume 60

Forschungszentrum Jülich GmbH
Institute for Advanced Simulation (IAS)
Zivile Sicherheitsforschung (IAS-7)

Elements for modeling pedestrian movement

from theory to application and back

Mohcine Chraibi

Schriften des Forschungszentrums Jülich
IAS Series
Band / Volume 60

ISSN 1868-8489
ISBN 978-3-95806-757-8

Bibliografische Information der Deutschen Nationalbibliothek.
Die Deutsche Nationalbibliothek verzeichnet diese Publikation in der
Deutschen Nationalbibliografie; detaillierte Bibliografische Daten
sind im Internet über http://dnb.d-nb.de abrufbar.

Herausgeber und Vertrieb: Forschungszentrum Jülich GmbH
Zentralbibliothek, Verlag
52425 Jülich
Tel.: +49 2461 61-5368
Fax: +49 2461 61-6103
zb-publikation@fz-juelich.de
www.fz-juelich.de/zb

Umschlaggestaltung: Grafische Medien, Forschungszentrum Jülich GmbH

Titelbild: Salah Benjelloun

Druck: Grafische Medien, Forschungszentrum Jülich GmbH

Schriften des Forschungszentrums Jülich
IAS Series, Band / Volume 60

D 468 (Habil. Wuppertal, Univ., 2023)

ISSN 1868-8489
ISBN 978-3-95806-757-8

Vollständig frei verfügbar über das Publikationsportal des Forschungszentrums Jülich (JuSER)
unter www.fz-juelich.de/zb/openaccess.

Elements for modeling pedestrian movement

from theory to application and back

ABSTRACT

The movement and decision-making of pedestrians are influenced by a complex interplay of internal and external factors, such as individual behavior, social interactions, and the built environment. In the context of civil engineering and traffic, understanding these factors is crucial for optimizing the design of buildings and transport infrastructures to promote safe and efficient pedestrian flow. In open spaces and crowds, these factors can shape the dynamics of pedestrian movement in ways that are not fully understood, so far.

This work presents a summary of the efforts made to uncover the underlying structures and laws that govern pedestrian dynamics, with a focus on how pedestrians interact with their environment. Through a combination of simulation experiments, literature review, and case studies, several models for pedestrian dynamics are presented, along with the ideas that motivated their development and enhancement. It is shown that the geometrical representation of pedestrians not only affects the realism of the simulations but also shapes the nature of the model itself.

With a focus on practical application of simulations in real-world scenarios, the importance of automatic methods for validation and verification of models is emphasized. Assessing the goodness of simulation results and the potential for reliable prediction helps to highlight the usefulness of developed models and methods for addressing safety-relevant questions in pedestrian dynamics.

This work is particularly relevant to civil engineers, transport engineers, architects and other professionals involved in the design and management of multi-functional buildings and crowd events. It covers the process of applying models to real-world situations and using the results to inform further theoretical development. I hope that these findings and suggestions for future research will be of value to researchers, practitioners, and policymakers working in the field of pedestrian dynamics.

Elemente der Modellierung von Fußgängerbewegungen

von einem, der auszog, das Laufen zu lernen

Kurzfassung

Bewegungen und Entscheidungen von Fußgängern werden durch ein komplexes Zusammenspiel interner und externer Faktoren wie beispielsweise das individuelle Verhalten, die soziale Interaktionen und die bauliche Umgebung beeinflusst. Im Bereich des Bauingenieurwesens und des Verkehrs ist das Verständnis dieser Faktoren entscheidend, um das Design von Gebäuden und Verkehrsinfrastrukturen zu optimieren und um einen sicheren und effizienten Fußgängerverkehr zu fördern. Auf freien Flächen und in Menschenmengen können sich diese Faktoren in einer Weise auf die Dynamik der Fußgängerbewegung auswirken, die bisher noch nicht vollständig verstanden ist.

Diese Arbeit fasst meine Bemühungen zusammen, die zugrundeliegenden Strukturen und Gesetze aufzudecken, die die Fußgängerdynamik bestimmen, wobei der Schwerpunkt auf dem Bewegungsverhalten von Fußgängern während der Interaktion mit ihrer Umgebung liegt.

Mithilfe einer Kombination aus Simulationsexperimenten, Literaturübersicht und Fallstudien stelle ich verschiedene Modelle der Fußgängerdynamik sowie die Ideen vor, die zu ihrer Entwicklung und Verbesserung geführt haben. Des weiteren zeige ich, dass die geometrische Darstellung von Fußgängern in diesen Modellen nicht nur den Realismus der Simulationen beeinflusst, sondern auch die Beschaffenheit der Modelle selbst prägt.

Mit Fokus auf die praktische Anwendung der Simulationen für realen Szenarien, wird die Bedeutung automatisierter Methoden zur Validierung und Verifizierung der Modelle unterstrichen. Durch die Beurteilung der Qualität der Simulationsergebnisse und des Potenzials für zuverlässige Vorhersagen hebe ich die Nützlichkeit der entwickelten Modelle und Methoden für die Beantwortung sicherheitsrelevanter Fragen hervor.

Diese Arbeit ist von besonderer Bedeutung für Bauingenieure, Verkehrsingenieure, Architekten und andere Fachleute, die an der Gestaltung und Verwaltung von Gebäuden und Verkehrsinfrastrukturen beteiligt sind. Sie umfasst den Prozess der Anwendung von Modellen auf reale Situationen und der Verwendung der Ergebnisse zur Weiterentwicklung der Theorie. Insgesamt behandelt diese Arbeit den Prozess der Anwendung theoretischer Ansätze auf reale Situationen und die Nutzung der Ergebnisse für die weitere Entwicklung von Modellen.

Die in dieser Arbeit enthaltenen Ergebnisse sowie Vorschläge sollen für aktuelle und zukünftige Arbeit von Forscher:innen, Praktiker:innen und politische Entscheidungsträger:innen nützlich sein, sowohl für ihre aktuelle als auch zukünftige Arbeit.

Contents

Listing of figures

The complexity of contemporary life is rapidly increasing and the need for effective models to understand and predict human behavior has never been greater.

B.F. Skinner

0

Introduction

Pedestrian dynamics is a complex and multi-disciplinary field that encompasses various aspects of urban planning and transportation engineering. It aims to understand and predict the movement of people in buildings and public spaces. This requires considering the interplay of various factors, including individual behavior, social interactions, and the built environment, which lead to a diverse range of interests and goals. Additionally, the dynamic nature of pedestrian behavior and the richness of emerging phenomena in a crowd further emphasize the interdisciplinary nature of the field.

Moreover, accurate modeling of pedestrian movement and behavior is crucial for the design and optimization of pedestrian facilities and for assessing the impact of different scenarios on pedestrian safety.

In this cumulative habilitation, I delve into various aspects of modeling pedestrian dynamics, starting with aspects related to modeling of pedestrian's shape to models of movement, methods of validation and verification, and finally examples of application. The main objectives of this work are to present a comprehensive overview of our research in pedestrian dynamics modeling, to identify and address challenges and limitations in existing models, and to propose new directions for future research.

Previous research in this area has focused on various aspects of pedestrian movement, such as individual and group behavior, decision-making processes, and interactions with the built environment. However, there is still much to learn about how to accurately and effectively model pedestrian dynamics in different contexts. Through this work, I aim to contribute to the advancement of knowledge in this field by presenting a nuanced and holistic approach to pedestrian dynamics modeling. I hope that our findings and suggestions for future research will be of great value to researchers, practitioners, and policymakers working in the field of pedestrian dynamics.

0.1 ORGANIZATION

I would like to acknowledge the contributions of my colleagues and collaborators throughout my research into pedestrian dynamics over the past years, which forms the basis of this habilitation thesis. See Appendix A.1 for contributions.

The content of this work is structured into multiple chapters, beginning with a concise summary of the key concepts and findings derived from our published articles. The articles are included in each chapter for ease of reference and are also reprinted in a neutral format in the appendix at the end.

The structure of this habilitation is as follows:

- Chapter 1: In this chapter I explore different pedestrian shape models and how they interact with movement models in this chapter.
- Chapter 2: Velocity-based models of pedestrian movement are introduced and discussed.
- Chapter 3: Here, various methods of validation and verification of pedestrian dynamics models are summarized.
- Chapter 4: In this chapter I give two examples of application of the models and show how they could be used in real-world scenarios.
- Chapter 5: Finally this chapter concludes this work with a brief summary. Furthermore, I give some thoughts for future work.

Figure 1 shows the interconnection between the chapters 1 to 4.

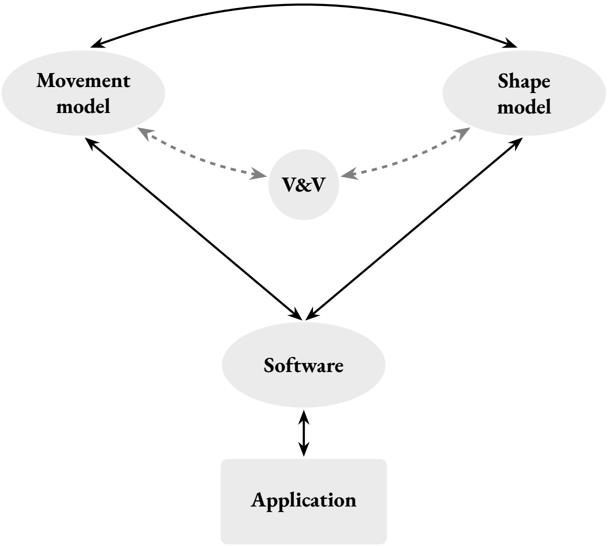

Figure 1: The elements of modeling of pedestrian dynamics, from theory, implementation to application. Shape models are closely related to movement models and have an impact on each other's definitions and properties. To ensure the accuracy and reliability of these models, they must undergo validation and verification (V&V) before being implemented in usable software that can be applied to relevant scenarios.

0.2 MOTIVATION AND KAIZEN

The increasing digitalization of architecture and civil safety, through tools such as Building Information Modeling (BIM), sensors, CCTV-cameras, RFID-systems, and data analysis, has changed the way we think about, plan, design buildings or to organize events. It is now possible to simulate and evaluate the usage of buildings by humans before they are even built, and pedestrian dynamics modeling is an important part of this process.

Applied scientists investigate ways to guarantee a certain level of safety in mass events, while architects and civil engineers develop evacuation concepts, especially designed for comfortable and efficient infrastructures that gather and transport big numbers of people on a daily basis. Safety relevant questions arise like for example: what is the capacity of a train station in case of a regional mass evacuation? Or which (economically affordable) possibilities do operators have to increase the performance of an airport in summer vacations? In most public buildings, e.g. hotels, evacuation plans indicate the evacuation escape route from a certain point in space (standing position of the reader) to the nearest exit to safe places. These evacuation plans are, however, static and in case of a real emergency do not include dynamic and probably more accurate information and assignments that respect the nature of the event that triggered, the evacuation in the first place. The shortest path to the exit may not always be the safest option for evacuating a building, especially in the case of a fire. Simulations of pedestrian dynamics can provide a solution to accurately assess and address the dynamic nature of such systems.

The work aims to continuously improve and enhance various elements of pedestrian dynamics, including the shape of pedestrians in models, models of pedestrian movement, and methods for validating and verifying simulations. The Kaizen philosophy, which emphasizes continuous improvement and the elimination of waste, serves as inspiration for this work. The goal is to better understand and predict the behavior of pedestrians in real-world scenarios through constant refinement and optimization of the models. The ultimate objective is to contribute to the development of safer and more efficient transport infrastructure and buildings, as well as to advance the fundamental understanding of pedestrian dynamics.

At the beginning of my activity in this research field, force-based models were the predominant approach for modeling pedestrian dynamics in continuous space. These models, largely based on the social force model, describe pedestrian movement as the result of interactions between individuals and their environment. Although attempts were made to address inherent issues and provide a comprehensive description, the resulting models became overly complicated, incorporating numerous modifications that detracted from the elegance and simplicity of the original social force model. Therefore, I sought to reduce the complexity and start from an even simpler model based on a first-order ordinary differential equation. This model could then be gradually improved in a structured way. To this end, I considered explicitly modeling the shape of pedestrians as a separate track alongside the operational model, that describes the movement of pedestrians.

Our research in pedestrian dynamics was motivated by the conviction that various real-world problems in this field can be broken down into simpler, more manageable components. This approach not only enhances the simplicity and understandability of models but also enables a systematic investigation of individual components. For instance, when simulating the movement of pedestrians in a building, it's crucial to examine the effect of bottlenecks on the flow and the behavior of pedestrians when turning corners. By understanding and developing simple and effective solutions for these components, we can advance the use of simulations in general to more sophisticated cases.

Maintaining a focus on real-world applications, efforts were made to pursue both fundamental research and novel approaches in pedestrian dynamics modeling.

0.3 On the importance of abstraction and experiments

To effectively address safety-related questions and comprehensively evaluate the comfort, usage and performance of buildings, a thorough theoretical comprehension of the principles governing crowd dynamics is crucial. This understanding must be based in science and must be robust enough to support reliable and convincing conclusions. For optimized evacuation plans, safety-aware architectural building designs, as well as mathematical modeling benefit from the ever-increasing number of empirical studies and the insights they generate.

For instance in large buildings bottlenecks are omnipresent and can not be avoided whether in the design phase nor later during their operation. Therefore, intensive experimental studies were conducted, investigating the impact that bottlenecks can have on the overall performance of the building. In this regard, special interest was dedicated to the relationship between the width of exits and the flow. While in early works it was assumed that the flow through an exit increased step-wise when the exit's width increased, later studies refuted this qualitative dependency in favor of a linear increase of the flow. This linearity can be explained by the so-called zipper-effect, which is observed when pedestrians close gaps and optimize the lateral utility of space in the bottleneck.

Another, no less controversially discussed and intensively investigated aspect of bottlenecks, is the supposedly positive effect of a static obstacle in front of an exit. Here, many experimental studies and numerical investigations were performed to shed more light on this matter. In a recent investigation [9] it was shown, that the effect of the obstacle on the dynamics of the bottleneck is two-fold. The presence of an obstacle may not necessarily improve the flow of people through the exit, but it can alleviate the pressure on those being evacuated by reducing congestion. In contrast to the behavior of granular materials, where it has been demonstrated that the presence of obstacles can increase the flow through a bottleneck, the situation in pedestrian dynamics is more complex. Human beings perceive obstacles differently, and their reactions to them can vary. This can be seen in experimental results, which can be inconsistent, with the effects of obstacles sometimes being observed and other times not.

Other examples of empirical works and experimental discussions spanning from the density-flow relationship* and the impact of cultural factors on its qualitative shape, route-choice behavior in buildings to lane-formation in corridors and their quantitative characteristics, were extensively investigated and documented. For a better review we refer the reader to [20].

0.4 MODELING OF PEDESTRIAN DYNAMICS

Within this section, I explore various perspectives regarding the quality and applicability of models. Specifically, I consider different opinions regarding the validity and accuracy of models, as well as their usefulness in practical applications. When referring to quality, I am specifically alluding to the precision and accuracy demonstrated by a model, as well as its capacity to consistently generate dependable

---

*also called the fundamental diagram, a concept borrowed from traffic flow theory.

and consistent outcomes that relate to a particular target or phenomenon. I also consider the extent to which a model is able to capture and represent real-world phenomena, and how well it is able to address the specific questions and objectives at hand.

The qualitative observations and quantitative measurements gained from empirical studies not only contribute to gaining more insights into the movement of people and better understanding of the risks bound to the crowd, but also offer an empirical ground for theoretical and numerical investigations of pedestrian dynamics. These insights often offer useful criteria that validate models' predictions and evaluate the simulacrum of reality they create. For example, the fundamental diagram mentioned above is often used as a "benchmark" for models to evaluate the extent to which they realistically capture pedestrian interactions and the resulting dynamics.

Models that are reliable and credible are useful resources for understanding and exploring the intricacies of crowds and for evaluating and testing new plans and strategies. This is especially true in situations where it may not be ethical or feasible to conduct empirical studies. For example, the phenomenon known as "faster-is-slower," which suggests that individuals' desire to move faster can actually slow down the speed of the crowd, can be more ethically and morally studied *in silico*. Therefore, scientists construct how-possibility models to understand the underlying mechanisms of crowd dynamics and predict what-if scenarios beyond the empirical realm. Often, the quality of these models is relative to a predefined and model-specific target. For instance, scientists may choose some phenomenon that has been observed in real-life situations and try to mimic it with a highly idealized model.

Although, mathematical models may be simple in nature (in contrary to the complex nature of pedestrians' behavior), they can be considered valuable and give how-possibility explanations, despite leaving many details of the target phenomenon unexplained. For example, a self-organization phenomenon that is often observed in corridors and straight bi-directional movements is *lane formation*. Lanes emerge in the crowd without any external trigger or controlled synchronization mechanisms.

They may impact positively the smoothness of the crowd's movement. In this sense they can be understood as an implicit self-optimization of the flow, avoiding collisions and congestion. Therefore, a compact model describing very well the collision-avoidance mechanisms among pedestrians, is sufficient to explain how lanes emerge and hence enhance our understanding of this phenomenon[†]. As such, the model fulfills the target it was designed for and hence meets its intended purpose. However, it may not accurately depict all aspects of its target, such as the number and spacing of formed lanes, which may differ from empirical data. Therefore, for a civil engineer or a crowd manager the model may still be seen as a poor simulacrum, and hence has a limited practical use, although it perfectly fulfills the target it was designed for.

The behavior of individuals within a crowd can be viewed as a close relationship between each person, making the crowd itself a complex system that can be analyzed with the help of a solid theoretical foundation. Researchers often develop numerous models when studying complex systems, and many of these modeling methods include implicit assumptions about how people move and interact with their surroundings. Some cellular automata, for instance, assume that a pedestrians' motile behavior is influenced by chemotaxis-like processes. Meaning, agents tend to follow trails left by other agents[‡]. While force-based models assume the change of an individual's velocity is contributed to external (social) forces.

Recently, a new paradigm has found increasing popularity in this field: data-based models [13]. With this Ansatz researchers try to capitalize on the impressive recent developments of artificial neural networks. The premise here focuses on accurately predicting the behavior of a crowd without attempting to fully comprehend the underlying causes and principles behind the crowd's dynamics. For instance, a model might be able to predict the formation of lanes, but it does not explain why this occurs or what factors contribute to its emergence. In [23], the authors applied a novel approach to accurately predict

---

[†] A model that describes well lane-formation, can be used to conduct several simulations and quantitatively uncover properties of lanes, e.g. number of lanes, distance between them, their change rate, etc.

[‡] In this work we refer to pedestrians in a computer simulation as agents.

the velocity of pedestrians in various complex spatial configurations. Unlike traditional physics-based models, which often require custom-tuning of model parameters for each specific scenario, this approach does not require such adjustments. Despite still being in the early stages of development, particularly in low-density scenarios, the efforts made in this field have demonstrated promising results in accurately predicting the movements of individuals in a crowd.

Another popular modeling approach describes the motile behavior of pedestrians using compact functions such as Newton's laws of motion or an analytical equations describing the states of the pedestrians as well as the transitions between these states. The state of a pedestrian is typically represented by variables such as position, speed, and acceleration. As time plays a role in the set of all possible states of pedestrians, referred to as the state space, differential equations are often utilized to describe the changes in the system and project the current states of pedestrians into future states, providing an understanding of the system's evolution as a whole.

The assumption that pedestrians in a crowd deviate from their intended path, implying the existence of an external force that pushes them away from obstacles or attracts them towards desired targets, forms the basis of the widely used second-order ordinary differential equation Ansatz. This flexible and robust template of models has been applied to study *in-situ* real-life evacuation scenarios since 1975. In their seminal work[11], Hirai and Tarui formulated a general model that employs several forces to simulate various behavioral aspects of pedestrians, such as group behavior, attraction to certain sites, repulsion from unfamiliar individuals, attraction to familiar individuals, routing forces, and more. Although the model is relatively complex, with nine different forces, it laid the foundation for a rich family of force-based models.

In his seminal work from 1953, Louis Pipes proposed two different models for the speed of leading vehicles in single-file movements: one using a piece-wise linear function, and the other using an exponential increase in speed. See Figure 2

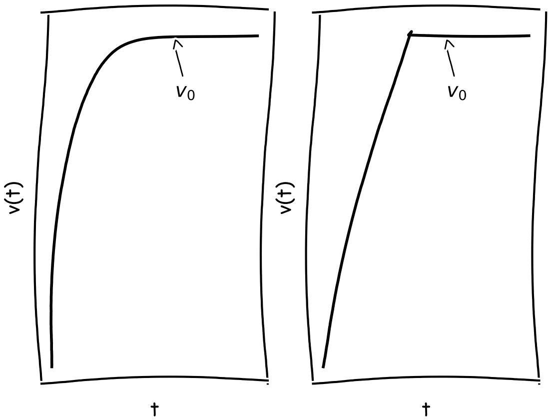

Figure 2: Illustration of different speed models as depicted in "a study of traffic streams"[18]. Left: An exponential increase of the speed towards a desired speed. Right: A linear increase of the speed towards a desired speed).

With the exception of Hirai and Tarui's model, which uses a constant driving force (a linear speed function), the driving force leading to the seemingly more realistic exponential speed function becomes the *de-facto* standard choice used in all developed force-based models, starting from the social force model[17] until today.

Despite their popularity and their relative success in describing certain aspects of the motile behavior of pedestrians, second-order ordinary differential equations, suffer from different limitations and inherent problems, as has been shown on many occasions by several researchers[16,5,14,4,15]. Various unrealistic behaviors have been observed, such as oscillations, violations of the exclusion principle[§] (e.g. overlapping of agents and "tunneling" through other agents), and acceleration to velocities larger than the desired velocity. These issues have been highlighted in previous studies[4,15]. Furthermore, it has been found that in order to achieve realistic motion, some physical parameters of the models must have

---

[§] The *exclusion principle* states that the space occupied by a particle is not available for other particles.

unrealistic values[16]. It is important to note that these issues are not caused by numerical problems in the discretization of the system of differential equations, but are fundamental conceptual issues. Another problem relates to the fact that social forces do not always obey Newton's third law, which can raise fundamental questions about the distinction between force and mass in classical mechanics. Additionally, the superposition of forces is often not valid in pedestrian dynamics, which can lead to unrealistic and numerical problems[22].

Interestingly, these limitations of force-based models, seem to be the reason of their ever-growing popularity and tireless efforts of researchers to develop new enhancements and modifications, although they often lead to artificially complicated versions of the original models, and thus loose their initial charm and appeal.

In this work, the focus lays on modeling pedestrians with first-order differential equations. The main motivation of this endeavor lays in Occam's razor[¶]: we prefer simpler models to more complex ones, and increase complexity only when absolutely necessary. This methodology has the advantage of potentially better understanding the impact of certain elements on the outcome of the simulations. For instance, a very simple model that guarantees collision-free movement in the crowd, tends to produce clogging in narrow bottlenecks and symmetrical setups. With respect to the aphorism "everything should be made simple, but not simpler" [‖], we may want to enhance the model by adding a new parameter that mitigates or even eliminates clogging without giving up its original collision-free-property. In Chapter 2, I describe this procedure based on the "collision-free speed mode", that has been co-developed by the author of this habilitation and progressively enhanced in different publications.

An important aspect of pedestrian dynamics that greatly impacts the nature of the defined model as well as the dynamics it is capable of producing, is the model of pedestrian shape. While people's

---

[¶] `https://math.ucr.edu/home/baez/physics/General/occam.html`

[‖] There is ambiguity regarding the author of this aphorism, therefore the author uses it without contribution to this ongoing debate, simply because it reflects well the idea discussed in this work.

bodies are naturally three-dimensional, a two-dimensional representation of the human body is often sufficient and necessary to capture the majority of observed phenomena in crowded environments. The concept of pedestrian shape, which refers to the physical characteristics and projection of the body on two-dimensional space, has been shown to play a significant role in influencing the movement and behavior of pedestrians in crowded environments. It is thus essential to consider and accurately model the shape of pedestrians in any study of pedestrian dynamics.

Despite its importance, researchers focused in the early stages of this field on describing the movement of pedestrians rather than their shape. Often then, the body representation of pedestrians was reduced to simple forms like points, circle disks, or in some cases a combination of them. In the second part of this work, I introduce my recent research on the impact of this aspect of modeling, namely the representation of the human body in two-dimensions and how it influences not only the simulation results but also the design and choice of the movement model itself.

In Chapter 1 I discuss the various aspects of pedestrian shape modeling and its impact on pedestrian dynamics. I delve into the different methods used for representing pedestrian shape, their advantages and limitations, and how they influence the movement and behavior of pedestrians in crowded environments.

The importance of validation and verification, or the process of assessing the quality of simulation results, has been recognized as a critical step in the modeling process. However, there are still challenges and limitations in the methods and approaches used for validation and verification in pedestrian dynamics modeling. The existing trend of application of computerized simulation studies to large and complex systems necessitates assessment methods to evaluate the validity of the obtained numerical results and their suitability to be used as a reliable tool by decision-makers. To ensure the practical value of the aforementioned models, especially in the context of practical civil engineering studies and safety relevant traffic projects, validation and verification of models is of paramount importance. Therefore, the verification and validation process is considered as key part in the development cycle of every model.

Since, all mathematical models for pedestrian dynamics have the aim to (realistically) simulate the movement of pedestrians, one can try to answer those questions by setting a collection of simple tests based on common-sense assumptions e.g. pedestrians do not move through walls, pedestrians move upstairs faster than moving downstairs, etc. A verification process alone does not assess the quality of a given mathematical model nor does it evaluate its realism, but gives merely more confidence in the available implementation and how faithfully does it match the underlying mathematical model. Therefore, the validation process is extremely important as it assesses the accuracy and realism of the model itself.

Validation in the context of pedestrian dynamics can benefit from the tremendous development in the area of empirical research. Several experiments were conducted to investigate the phenomena that emerges in crowds and to build a well-documented database[**], that not only contains data of controlled experiments, but also data issued from field studies. These empirical works capture relevant properties of crowds in *normal* situations. Therefore, in order to gain credibility and confidence from users, it is essential to demonstrate the ability of a simulation to accurately reproduce the properties of relatively simple scenarios. In Chapter 3, I discuss different works by the author of this habilitation that aim to develop benchmarks for pedestrian dynamics models, testing and quantifying their validity.

As was mentioned before, the term verification is understood in relation to an implemented version of the mathematical model. Since 2012, research on pedestrian dynamics has been conducted and implemented in a reproducible way within the framework of the open-source software JuPedSim[8]. In Chapter 4, a sample of numerical studies powered by JuPedSim will be discussed. This demonstrates that the software can be utilized by practitioners in applied projects, researchers for in-

---

[**] Notably the Pedestrian Dynamics Data Archive published and maintained by Forschungszentrum Jülich `https://ped.fz-juelich.de/db/`.

vestigating and reproducing research results, and lecturers for educational purposes.

The body is a living laboratory, a site of endless experimentation and discovery.

Rebecca Solnit

1

Pedestrians get in shape

One of the first questions to solve or at least to consider when developing microscopic models, is the representation of the three-dimensional human body in two-dimensional space without loss of valuable information. While I initially considered the safety applications for these models, I realize that in other industries such as gaming and movies, three-dimensional (3D) models of the body are crucial. This distinction is important because in the context of pedestrian movement, a reduction of dimensionality is necessary, with models being limited to describing pedestrian movement in only two dimensions.

In the literature, pedestrians are often represented as constant circular disks, which has the advantage of allowing for quick calculations of the distances between individuals. These distances are then used to calculate repulsive forces or prevent collisions among agents. However, representing pedestrians as circular shapes, while a simple approximation of their projection on two-dimensional space, can obscure many nuances of their motion, particularly at high densities. This includes body turning to pass through an exit and variations in the effectively occupied space.

1.1 On the body-ellipse

The concept of using dynamic and variable ellipses as a representation of the human body, proposed by the author in[7], aims to capture the nuances of human motion, especially at high densities such as the turning of the body to pass through an exit or the variability of the effectively occupied space. The idea is to improve upon the commonly used circular shapes, which tend to overestimate the occupied space and obfuscate these nuances of human motion, specifically the tendency of people to move their bodies laterally when moving slowly and occupy more space in the shoulder direction. Oppositely, fast pedestrians make wide strides and thus need more space in the moving direction than in the shoulder direction. These two observations were modeled efficiently with an ellipse defined by two speed-dependent semi-axes using a linear relationship.

This suggested elliptical model leads to a better match with experimental data. Mathematical calculations involving two different ellipses are not trivial and need to be developed in a rigorous manner. Therefore, in a subsequent work (Appendix A.4), the original ellipse-model was enhanced by means of a Sigmoid function inspired by the observation that pedestrians often reduce their occupied space in the vertical direction of motion by turning their body to walk faster and pass through narrow gaps that are smaller than the width of their shoulder.*

In the paper reproduced in Appendix A.3 Hughes and Chraibi developed a method for accurately calculating the overlap area between two ellipses that does not rely on proxy curves, taking advantage of the Gauss-Green formula to determine a segment area between two points on an ellipse. Overlap between two ellipses is calculated by combining the areas of appropriate segments and polygons in each ellipse. The developed algorithm was implemented in C++ and analyzed for accuracy, precision and robustness with a range of input ellipses. A prototype of a model that relies on the overlap area instead of the distance between ellipses, was developed but not yet published.

Previous research has demonstrated that utilizing ellipses to model pedestrian bodies results in a superior representation of agent shapes, and thus, a more accurate depiction of flow, density, and velocity. However, this approach is significantly computationally demanding, which poses a significant limitation and obstacle for real-time simulations that involve a large number of agents. Moreover, important human walking characteristics can not be reproduced by models based on these geometrical shapes (circles, ellipses, ...). Pedestrians are bipedal by nature, and representing them, in a two-dimensional fashion at least, as stepping agents, calls for a totally different paradigm. This naturally includes some important human walking characteristics, such as the periodicity of stepping, the adjustment of step frequency and step length, and the change of personal space within the same step cycle.

1.2 The biped model

In Appendix A.8 we developed the so-called "biped-model" with the main goal to represent pedestrians and describe their locomotion by physical steps. This model enables investigation of human walking characteristics, such as the periodicity of stepping, the adjustment of step frequency and step

---

*Note that while the first ellipse-model was used together with a force-based motion model, the second enhancement was used together with a velocity-based model.

length. Besides the model's ability to reproduce measured empirical results, like stop-and-go waved and the speed-density relationship, it provides new possibility to get insights into step-specific behavior, like for instance the lock-step phenomenon. The model presented in Appendix A.8 shows how the shape of agents not only influences the results of the simulations, but shapes even the character of the model and hence opens new possibilities to investigate phenomena that could be eventually not investigated otherwise.

1.3 VORONOI MODEL

In another work that showcases the importance of the shape of pedestrians, pedestrians were represented as Voronoi cells (Appendix A.9). The chosen shape, which can be calculated naturally at each time given a distribution of agents, investigates mainly the orientation behavior of pedestrians in space. With help of this model we decompose the directional behavior of pedestrian in three basic components and show that with this choice the model can describe reasonably well the dynamics of pedestrians in comparison to experimental data. The different pedestrian motion patterns are the direction moving to the destination, the direction following another pedestrian, and the direction for making a detour, in case of an eminent conflict. The definition of the three basic direction rely heavily on the definition of the shape of agents, which is in this case, unlike cellular automata, a dynamic tessellation of the space that represents the space requirement of agents at each time step in dependence of the local density.

Figure 1.1 shows the different shape models, as explained above.

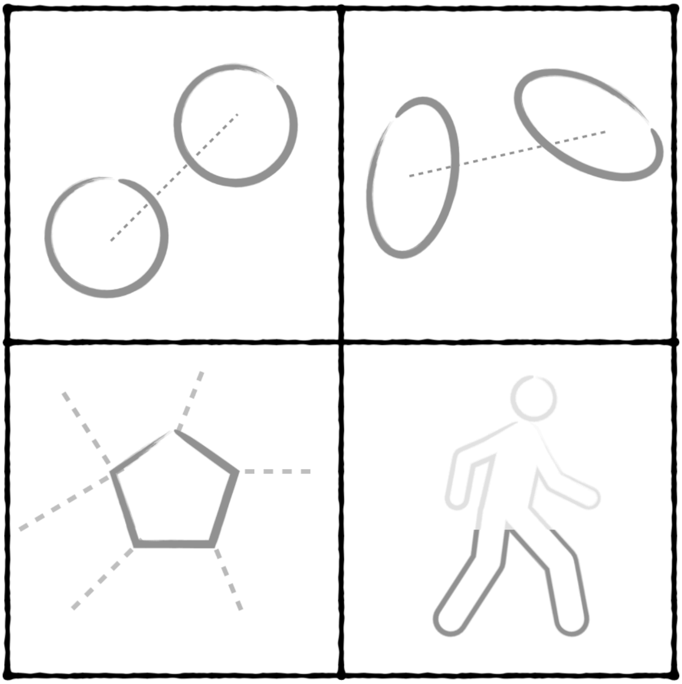

Figure 1.1: Different models for the shape of agents. Top left: circles. Top right: ellipses. Bottom left: Voronoi diagrams. Bottom right: Biped model. The model represents only the step movement, therefore the rest of the body in “invisible”.

1.4 ARTICLES DISCUSSED IN THIS CHAPTER

The following articles are discussed in this chapter and are part of this habilitation:

- G. B. Hughes and M. Chraibi.

  Calculating ellipse overlap areas.

  Computing and Visualization in Science 15(5):291–301 (**2012**).

  See Appendix A.3.

- Z. Huang, M. Chraibi, and W. Song.

  Simulation of pedestrian single-lane movement by a biped model.

  Physical Review E, 98(4):042309 (**2018**).

  See Appendix A.8.

- Y. Xiao, M. Chraibi, Y. Qu, A. Tordeux, and Z. Gao.

  Investigation of Voronoi diagram based direction choices using uni- and bi-directional trajectory data.

  Physical Review E, 97(5):052127 (**2018**).

  See Appendix A.9.

The crowd has no appreciation of individuality.

James M. Henslin

2

Overview of model developments

Kaizen is a Japanese word meaning change for the better or continuous improvement. In the context of simulating pedestrian movement, a kaizen-based approach involves continually refining and improving the model through small, incremental changes in order to achieve more accurate and reliable simulations.

This chapter provides a summary of our research aimed at enhancing a fundamental model, which was originally developed by the author of this work, grounded on the fundamental principles. The main focus of this work centers around velocity-based models. These are models that describe the change of agent's speed with respect to time. In general velocity-based models can be "behavioral" in the sense that they are based on discrete-choices. Typically they find use in the field of robotics and put emphasis on collision-avoidance, a priority that comes handy in low to medium dense scenarios.

In every velocity model, there is a mechanism for collision avoidance that employs different strategies. The impact of this collision avoidance on various phenomena, such as clogging and lane formation, can vary. Despite all models having collision avoidance capabilities in principle, there are always unrealistic outcomes that indicate a non-realistic strategy. This section of my work examines studies that introduce alternative strategies and explores their relationship to these phenomena.

2.1 Collision-free speed model

In this work we investigate space-continuous velocity-based model that emerge from first-order ordinary differential equations. First, we describe the development principles of a simple velocity-based model (Appendix A.2), the "collision-free speed model". Then, we describe how this basic model was generalized and progressively enhanced.

The motivation to develop the collision-free speed model is two-fold: first, the motile behavior of agents should be described with a minimal first-order model[*]. First, a first-order model is supposed to be solved faster that a second-order model. Second, the model should be by design collision-free. The collision-free speed model consists of two sub-models, based on the assumption that pedestrians avoid collision by two mechanisms: Changing speed and/or changing direction. Hence, the first sub-model regulates the speed of pedestrians in dependence of their distance to the nearest neighbor. The second sub-model regulates the actual direction of agents with respect to a given desired direction (to

---

[*] Investigations that were part of my PhD-thesis showed that second-order models create more problems than they possibly solve. Besides, unlike car traffic, where inertia plays an important role, pedestrians change their speed almost instantaneously. Therefore, it seems obvious to model the change of velocity directly, instead of emphasizing inertia effects which lead to second order models.

the goal) and to other pedestrians in a visible surrounding area.

The results of the model agreed quite well with the empirical data. Another advantage is that the FD in the model is implicitly predicted by a simple velocity-distance function. Qualitative phenomena, such as lane-formation and oscillations at bottlenecks, could be reproduced. However, in later investigations, the model showed some limitations that could be addressed in future works. One of the problems encountered by the model emerges from the additive nature of the direction sub-model, which was responsible for an oscillatory behavior of the overall direction of agents in certain dense situations. Another problem becomes apparent in narrow bottlenecks, where, paradoxically, the collision-free nature of the model leads to excessive clogging of agents.

2.2 GENERALIZED COLLISION-FREE SPEED MODELS

In Appendix A.4 we introduced the first generalization of the collision-free speed model[†]. Another limitation of the original model was that it only considered interactions between agents and did not take into account interactions between agents and their physical environment. To address this, an additional formula was formulated to account for interactions between agents and static obstacles. Another component of the model that was also subject to generalization was the presentation of the shape of agents, which in the original model was restricted to disks of constant circles, to ellipses with speed-dependent axes. As discussed in Chapter 1, pedestrian's shape has an important influence on the emerging dynamics and the definition of the model. Having now a non-circular shape, exposed a shortcoming of the original model which became apparent in simulations of dense situations. The directional sub-module was enhanced in a way that mitigated sharp changes in the direction of movement as well as unintentional backwards movements. These improvements led to more realistic distribution of pedestrians, especially in bottleneck scenarios as well as a better agreement of the model

---

[†] We may refer to this model as GCFM.

with empirical results in corridors (fundamental diagram) and bottlenecks (flow-width relationship).

With the GCFM, we investigated in Appendix A.7 the dynamics of pedestrians in bottlenecks, with focus on the clogging phenomenon or what we call prolonged clogs. Prolonged clogs occur when the flow through a bottleneck ceases for an extended period, which could be infinite. However, in practice, clogging tends to occur for a relatively short duration. Additionally, the models often depict these phenomena at boundary conditions and for parameter values where such occurrences are unrealistic. The present analysis concentrates on investigating the impacts of three distinct factors: the model parameters, parameters related to spatial boundaries, and simulation-specific parameters, such as the time step and update method.

The results of the analysis revealed that clogging is not caused by simulation-specific parameters, but rather by model parameters, particularly the time gap, which is linked to the "motivation" of the agents. A narrower width of the bottleneck favors the formation of prolonged clogs as well. In the future, special work has to be dedicated to explicitly model cooperation processes that may solve prolonged clogging situations. Although, clogging for a some amount of time has been observed in the past in real-word scenarios.

One important concept that directly influences the directional sub-model is the desired direction. For example in straight corridors it may simply be pointing parallel to the walls. In bottleneck, for instance, it may be directed towards the middle of the exit. However, these seemingly simple choices do not necessarily lead to realistic simulations. In [19] for instance we showed that because of the collision-free property of collision-free speed model, agents can get into a deadlock. The tendency of the model to run into clogging situation is reinforced by the deterministic choice of the intended target.Hence, we proposed in [19] a simple mechanism to solve this problem, by adding a white noise term to the desired direction. This choice was designed to capture the imperfect choice of direction, even if the proposed solution was simple.

Taking a step further in this direction, the influence of walking preferences on pedestrian movements was examined in Appendix A.5, wherein the expectations of comfortable walking for an agent were considered. The collision-free speed model was extended by modeling the walking directions of pedestrians, such that human perception of comfort and preference for walking straight to their intended destinations was taking into account. The restriction of walls in heading direction on pedestrian's walking is introduced to avoid potential collisions among pedestrians and obstacles. The enhancements lead to a model that outperforms the original model with regards to the trajectory's distribution in bottlenecks. Furthermore, the speed-density relation in corridor inferred from the new model fits the experimental data well and the model performs more accurately in simulating the flow-width relation in bottleneck scenarios than the original model.

2.3 ANTICIPATIVE COLLISION-FREE SPEED MODEL

In the final work in this category (Appendix A.6), the aim was to determine the factors that describe and explain the phenomenon of lane-formation in bi-directional flow, with the motivation of investigating and reproducing it both qualitatively and quantitatively. Based on the collision-free speed model we developed a new speed model that takes into account pedestrian anticipation[‡]. In this context, anticipation refers to the fact that agents use calculations of distances based on the expected positions of other agents in the near future. For this purpose, the process of anticipation is divided into three parts: Perception of the current situation, prediction of a future situation, and selection of a strategy leading to an action. AVM outperformed both models collision-free speed model and GCFM when simulating binary interaction scenarios, that were designed to maximize collisions between agents. Furthermore, to better assess the dynamics in bi-directional flow, which is closely related to the emergence of lane formation, the notion of "jamming state" and "moving state" was introduced, based on the number of static or blocked agents in the simulation.

[‡] We call this model AVM.

Simulation results with the new model showed that compared to the other two models, the critical density between the moving states and jamming states is shifted to higher values using the AVM, which indicates that the new model is able to better prevent imminent collisions.

ein neues Modell entwickelt wird, das dann die gleichen Probleme hat wie das dessen Probleme man eigentlich lösen wollte! Dann fragt man sich, warum man die Probleme nicht direkt im SFM gelöst hat, statt erst den Umweg über ein neues zu gehen! Ich weiß natürlich, was dahintersteckt! Aber das kommt im Text nicht unbedingt raus! Hier wird ein anderer Spin benötigt!

2.4 Articles discussed in this chapter

The following articles are discussed in this chapter and are part of this habilitation.

- A. Tordeux, M. Chraibi, and A. Seyfried.

  Collision-Free Speed Model for Pedestrian Dynamics.

  In Traffic and Granular Flow ’15, pages 225–232, Springer International Publishing (**2016**).

  See Appendix A.2.

- Q. Xu, M. Chraibi, A. Tordeux, and J. Zhang.

  Generalized collision-free velocity model for pedestrian dynamics.

  Physica A: Statistical Mechanics and its Applications, 535:122521 **2019**).

  See Appendix A.4.

- S. Zhang, J. Zhang, M. Chraibi, and W. Song.

  A speed-based model for crowd simulation considering walking preferences.

  Communications in Nonlinear Science and Numerical Simulation, 95:105624 (**2021**).

  See Appendix A.5.

- Q. Xu, M. Chraibi, and A. Seyfried.

  Anticipation in a velocity-based model for pedestrian dynamics.

  Transportation Research Part C: Emerging Technologies, 133:103464 (**2021**).

  See Appendix A.6.

- Q. Xu, M. Chraibi, and A. Seyfried.

  Prolonged clogs in bottleneck simulations for pedestrian dynamics.

  Physica A: Statistical Mechanics and its Applications, 573:125934 (**2021**).

  See Appendix A.7.

Verification is showing that something is true, while validation is showing that something is correct.

Barry W. Boehm

3

Validation and verification

3.1 INTRODUCTION AND DEFINITIONS

To investigate and describe certain properties in a real-world system, say for example capacity of a train station, models can be developed based on assumptions. In general these models are implemented in computer software, that can be used as a convenient and extremely versatile tool to investigate various possibilities and evaluate the impact of certain measures on the overall performance of some system of interest. From this point on we are dealing with two entities: A mathematical model and a computer software, where the later acts as a proxy between the model and the system to be described. Therefore, we might ask to what degree does the computer software simulate the behavior described by the mathematical model? Furthermore, are these simulation results comparable, to a certain confidence degree, to the behavior of the real-world system? The process required to answer the first question is called *verification*. It ensures, that the computerized model is indeed a faithful (numerical) representation of the underlying mathematical model. *Validation* however, can be seen as an integral part of model development, with the goal to ensure good agreement between model's outcome and the system's behavior. The latter is often described by empirical observations and common sense assumptions.

Validation of a model can take several forms, as it involves both the description of the model itself and its implementation (such as in software). Despite the close relationship between the two, they are distinct entities that require separate validation.

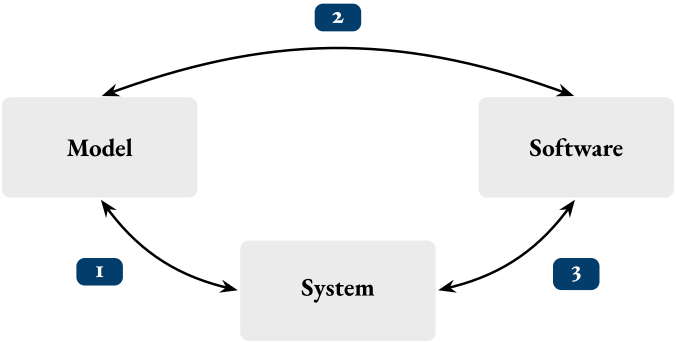

Figure 3.1: Validation process involving a model, a software and a system. 1 and 3 validate the results of the model and its implementation, while 2 verifies that the model is being implemented faithfully.

Model-validation, specifically, is a process of comparing the outcomes of the model to the behavior of the real-world system it is attempting to replicate. This comparison ensures that the assumptions made by the model are realistic to some extent. If large discrepancies between the model and reality are identified during this validation process, the model can be modified in order to increase its accuracy and shape its definition.

As example, consider a second-order ordinary differential equation describing the acceleration of a pedestrian in space[*] without interaction with its environment:

$$\ddot{x} = \frac{v^0 - \dot{x}}{\tau}, \tag{3.1}$$

This model defines an exponential time function for pedestrian speed, characterized by a physical parameter, v^0, representing the normal walking speed of pedestrians, and a model parameter, $\tau > 0$, which determines the rate of increase in speed. Since the solution of this simple model can be calculated analytically (exponential function), verification of the software ($\boxed{2}$ in Figure 3.1), is straightforward. It suffices to run several simulations with different parameter values and different initial conditions and compare the speed of the agent in time with the expected numerical value given by the exponential function.

To validate this model, it is necessary to measure experimentally the change of speed of standing pedestrians towards a certain desired walking speed and directly compare the measured curve with the model's output ($\boxed{1}$ in Figure 3.1). While the physical parameter represents a physical property of pedestrians (and hence is somehow known), the model parameter can be varied to minimize the deviations between the model and the system. Note, this step does not necessitate any simulation of the system. It is purely based on the expected mathematical outcome of the model. Now, consider the system involves several pedestrians that interact with each other. Obviously, the aforementioned model needs to be extended adequately. For simple cases, like a system of two pedestrians, the model can be solved analytically and compared to experimental data. For example, one might imagine two pedestrians moving towards each other on a collision course, and then avoiding each other at a certain

---

[*] The position of the pedestrian x is a function of time.

moment in time and space. This basic behavior can be reproduced (or not) by the model and hence a comparability between model and system is possible.

However, for complex systems, say a train station with thousands of passengers, model-validation becomes infeasible, in favor of *software-validation*, where the computerized model is being validated with respect to some pre-defined system measure ($\boxed{3}$ in Figure 3.1). The true challenge is to establish an accurate measure that can effectively capture the key characteristics of the system, such as the flow through narrow passageways or the relationship between flow and density. Note that a model can be valid for one measure and be invalid for another. Therefore, it is important to consider the validity of a model as the result of a complex process with results ranging from "absolutely invalid" to "absolutely valid."[†]

3.2 Summary of previous work

In several works, we developed tools and methods for *automatic* model assessment, both to compare models with each other or with reality. For instance in the paper replicated in Appendix A.10 we took advantage of the fact that trajectories are functional data to use principal component analysis (PCA) as a tool to assess the quality of models. We demonstrated, through a comparison of two different space-continuous models with experimental data, that using PCA as a diagnostic tool is effective in assessing the quality of agent-based simulations of pedestrian flows with respect to average behavior. Additionally, this method revealed statistically significant deviations of the models from the experimental data. A limitation of this approach is that it relies on trajectories, which limits its ability to validate discrete models such as cellular automata.

In the paper reproduced in Appendix A.11 we developed a systematic methodology to quantify the level of verification and validation of space-continuous models. The framework takes advantage

---

[†] with the upper bound being for pedestrian dynamics unlikely, due to the complexity and unpredictability of the system.

of the so called "Kolmogorov-Smirnov distance" that measures the degree of discrepancy between two different data sets: a simulated and an empirical. Hence, we present a metric that quantifies the goodness of the model under evaluation in an automatic way, which is of advantage, for instance to determine an "optimal" set of model parameters.

In the paper reproduced in Appendix A.12 we proposed a microscopic method to evaluate continuous pedestrian dynamic models at the trajectory level, which may be considered as a further development of the framework previously developed in Appendix A.10, since both approaches are based on trajectories. We compared experimental and simulated trajectory in four directions. The evaluation of the model can be described by a radar chart, with which both qualitative and quantitative conclusions could be obtained. This method is based solely on trajectory data, as opposed to evaluating models by comparing collective features such as the fundamental diagram.

Finally, in the paper reproduced in Appendix A.13 we presented a novel approach that combines previously developed methods. This approach leverages the Kolmogorov-Smirnov and dynamic time-warping methods to extract eight different metrics from trajectory data. The practicability of the proposed approach was tested on the example of the empirical circle antipode experiments with two different space-continuous models.

These efforts show that the process of validation and verification of models is complex, but necessary to quantify the correctness of the applied models. They increase their fidelity and hence their acceptance in safety-relevant projects. Parts of these efforts found application in validation of software for pedestrian dynamics that are used in civil engineering offices. See for example the works published in [25] and in [24].

When validating models, it is important to agree on the specific property of the system to be examined. However, there is no consensus on this matter. The complexity of this problem for pedestrian dynamics is illustrated by the different works presented in this section.

The attentive reader might note that the methods presented thus far are only applicable to models that are continuous in space. Models such as cellular automata, which are typically stochastic and discrete in space and time cannot be validated using these methods. In future research, a general model-agnostic framework needs to be developed.

3.3 ARTICLES DISCUSSED IN THIS CHAPTER

The following articles are discussed in this chapter and are part of this habilitation.

- M. Chraibi, T. Ensslen, H. Gottschalk, M. Saadi, and A. Seyfried

  Assessment of models for pedestrian dynamics with functional principal component analysis

  Physica A, 451:475–489 (**2016**).

  See Appendix A.10.

- V. Kurtc, M. Chraibi, and A. Tordeux

  Automated Quality Assessment of Space-Continuous Models for Pedestrian Dynamics

  Traffic and Granular Flow '17 (**2017**).

  See Appendix A.11.

- Z. Huang, M. Chraibi, S. Cao, C. Huang, Z. Fang, and W. Song

  A microscopic method for the evaluating of continuous pedestrian dynamic models

  Physica A: Statistical Mechanics and its Applications (**2019**).

  See Appendix A.12.

- A generalized trajectories-based evaluation approach for pedestrian evacuation models

  Y. Xiao, J. Xu, M. Chraibi, J. Zhang, and C. Gou.

  Safety Science 147:105574. (**2020**).

  See Appendix A.13.

The one thing that is most useful is to know

what is not useful.

Confucius

4

Application

4.1 Project-based evolution of JuPedSim

The previously discussed models and concepts were integrated into the JuPedSim framework for their practical implementation[8]. JuPedSim stands for Jülich Pedestrian Simulator and is a software maintained by the author of this habilitation since 2012. It is designed to serve scientists as an open platform to implement and use models for pedestrian dynamics in an easy manner. Hereby, the focus was laid on simplicity of use, transparency and reproducibility of simulation results. JuPedSim's main component is jpscore which is the simulation core of the software. It implements different models from Chapter 2.

Despite its research-oriented character, JuPedSim has been used and further developed in diverse applied projects. In KapaKrit[*], JuPedSim was applied to investigate the capacity of train stations with focus on the Dortmund main station[3]. In another project focusing on metro stations, ORPHEUS[†], JuPedSim was extended by an knowledge-based routing algorithm[6] and an interface to Fire Dynamics Simulator (FDS)[12], which enables agents to navigate through the space and interact with the spreading of smoke in case of fire[21].

This work was continued in the project BaSiGo[‡] by developing a general purpose routing algorithm in JuPedSim, to investigate route choices of pedestrians in dependency on their familiarity with the building[1]. With this approach we could model the inaccurate mental representation of pedestrians' spatial knowledge. In addition, the model considers further principles and constraints of human wayfinding.

Lately, knowledge-transfer became in focus, and rightly so, in the research landscape in Germany. With the project SISAME[§], JuPedSim was applied and used for training purposes. Planers and organizers of events were taught the usability of simulations and their interpretability by means of a fused version of JuPedSim together with SUMO, a software for urban traffic simulations developed by DLR[2]. The main results of SISAME were on one hand the valuable exchange and feedback that researchers became from practitioners which influenced JuPedSim's road-map of software development and shifted the attention towards increasing the user-friendliness of the software. On the other hand, the overall architecture of JuPedSim was changed. Instead of a standalone software, JuPed-

---

[*] `http://kapakrit.de/`

[†] `http://www.orpheus-projekt.de/`

[‡] `http://www.basigo.de/`

[§] `https://www.sisame.de/`

Sim is now implemented in form of a hybrid library, in C++ and Python, and offers interfaces for other software, like for example SUMO and basically any hybrid simulation software.

4.2 Large-scale simulation with MATSim and JuPedSim

This was the case in Appendix A.14, where JuPedSim was coupled with the software MATSim to implement a hybrid approach, allowing simulations of large-scale scenarios. Both frameworks are developed in different programming languages[¶], which makes a hybrid coupling challenging. In order to improve the efficiency of our simulations, we developed a general interface that can be integrated with any simulation framework. This interface allows for faster computation while maintaining a level of accuracy sufficient for reliable predictions. We demonstrated the effectiveness of this hybrid simulation approach in a case study involving the evacuation of a district in Hamburg, Germany in the event of a storm surge. The scenario involved the evacuation of up to 50,000 people from the Wilhelmsburg district of Hamburg.

Our proposed interface allows only for a static coupling of two different models. Therefore further research is needed to allow coupling of multiple models at arbitrary spatio-temporal coordinates.

4.3 Numerical investigation of COVID-19-measures with JuPedSim

In the rest of this chapter we introduce two recent applied developments in the framework of JuPedSim. Appendix A.15 was influenced by the global COVID-19 pandemic that impacted human life worldwide. To mitigate its effects, various measures were implemented such as wearing masks in public places and maintaining social distance. The objective was to slow down the transmission of the disease by reducing contact between individuals.

[¶] MATSim is implemented in the programming language Java, while JuPedSim is implemented in C++.

In Appendix A.15, we used numerical simulations to investigate the effectiveness of such measures in reducing contact among customers in a typical supermarket setting in Germany. The movements of customers are simulated by the model introduced in Appendix A.4. We designed several scenarios with different control measures and used the model introduced in a previous section to simulate the movements of customers in the supermarket.

A quantitative evaluation of the degree of contact between customers was performed by defining an index based on the distance between them. The degree of contact, in this context, refers to the duration for which customers remained within the allowed minimal distance to others. The effect of these measures on the average contact degree of each customer was explored, and the spatial distribution of contact among customers in the supermarket was determined in a qualitative way. Our simulation results showed that, while the measure of requiring customers to use a shopping cart did not have a significant impact, the measures of limiting the number of customers and enforcing a minimum social distance were effective in reducing interactions among customers. Additionally, we found that bottlenecks in intersections of shelves, unless addressed through changes in the design of the supermarket, can lead to a temporary increase in the contact index among customers, and thus increase the probability of infection.

4.4 Unified escalator capacity formula

In the second work (Appendix A.16), we focused on various aspects of the simulation of passenger dynamics on escalators, with a particular emphasis on the discrepancy between the "theoretical" and "practical" capacity that is often observed for the literature. The "theoretical" capacity of an escalator is based on the assumption that its capacity increases linearly with speed. However, this relationship does not hold up well at higher speeds, particularly due to hesitation by passengers when entering the escalator. As a result, the "practical" capacity, which is provided in handbooks and recommendations from manufacturers, is often used although it lacks a scientific basis. To address this discrepancy and derive a unified formulation of the capacity function with respect to escalator speed, we further developed the model introduced in Appendix A.2 to describe the transition of agents from walking on the flat surface to standing on the escalator. This allowed us to conduct various numerical studies and examine key metrics such as minimum distances between standing agents and average occupancy of the escalator steps.

More importantly, we were able to develop a generalized analytical formula that accurately describes the escalator capacity, and we showed that, in addition to conveyor speed, the capacity is largely dependent on the time gap between alighting passengers. By comparing our simulation results with corresponding empirical data from field studies and experiments, we were able to measure a minimum human reaction time in the range of 0.15–0.30 seconds, which is in line with findings from social psychology.

This study allows for a science-based performance evaluation of buildings and metro stations with escalators by accurately determining the relationship between capacity and speed. Although the developed capacity formula fits well with known field measurements in the literature, future experimental works may be necessary to validate its correctness.

4.5 ARTICLES DISCUSSED IN THIS CHAPTER

The following articles are discussed in this chapter and are part of this habilitation.

- G. Lämmel, M. Chraibi, A. Kemloh, B. Steffen

  Transportation Research Record, 2561(1), 1–8. (**2016**)

  See Appendix A.14.

- Q. Xu and M. Chraibi.

  On the Effectiveness of the Measures in Supermarkets for Reducing Contact among Customers during COVID-19 Period.

  Sustainability (**2020**).

  See. Appendix A.15.

- C. Gnendiger, M. Chraibi, A. Tordeux.

  Come together: A unified description of the escalator capacity.

  PLOS, *under review* (2023).

  See. Appendix A.16.

The end is in the beginning and lies far ahead.

Ralph Waldo Emerson

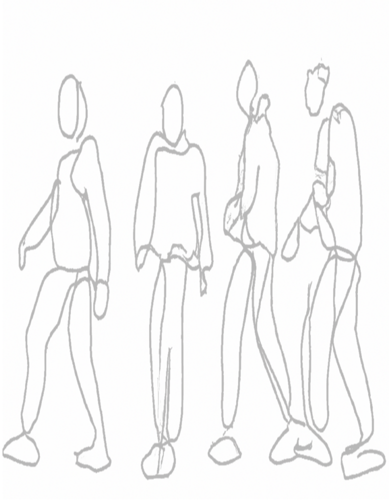

5

Final remarks

5.1 Thoughts for future work

In this cumulative habilitation I have focused on comprehending and modeling pedestrian dynamics, with an emphasis on identifying and addressing areas where our current understanding is incomplete. By combining theoretical and practical approaches, we have developed new models and methods for simulating pedestrian movement and their shape. Additionally, significant efforts have been made to validate and verify the models, recognizing the importance of these processes in model development and deployment. By using these methods, I have been able to create and implement reliable simulations in JuPedSim, which was be applied in various application-oriented projects.

This work contains several areas that can be improved upon through additional research. For instance, many facets of the human movement are left out by two-dimensional shapes, like for example stepping on stairs and stumbling. Therefore, the shape models developed in Chapter 1 can be further explored in three-dimensional space.

The movement models developed in Chapter 2 mostly rely on a single homogeneous mathematical equation to describe the movement of pedestrians in space. However, the motile behavior of pedestrians is multi-faceted. Therefore, it may be necessary in the future to identify different and separate strategies for the movement of pedestrians, based on several heuristics representing different aspects of the human walking behavior. In addition, physics-based models as introduced in this work need to be augmented with socio-psychological factors. For example, the motivation of individuals passing through an exit varies, which can significantly affect the flow through the exit. Simulations with these models can provide a more nuanced view of pedestrian dynamics, leading to more customized planning of events and multifunctional buildings.

The validation and verification methods developed in Chapter 3, are mostly focused on space-continuous models. Obviously, this tendency is influenced by the work of the author in this domain. In the future however, model-agnostic validation and verification methods shall be developed and implemented for general-purpose models.

5.2 On sustainable mobility in a post-pandemic society

The research, as presented in this work, has been primarily focused on safety-related issues in high-density scenarios where large crowds gather. In open spaces, the primary concern in these situations is to carefully plan evacuations to ensure smooth processes and avoid bottlenecks, bidirectional flows, or any other situations that may reduce flow as density increases, which increases the risk of deadly crowd crushes. Architects and civil engineers also face similar concerns as they try to minimize evacuation times within buildings in case of emergencies. However, in the past two years, the situation has changed somewhat, as other problems, mostly related to low density situations, have emerged. Since the COVID-19 pandemic, people's perceptions of crowded spaces and their definitions of comfort at various density levels have changed significantly. Passengers' convenience or discomfort depends not only on physical and perceived density, but also on their location and duration.

In 2020, demand for passenger transport in the European Union was halved due to the pandemic*, but it is expected to increase again to reach peak levels comparable to or higher than pre-pandemic levels in order to keep railways profitable, safe, and sustainable. In Great Britain, for example, the number of rail passenger journeys in 2022 increased by 85.5% compared to 2021, although usage remains considerably lower than before 2019. These numbers show a clear upward trend, which will inevitably lead to crowded railway stations. See Figure 5.1.

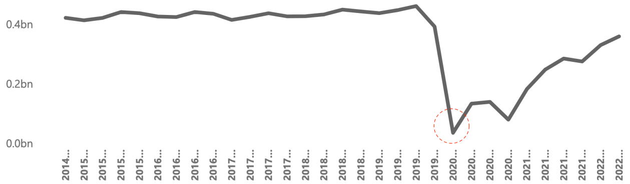

Figure 5.1: Passenger rail usage in Great Britain from July to September 2022. In Q1 2020, usage dropped significantly, going from 392 million users in the previous quarter to 35 million users. However the usage shows an increasing trend after the pandemics.

As the demand for passenger transportation continues to increase in the wake of the COVID-19 pandemics, it is important to address the potential safety concerns that may arise in crowded train

---

[*] `https://dataportal.orr.gov.uk/statistics/usage/passenger-rail-usage/`
(Accessed on 27.01.2023. Published on 15.12.2022.)

stations. Operators are implementing measures such as expanding services and introducing new vehicles with higher seating capacities to meet this demand. In February 2020 the German train operator (DB) announced a budget of 13,6 Billion euros to increase the capacity of the German railway system in 2022[†]. In the controversial project Stuttgart 21, the increase of the capacity was originally forecasted to add at least 2,2 million passengers/year for the regional and local rapid transit railway transport. The new infrastructure of the train station was designed so that the capacity increases by 75% (long-distance trains) and by 56% (regional transit trains). For a more in-depth review, we refer to [10].

These efforts to increase the capacity of railway infrastructures fail to take into account the demographic change brought about by a prolonged pandemic; People perceive crowded scenarios differently than before the pandemics. Efforts to increase the capacity of railway infrastructures may not fully account for the demographic changes resulting from the prolonged pandemic. It is observed that people perceive crowded scenarios differently than before, which underscores the importance of more in-depth research to quantify and investigate this change and its impact on safety of events and multi-functional buildings like train stations. Increasing the system's capacity by merely redesigning the train stations or even building more considerable infrastructure (re)design does not necessarily lead to improved service and several safety issues may arise, risks associated with overcrowding on platforms and in stairwells. Waiting passengers and passengers embarking, disembarking and transferring cause overcrowded platforms and congestion at stairs or overpasses. Already today, disruptions caused by natural events, or construction sites trigger massive congestion at train or subway stations. Access to transportation risks to become a limited resource and can lead to dangerous crowding. Moreover, the decreased comfort of passengers and their altered sensibility and perception towards dense and over-filled spaces may discourage them from using the railways as their primary transport tool in favor of cars or domestic flights.

[†] `https://www.deutschebahn.com/de/presse/pressestart_zentrales_uebersicht/13-6-Milliarden-Euro-Rekordinvestition-DB-macht-Netz-und-Bahnhoefe-fit-fuer-die-Zukunft-7251600` (Accessed on 01.02.2023. Published on 03.02.2022.)

To improve the resilience of train stations, it is essential to not only increase capacity through infrastructure improvements, but also consider the quality of service and the potential for congestion at narrow points or complete standstills, taking into account the passenger behavior in the aftermath of the pandemic. Further research on these issues that break with conventional approaches by shifting the perspective of study from optimizing and controlling a “mindless crowd” to incorporating the passenger’s view and perception of different social rules in the management process, is necessary to ensure the safe and efficient operation of train stations in the future.

Additionally, it is crucial to not only model the movement of crowds in simulation studies, but also their waiting behavior in crowded areas, such as train stations. This waiting behavior can vary based on different categories of people who use the facility, such as commuters, tourists, shoppers, and people waiting for changeover. For example, commuters may exhibit different waiting behavior compared to tourists or shoppers. Commuters may be in a rush and prioritize getting to their destination quickly, while tourists may have more leisurely attitudes towards waiting and may be more willing to wait for a better experience. Shoppers may have different waiting behaviors based on the type of shopping experience they are looking for, such as a quick in-and-out trip or a more leisurely browsing experience. In general, it is important to consider different behaviors related to different categories of people when simulating crowd movement in various environments. This can help ensure that the simulation accurately reflects real-world scenarios and can inform better decision-making for facility management and crowd control measures.

A

Articles

A.1 AUTHOR'S CONTRIBUTION

The articles discussed in this habilitation are reprinted in the following sections. They are part of this cumulative habilitation and were published in peer-reviewed journals and conferences. In the publications Appendix A.2, Appendix A.3, Appendix A.16 and Appendix A.14, the author contributed together with his co-authors in the conceptualization of the models, analysis of the results, drafting and writing of the articles. The other publications in this appendix were all conceptualized, written, edited, and finalized under my supervision as the habilitation author and the supervisor of the PhD students who served as first authors.

Most of the models were implemented by the author in JuPedSim[*].

---

[*] `https://github.com/JuPedSim/jpscore`

A.2 ARTICLE I

Collision-Free Speed Model for Pedestrian Dynamics

A. TORDEUX, M. CHRAIBI, AND A. SEYFRIED

TRAFFIC AND GRANULAR FLOW '15 (2016)

TGF'15, 225-232, Springer, 2016
arXiv:1512.05597

Collision-free speed model for pedestrian dynamics

Antoine Tordeux[1], Mohcine Chraibi[1], Armin Seyfried[1,2]

Abstract
We propose in this paper a minimal speed-based pedestrian model for which particle dynamics are intrinsically collision-free. The speed model is an optimal velocity function depending on the agent length (i.e. particle diameter), maximum speed and time gap parameters. The direction model is a weighted sum of exponential repulsion from the neighbors, calibrated by the repulsion rate and distance. The model's main features like the reproduction of empirical phenomena are analysed by simulation. We point out that phenomena of self-organisation observable in force-based models and field studies can be reproduced by the collision-free model with low computational effort.

Keywords
Model

[1] *Jülich Supercomputing Centre, Forschungszentrum Jülich*
[2] *Computer Simulation for Fire Safety and Pedestrian Traffic, Bergische Universität Wuppertal, Germany*

Contents

Introduction

Modelling of pedestrian dynamics have been strongly developed since the 1990's [4, 23, 8]. Microscopic models describe the movement of individuals in two-dimensional representation of space. They are used for theoretical purposes [14, 13], as well as for applications e.g. design and conception of escape routes in buildings [24, 25] or optimal organization of mass events or public transport facilities (VISWalk [22], Legion [3], ...). In the microscopic class of models, pedestrians are represented as autonomous entities (Lagrangian representation) with local interactions. Complex collective phenomena of self-organisation emerge from the interactions. Examples are the lane formation, clogging at bottlenecks, zipper effect or intermittent flow at bottlenecks, stop-and-go waves, herding, strip formation or circular flows (see [4, 12] and references therein). Even simple microscopic models can yield in rich dynamics [15, 6]. Yet, the relations between the microscopic model parameters and the emergence of phenomena of self-organisation are not straightforward. In most of the cases, they have to be analysed by simulation.

Microscopic pedestrian models could be defined in continuous or discrete time, space and state variables (see [23, Chapter 5]). One of the most investigated class is the class of *force-based* (or acceleration) models [15, 6, 5]. They use an analogy between pedestrian movement and Newtonian dynamics. Force-based approaches allow to describe a large variety of pedestrian dynamics [15, 6]. Yet, this model class describes particles with inertia and does not exclude particle collision and overlapping.

This is especially problematic at high densities [5]. Moreover, the force-based approach may lead to numerical difficulties resulting in small time steps and high computational complexity, or use of mollifies [16].

Pedestrian behaviors result from repulsive and attractive forces with the acceleration models. They are based on the visual perception of distances or obstacle speeds resulting in instantaneous changing of the speed or the direction within the speed models. Also, this model class is generally called *vision-based*. One example is the *synthetic-vision-based steering approach* that notably allows to describe complex collective structures avoiding gridlocks [20]. Also the *velocity obstacle models* or *reciprocal velocity obstacle model* borrowed from robotics exist [10, 2]. These models are defined in discrete time and are driven by collision avoidance. They are by construction collision-free if the time step is smaller than a horizon time of anticipation. In the evacuation model by Venel, the pedestrians move as fast as possible to the desired destination with no overlapping [17]. There exits some variants of the model with different interaction strategies [26]. Note that there exists also rule based multi-agent models aiming to describe pedestrian psychology (see for instance [21, 11]) or mixed models, see for instance the *gradient navigation model* where the direction model is defined at first order while the speed is of second order [9]. In most of cases, these models need a large number of parameters with inherent calibration difficulties and, as for force-based models, high computational efforts.

In this paper, we aim to develop a minimal model for which the dynamics are by construction collision-free (i.e. overlapping-free). The model belongs to Maury and Venel mathematical framework [17]. We show by simulation that it allows to describe some expected phenomena of self-organisation observed in field studies or in simulations with forced based models. The model is defined in section 1 while the simulation results are presented in section 2. Conclusion and working perspective are given in section 3.

1. Collision-free speed-based pedestrian model

A continuous speed model is a derivative equation for the velocity. Typical examples are

$$\dot{\mathbf{x}}_i = \mathbf{v}(\mathbf{x}_i, \mathbf{x}_j, \ldots) \qquad \text{or} \qquad \dot{\mathbf{x}}_i = V(\mathbf{x}_i, \mathbf{x}_j, \ldots) \times \mathbf{e}_i(\mathbf{x}_i, \mathbf{x}_j, \ldots), \tag{1}$$

with $\mathbf{x}_i$ the pedestrian position and $\dot{\mathbf{x}}_i$ the velocity of pedestrian i (see figure 1). The velocity in regulated in one function for the first equality while the speed V and the direction $\mathbf{e}_i$ (unit vector) are regulated separately in the second approach.

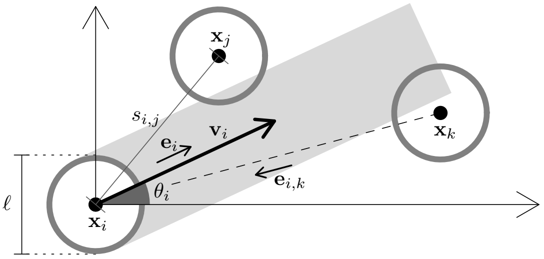

Figure 1. Notations used. $\mathbf{x}_i$, $\mathbf{v}_i$ and θ_i are the position, velocity and direction of the pedestrian i ; ℓ is the pedestrian size ; $\mathbf{e}_{i,j}$ is the unit vector from $\mathbf{x}_j$ to $\mathbf{x}_i$; $\mathbf{e}_i = (\cos\theta_i, \sin\theta_i)$; $s_{i,j} = ||\mathbf{x}_i - \mathbf{x}_j||$.

1.1 Definition of the model

The speed model is the optimal speed (OV) function depending on the minimal spacing in front. The approach is borrowed from road traffic model [1]. The OV approach has been already developed with a force-based model [19]. Here we use the OV function at the first order with the minimal spacing in front.

For a given pedestrian i, the set of the pedestrians in front is defined by

$$J_i = \left\{ j, \ \mathbf{e}_i \cdot \mathbf{e}_{i,j} \leq 0 \ \text{ and } \ |\mathbf{e}_i^{\perp} \cdot \mathbf{e}_{i,j}| \leq \ell / s_{i,j} \right\}. \tag{2}$$

The pedestrians in front are the pedestrians overlapping the grey area in figure 1. The minimum distance in front s_i is

$$s_i = \min_{j \in J_i} s_{i,j}. \tag{3}$$

The model is

$$\dot{\mathbf{x}}_i = V\big(s_i(\mathbf{x}_i,\mathbf{x}_j,\ldots)\big)\times \mathbf{e}_i(\mathbf{x}_i,\mathbf{x}_j,\ldots), \tag{4}$$

with $V(\cdot)$ the OV function and $\mathbf{e}_i(\mathbf{x}_i,\mathbf{x}_j,\ldots)$ the direction model to define. As shown below, such model is by construction collision-free if

$$V(s)\geq 0 \quad \text{for all } s \qquad \text{and} \qquad V(s)=0 \quad \text{for all } s\leq \ell. \tag{5}$$

In the following, the OV function is the piecewise linear $V(s)=\min\{v_0,\max\{0,(s-\ell)/T\}\}$, with v_0 the desired speed and T the time gap in following situations (ℓ is the pedestrian diameter, see figure 1). This OV function satisfies the collision-free assumption (5). The direction model is a simplified version of the additive form of the *gradient navigation model* [9]. It is based on a repulsion function depending on the distances $(s_{i,j})$ with the neighbours

$$\mathbf{e}_i(\mathbf{x}_i,\mathbf{x}_j,\ldots)=\tfrac{1}{N}\big(\mathbf{e}_0+\textstyle\sum_j R(s_{i,j})\,\mathbf{e}_{i,j}\big)\,, \tag{6}$$

with $\mathbf{e}_0$ the desired direction given by a strategic model, N a normalization constant such that $\|\mathbf{e}_i\|=1$ and $R(s)=a\exp\big((\ell-s)/D\big)$ the repulsion function, calibrated by the coefficient $a>0$ and distance $D>0$. The parameter values used in the simulation are presented in figure 2.

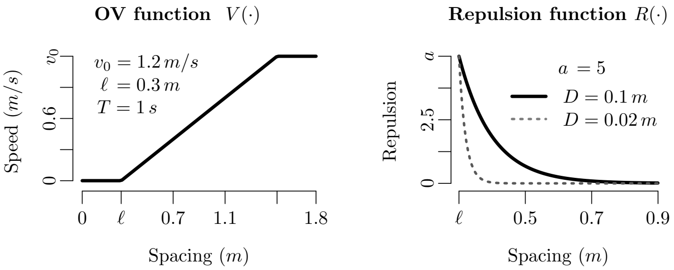

Figure 2. Functions and associated parameters for the model: The OV function (3 parameters, left panel), and the repulsion function (2 parameters, right panel).

1.2 Collision-free property

Oppositely to the force-based models, the presence of collision and overlapping can be controlled by construction with the speed-based models (non-overlapping constraint). If pedestrians are considered as discs with diameter ℓ, the set of collision-free configurations is for a given pedestrian i

$$Q_i=\big\{\mathbf{x}_i\in\mathbb{R}^2,\ s_{i,j}\geq \ell\ \ \forall j\big\}\,. \tag{7}$$

The set of collision-free velocities

$$C_{\mathbf{x}_i}=\big\{\mathbf{v}\in\mathbb{R}^4,\ s_{i,j}=\ell\ \Rightarrow\ \mathbf{e}_{i,j}\cdot\mathbf{v}_i\geq 0\ \text{ and }\ \mathbf{e}_{j,i}\cdot\mathbf{v}_j\geq 0\big\} \tag{8}$$

is such that the speeds are nil or in opposite direction for a pedestrian in contact with an other (see [17] for more general conditions). Therefore, if initially $\mathbf{x}_i(0)\in Q_i$, then $\mathbf{x}_i$ remains in Q_i for any dynamics in $C_{\mathbf{x}_i}$. In these conditions Q_i is an invariant set for $\mathbf{x}_i$, i.e. the dynamics are collision-free (see also [18]). It is easy to see that the model (4) belongs to this class if assumption (5) is satisfied. Consider $s_{i,j}=\ell$ then either $\mathbf{e}_i\cdot\mathbf{e}_{i,j}\leq 0$ and then $j\in J_i$, i.e. $s_i\leq s_{i,j}=\ell$ and $V(s_i)=0$, or neither $\mathbf{e}_i\cdot\mathbf{e}_{i,j}\geq 0$ and then $V(s_i)\geq 0$ since $V(\cdot)\geq 0$. Therefore $\mathbf{v}_i\cdot\mathbf{e}_{i,j}=V(s_i)\times\mathbf{e}_i\cdot\mathbf{e}_{i,j}\geq 0$ and the velocity belongs to $C_{\mathbf{x}_i}$. The arguments are valid for any direction model $\mathbf{e}_i$.

2. Model features

We describe in this section by simulation some characteristics of the model with uni- and bi-directional flows. The parameter settings are given in figure 2. The simulations are done on rectangular systems with length $L=9$ m and width $W=3$ m from random initial configurations and by using explicit Euler numerical scheme with time step $dt=0.01$ s.

2.1 Counter flows and the lane formation

We observed with the model the formation of lanes by direction for counter flows (figure 3, left panels). Such phenomena frequently occurs in real data (see for instance [27]). The system needs an organization time for that the lanes emerge (figure 3, top right panel), where the mean flow to the desired direction for counter flows is compared to uni-directional ones). The formation of lanes is observed with the model for some density levels up to $\rho = 6$ ped/m^2 (figure 3, bottom right panel). As expected, the density threshold value for that the lanes appear depends on the pedestrian size ℓ (here $\ell = 0.3$ m). Note that the lane formation phenomenon disappears when a noise is introduced in the model (freezing by heating phenomenon, see [13] and in figure 3, thin dotted line in bottom right panel where a Brownian noise with standard deviation $\sigma = 0.1$ m/s is added to the model – the lane formation breaks as soon as $\rho \geq 2$ ped/m^2).

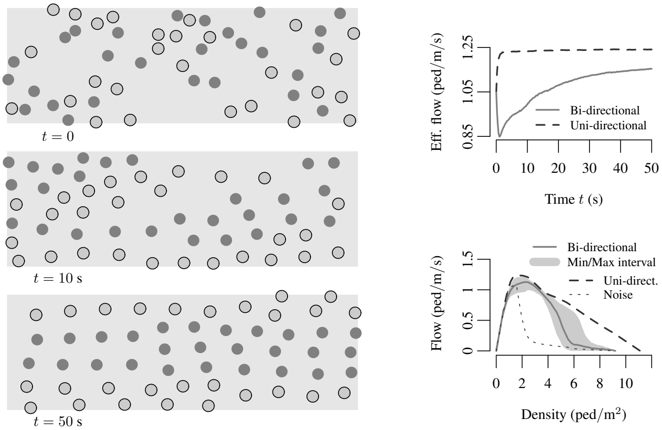

Figure 3. Counter flows. Left panels, snapshots of the system at time $t = 0$, 10 and 20 s from random initial conditions ($\rho = 2$ ped/m^2). Right panels, the mean flow sequence to the desired direction and the fundamental diagram.

2.2 Intermittent bottleneck flows

Oscillating phenomena for counter flows in bottlenecks are observed with both real data and models ([15, 12, 7]). Such phenomena are related as intermittent bottleneck flows in the literature [14]. We observe that the speed-based model is able to reproduce them (see figure 4, left and top right panels). The phenomenon occurs even at relatively high density levels (see figure 4, bottom right panel). Yet it induces frictions and the flow volumes obtained for counter flows are less than the ones of uni-direction. As expected, the frictions tend to increase as the density increases. Some simulation results not presented here show that the intermittent flow phenomenon subsists for high density levels when D is sufficiently high and that the frequency of the flows oscillations tend to increase as the density increases.

3. Conclusion and working perspective

A new speed-based model is proposed for pedestrian dynamics in two dimensions. Oppositely to classical force-based approaches, the model is intrinsically collision-free and no overlapping phenomena occur, for any density level. The model has five parameters. Three of them concern the optimal speed function. They are the pedestrian length, desired speed and time gap with the predecessor. The two others calibrate the direction model. They are the repulsion rate and repulsion distance.

The model main properties are described by simulation. A large range of dynamics observed in real data and force-based models are reproduced. For instance, linear increase of flow with the bottleneck width, lane formation for counter flows (with the freezing by heating effect) or intermittent flows, are obtained with identical setting of the parameters. However, other well-known characteristic such that stop-and-go phenomena can not be described. Further mechanisms (and parameters) remain to be introduced to the model.

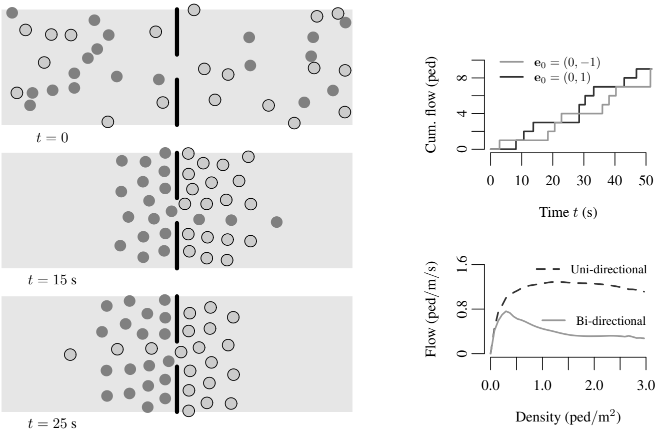

Figure 4. Counter flows with bottleneck. Left panels, snapshots of the system at time $t = 0$, 10 and 20 s from random initial conditions ($\rho = 1.4$ ped/m^2 and $\omega = 0.6$ m). Right panels, the corresponding flow sequences by direction and the fundamental diagram.

References

[1] Bando, M., Hasebe, K., Nakayama, A., Shibata, A., Sugiyama, Y.: Dynamical model of traffic congestion and numerical simulation. Phys. Rev. E **51**(2), 1035–1042 (1995)

[2] van den Berg, J., Lin, M., Manocha, D.: Reciprocal velocity obstacles for real-time multi-agent navigation. In: Robotics and Automation, 2008. ICRA 2008. IEEE International Conference on. 2008 IEEE International Conference on Robotics and Automation Pasadena, CA, USA, May 19-23, 2008 (2008)

[3] Berrou, J., Beecham, J., Quaglia, P., Kagarlis, M., Gerodimos, A.: Calibration and validation of the legion simulation model using empirical data. In: N. Waldau, P. Gattermann, H. Knoflacher, M. Schreckenberg (eds.) Pedestrian and Evacuation Dynamics 2005, pp. 167–181. Springer Berlin Heidelberg (2007).

[4] Chowdhury, D., Santen, L., Schadschneider, A.: Statistical physics of vehicular traffic and some related systems. Phys. Rep. **329**(4–6), 199–329 (2000).

[5] Chraibi, M., Kemloh, U., Seyfried, A., Schadschneider, A.: Force-based models of pedestrian dynamics. Netw. Heterog. Media **6**(3), 425–442 (2011)

[6] Chraibi, M., Seyfried, A., Schadschneider, A.: Generalized centrifugal force model for pedestrian dynamics. Phys. Rev. E **82**, 046,111 (2010).

[7] Corradi, O., Hjorth, P., Starke, J.: Equation-free detection and continuation of a hopf bifurcation point in a particle model of pedestrian flow. SIAM J. Appl. Dyn. Syst. **11**(3), 1007–1032 (2012)

[8] Degond, P., Appert-Rolland, C., Moussaid, M., Petté, J., Theraulaz, G.: A hierarchy of heuristic-based models of crowd dynamics. J. Stat. Phys. **152**(6), 1033–1068 (2013)

[9] Dietrich, F., Köster, G.: Gradient navigation model for pedestrian dynamics. Phys. Rev. E **89**, 062,801 (2014)

[10] Fiorini, P., Shiller, Z.: Motion planning in dynamic environments using velocity obstacles. Int. J. Robot. Res. **17**(7), 760–772 (1998).

[11] Guo, R., Wong, S.C., Huang, H., Lam, W.H.K.: A microscopic pedestrian-simulation model and its application to intersecting flows. Phys. A **389**(3), 515–526 (2010)

[12] Helbing, D.: Traffic and related self-driven many-particle systems. Rev. Mod. Phys. **73**, 1067–1141 (2001).

[13] Helbing, D., Farkas, I., Vicsek, T.: Freezing by heating in a driven mesoscopic system. Phys. Rev. Lett. **84**, 1240–1243 (2000)

[14] Helbing, D., Johansson, A., Mathiesen, J., Jensen, M.H., Hansen, A.: Analytical approach to continuous and intermittent bottleneck flows. Phys. Rev. Lett. **97**, 168,001 (2006).

[15] Helbing, D., Molnár, P.: Social force model for pedestrian dynamics. Phys. Rev. E **51**, 4282–4286 (1995).

[16] Köster, G., Treml, F., Gödel, M.: Avoiding numerical pitfalls in social force models. Phys. Rev. E **87** (2013)

[17] Maury, B., Venel, J.: Un modèle de mouvement de foule. ESSAIM: Proc. **18**, 143–152 (2007)

[18] Monneau, R., Roussignol, M., Tordeux, A.: Invariance and homogenization of an adaptive time gap car-following model. Nonlinear Differ. Equ. Appli. **21**(4), 491–517 (2014)

[19] Nakayama, A., Hasebe, K., Sugiyama, Y.: Instability of pedestrian flow and phase structure in a two-dimensional optimal velocity model. Phys. Rev. E **71**, 036,121 (2005)

[20] Ondřej, J., Pettré, J., Olivier, A.H., Donikian, S.: A synthetic-vision-based steering approach for crowd simulation. In: ACM Trans. Graph., vol. 29, pp. 123:1 – 123:9. ACM, New York, NY, USA (2010)

[21] Pelechano, N., O'Brien, K., Silverman, B., Badler, N.: Crowd simulation incorporating agent psychological models, roles and communication. In: First International Workshop on Crowd Simulation, vol. 2, pp. 21–30. Lausanne (2005)

[22] PTV AG: PTV Vissim 7.0 – User Manual. PTV Group, Haid-und-Neu-Str. 15, D-76131 Karlsruhe, Germany (2014)

[23] Schadschneider, A., Chowdhury, D., Nishinari, K.: Stochastic Transport in Complex Systems. From Molecules to Vehicles. Elsevier Science Publishing Co Inc. (2010)

[24] Schneider, V., Könnecke, R.: Simulating evacuation processes with aseri. In: Pedestrian and Evacuation Dynamics, pp. 303–314. Springer (2002)

[25] TraffGo HT GmbH: Handbuch PedGo 2, PedGo Editor 2 (2005). Www.evacuation-simulation.com

[26] Venel, J.: Integrating strategies in numerical modelling of crowd motion. In: Pedestrian and Evacuation Dynamics 2008 (2010)

[27] Zhang, J., Klingsch, W., Schadschneider, A., Seyfried, A.: Ordering in bidirectional pedestrian flows and its influence on the fundamental diagram. J. Stat. Mech. Theor. Exp. **2012**(02), P02,002 (2012).

A.3 ARTICLE II

Calculating ellipse overlap areas

G. B. HUGHES AND M. CHRAIBI

COMPUTING AND VISUALIZATION IN SCIENCE (2012)

Comput Visual Sci (2012) 15:291–301, 2012
10.1007/s00791-013-0214-3

Calculating Ellipse Overlap Areas

Gary B. Hughes[1], Mohcine Chraibi[2]

Abstract
We present a general algorithm for finding the overlap area between two ellipses. The algorithm is based on finding a segment area (the area between an ellipse and a secant line) given two points on the ellipse. The Gauss-Green formula is used to determine the ellipse sector area between two points, and a triangular area is added or subtracted to give the segment area. For two ellipses, overlap area is calculated by adding the areas of appropriate sectors and polygons. Intersection points for two general ellipses are found using Ferrari's quartic formula to solve the polynomial that results from combining the two ellipse equations. All cases for the number of intersection points (0, 1, 2, 3, 4) are handled. The algorithm is implemented in c-code, and has been tested with a range of input ellipses. The code is efficient enough for use in simulations that require many overlap area calculations.

Keywords
Shape; Ellipse Area; Ellipse Sector; Ellipse Segment; Ellipse Overlap; Algorithm; Quartic Formula

[1] *California Polytechnic State University, Statistics Department, San Luis Obispo, CA 93407-0405, USA*
[2] *Jülich Supercomputing Centre, Forschungszentrum Jülich GmbH, D-52425 Jülich, Germany*

Contents

Introduction

Ellipses are useful in many applied scenarios, and in widely disparate fields. In our research, which happens to be in two very different areas, we have encountered a common need for efficiently calculating the overlap area between two ellipses.

In one case, the design for a solar calibrator on-board an orbiting satellite required an efficient algorithm for ellipse overlap area. Imaging systems aboard satellites rely on semi-conductor detectors whose performance changes over time due to many factors. To produce consistent data, some means of calibrating the detectors is required; see, e.g., [1]. Some systems use the sun as a light source for calibration. In a typical solar calibrator, incident sunlight passes through an attenuator grating and impinges on a diffuser plate, which is oriented obliquely to the attenuator grating. The attenuator grating is a pattern of circular openings. When sunlight passes through the circular openings, projections of the circles onto the oblique diffuser plate become small ellipses. The projection of the large circular entrance aperture on the oblique diffuser plate is also an ellipse. The total incident light on the calibrator is proportional to the sum of all the areas of the smaller ellipses that are contained within the larger entrance aperture ellipse. However, as the calibration process proceeds, the satellite is moving through its orbit, and the angle from the sun into the calibrator changes (˜7° in 2 minutes). The attenuator grating ellipses thus move across the entrance aperture, and some of the smaller ellipses pass in and out of the entrance aperture ellipse during calibration. Movement of the small ellipses across the aperture creates fluctuations in the total amount of incident sunlight reaching the calibrator in the range of 0.3 to 0.5%. This jitter creates errors in the calibration algorithms. In order to model the jitter, an algorithm is required for determining the overlap area of two ellipses. Monte Carlo integration had been used; however, the method is numerically intensive because it converges very slowly, so it was not an attractive approach for modeling the calibrator due to the large number of ellipses that must be modeled.

In a more down-to-earth setting, populated places such as city streets or building corridors can become quite congested while crowds of people are moving about. Understanding the dynamics of pedestrian movement in these scenarios can be beneficial in many ways. Pedestrian dynamics can provide critical input to the design of buildings or city infrastructure, for example by predicting the effects of specific crowd management strategies, or the behavior of crowds utilizing emergency escape routes. Current research in pedestrian dynamics is making steady progress toward realistic modeling of local movement; see, e.g., [2]. The model presented in [2] is based on the concept of elliptical volume exclusion for individual pedestrians. Each model pedestrian is surrounded by an elliptical footprint area that the model uses to anticipate obstacles and other pedestrians in or near the intended path. The footprint area is influenced by an individuals' velocity; for example, the exclusion area in front of a fast-moving pedestrian is elongated when compared to a slower-moving individual, since a pedestrian is generally thinking a few steps ahead. As pedestrians travel through a confined space, their collective exclusion areas become denser, and the areas will eventually begin to overlap. A force-based model will produce a repulsive force between overlapping exclusion areas, causing the pedestrians to slow down or change course when the exclusion force becomes large. Implementing the force-based model with elliptical exclusion areas in a simulation requires calculating the overlap area between many different ellipses in the most general orientations. The ellipse area overlap algorithm must also be efficient, so as not to bog down the simulation.

Simulations for both the satellite solar calibrator and force-based pedestrian dynamic model require efficient calculation of the overlap area between two ellipses. In this paper, we provide an algorithm that has served well for both applications. The core component of the overlap area algorithm is based on determining the area of an *ellipse segment*, which is the area between a secant line and the ellipse boundary. The segment algorithm forms the basis of an application for calculating the overlap area between two general ellipses.

1. Ellipse area, sector area and segment area

1.1 Ellipse Area

Consider an ellipse that is centered at the origin, with its axes aligned to the coordinate axes. If the semi-axis length along the x-axis is A, and the semi-axis length along the y-axis is B, then the ellipse is defined by a locus of points that satisfy the implicit polynomial equation

$$\frac{x^2}{A^2} \quad \frac{y^2}{B^2} \quad 1 \tag{1}$$

The same ellipse can be defined parametrically by:

$$\left.\begin{array}{ll} x & A \cdot \cos\ t \\ y & B \cdot \sin\ t \end{array}\right\} \ 0 \leq t \leq 2\pi \tag{2}$$

The area of such an ellipse can be found using the parameterized form with the Gauss-Green formula:

$$\begin{aligned} \text{Area} \quad & \frac{1}{2}\int_A^B x\ t\ \cdot y'\ t\ - y\ t\ \cdot x'\ t\ \ dt \\ & \frac{1}{2}\int_0^{2\pi} A \cdot \cos\ t\ \cdot B \cdot \cos\ t\ - B \cdot \sin\ t\ \cdot\ -A\ \cdot \sin\ t\ \ dt \\ & \frac{A \cdot B}{2}\int_0^{2\pi} \cos^2\ t \quad \sin^2\ t\ \ dt \quad \frac{A \cdot B}{2}\int_0^{2\pi} dt \\ & \pi \cdot A \cdot B \end{aligned} \tag{3}$$

1.2 Ellipse Sector Areas

We define the *ellipse sector* between two points (x_1, y_1) and (x_2, y_2) on the ellipse as the area that is swept out by a vector from the origin to the ellipse, beginning at (x_1, y_1), as the vector travels along the ellipse in a counter-clockwise direction from (x_1, y_1) to (x_2, y_2). An example is shown in Fig. 1. The Gauss-Green formula can also be used to determine the area of such an ellipse sector.

$$\text{Sector Area} \quad \frac{A\cdot B}{2}\int_{\theta_1}^{\theta_2} dt$$
$$\frac{\theta_2-\theta_1 \quad \cdot A\cdot B}{2} \tag{4}$$

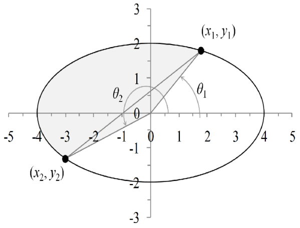

Figure 1. The area of an *ellipse sector* between two points on the ellipse is the area swept out by a vector from the origin to the first point as the vector travels along the ellipse in a counter-clockwise direction to the second point. The area of an ellipse sector can be determined with the Gauss-Green formula, using the parametric angles θ_1 and θ_2.

The parametric angle θ that is formed between the x-axis and a point (x, y) on the ellipse is found from the ellipse parameterizations:

$$x \quad A\cdot\cos\ \theta \qquad \Rightarrow \theta \quad \cos^{-1}\ x/A$$
$$y \quad B\cdot\sin\ \theta \qquad \Rightarrow \theta \quad \sin^{-1}\ y/B$$

For a circle (A B in the ellipse implicit polynomial form), the parametric angle corresponds to the geometric (visual) angle that a line from the origin to the point (x, y) makes with the x-axis. However, the same cannot be said for an ellipse; that is, the geometric (visual) angle is *not* the same as the parametric angle used in the area calculation. For example, consider the ellipse in Fig. 1; the implicit polynomial form is

$$\frac{x^2}{4^2} \quad \frac{y^2}{2^2} \quad 1 \tag{5}$$

Suppose the point (x_1, y_1) is at $\left(4/\sqrt{5}, 4/\sqrt{5}\right)$. The point is on the ellipse, since

$$\frac{\left(4/\sqrt{5}\right)^2}{4^2} \quad \frac{\left(4/\sqrt{5}\right)^2}{2^2} \quad \frac{4^2/5}{4^2} \quad \frac{4^2/5}{2^2} \quad \frac{1}{5} \quad \frac{4}{5} \quad 1$$

A line segment from the origin to $\left(4/\sqrt{5}, 4/\sqrt{5}\right)$ forms an angle with the x-axis of $\pi/4$ ($\approx$0.7485398). However, the ellipse parametric angle to the same point is:

$$\theta \quad \cos^{-1}\left(\frac{4/\sqrt{5}}{4}\right) \quad \cos^{-1}\left(\frac{1}{\sqrt{5}}\right) \approx 1.10715$$

The same angle can also be found from the parametric equation for y:

$$\theta \quad \sin^{-1}\left(\frac{4/\sqrt{5}}{2}\right) \quad \sin^{-1}\left(\frac{2}{\sqrt{5}}\right) \approx 1.10715$$

The angle found by using the parametric equations does not match the geometric angle to the point that defines the angle.

When determining the parametric angle for a given point (x, y) on the ellipse, the angle must be chosen in the proper quadrant, based on the signs of x and y. For the ellipse in Fig. 1, suppose the point (x_2, y_2) is at $\left(-3, -\sqrt{7}/2\right)$. The parametric angle that is determined from the equation for x is:

$$\theta \quad \cos^{-1}\left(\frac{-3}{4}\right) \approx 2.41886$$

Quadrant II ($x < 0$ and $y \geq 0$) $\theta \quad \arccos\ x/A$ $\quad \pi - \arcsin\ y/B$	**Quadrant I** ($x \geq 0$ and $y \geq 0$ $\theta \quad \arccos\ x/A$ $\quad \arcsin\ y/B$
Quadrant III ($x < 0$ and $y < 0$) $\theta \quad 2\pi - \arccos\ x/A$ $\quad \pi - \arcsin\ y/B$	**Quadrant IV** ($x \geq 0 \quad y < 0$) $\theta \quad 2\pi - \arccos\ x/A$ $\quad 2\pi \quad \arcsin\ y/B$

Table 1. Relations for finding the parametric angle that corresponds to a given point (x, y) on the ellipse $x^2/A^2 + y^2/B^2 = 1$. The parametric angle is formed between the positive x-axis and a line drawn from the origin to the given point, with counterclockwise being positive. For the standard (principal-valued) inverse trigonometric functions, the resulting angle will be in the range $0 \leq \theta < 2\pi$ for any point on the ellipse.

The parametric angle that is determined from the equation for y is:

$$\theta \quad \sin^{-1}\left(\frac{-\sqrt{7}/2}{2}\right) \quad \sin^{-1}\left(\frac{-\sqrt{7}}{4}\right) \approx -.722734$$

The apparent discrepancy is resolved by recalling that inverse trigonometric functions are usually implemented to return a ‘principal value’ that is within a conventional range. The typical (principal-valued) $\theta \quad \arccos\ x$ function returns angles in the range $0 = \theta = \pi$, and the typical (principal-valued) $\theta \quad \arcsin\ x$ function returns angles in the range $-\pi/2 \quad \theta \quad \pi/2$. When the principal-valued inverse trigonometric functions return angles in the typical ranges, the ellipse parametric angles, defined to be from the x-axis, with positive angles in the counter-clockwise direction, can be found with the relations in Table **??**.

The point at $\left(-3, -\sqrt{7}/2\right)$ on the ellipse of Fig. 1 is in Quadrant III. Using the relations in Table **??**, the parametric angle that is determined from the equation for x is:

$$\theta \quad 2\pi - \arccos\ \frac{-3}{4} \ \approx 3.86433$$

The parametric angle that is determined from the equation for y is:

$$\theta \quad \pi - \arcsin\ \frac{-\sqrt{7}/2}{2} \ \approx 3.86433$$

With the proper angles, the Gauss-Green formula can be used to determine the area of the sector from the point at $\left(4/\sqrt{5}, 4/\sqrt{5}\right)$ to the point $\left(-3, -\sqrt{7}/2\right)$ in the ellipse of Fig. 1.

$$\begin{aligned} \text{Sector Area} \quad & \frac{\theta_2 - \theta_1 \quad \cdot A \cdot B}{2} \\ & \frac{\left[\left(2\pi - \arccos\left(\frac{-3}{4}\right)\right) - \arccos\left(\frac{4/\sqrt{5}}{4}\right) \quad \right] \cdot 4 \cdot 2}{2} \\ \approx & 11.0287 \end{aligned} \tag{6}$$

The Gauss-Green formula is sensitive to the direction of integration. For the larger goal of determining ellipse overlap areas, we define the ellipse sector area to be calculated from the first point (x_1, y_1) to the second point (x_2, y_2) in a *counter-clockwise* direction along the ellipse. For example, if the points (x_1, x_1) and (x_2, y_2) of Fig. 1 were to have their labels switched, then the ellipse sector defined by the new points will have an area that is complementary to that of the sector in Fig. 1, as shown in Fig. 2.

Switching the point labels, as shown in Fig. 2, also causes the angle labels to be switched, resulting in the condition that $\theta_1 > \theta_2$. Since using the definitions in Table **??** will always produce an angle in the range $0 \quad \theta < 2\pi$ for any point on the ellipse, the first angle can be transformed by subtracting 2π to restore the condition that $\theta_1 < \theta_2$. The sector area formula given above can then be used, with the integration angle from $(\theta_1 - 2\pi)$ through θ_2. With the angle labels shown in Fig. 2, the area of

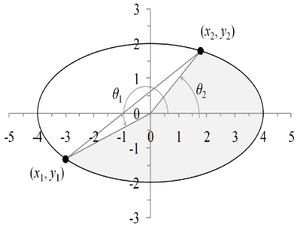

Figure 2. We define the ellipse sector area to be calculated from the first point (x_1, y_1) to the second point (x_2, y_2) in a counter-clockwise direction along the ellipse.

the sector from the point at $\left(-3, -\sqrt{7}/2\right)$ to the point at $\left(4/\sqrt{5}, 4/\sqrt{5}\right)$ in a counter-clockwise direction is:

$$\begin{aligned} \text{Sector Area} \quad & \frac{\theta_2 - \quad \theta_1 - 2\pi \quad \cdot A \cdot B}{2} \\ & \frac{\left[\left(2\pi - \arccos\left(\frac{-3}{4}\right)\right) - \left(\arccos\left(\frac{4/\sqrt{5}}{4}\right) - 2\pi\right)\right] \cdot 4 \cdot 2}{2} \\ \approx & 14.1040 \end{aligned} \tag{7}$$

The two sector areas shown in Fig. 1 and Fig. 2 are complementary, in that they add to the total ellipse area. Using the angle labels as shown in Fig. 1 for both sector areas:

$$\begin{aligned} \text{Total Area} \quad & \frac{\theta_2 - \theta_1 \quad \cdot A \cdot B}{2} \qquad \frac{\theta_1 - \quad \theta_2 - 2\pi \quad \cdot A \cdot B}{2} \\ & \frac{2\pi \quad \cdot A \cdot B}{2} \qquad \pi \cdot A \cdot B \\ & \pi \cdot 4 \cdot 2 \\ \approx & 25.1327 \end{aligned} \tag{8}$$

1.3 Ellipse Segment Areas

For the overall goal of determining overlap areas between ellipses and other curves, a useful measure is the area of what we will call an *ellipse segment*. A secant line drawn between two points on an ellipse partitions the ellipse area into two fractions, as shown in Fig. 1 and Fig. 2. We define the ellipse segment as the area confined by the secant line and the portion of the ellipse from the first point (x_1, y_1) to the second point (x_2, y_2) *traversed in a counter-clockwise direction*. The segment's complement is the second of the two areas that are demarcated by the secant line. For the ellipse of Fig. 1, the area of the segment defined by the secant line through the points (x_1, y_1) and (x_2, y_2) is the area of the sector *minus* the area of the triangle defined by the two points and the ellipse center. To find the area of the triangle, suppose that the coordinates for the vertices of are known, e.g., as (x_1, y_1), (x_2, y_2) and (x_3, y_3). Then the triangle area can be found by:

$$\begin{aligned} \text{Triangle Area} \quad & \frac{1}{2} \cdot \left| det \begin{pmatrix} x_1 & x_2 & x_3 \\ y_1 & y_2 & y_3 \\ 1 & 1 & 1 \end{pmatrix} \right| \\ & \frac{1}{2} \cdot \left| x_1 \cdot \quad y_2 - y_3 \quad - x_2 \cdot \quad y_1 - y_3 \qquad x_3 \cdot \quad y_1 - y_2 \quad \right| \end{aligned} \tag{9}$$

In the case where one vertex, say (x_3, y_3), is at the origin, then the area formula for the triangle can be simplified to:

$$\text{Triangle Area} \quad \frac{1}{2} \cdot |x_1 \cdot y_2 - x_2 \cdot y_1| \tag{10}$$

For the case depicted in Fig. 1, subtracting the triangle area from the area of the ellipse sector area gives the area between the secant line and the ellipse, i.e., the area of the ellipse segment counter-clockwise from (x_1, y_1) to (x_2, y_2):

$$\text{Segment Area} \quad \frac{\theta_2 - \theta_1 \quad \cdot A \cdot B}{2} - \frac{1}{2} \cdot |x_1 \cdot y_2 - x_2 \cdot y_1| \tag{11}$$

For the ellipse of Fig. 1, with the points at $\left(4/\sqrt{5}, 4/\sqrt{5}\right)$ and $\left(-3, -\sqrt{7}/2\right)$, the area of the segment defined by the secant line is:

$$\frac{\left[\left(2\pi - \arccos\left(\frac{-3}{4}\right)\right) - \arccos\left(\frac{4/\sqrt{5}}{4}\right)\ \right]\cdot 4\cdot 2}{2} - \frac{1}{2}\cdot\left|\frac{4}{\sqrt{5}}\cdot\frac{-\sqrt{7}}{2} - \frac{4}{\sqrt{5}}\cdot -3\right|$$
$$\approx 9.52865$$

For the ellipse of Fig. 2, the area of the segment shown is the sector area *plus* the area of the triangle.

$$\text{Segment Area} \quad \frac{\theta_2 - \quad \theta_1 - 2\pi \quad \cdot A\cdot B}{2} \quad \frac{1}{2}\cdot|x_1\cdot y_2 - x_2\cdot y_1| \tag{12}$$

With the points at $\left(-3, -\sqrt{7}/2\right)$ and $\left(4/\sqrt{5}, 4/\sqrt{5}\right)$ the area of the segment is:

$$\frac{\left[\left(2\pi - \arccos\left(\frac{-3}{4}\right)\right) - \left(\arccos\left(\frac{4/\sqrt{5}}{4}\right) - 2\pi\ \right)\right]\cdot 4\cdot 2}{2} \quad \frac{1}{2}\cdot\left|\frac{4}{\sqrt{5}}\cdot\frac{-\sqrt{7}}{2} - \frac{4}{\sqrt{5}}\cdot -3\right|$$
$$\approx 15.60409411$$

For the case shown in Fig. 1 and Fig. 2, the sector areas were shown to be complementary. The segment areas are also complementary, since the triangle area is added to the sector of Fig. 1, but subtracted from the sector of Fig. 2. Using the angle labels as shown in Fig. 1 for both sector areas:

$$\begin{aligned}\text{Total Area} \quad & \left[\frac{\theta_2 - \theta_1 \quad \cdot A\cdot B}{2} - \frac{1}{2}\cdot|x_1\cdot y_2 - x_2\cdot y_1|\right] \\ & \left[\frac{\theta_1 - \quad \theta_2 - 2\pi \quad \cdot A\cdot B}{2} \quad \frac{1}{2}\cdot|x_1\cdot y_2 - x_2\cdot y_1|\right] \\ & \pi\cdot A\cdot B \quad \pi\cdot 4\cdot 2 \approx 25.1327\end{aligned} \tag{13}$$

The key difference between the cases in Fig. 1 and Fig. 2 that requires the area of the triangle to be either subtracted from, or added to, the sector area is the size of the *integration angle*. If the integration angle is less than π, then the triangle area must be subtracted from the sector area to give the segment area. If the integration angle is greater than π, the triangle area must be added to the sector area.

1.4 A Core Algorithm for Ellipse Segment Area

A generalization of the cases given in Fig. 1 and Fig. 2 suggests a robust approach for determining the ellipse segment area defined by a secant line drawn between two given points on the ellipse. The ellipse is assumed to be centered at the origin, with its axes parallel to the coordinate axes. We define the segment area to be demarcated by the secant line and the ellipse proceeding counter-clockwise from the first given point (x_1, y_1) to the second given point (x_2, y_2). The ELLIPSE_SEGMENT algorithm is outlined in Table 2, with pseudo-code presented in List. 1. The ellipse is passed to the algorithm by specifying the semi-axes lengths, $A > 0$ and $B > 0$. The points are passed to the algorithm as (x_1, x_1) and (x_2, y_2), which must be on the ellipse.

For robustness, the algorithm should avoid divide-by-zero and inverse-trigonometric errors, so data checks should be included. The ellipse parameters A and B must be greater than zero. A check is provided to determine whether the points are on the ellipse, to within some numerical tolerance, ε. Since the points can only be checked as being on the ellipse to within some numerical tolerance, it may still be possible for the x-values to be slightly larger than A, leading to an error when calling the inverse trigonometric functions with the argument x/A. In this case, the algorithm checks whether the x-value close to A or $-A$, that is within a distance that is less than the numerical tolerance. If the closeness condition is met, then the algorithm assumes that the calling function passed a value that is indeed on the ellipse near the point $(A, 0)$ or $(-A, 0)$, so the value of x is nudged back to A or $-A$ to avoid any error when calling the inverse trigonometric functions. The core algorithm, including all data checks, is shown in List. 1.

ELLIPSE_SEGMENT Area Algorithm:

1. $$\theta_1 \quad \begin{cases} \arccos\ x_1/A & ,\ y_1 \geq 0 \\ 2\pi - \arccos\ x_1/A & ,\ y_1 < 0 \end{cases}$$
$$\theta_2 \quad \begin{cases} \arccos\ x_2/A & ,\ y_2 \geq 0 \\ 2\pi - \arccos\ x_2/A & ,\ y_2 < 0 \end{cases}$$

2. $$\widehat{\theta}_1 \quad \begin{cases} \theta_1 & ,\ \theta_1 < \theta_2 \\ \theta_1 - 2\pi, & \theta_1 > \theta_2 \end{cases}$$

3. $$\text{Area} \quad \frac{\theta_2 - \widehat{\theta}_1 \ \cdot A \cdot B}{2} \quad \frac{sign \ \ \theta_2 - \widehat{\theta}_1 - \pi}{2} \cdot |x_1 \cdot y_2 - x_2 \cdot y_1|$$

where:

the ellipse implicit polynomial equation is

$$\frac{x^2}{A^2} \quad \frac{y^2}{B^2} \quad 1$$

$A > 0$ is the semi-axis length along the x-axis

$B > 0$ is the semi-axis length along the y-axis

(x_1, y_1) is the first given point on the ellipse

(x_2, y_2) is the second given point on the ellipse

θ_1 and θ_2 are the parametric angles corresponding to the points (x_1, y_1) and (x_2, y_2)

Table 2. An outline of the ELLIPSE_SEGMENT area algorithm.

Listing 1. The ELLIPSE_SEGMENT algorithm is shown for calculating the area of a segment defined by the secant line drawn between two given points (x_1, y_1) and (x_2, y_2) on the ellipse $x_2/A_2 \quad y_2/B_2 \quad 1$. We define the segment area for this algorithm to be demarcated by the secant line and the ellipse proceeding counter-clockwise from the first given point (x_1, y_1) to the second given point (x_2, y_2).

```
   ELLIPSE_SEGMENT (A, B, X1, Y1, X2, Y2)
do if (A  0 or B  0)
    then return (-1, ERROR_ELLIPSE_PARAMETERS)                 :DATA CHECK
               2    2        2   2                      2   2        2   2
do if (|X1  /A + Y1  /B  Â  1| >  or |X1  /A + Y1  /B  Â  1| > )
    then return (-1, ERROR_POINTS_NOT_ON_ELLIPSE)              :DATA CHECK
do if (|X1|/A > )
    do if |X1| - A >
       then return (-1, ERROR_INVERSE_TRIG)                    :DATA CHECK
       else do if X1 < 0
            then X1  -A
            else X1  A
do if (|X2|/A > )
    do if |X2| - A >
       then return (-1, ERROR_INVERSE_TRIG)                    :DATA CHECK
       else do if X2 < 0
                then X2  -A
                else X2  A
do if (Y1 < 0)                          :ANGLE QUADRANT FORMULA (TABLE 1)
    then 1  2 Â acos (X1/A)
    else 1  acos (X1/A)
do if (Y2 < 0)                          :ANGLE QUADRANT FORMULA (TABLE 1)
    then 2  2 Â acos (X2/A)
    else 2  acos (X2/A)
do if (1 > 2)                                   :MUST START WITH 1 < 2
    then 1  1 - 2
do if ((2  Â  1) > )                         :STORE SIGN OF TRIANGLE AREA
    then trsgn  +1.0
    else trsgn  +1.0
area  0.5*(A*B*(2 - 1) Â trsgn*|X1*Y2 - X2*Y1|)
return (area, NORMAL_TERMINATION)
```

An implementation of the ELLIPSE_SEGMENT algorithm written in c–code is shown in Appendix **??**. The code compiles under Cygwin-1.7.7-1, and returns the following values for the two test cases presented in Fig. 1 and Fig. 2:

Listing 2. Return values for the test cases in Fig. 1 and Fig. 2

```
     cc call_es.c ellipse_segment.c -o call_es.exe
     ./call_es
    Calling ellipse_segment.c
    Fig. 1: segment area =          9.52864712, return_value = 0
    Fig. 2: segment area =         15.60409411, return_value = 0
    sum of ellipse segments = 25.13274123
```

```
        ellipse area by pi*A*B =             25.13274123
```

2. Extending the Core Segment Algorithm to more General Cases

2.1 Segment Area for a (Directional) Line through a General Ellipse

The core segment algorithm is based on an ellipse that is centered at the origin with its axes aligned to the coordinate axes. The algorithm can be extended to more general ellipses, such as rotated and/or translated ellipse forms. Start by considering the case for a standard ellipse with semi-major axis lengths of A and B that is centered at the origin and with its axes aligned with the coordinate axes. Suppose that the ellipse is rotated through a counter-clockwise angle φ, and that the ellipse is then translated so that its center is at the point (h, k). The rotated+translated ellipse could then be defined by the set of parameters (A, B, h, k, φ), with the understanding that the rotation through φ is performed before the translation through (h, k). The approach for extending the core segment area algorithm will be to determine analogs on the standard ellipse corresponding to any points of intersection between a shape of interest and the general rotated and translated ellipse. To identify corresponding points, features of the shape of interest are translated by $(-h, -k)$, and then rotated by $-\varphi$. The translated+rotated features are used to determine any points of intersection with a similar ellipse that is centered at the origin with its axes aligned to the coordinate axes. Then, the core segment algorithm can be called with the translated+rotated intersection points.

Rotation and translation are affine transformations that are also length- and area-preserving. In particular, the semi-axis lengths in the general rotated ellipse are preserved by both transformations, and corresponding points on the two ellipses will demarcate equal partition areas. Fig. 3 illustrates this idea, showing the ellipse of Fig. 1 which has been rotated counter-clockwise through an angle $\varphi = 3\pi/8$, then translated by $(h,k) = (-6, 3)$.

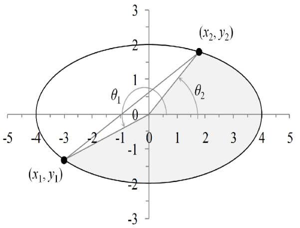

Figure 3. Translation and rotation are affine transformations that are also length-and area-preserving. Corresponding points on the two ellipses will demarcate equal partition areas.

Suppose that we desire to find the area of the rotated+translated ellipse sector defined by the line $y = -x$, where the line 'direction' travels from lower-right to upper-left, as shown in Fig. 3. We describe an approach for finding a segment in a rotated+translated ellipse, based on the core ellipse segment algorithm.

An ellipse that is centered at the origin, with its axes aligned to the coordinate axes, is defined parametrically by

$$\left.\begin{array}{l} x = A\cdot\cos\, t \\ y = B\cdot\sin\, t \end{array}\right\} \; 0 \le t \le 2\pi$$

Suppose the ellipse is rotated through an angle φ, with counter-clockwise being positive, and that the ellipse is then to be translated to put its center is at the point (h, k). Any point (x, y) on the standard ellipse can be rotated and translated to end up in a corresponding location on the new ellipse by using the transformation:

$$\begin{bmatrix} x_{TR} \\ y_{TR} \end{bmatrix} = \begin{bmatrix} \cos\,\varphi & -\sin\,\varphi \\ \sin\,\varphi & \cos\,\varphi \end{bmatrix} \cdot \begin{bmatrix} x \\ y \end{bmatrix} + \begin{bmatrix} h \\ k \end{bmatrix} \tag{14}$$

Rotation and translation of the original standard ellipse does not change the ellipse area, or the semi-axis lengths. One important feature of the algorithms presented here is that the semi-axis lengths A and B are in the direction of the x- and y-axes, respectively, in the *un-rotated* (standard) ellipse. In its rotated orientation, the semi-axis length A will rarely be oriented horizontally (in fact, for $\varphi = \pi/4$, the semi-axis length A will be oriented vertically). Regardless of the orientation of the rotated+translated ellipse, the algorithms presented here assume that the values of A and B passed into the algorithm represent the semi-axis lengths along the x- and y-axes, respectively, for the corresponding un-rotated, un-translated ellipse. The angle φ is the amount of counter-clockwise rotation required to put the ellipse into its desired location. Specifying a negative value for φ will rotate the standard ellipse through a clockwise angle. The angle φ can be specified in anywhere in the range (–8, +8); the working angle in the code will be computed from the given angle, modulo 2π, to avoid any potential errors (?) when calculating trigonometric values. The translation (h, k) is the absolute movement along the coordinate axes of the ellipse center to move a standard ellipse into its desired location. Negative values of h move the standard ellipse to the left; negative values of k move the standard ellipse down.

To find the area between the given line and the rotated+translated ellipse, the two curve equations can be solved simultaneously to find any points of intersection. But instead of searching for the points of intersection with the rotated+translated ellipse, it is more efficient to transform the two given points that define the line back through the translation (–h, –k) then rotation through $-\varphi$. The new line determined by the translated+rotated points will pass through the standard ellipse at points that are analogous to where the original line intersects the rotated+translated ellipse.

The transformations required to move the given points (x_1, y_1) and (x_2, y_2) into an orientation with respect to a standard ellipse that is analogous to their orientation to the given ellipse are the inverse of what it took to rotate+translate the ellipse to its desired position. The translation is performed first, then the rotation:

$$\begin{bmatrix} x_{i_0} \\ y_{i_0} \end{bmatrix} \quad \begin{bmatrix} \cos\ -\varphi & -\sin\ -\varphi \\ \sin\ -\varphi & \cos\ -\varphi \end{bmatrix} \cdot \begin{bmatrix} x_i - h \\ y_i - k \end{bmatrix} \tag{15}$$

Multiplying the vector by the matrix, and simplifying the negative-angle trig functions gives the following expressions for the translated+rotated points:

$$\begin{aligned} x_{i_0} &\quad \cos\ \varphi\ \cdot\ x_i - h \quad \sin\ \varphi\ \cdot\ y_i - k \\ y_{i_0} &\quad -\sin\ \varphi\ \cdot\ x_i - h \quad \cos\ \varphi\ \cdot\ y_i - k \end{aligned}$$

The two new points $\left(x_{1_0}, y_{1_0}\right)$ and $\left(x_{2_0}, y_{2_0}\right)$ can be used to determine a line, *e.g.*, by the point-slope method:

$$y \quad y_{1_0} \quad \frac{y_{2_0} - y_{1_0}}{x_{2_0} - x_{1_0}} \left(x - x_{1_0}\right) \tag{16}$$

The equation can also be formulated in an alternative way to accommodate cases where the translated+rotated line is vertical, or nearly so:

$$x \quad x_{1_0} \quad \frac{x_{2_0} - x_{1_0}}{y_{2_0} - y_{1_0}} \left(y - y_{1_0}\right) \tag{17}$$

Points of intersection are found by substituting the line equations into the standard ellipse equation, and solving for the remaining variable. For each case, define the slope as:

$$m_{yx} \quad \frac{y_{2_0} - y_{1_0}}{x_{2_0} - x_{1_0}}, \ m_{xy} \quad \frac{x_{2_0} - x_{1_0}}{y_{2_0} - y_{1_0}} \tag{18}$$

Then the two substitutions proceed as follows:

$$\begin{aligned} & y \quad y_{1_0} \quad m_{yx} \cdot \left(x - x_{1_0}\right) \ \text{into} \ \frac{x^2}{A^2} \quad \frac{y^2}{B^2} \quad 1 \\ & \Rightarrow \frac{x^2}{A^2} \quad \frac{\left(y_{1_0} \quad m_{yx} \cdot \left(x - x_{1_0}\right)\right)^2}{B^2} \quad 1 \\ & \Rightarrow \left[\frac{B^2 \quad A^2 \cdot \ m_{yx}\ ^2}{A^2}\right] \cdot x^2 \\ & \quad \left[2 \cdot \left(y_{1_0} \cdot m_{yx} - \ m_{yx}\ ^2 \cdot x_{1_0}\right)\right] \cdot x \\ & \quad \left[\left(y_{1_0}\right)^2 - 2 \cdot m_{yx} \cdot x_{1_0} \cdot y_{1_0} \quad \left(m_{yx} \cdot x_{1_0}\right)^2 - B^2\right] \\ & \quad 0 \end{aligned} \tag{19}$$

$$\begin{aligned} & x \quad x_{1_0} \quad m_{xy} \cdot \left(y - y_{1_0}\right) \text{ into } \frac{x^2}{A^2} \quad \frac{y^2}{B^2} \quad 1 \\ & \Rightarrow \frac{\left(x_{1_0} \quad m_{xy} \cdot \left(y - y_{1_0}\right)\right)^2}{A^2} \quad \frac{y^2}{B^2} \quad 1 \\ & \Rightarrow \left[\frac{A^2 \quad B^2 \cdot \quad m_{xy} \quad ^2}{B^2}\right] \cdot y^2 \\ & \quad \left[2 \cdot \left(x_{1_0} \cdot m_{xy} - \quad m_{xy} \quad ^2 \cdot y_{1_0}\right)\right] \cdot y \\ & \quad \left[\left(x_{1_0}\right)^2 - 2 \cdot m_{xy} \cdot x_{1_0} \cdot y_{1_0} \quad \left(m_{xy} \cdot y_{1_0}\right)^2 - A^2\right] \\ & \quad 0 \end{aligned} \tag{20}$$

If the translated+rotated line is not vertical, then use the first equation to find the x-values for any points of intersection. If the translated+rotated line is close to vertical, then the second equation can be used to find the y-values for any points of intersection. Since points of intersection between the line and the ellipse are determined by solving a quadratic equation $ax^2 \quad bx \quad c$, there are three cases to consider:

1. $\Delta \quad b^2 - 4ac < 0$: Complex Conjugate Roots (no points of intersection)
2. $\Delta \quad b^2 - 4ac \quad 0$: One Double Real Root (1 point of intersection; line tangent to ellipse)
3. $\Delta \quad b^2 - 4ac > 0$: Two Real Roots (2 points of intersection; line crosses ellipse)

For the first two cases, the segment area will be zero. For the third case, the two points of intersection can be sent to the core segment area algorithm. However, to enforce a consistency in area measures returned by the core algorithm, the integration direction is specified to be from the first point to the second point. As such, the ellipse line overlap algorithm should be sensitive to the order that the points are passed to the core segment algorithm. We suggest giving the line a 'direction' from the first given point on the line to the second. The line 'direction' can then be used to determine which is to be the first point of intersection, i.e., the first intersection point is where the line enters the ellipse based on what 'direction' the line is pointing. The segment area that will be returned from ELLIPSE_SEGMENT by passing the line's entry location as the first intersection point is the area within the ellipse to the right of the line's path.

The approach outlined above for finding the overlap area between a line and a general ellipse is implemented in the ELLIPSE_LINE_OVERLAP algorithm, with pseudo-code shown in List. 3. The ellipse is passed to the algorithm by specifying the counterclockwise rotation angle φ and the translation (h, k) that takes a standard ellipse and moves it to the desired orientation, along with the semi-axes lengths, $A > 0$ and > 0. The line is passed to the algorithm as two points on the line, (x_1, y_1) and (x_2, y_2). The 'direction' of the line is taken to be from (x_1, y_1) toward (x_2, y_2). Then, the segment area returned from ELLIPSE_SEGMENT will be the area within the ellipse to the right of the line's path.

Listing 3. The ELLIPSE_LINE_OVERLAP algorithm is shown for calculating the area of a segment in a general ellipse that is defined by a given line. The line is considered to have a 'direction' that runs from the first given point (x_1, y_1) to the second given point (x_2, y_2). The line 'direction' determines the order in which intersection points are passed to the ELLIPSE_SEGMENT algorithm, which will return the area of the segment that runs along the ellipse from the first point to the second in a counter-clockwise direction. Any routine that calls the algorithm ELLIPSE_LINE_OVERLAP must be sensitive to the order of points that are passed in.

```
(Area, Code) ← ELLIPSE\_LINE\_OVERLAP (A,B,H,K,$\varphi$,X1,Y1,X2,Y2)
 do if (A ≤ 0 or B ≤ 0)

     then return (-1, ERROR_ELLIPSE_PARAMETERS)        :DATA_CHECK

 do if ( $|\varphi| > 2\pi$)

     then $\varphi \leftarrow \varphi$ modulo $2\pi$   :BRING $\varphi$ INTO $-2\pi \le \varphi < 2\pi$ (?)

 do if ($|X1|/A > 2\pi$)

     then X1 ← -A

 X10 $\leftarrow \cos\varphi * X1 - H \quad \sin\varphi * Y1 - K$

```

```
Y10 ← $-\sin\varphi * X1 - H \quad \cos\varphi * Y1 - K$

X20 ← $\cos\varphi * X2 - H \quad \sin\varphi * Y2 - K$

Y20 ← $-\sin\varphi * X2 - H \quad \cos\varphi * Y2 - K$

do if ($|X20 - X10| > \varepsilon$ )                    :LINE IS NOT VERTICAL

    then m ← (Y20 − Y10)/(X20 − X10)  :STORE QUADRATIC COEFFICIENTS

        a ← ($B^2$ + $(A*m)^2$)/$A^2$

        b ← (2.0*(Y10*m −− $m^2$*X10))

        c ← ($Y10^2$ − 2.0*m*Y10*X10 + $(m*X10)^2$ −− $B^2$)

    else if (|Y20 −− Y10|  $> \varepsilon$)              :LINE IS NOT HORIZONTAL

        then m ← (X20 − X10)/(Y20 − Y10)   :STORE QUADRATIC COEFFS

            a ← ($A^2$ + $(B*m)^2$)/$B^2$

            b ← (2.0*(X10*m −− $m^2$*Y10))

            c ←($X10^2$ − 2.0*m*Y10*X10 + $(m*Y10)^2$ −− $A^2$)

    else return (−1, ERROR_LINE_POINTS)       :LINE POINTS TOO CLOSE

discrim ← $b^2$ − 4.0*a*c

do if (discrim < 0.0)                    :LINE DOES NOT CROSS ELLIPSE

    then return (0, NO_INTERSECT)

    else if (discrim > 0.0)                :TWO INTERSECTION POINTS

    then root1 ← (−b − sqrt (discrim))/(2.0*a)

        root2 ← (−b + sqrt (discrim))/(2.0*a)

    else return (0, TANGENT)                :LINE TANGENT TO ELLIPSE

do if ($|X20 - X10| > \varepsilon$)               :ROOTS ARE X−VALUES

    then do if (X10 < X20)         :ORDER PTS SAME AS LINE DIRECTION

            then x1 ← root1

                x2 ← root2

            else x1 ← root2

                x2 ← root1

    else do if (Y10 < Y20)                        :ROOTS ARE Y−VALUES

            then y1 ← root1        :ORDER PTS SAME AS LINE DIRECTION

                y2 ← root2

            else y1 ← root2

                y2 ← root1

(Area, Code) ← ELLIPSE_SEGMENT (A,B,x1,y1,x2,y2)

do if (Code < NORMAL_TERMINATION)

    then return (−1.0, Code)

    else return (Area, TWO_INTERSECTION_POINTS)
```

An implementation of the ELLIPSE_LINE_OVERLAP algorithm in c-code is shown in Appendix **??**. The code compiles under Cygwin-1.7.7-1, and returns the following values for the test cases presented above in Fig. 3, with both line ‘directions’:

Listing 4. Return values for the test cases in Fig. 3.

```
cc call_el.c ellipse_line_overlap.c ellipse_segment.c −o call_el.exe

./call_el

```

```
Calling ellipse_line_overlap.c

 area =                        4.07186819, return_value = 102

 reverse: area =               21.06087304, return_value = 102

 sum of ellipse segments =         25.13274123

 total ellipse area by pi*A*B =  25.13274123
```

2.2 Ellipse-Ellipse Overlap Area

The method described above for determining the area between a line and an ellipse can be extended to the task of finding the overlap area between two general ellipses. Suppose the two ellipses are defined by their semi-axis lengths, center locations and axis rotation angles. Let the two sets of parameters (A_1, B_1, h_1, k_1, φ_1) and (A_2, B_2, h_2, k_2, φ_2) define the two ellipses for which overlap area is sought. The approach presented here will be to first translate both ellipses by an amount ($-h_1$, $-k_1$) that puts the center of the first ellipse at the origin. Then, both translated ellipses are rotated about the origin by an angle $-\varphi_1$ that aligns the axes of the first ellipse with the coordinate axes; see Fig. 4. Intersection points are found for the two translated+rotated ellipses, using Ferrari's quartic formula. Finally, the segment algorithm described above is employed to find all the pieces of the overlap area.

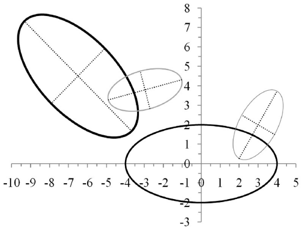

Figure 4. Intersection points on each curve are used with the ellipse segment area algorithm to determine overlap area, by calculating the area of appropriate segments, and polygons in certain cases. For the case of two intersection points, as shown above, the overlap area can be found by adding two segments, as shown in Fig. 5.

For example, consider a case of two general ellipses with two (non-tangential) points of intersection, as shown in Fig. 4. The translation+rotation transformations that put the first ellipse at the origin and aligned with the coordinate axes do not alter the overlap area. In the case shown in Fig. 4, the overlap area consists of one segment from the first ellipse and one segment from the second ellipse. The segment algorithm presented above can be used directly for ellipses centered at the origin and aligned with the coordinate axes. As such, the desired segment from the first ellipse can be found immediately with the segment algorithm, based on the points of intersection. To find the desired segment of the second ellipse, the approach presented here further translates and rotates the second ellipse so that the segment algorithm can also be used directly. The overlap area for the case shown in Fig. 4 is equal to the sum of the two segment areas, as shown in Fig. 5. Other cases, e.g. with 3 and 4 points of intersection, can also be handled using the segment algorithm.

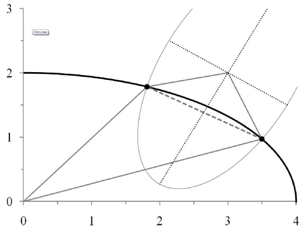

Figure 5. The area of overlap between two intersecting ellipses can be found by using the ellipse sector algorithm. In the case of two (non-tangential) intersection points, the overlap area is equal to the sum of two ellipse sectors. The sector in each ellipse is demarcated by the intersection points.

The overlap area algorithm presented here finds the area of appropriate sector(s) of each ellipse, which are demarcated by any points of intersection between the two ellipse curves. To find intersection points, the two ellipse equations are solved simultaneously. This step can be accomplished by using the implicit polynomial forms for each ellipse. The first ellipse equation, in its translated+rotated position is written as an implicit polynomial using the appropriate semi-axis lengths:

$$\frac{x^2}{A_1^2} \quad \frac{y^2}{B_1^2} \quad 1 \tag{21}$$

In a general form of this problem, the translation+rotation that puts the first ellipse centered at the origin and oriented with the coordinate axes will typically leave the second ellipse displaced and rotated. The implicit polynomial form for a more general ellipse that is rotated and/or translated away from the origin is written in the conventional way as:

$$AA \cdot x^2 \quad BB \cdot x \cdot y \quad CC \cdot y^2 \quad DD \cdot x \quad EE \cdot y \quad FF \quad 0 \tag{22}$$

Any points of intersection for the two ellipses will satisfy these two equations simultaneously. An intermediate goal is to find the implicit polynomial coefficients in Ellipse Eq. 22 that describe the second ellipse after the translation+rotation that puts the first ellipse centered at the origin and oriented with the coordinate axes. The parameters that describe the second ellipse after the translation+rotation can be determined from the original parameters for the two ellipses. The first step is to translate the second ellipse center (h_2, k_2) through an amount $(–h_1, –k_1)$, then rotate the center-point through $–\varphi_1$ to give a new center point (h_{2TR}, k_{2TR}):

$$\begin{aligned} h_{2TR} &\quad \cos \; -\varphi_1 \; \cdot \; h_2 - h_1 \; - \sin \; -\varphi_1 \; \cdot \; k_2 - k_1 \\ k_{2TR} &\quad \sin \; -\varphi_1 \; \cdot \; h_2 - h_1 \quad \cos \; -\varphi_1 \; \cdot \; k_2 - k_1 \end{aligned}$$

The coordinates for a point (x_{TR}, y_{TR}) on the second ellipse in its new translated+rotated position can be found from the following parametric equations, based on an ellipse with semi-axis lengths A_2 and B_2 that is centered at the origin, then rotated and translated to the desired position:

$$\left.\begin{aligned} x_{TR} &\quad A_2 \cdot \cos \; t \; \cdot \cos \; \varphi_2 - \varphi_1 \; - B_2 \cdot \sin \; t \; \cdot \sin \; \varphi_2 - \varphi_1 \quad h_{2_{TR}} \\ y_{TR} &\quad A_2 \cdot \cos \; t \; \cdot \sin \; \varphi_2 - \varphi_1 \quad B_2 \cdot \sin \; t \; \cdot \cos \; \varphi_2 - \varphi_1 \quad k_{2_{TR}} \end{aligned}\right\} \; 0 \leq t \leq 2\pi$$

To find the implicit polynomial coefficients from the parametric form, further transform the locus of points (x_{TR}, y_{TR}) so that they lie on the ellipse $(A_2, B_2, 0, 0, 0)$, which is accomplished by first translating (x_{TR}, y_{TR}) through $(–(h_1 – h_2), –(k_1 – k_2))$ and then rotating the point through the angle $–(\varphi_1 – \varphi_2)$:

$$\begin{aligned} x &\quad \cos \; \varphi_2 - \varphi_1 \; \cdot \; x_{TR} - \; h_1 - h_2 \; - \sin \; \varphi_2 - \varphi_1 \; \cdot \; y_{TR} - \; k_1 - k_2 \\ y &\quad \sin \; \varphi_2 - \varphi_1 \; \cdot \; x_{TR} - \; h_1 - h_2 \quad \cos \; \varphi_2 - \varphi_1 \; \cdot \; y_{TR} - \; k_1 - k_2 \end{aligned}$$

The locus of points (x, y) should satisfy the standard ellipse equation with the appropriate semi-axis lengths:

$$\frac{x^2}{A_2^2} \quad \frac{y^2}{B_2^2} \quad 1 \tag{23}$$

Finally, the implicit polynomial coefficients for Ellipse Eq. 22 are found by substituting the expressions for the point (x, y) into the standard ellipse equation, yielding the following ellipse equation:

$$\begin{aligned} &\frac{\cos \; \varphi_2 - \varphi_1 \; \cdot \; x_{TR} - \; h_1 - h_2 \; - \sin \; \varphi_2 - \varphi_1 \; \cdot \; y_{TR} - \; k_1 - k_2 \quad ^2}{A_2^2} \\ &\frac{\sin \; \varphi_2 - \varphi_1 \; \cdot \; x_{TR} - \; h_1 - h_2 \quad \cos \; \varphi_2 - \varphi_1 \; \cdot \; y_{TR} - \; k_1 - k_2 \quad ^2}{B_2^2} \\ &1 \end{aligned} \tag{24}$$

where (xx_{TR}, y_{TR}) are defined as above. Expanding the terms, and then re-arranging the order to isolate like terms yields the following expressions for the implicit polynomial coefficients of a general ellipse with the set of parameters $(A_2, B_2, h_{2TR}, k_{2TR}, \varphi_2 - \varphi_1)$:

$$
\begin{aligned}
AA \quad & \frac{\cos^2\ \varphi_2-\varphi_1}{A_2^2} \quad \frac{\sin^2\ \varphi_2-\varphi_1}{B_2^2} \\
BB \quad & \frac{2\cdot\sin\ \varphi_2-\varphi_1\ \cdot\cos\ \varphi_2-\varphi_1}{A_2^2} - \frac{2\cdot\sin\ \varphi_2-\varphi_1\ \cdot\cos\ \varphi_2-\varphi_1}{B_2^2} \\
CC \quad & \frac{\sin^2\ \varphi_2-\varphi_1}{A_2^2} \quad \frac{\cos^2\ \varphi_2-\varphi_1}{B_2^2} \\
DD \quad & \frac{-2\cdot\cos\ \varphi_2-\varphi_1\ \cdot\ h_{2_{TR}}\cdot\cos\ \varphi_2-\varphi_1\quad k_{2_{TR}}\cdot\sin\ \varphi_2-\varphi_1}{A_2^2} \\
& \frac{2\cdot\sin\ \varphi_2-\varphi_1\ \cdot\ k_{2_{TR}}\cdot\cos\ \varphi_2-\varphi_1\ -h_{2_{TR}}\cdot\sin\ \varphi_2-\varphi_1}{B_2^2} \\
EE \quad & \frac{-2\cdot\sin\ \varphi_2-\varphi_1\ \cdot\ h_{2_{TR}}\cdot\cos\ \varphi_2-\varphi_1\quad k_{2_{TR}}\cdot\sin\ \varphi_2-\varphi_1}{A_2^2} \\
& \frac{2\cdot\cos\ \varphi_2-\varphi_1\ \cdot\ h_{2_{TR}}\cdot\sin\ \varphi_2-\varphi_1\ -k_{2_{TR}}\cdot\cos\ \varphi_2-\varphi_1}{B_2^2} \\
FF \quad & \frac{h_{2_{TR}}\cdot\cos\ \varphi_2-\varphi_1\quad k_{2_{TR}}\cdot\sin\ \varphi_2-\varphi_1\quad {}^{2}}{A_2^2} \\
& \frac{h_{2_{TR}}\cdot\sin\ \varphi_2-\varphi_1\ -k_{2_{TR}}\cdot\cos\ \varphi_2-\varphi_1\quad {}^{2}}{B_2^2} - 1
\end{aligned}
\tag{25}
$$

For the area overlap algorithm presented in this paper, the points of intersection between the two general ellipses are found by solving simultaneously the two implicit polynomials denoted above as Ellipse Eq. 21 and Ellipse Eq. 22. Solving for x in the first equation:

$$\frac{x^2}{A_1^2}\quad\frac{y^2}{B_1^2}\quad 1\quad\Rightarrow\quad x\quad\pm\sqrt{A_1^2\cdot\left(1-\frac{y^2}{B_1^2}\right)} \tag{26}$$

Substituting these expressions for x into Ellipse Eq. 22 and then collecting terms yields a quartic polynomial in y. It turns out that substituting either the positive or the negative root gives the same quartic polynomial coefficients, which are:

$$cy\ 4\ \cdot y^4\quad cy\ 3\ \cdot y^3\quad cy\ 2\ \cdot y^2\quad cy\ 1\ \cdot y\quad cy\ 0\quad 0 \tag{27}$$

where:

$$
\begin{aligned}
\frac{cy\ 4}{B_1} \quad & A_1^4\cdot AA^2\quad B_1^2\cdot\left[A_1^2\cdot\left(BB^2-2\cdot AA\cdot CC\right)\quad B_1^2\cdot CC^2\right] \\
\frac{cy\ 3}{B_1} \quad & 2\cdot B_1\cdot\left[B_1^2\cdot CC\cdot EE\quad A_1^2\cdot\ BB\cdot DD-AA\cdot EE\ \right] \\
\frac{cy\ 2}{B_1} \quad & A_1^2\cdot\left\{\left[B_1^2\cdot\left(2\cdot AA\cdot CC-BB^2\right)\quad DD^2-2\cdot AA\cdot FF\right]-2\cdot A_1^2\cdot AA^2\right\} \\
& B_1^2\cdot\left(2\cdot CC\cdot FF\quad EE^2\right) \\
\frac{cy\ 1}{B_1} \quad & 2\cdot B_1\cdot\left[A_1^2\cdot\ AA\cdot EE-BB\cdot DD\quad EE\cdot FF\right] \\
\frac{cy\ 0}{B_1} \quad & A_1\cdot\ A_1\cdot AA-DD\quad FF\ \cdot\ A_1\cdot\ A_1\cdot AA\quad DD\quad FF
\end{aligned}
\tag{28}
$$

In theory, the quartic polynomial will have real roots if and only if the two curves intersect. If the ellipses do not intersect, then the quartic will have only complex roots. Furthermore, any real roots of the quartic polynomial will represent y-values of intersection points between the two ellipse curves. As with the quadratic equation that arises in the ellipse-line overlap calculation, the ellipse-ellipse overlap algorithm should handle all possible cases for the types of quartic polynomial roots:

1. Four real roots (distinct or not); the ellipse curves intersect.
2. Two real roots (distinct or not) and one complex-conjugate pair; the ellipse curves intersect.
3. No real roots (two complex-conjugate pairs); the ellipse curves do not intersect.

For the method we present here, polynomial roots are found using Ferrari's quartic formula. A numerical implementation of Ferrari's formula is given in [3]. For complex roots are returned, and any roots whose imaginary part is returned as zero is a real root.

When the polynomial coefficients are constructed as shown above, the general case of two distinct ellipses typically results in a quartic polynomial, i.e., the coefficient $cy\ 4$ is non-zero. However, certain cases lead to polynomials of lesser degree. Fortunately, the solver in [3] is conveniently modular, providing separate functions BIQUADROOTS, CUBICROOTS and QUADROOTS to handle all the possible polynomial cases that arise when seeking points of intersection for two ellipses.

If the polynomial solver returns no real roots to the polynomial, then the ellipse *curves* do not intersect. It follows that the two ellipse *areas* are either disjoint, or one ellipse area is fully contained inside the other; all three possibilities are shown in Fig. 6. Each sub-case in Fig. 6 requires a different overlap-area calculation, i.e. either the overlap area is zero (Case 0-3), or the overlap is the area of the first ellipse (Case 0-2), or the overlap is the area of the second ellipse (Case 0-1). When the polynomial has no real roots, geometry can be used to determine which specific sub-case of Fig. 6 is represented. An efficient logic starts by determining the relative size of the two ellipses, e.g., by comparing the product of semi-axis lengths for each ellipse. The area of an ellipse is proportional to the product of its two semi-axis lengths, so the relative size of two ellipses can be determined by comparing the product of semi-axis lengths:

$$\pi \cdot A_1 \cdot B_1 \ \ \alpha \ \ \pi \cdot A_2 \cdot B_2 \qquad \Rightarrow \qquad A_1 \cdot B_1 \ \ \alpha \ \ A_2 \cdot B_2 \ , \ \ \alpha \in \{'<', '>'\} \tag{29}$$

Suppose the first ellipse is larger than the second ellipse, then $A_1B_1 > A_2B_2$. In this case, if the second ellipse center (h_{2TR}, k_{2TR}) is inside the first ellipse, then the second ellipse is wholly contained within the first ellipse (Case 0-1); otherwise, the ellipses are disjoint (Case 0-3). The logic relies on the fact that there are no intersection points, which is indicated whenever there are no real solutions to the quartic polynomial. To test whether the second ellipse center (h_{2TR}, k_{2TR}) is inside the first ellipse, evaluate the first ellipse equation at the point $x \quad h_{2TR}$, and $y \quad k_{2TR}$; if the result is less than one, then the point (h_{2TR}, k_{2TR}) is inside the first ellipse. The complete logic for determining overlap area when $A_1B_1 > A_2B_2$ is:

If the polynomial has no real roots, and $A_1B_1 > A_2B_2$, and $\frac{h_{2TR}^2}{A_1^2} \quad \frac{k_{2TR}^2}{B_1^2} < 1$, then the first ellipse wholly contains the second, otherwise the two ellipses are disjoint.

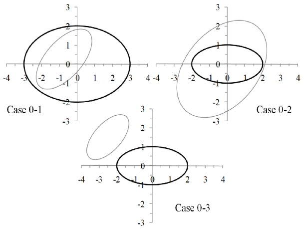

Figure 6. When the quartic polynomial has no real roots, the ellipse curves do not intersect. It follows that either one ellipse is fully contained within the other, or the ellipse areas are completely disjoint, resulting in three distinct cases for overlap area.

Alternatively, suppose that the second ellipse is larger than the first ellipse, then $A_1B_1 < A_2B_2$. If the first ellipse center (0, 0) is inside the second ellipse, then the first ellipse is wholly contained within the second ellipse (Case 0-2); otherwise the ellipses are disjoint (Case 0-3). Again, the logic relies on the fact that there are no intersection points, To test whether (0, 0) is inside the second ellipse, evaluate the second ellipse equation at the origin; if the result is less than zero, then the origin is inside the second ellipse. The complete logic for determining overlap area when $A_1B_1 < A_2B_2$ is:

If the polynomial has no real roots, and $A_1B_1 < A_2B_2$, and $FF < 0$, then the second ellipse wholly contains the first, otherwise the two ellipses are disjoint.

Suppose that the two ellipses are the same size, i.e., $A_1B_1 \quad A_2B_2$. In this case, when no intersection points exist, the ellipses must be disjoint (Case 0-3). It also turns out that the polynomial solver of [3] will return no real solutions if the ellipses are identical. This special case is also handled in the overlap area algorithm presented below. Pseudo-code for a function NOINTPTS that determines overlap area for the cases depicted in Fig. 6 is shown in Fig. 14.

If the polynomial solver returns either two or four real roots to the quartic equation, then the ellipse curves intersect. For the algorithm presented here, all of the various possibilities for the number and type of real roots are addressed by creating a list of distinct real roots. The first step is to loop through the entire array of complex roots returned by the polynomial solver, and retrieve only real roots, i.e., only those roots whose imaginary component is zero. The algorithm presented here then sorts the real roots, allowing for an efficient check for multiple roots. As the sorted list of real roots is traversed, any root that is ‘identical’ to the previous root can be skipped.

Each distinct real root of the polynomial represents a y-value where the two ellipses intersect. Each y-value can represent either one or two potential points of intersection. In the first case, suppose that the polynomial root is $y \quad B_1$ (or $y \quad -B_1$), then the y-value produces a single intersection point, which is at $(0, B_1)$ (or $(0, -B_1)$). In the second case, if the y-value is in the open interval $(-B_1, B_1)$, then there are two potential intersection points where the y-value is on the first ellipse:

$$\left(A_1 \cdot \sqrt{1-\frac{y^2}{B_1^2}},\ y\right) \text{ and}$$
$$\left(-A_1 \cdot \sqrt{1-\frac{y^2}{B_1^2}},\ y\right)$$

Each potential intersection point (x_i, y_i) is evaluated in the second ellipse equation:

$$AA \cdot x_i^2 \quad BB \cdot x_i \cdot y_i \quad CC \cdot y_i^2 \quad DD \cdot x_i \quad EE \cdot y_i \quad FF, \ i \quad 1,2$$

If the expression evaluates to zero, then the point (x, y) is on both ellipses, i.e., it is an intersection point. By checking all points (x, y) for each value of y that is a root of the polynomial, a list of distinct intersection points is generated. The number of distinct intersection points must be either 0, 1, 2, 3 or 4. The case of zero intersection points is described above, with all possible sub-cases illustrated in Fig. 6. If there is only one distinct intersection point, then the two ellipses must be tangent at that point. The three possibilities for a single tangent point are shown in Fig. 7.

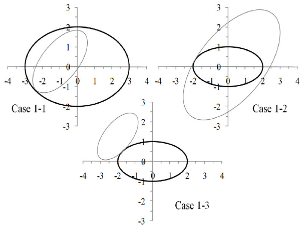

Figure 7. When only one intersection point exists, the ellipses must be tangent at the intersection point. As with the case of zero intersection points, either one ellipse is fully contained within the other, or the ellipse areas are disjoint. The algorithm for finding overlap area in the case of zero intersection points can also be used when there is a single intersection point.

For the purpose of determining overlap area, the cases of 0 or 1 intersection points can be handled in the same way. When two intersection points exist, there are three possible sub-cases, shown in Fig. 8. It is possible that both of the intersection points are tangents (Case 2-1 and Case 2-2). In both of these sub-cases, one ellipse must be fully contained within the other. The only other possibility for two intersection points is a partial overlap (Case 2-3).

Each sub-case in Fig. 8 requires a different overlap-area calculation. When two intersection points exist, either both of the points are tangents, or the ellipse curves cross at both points. Specifically, when there are two intersection points, if one point is a tangent, then both points must be tangents. And, if one point is not a tangent, then neither point is a tangent. So, it suffices to

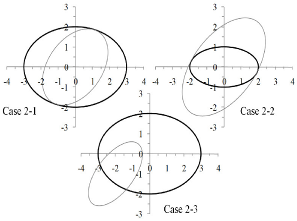

Figure 8. When two intersection points exist, either both of the points are tangents, or the ellipse curves cross at both points. For two tangent points, one ellipse must be fully contained within the other. For two crossing points, a partial overlap must exist

check one of the intersection points for tangency. Suppose the ellipses are tangent at an intersection point; then, points that lie along the first ellipse on either side of the intersection will lie in the same region of the second ellipse (inside or outside). That is, if two points are chosen that lie on the first ellipse, one on each side of the intersection, then both points will either be inside the second ellipse, or they will both be outside the second ellipse. If the ellipse curves cross at the intersection point, then the two chosen points will be in different regions of the second ellipse.

A logic based on testing points that are adjacent to a tangent point can be implemented numerically to test whether an intersection point is a tangent or a cross-point. Starting with an intersection point (x, y), calculate the parametric angle on the first ellipse, by the rules in Table **??**:

$$\theta \quad \begin{cases} \arccos\ x/A_1 & y \geq 0 \\ 2\pi - \arccos\ x/A_1 & y < 0 \end{cases} \tag{30}$$

A small perturbation angle is then calculated. For the method presented here, we seek to establish an angle that corresponds to a point on the first ellipse that is a given distance, approximately $2EPS$, away from the intersection point:

$$EPS_{\text{Radian}} \quad \arcsin\left(\frac{2\cdot\text{EPS}}{\sqrt{x^2 \quad y^2}}\right) \tag{31}$$

The angle EPS_{Radian} is then used with the parametric form of the first ellipse to determine two points adjacent to (x, y):

$$\begin{aligned} x_1 &\quad A_1\cdot\cos\ \theta \quad EPS_{\text{Radian}} \\ y_1 &\quad B_1\cdot\sin\ \theta \quad EPS_{\text{Radian}} \\ x_2 &\quad A_1\cdot\cos\ \theta - EPS_{\text{Radian}} \\ y_2 &\quad B_1\cdot\sin\ \theta - EPS_{\text{Radian}} \end{aligned} \tag{32}$$

Each of the points is then evaluated in the second ellipse equation:

$$\text{test}_i \quad AA\cdot x_i^2 \quad BB\cdot x_i\cdot y_i \quad CC\cdot y_i^2 \quad DD\cdot x_i \quad EE\cdot y_i \quad FF,\ i \quad 1,2 \tag{33}$$

If the value of test$_i$ is positive, then the point (x_i, y_i) is outside the second ellipse. It follows that the product of the two test-point evaluations test$_1$test$_2$ will be positive if the intersection point is a tangent, since at a tangent point both test points will be on the same side of the ellipse. The product of the test-point evaluations will be negative if the two ellipse curves cross at the intersection point, since the test points will be on opposite sides of the ellipse. The function ISTANPT implements this logic to check whether an intersection point is a tangent or a cross-point; pseudo-code is shown in Fig. 18.

When there are two intersection points, the ISTANPT function can be used to differentiate the case 2-3 (Fig. 8) from the cases 2-1 and 2-2. Either of the two known intersection points can be checked with ISTANPT. If the intersection point is a tangent, then both of the intersection points must be tangents, so the case is either 2-1 or 2-2, and one ellipse must be fully contained within the other. For cases 2-1 and 2-2, the geometric logic used for 0 or 1 intersection points can also be used, i.e., the function NOINTPTS can be used to determine the overlap area for these cases. If the two ellipse curves cross at the tested intersection point, then the case must be 2-3, representing a partial overlap between the two ellipse areas.

For case 2-3, with partial overlap between the two ellipses, the approach for finding overlap area is based on using the two points (x_1, y_1) and (x_2, y_2) with segment the algorithm (Table 2; Fig. 2) to determine the partial overlap area contributed by each ellipse. The total overlap area is the sum of the two segment areas. The two intersection points divide each ellipse into two segment areas (see Fig. 5). Only one sector area from each ellipse contributes to the overlap area. The segment algorithm returns the area between the secant line and the portion of the ellipse from the first point to the second point traversed in a counter-clockwise direction. For the overlap area calculation, the two points must be passed to the segment algorithm in the order that will return the correct segment area. The default order is counter-clockwise from the first point (x_1, y_1) to the second point (x_2, y_2). A check is made to determine whether this order will return the desired segment area. First, the parametric angles corresponding to (x_1, y_1) and (x_2, y_2) on the first ellipse are determined, by the rules in Table **??**:

$$\theta_1 \quad \begin{cases} \arccos\ x_1/A_1 & y_1 \geq 0 \\ 2\pi - \arccos\ x_1/A_1 & y_1 < 0 \end{cases} \tag{34}$$

$$\theta_2 \quad \begin{cases} \arccos\ x_2/A_1 & y_2 \geq 0 \\ 2\pi - \arccos\ x_2/A_1 & y_2 < 0 \end{cases} \tag{35}$$

Then, a point between (x_1, y_1) and (x_2, y_2) that is on the first ellipse is found:

$$\begin{aligned} x_{\text{mid}} \quad & A_1 \cdot \cos\left(\frac{\theta_1 \quad \theta_2}{2}\right) \\ y_{\text{mid}} \quad & B_1 \cdot \sin\left(\frac{\theta_1 \quad \theta_2}{2}\right) \end{aligned} \tag{36}$$

The point $(x_{\text{mid}}, y_{\text{mid}})$ is on the first ellipse between (x_1, y_1) and (x_2, y_2) when travelling counter- clockwise from (x_1, y_1) and (x_2, y_2). If $(x_{\text{mid}}, y_{\text{mid}})$ is inside the second ellipse, then the desired segment of the first ellipse contains the point $(x_{\text{mid}}, y_{\text{mid}})$. In this case, the segment algorithm should integrate in the default order, counterclockwise from (x_1,y_1) to (x_2, y_2). Otherwise, the order of the points should be reversed before calling the segment algorithm, causing it to integrate counterclockwise from (x_2, y_2) to (x_1, y_1). The area returned by the segment algorithm is the area contributed by the first ellipse to the partial overlap.

The desired segment from the second ellipse is found in a manner to the first ellipse segment. A slight difference in the approach is required because the segment algorithm is implemented for ellipses that are centered at the origin and oriented with the coordinate axes; but, in the general case the intersection points (x_1, y_1) and (x_2, y_2) lie on the second ellipse that is in a displaced and rotated location. The approach presented here translates and rotates the second ellipse to the origin so that the segment algorithm can be used. It suffices to translate then rotate the two intersection points by amounts that put the second ellipse centered at the origin and oriented with the coordinate axes:

$$\begin{aligned} x_{1\text{TR}} \quad & x_1 - h_{2\text{TR}} \ \cdot \cos\ \varphi_1 - \varphi_2 \qquad y_1 - k_{2\text{TR}} \ \cdot \sin\ \varphi_2 - \varphi_1 \\ y_{1\text{TR}} \quad & x_1 - h_{2\text{TR}} \ \cdot \sin\ \varphi_1 - \varphi_2 \qquad y_1 - k_{2\text{TR}} \ \cdot \cos\ \varphi_1 - \varphi_2 \\ x_{2\text{TR}} \quad & x_2 - h_{2\text{TR}} \ \cdot \cos\ \varphi_1 - \varphi_2 \qquad y_2 - k_{2\text{TR}} \ \cdot \sin\ \varphi_2 - \varphi_1 \\ y_{2\text{TR}} \quad & x_2 - h_{2\text{TR}} \ \cdot \sin\ \varphi_1 - \varphi_2 \qquad y_2 - k_{2\text{TR}} \ \cdot \cos\ \varphi_1 - \varphi_2 \end{aligned} \tag{37}$$

The new points $(x_{1\text{TR}}, y_{1\text{TR}})$ and $(x_{2\text{TR}}, y_{2\text{TR}})$ lie on the second ellipse after a translation+rotation that puts the second ellipse at the origin, oriented with the coordinate axes. The new points can be used as inputs to the segment algorithm to determine the overlap area contributed by the second ellipse. As with the first ellipse, the order of the points must be determined so that the segment algorithm returns the appropriate area. The default order is counter-clockwise from the first point $(x_{1\text{TR}}, y_{1\text{TR}})$ to the second point $(x_{2\text{TR}}, y_{2\text{TR}})$. A check is made to determine whether this order will return the desired segment area. First, the parametric angles corresponding to points $(x_{1\text{TR}}, y_{1\text{TR}})$ and $(x_{2\text{TR}}, y_{2\text{TR}})$ on the second ellipse are determined, by the rules in Table **??**:

$$\theta_1 \quad \begin{cases} \arccos\ x_{1\text{TR}}/A_2 & y_{1\text{TR}} \geq 0 \\ 2\pi - \arccos\ x_{1\text{TR}}/A_2 & y_{1\text{TR}} < 0 \end{cases} \tag{38}$$

$$\theta_2 \quad \begin{cases} \arccos\ x_{2\text{TR}}/A_2 & y_{2\text{TR}} \geq 0 \\ 2\pi - \arccos\ x_{2\text{TR}}/A_2 & y_{2\text{TR}} < 0 \end{cases} \tag{39}$$

Then, a point on the second ellipse between $(x_{1\text{TR}}, y_{1\text{TR}})$ and $(x_{2\text{TR}}, y_{2\text{TR}})$ is found:

$$
\begin{aligned}
x_{\text{mid}} &\quad A_2 \cdot \cos\left(\frac{\theta_1 \quad \theta_2}{2}\right) \\
y_{\text{mid}} &\quad B_2 \cdot \sin\left(\frac{\theta_1 \quad \theta_2}{2}\right)
\end{aligned}
$$

The point $(x_{\text{mid}}, y_{\text{mid}})$ is on the second ellipse between $(x_{1\text{TR}}, y_{1\text{TR}})$ and $(x_{2\text{TR}}, y_{2\text{TR}})$ when travelling counter- clockwise from $(x_{1\text{TR}}, y_{1\text{TR}})$ and $(x_{2\text{TR}}, y_{2\text{TR}})$. The new point (x_{mid}, y_{mid}) lies on the centered second ellipse. To determine the desired segment of the second ellipse, the new point $(x_{\text{mid}}, y_{\text{mid}})$ must be rotated then translated back to a corresponding position on the once-translated+rotated second ellipse:

$$
\begin{aligned}
x_{\text{midRT}} &\quad x_{\text{mid}} \cdot \cos\ \varphi_2 - \varphi_1 \quad y_{\text{mid}} \cdot \sin\ \varphi_1 - \varphi_2 \quad h_{2\text{TR}} \\
y_{\text{midRT}} &\quad x_{\text{mid}} \cdot \sin\ \varphi_2 - \varphi_1 \quad y_{\text{mid}} \cdot \cos\ \varphi_1 - \varphi_2 \quad k_{2\text{TR}}
\end{aligned}
$$

If $(x_{\text{mid}RT}, y_{\text{midRT}})$ is inside the first ellipse, then the desired segment of the second ellipse contains the point $(x_{\text{mid}}, y_{\text{mid}})$. In this case, the segment algorithm should integrate in the default order, counterclockwise from $(x_{1\text{TR}}, y_{1\text{TR}})$ to $(x_{2\text{TR}}, y_{2\text{TR}})$. Otherwise, the order of the points should be reversed before calling the segment algorithm, causing it to integrate counterclockwise from $(x_{2\text{TR}}, y_{2\text{TR}})$ to $(x_{1\text{TR}}, y_{1\text{TR}})$. The area returned by the segment algorithm is the area contributed by the second ellipse to the partial overlap. The sum of the segment areas from the two ellipses is then equal to the ellipse overlap area. The TWOINTPTS function calculates the overlap area for partial overlap with two intersection points (Case 2-3); pseudo-code is shown in Fig. 15.

There are two possible sub-cases for three intersection points, shown in Fig. 9. One of the three points must be a tangent point, and the ellipses must cross at the other two points. The cases are distinct only in the sense that the tangent point occurs with ellipse 2 on the interior side of ellipse 1 (Case 3-1), or with ellipse 2 on the exterior side of ellipse 1 (Case 3-2). The overlap area calculation is performed in the same manner for both cases, by calling the TWOINTPTS function with the two cross-point intersections. The ISTANPT function can be used to determine which point is a tangent; the remaining two intersection points are then passed to TWOINTPTS. This logic is implemented in the THREEINTPTS function, with pseudo-code in Fig. 16.

There is only one possible case for four intersection points, shown in Fig. 9. The two ellipse curves must cross at all four of the intersection points, resulting in a partial overlap. The overlap area consists of two segments from each ellipse, and a central convex quadrilateral. For the approach presented here, the four intersection points are sorted ascending in a counter-clockwise order around the first ellipse. The ordered set of intersection points is (x_1, y_1), (x_2, y_2), (x_3, y_3) and (x_4, y_4). The ordering allows a direct calculation of the quadrilateral area. The standard formula uses the cross-product of the two diagonals:

$$
\begin{aligned}
\text{area} &\quad \frac{1}{2} |\ x_3 - x_1, y_3 - y_1\ \times\ x_4 - x_2, y_4 - y_2\ | \\
&\quad \frac{1}{2} |\ x_3 - x_1\ \cdot\ y_4 - y_2\ -\ x_4 - x_2\ \cdot\ x_3 - x_1\ |
\end{aligned}
\tag{40}
$$

The point ordering also simplifies the search for the appropriate segments of each ellipse that contribute to the overlap area.

Suppose that the first two sorted points (x_1, y_1) and (x_2, y_2) demarcate a segment of the first ellipse that contributes to the overlap area, as shown in Fig. 9 and Fig. 10. It follows that the contributing segments from the first ellipse are between (x_1, y_1) and (x_2, y_2), and also between (x_3, y_3) and (x_4, y_4). In this case, the contributing segments from the second ellipse are between (x_2, y_2) and (x_3, y_3), and between (x_4, y_4) and (x_1, y_1). To determine which segments contribute to the overlap area, it suffices to test whether a point midway between (x_1, y_1) and (x_2, y_2) is inside or outside the second ellipse. The segment algorithm is used for each of the four areas, and added to the quadrilateral to obtain the total overlap area.

An implementation of the ELLIPSE_ELLIPSE_OVERLAP algorithm in c-code in `https://github.com/chraibi/EEOver`. The code compiles under Cygwin-1.7.7-1, and returns the following values for the test cases presented above in Fig. 6, Fig. 7 , Fig. 8 and Fig. 9:

Listing 5. Return values for the test cases presented above in Fig. 6, Fig. 7 , Fig. 8 and Fig. 9.

```
cc call\_ee.c ellipse\_ellipse\_overlap.c –o call\_ee.exe

./call\_ee

Calling ellipse\_ellipse\_overlap.c
```

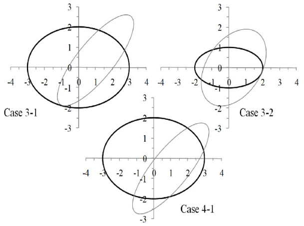

Figure 9. When three intersection points exist, one must be a tangent, and the ellipse curves must cross at the other two points, always resulting in a partial overlap. When four intersection points exist, the ellipse curves must cross at all four points, again resulting in a partial overlap

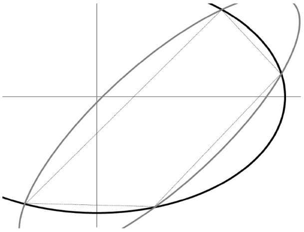

Figure 10. Overlap Area with four intersection points (Case 4-1). The overlap area consists of two segments from each ellipse, and a central convex quadrilateral.

```



Case 0-1: area =      6.28318531, return_value = 111

          ellipse 2 area by pi*a2*b2 =      6.28318531

Case 0-2: area =      6.28318531, return_value = 110

          ellipse 1 area by pi*a1*b1 =      6.28318531

Case 0-3: area =      0.00000000, return_value = 103

          Ellipses are disjoint, ovelap area = 0.0



Case 1-1: area =      6.28318531, return_value = 111

          ellipse 2 area by pi*a2*b2 =      6.28318531

Case 1-2: area =      6.28318531, return_value = 110

          ellipse 1 area by pi*a1b1 =      6.28318531

Case 1-3: area =     -0.00000000, return_value = 107

          Ellipses are disjoint, ovelap area = 0.0



Case 2-1: area =     10.60055478, return_value = 109

          ellipse 2 area by pi*a2*b2 =     10.60287521

Case 2-2: area =      6.28318531, return_value = 110

          ellipse 1 area by pi*a1b1 =      6.28318531

Case 2-3: area =      3.82254574, return_value = 107

```

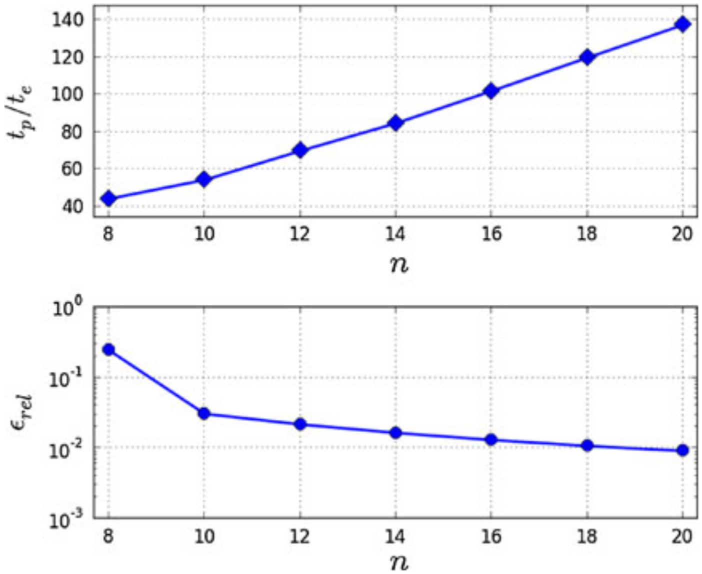

Figure 11. Top: The ratio of the run-time of the polygon-based method (tp) and the analytical solution presented in this paper as implemented in C++ (te) with respect to the number of edges. Bottom: The relative error of the calculated overlap areas with respect to the number of edges of a corresponding n-sided polygons used to approximate the area

```


Case 3-1: area =       7.55370392, return_value = 107

Case 3-2: area =       5.67996234, return_value = 107



Case 4-1: area =      16.93791852, return_value = 109
```

The accuracy of the algorithm, as implemented in C and C++, was tested extensively. We compare the results of 1,000 selected pairs of ellipses with the overlap areas and calculation times of the corresponding n-sided polygons. Figure 11 shows that implementation of the analytical solution on an Intel Core i7-2620M, 2,7 GHz, 4MB Cache, is 40–140 times faster than the solution based a polygon-approximation of ellipses. For the results presented in Fig. 6,we make use of the C++-library Boost-polygon. Figure 12 shows a quantitative visualization of the calculated crossing points of selected ellipses. The code is open source and can be downloaded from `https://github.com/chraibi/EEOver`.

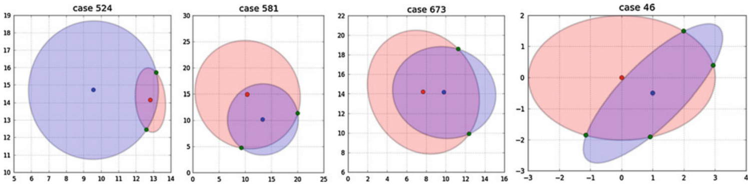

Figure 12. Results of selected test cases. The red and blue points represent ellipse centers, and green points represent intersection points, calculated with the algorithm as implemented in C++.

References

[1] Kent, S., Kaiser, M. E., Deustua, S. E., Smith, J. A. *Photometric calibrations for 21st century science*, Astronomy 2010 **8** (2009).

[2] M. Chraibi, A. Seyfried, and A. Schadschneider, *Generalized centrifugal force model for pedestrian dynamics*, Phys. Rev. E, **82** (2010), 046111.

[3] Nonweiler, Terence R.F., *CACM Algorithm 326: Roots of low order polynomials*, Communications of the ACM, vol. **11** no. 4, pages 269-270 (1968). Translated into c and programmed by M. Dow, ANUSF, Australian National University, Canberra, Australia. Accessed at `http://www.netlib.org/toms/326.`

[4] Abramowitz, M. and Stegun, I. A. (Eds.). *Solutions of Quartic Equations.*

A.4 ARTICLE III

Generalized collision-free velocity model for pedestrian dynamics

Q. XU, M. CHRAIBI, A. TORDEUX, AND J. ZHANG

PHYSICA A: STATISTICAL MECHANICS AND ITS APPLICATIONS (**2019**)

Physica A: Statistical Mechanics and its Applications, 535, 122521, 2019
10.1016/j.physa.2019.122521

Generalized Collision-free Velocity Model for Pedestrian Dynamics

Qiancheng Xu[1], Mohcine Chraibi[1], Antoine Tordeux[2], Jun Zhang[3]

Abstract
The collision-free velocity model is a microscopic pedestrian model, which despite its simplicity, reproduces fairly well several self-organization phenomena in pedestrian dynamics. The model consists of two components: a direction sub-model that combines individual desired moving direction and neighbor's influence to imitate the process of navigating in a two-dimensional space, and an intrinsically collision-free speed sub-model which controls the speed of the agents with respect to the distance to their neighbors.

In this paper we generalize the collision-free velocity model by introducing the influence of walls and extending the distance calculations to velocity-based ellipses. Besides, we introduce enhancements to the direction sub-module that smooth the direction changes of pedestrians in the simulation; a shortcoming that was not visible in the original model due to the symmetry of the circular shapes. Moreover, the introduced improvements mitigate backward movements, leading to a more realistic distribution of pedestrians especially in bottleneck scenarios.

We study by simulation the effects of the pedestrian's shape by comparing the fundamental diagram in narrow and wide corridors. Furthermore, we validate our generalized approach by investigating the flow through bottlenecks with varying exit's widths.

Keywords
Model; pedestrian dynamics; dynamical ellipse; fundamental diagram; validation

[1] *Institute for Advanced Simulation, Forschungszentrum Jülich GmbH, 52425 Jülich, Germany*
[2] *School of Mechanical Engineering and Safety Engineering, University of Wuppertal, 42119 Wuppertal, Germany*
[3] *State Key Laboratory of Fire Science, University of Science and Technology of China, 230027 Hefei, China*

Contents

Introduction

Nowadays, the scale of crowd activities is getting bigger with the constant increase in the world population and the convenience of transport. Although these events usually are carefully planned before they are held, the probability of accidents cannot be neglected, especially when the number of participants is considerably high. Besides, in some complex buildings, such as train stations, airports, stadiums, and commercial malls, crowd density can be relatively high, in particular during rush hours.

For increasing the comfort and usability of these facilities, simulations of pedestrian dynamics may help during the design of buildings and even after their construction to identify potential bottlenecks and mitigate their effects [1, 2].

In general, models used to describe pedestrian dynamics can be categorized according to their scale of definition into macroscopic models, mesoscopic models, and microscopic models. Microscopic models describe individual trajectories of pedestrians while macroscopic models rely on aggregated quantities e.g. density, velocity, and flow to describe pedestrian dynamics in partial differential equation systems [3, 4, 5, 6]. For instance, recent macroscopic approaches rely on mean-field game theory and the coupling of Hamilton-Jacobi-Bellman and Fokker-Planck equations [7, 8, 9, 10]. The intermediate scale between microscopic and macroscopic classes is mesoscopic. Kinetic models [11, 12, 13, 14, 15] describing the crowd through distribution functions with Boltzmann-type equations and discrete queuing models [16, 17, 18] belong to the mesoscopic modeling category. Mesoscopic models can take in consideration behavior heterogeneity [18, 19, 20] or stochastic components in the interaction. Generally speaking, macroscopic and mesoscopic models consider pedestrian flow as a continuum and deal with large modeling scales, while microscopic models operate at local scales. Yet a systematic classification of model features according to the model form is difficult. We refer to [21, 22, 23, 24, 25, 26, 27] for overviews of modeling approaches for pedestrian dynamics.

We aim in this article to tackle pedestrians' interactions as well as their granular aspects (e.g. pedestrian shape and collision-free property) and to describe their dynamics locally in simple geometries such as corridors and bottlenecks. Objectives are mainly addressed on the microscopic modeling scale.

Microscopic models are largely used in traffic engineering to simulate pedestrian dynamics. They describe pedestrians individually and can naturally take into account the heterogeneity and stochasticity of the pedestrians' behavior. Most of the models can reproduce fairly well several collective phenomena in pedestrian dynamics [26, 28, 29]. After more than 50 years of development, many kinds of microscopic models exist in the literature. We can distinguish between cellular automate models [30, 31, 32, 33, 34] (0th order models), velocity models [35, 36, 37, 38] (1st order models) and force-based models [39, 40, 41, 42] (2nd order models). While the former models are discrete in space and computationally fast, the later models are continuous in space and hence are easier to be used in complex geometries. Whether continuous models are computationally expensive depends not only on the order of the model but also on its definition. However, generally speaking, first-order models are less expensive since their numerical solution involves only one integration step, while two integration steps are required for second-order models. Furthermore, for numerical reasons fine discretization generally requires small integration time steps. In any case, microscopic models remain however generally much more computationally expensive than continuum pedestrian models.

In this paper, we focus on the extension of the collision-free velocity model introduced in [36]. The collision-free velocity model (for short CVM) is a velocity-model, composed of a speed and a direction sub-models. Unlike most force-based models, CVM, being a first-order model, is by definition collision-free.

We generalize the CVM by considering the influence of walls and integrating two extensions. First, we change the shape of agents from circle to dynamical ellipse. In the original model, circles are used to express the projection of the pedestrian's body on the two-dimensional plane. However, many references and researches indicate that a dynamical ellipse can represent pedestrian's shape more accurately since the space a pedestrian occupied is influenced by the length of the legs during the motion and the lateral swaying of the body [40]. Therefore, we generalize CVM by extending the distance calculation to velocity-based ellipse and compare the simulation results with the original model (circles). After introducing the first extension, an unnatural "shaking" was observed during the simulation, which is caused by the zero-order direction sub-model. We propose a new first-order direction sub-model, designed to stabilize the direction changes of pedestrians in the simulation.

For the sake of completeness, we briefly introduce the original CVM in section 1. The generalization of the model from circle-based to an ellipse-based definition and the new direction sub-model are presented in section 2. In section 3, the comparison between the simulation results of a circle and a velocity-based ellipse is given and the performances of the new direction sub-model are compared to the original CVM. Finally, we give a summary of the extensions and discuss limitations of the model as well as future research directions in the concluding section 4.

1. Collision-free velocity model

In the original model, the moving direction and speed of each pedestrian are updated at each time step. Moving direction of a pedestrian is obtained by superposing the influence of the surrounding pedestrians and the desired moving direction. The value of the speed depends on the minimum spacing in the moving direction. In figure 1 (borrowed from [36]), pedestrians are modeled as circles with constant diameter ℓ. X_i, X_j and X_k are positions of pedestrians i, j and k. The original CVM is described as

$$\dot{X}_i(X_i, X_j, \dots) = V_i(X_i, X_j, \dots) \cdot \vec{e}_i(X_i, X_j, \dots), \tag{1}$$

where V_i is the speed of pedestrian i and $\vec{e}_i$ is the moving direction.

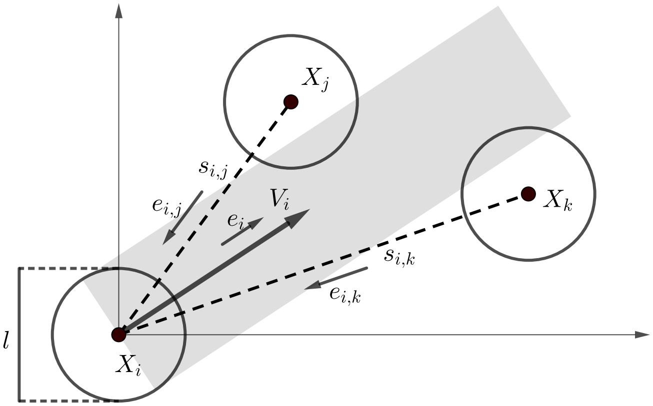

Figure 1. Notations used in the collision-free velocity model. ℓ is the size of agents, X_i, X_j and X_k are positions of pedestrians, $\vec{e}_i$ is the moving direction of pedestrian i and V_i is the moving speed, $s_{i,j}$ and $s_{i,k}$ are distances between the centers of pedestrians, $\vec{e}_{i,j}$ and $\vec{e}_{i,k}$ and the unit vector from X_j and X_k to X_i.

Moving direction $\vec{e}_i$ is obtained from the direction sub-model

$$\vec{e}_i(X_i, X_j, ...) = u_1 \cdot \Big(\vec{e}_i^{\,0} + \sum_{j \in N_i} R(s_{i,j}) \cdot \vec{e}_{i,j}\Big), \tag{2}$$

where u_1 is a normalization constant such that $||\vec{e}_i|| = 1$, $\vec{e}_i^{\,0}$ is the desired direction towards a certain goal, N_i is the set containing all the neighbours of the pedestrian i, $\vec{e}_{i,j}$ is the unit vector from the center of the pedestrian j towards the center of the pedestrian i. The function

$$R(s_{i,j}) = k \cdot \exp\Big(\frac{\ell - s_{i,j}}{D}\Big), \tag{3}$$

is used to describe the influence that neighbours act on the moving direction of pedestrian i. The strength coefficient $k > 0$ and the distance coefficient $D > 0$ calibrate the function accordingly. As mentioned before, ℓ is the diameter of the circle used to represent the pedestrians and $s_{i,j}$ is the distance between the centers of pedestrian i and j.

After obtaining the moving direction $\vec{e}_i$, the speed model

$$V_i(s_{i,j}) = \min\Big\{V_i^0, \max\big\{0, \frac{s_i - \ell}{T}\big\}\Big\}, \tag{4}$$

is used to determine the scale of velocity V_i in the direction $\vec{e}_i$. In Eq. (4), V_i^0 is the desired speed of pedestrian i, which depends on various environmental factors such as the existence of stairs or smoke produced by a fire.

$$s_i = \min_{j \in J_i} s_{i,j}, \tag{5}$$

is the distance between the center of pedestrian i and the center of the closet pedestrian in front of pedestrian i, when pedestrian i moving in the direction $\vec{e}_i$. The definition of set J_i in Eq. (5) is

$$J_i = \Big\{j, \vec{e}_i \cdot \vec{e}_{i,j} \leq 0 \text{ and } \Big|\vec{e}_i^{\perp} \cdot \vec{e}_{i,j}\Big| \leq \frac{\ell}{s_{i,j}}\Big\}, \tag{6}$$

where $\vec{e}_i^{\perp} \cdot \vec{e}_i = 0$. J_i is the set of all pedestrians overlapping with the grey area in figure 1. The only coefficient in the speed model is $T > 0$ which is used to adjust the gap between pedestrians.

The above-mentioned definition of the CVM describes specifically interactions among pedestrians. However, the influence of walls and obstacles has been left from the definition of the model. In this work, we close this gap by only considering straight walls. If the shape of the wall in the simulation is irregular, then we will approximate it to a few straight walls. In figure 2, X_i, $\vec{e}_i$

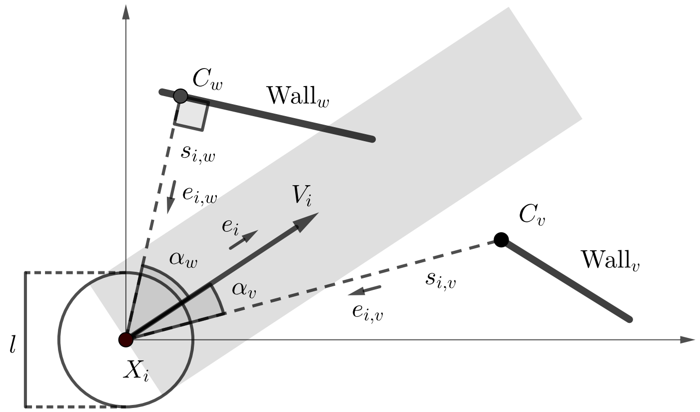

Figure 2. Notations used in the collision-free velocity model when calculating the influence of walls. ℓ, X_i, $\vec{e}_i$, V_i are the size, position, moving direction and moving speed of pedestrian i, C_v and C_w are the closest points in wall v and w to X_i, $\vec{e}_{i,v}$ and $\vec{e}_{i,w}$ are the unit vectors from C_v and C_w to X_i, $s_{i,v}$ and $s_{i,w}$ are the distances from C_v and C_w to X_i, α_v is the angle between $\vec{e}_i$ and $-\vec{e}_{i,v}$, α_w is the angle between $\vec{e}_i$ and $-\vec{e}_{i,w}$.

and V_i have the same definitions as in figure 1. Besides, there are two walls in the figure, wall v and w. C_v and C_w are the closest points in wall v and w to the center of pedestrian i respectively. $\vec{e}_{i,v}$ and $\vec{e}_{i,w}$ are the unit vectors from C_v and C_w to X_i. $s_{i,v}$ and $s_{i,w}$ are the distances from C_v and C_w to X_i. The angle between $\vec{e}_i$ and $-\vec{e}_{i,v}$ is α_v and the angle between $\vec{e}_i$ and $-\vec{e}_{i,w}$ is α_w.

After introducing the influence of walls, the direction model becomes

$$\vec{e}_i = u_2 \cdot \Big(\vec{e}_i^{\,0} + \sum_{j\in N_i} R(s_{i,j}) \cdot \vec{e}_{i,j} + \sum_{v\in W_i} R_w(s_{i,v}) \cdot \vec{e}_{i,v}\Big), \tag{7}$$

where u_2 is a normalization constant such that $||\vec{e}_i|| = 1$, W_i is the set of walls nearby pedestrian i, and

$$R_w(s_{i,v}) = k_w \cdot \exp\Big(\frac{\frac{\ell}{2} - s_{i,v}}{D_w}\Big), \tag{8}$$

where $k_w > 0$ and $D_w > 0$ are used to calibrate the function accordingly.

To avoid overlaps of pedestrians with walls, walls should not only influence pedestrian's moving direction but also their speed. The expanded speed model is

$$V_i = \min\Big\{V_i^0, \max\big\{0, \frac{s_i - \ell}{T}\big\}, \max\big\{0, \frac{sw_i}{T}\big\}\Big\}, \tag{9}$$

where the definitions of s_i, ℓ, T are same as in Eq. (4) and

$$sw_i = \min_{v\in JW_i} \frac{s_{i,v} - \frac{\ell}{2}}{\cos\alpha_v}, \tag{10}$$

where JW_i is the set containing all the walls in the moving direction of pedestrian i (grey area in figure 2).

2. Generalization of the collision-free velocity model

In this section we introduce extensions of the CVM. We also show how every extension influences the resulting dynamics and eventually enhances the simulation results.

2.1 From circle to ellipse

We generalize the collision-free velocity model by extending the distance calculations to velocity-based ellipses. The plane view of the pedestrian i's body is represented by an ellipse [43]. The major semi-axis a_i and minor semi-axis b_i of the ellipse represent the space requirement in the direction of motion and along the shoulder axis respectively.

In [40] the semi-axis along the walking direction is defined as

$$a_i = a_{\min} + \tau_a V_i, \tag{11}$$

where V_i is the speed of pedestrian i, while $a_{\min} > 0$ and $\tau_a > 0$ are two parameters.

The idea that the semi-axis of the ellipse along the walking direction vary with speed is derived from the fact that the spacing a pedestrian needed in her moving direction has a positive correlation with her speed [44]. This, in turn, is also the role of parameter T which is defined in the speed sub-model to adjust the gap between agents. We conclude that in our model T and τ_a model the same behavior of pedestrians even if their physical interpretations are different.

This becomes apparent after performing a basic stability analysis of the model. Assuming an one-dimensional system in steady-state , we can derive from the speed sub-model in Eq. (4) the following relation

$$V_{\text{steady}} = \frac{1/\rho_{\text{steady}} - 2 \cdot a_{\min}}{\tilde{T}}, \tag{12}$$

where V_{steady} and ρ_{steady} are the speed and the density of pedestrians flow in steady state, and $\tilde{T} = T + 2\tau_a$. Hence, the parameter τ_a and the parameter T in speed sub-model have the same influence on the dynamics. To confirm our assumption we perform numerical simulations by varying these two parameters while maintaining a constant value of $\tilde{T}$. We can observe from figure 3 that although the values of τ_a are different in these simulations, the results obtained are almost identical when $\tilde{T}$ is constant. In the spirit of Occam's razor, we dispense with parameter τ_a and opt for a constant semi-axis a_i.

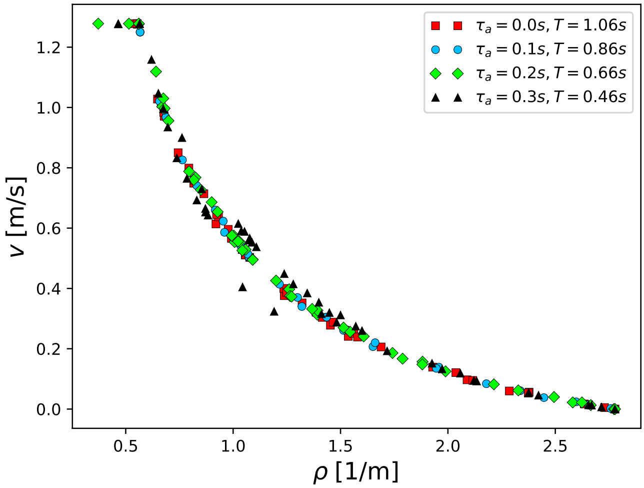

Figure 3. The fundamental diagram obtained in 1D simulations with $\tilde{T} = 1.06$.

The other semi-axis along the shoulder axis b_i is defined according to [40] as a linear function:

$$b_i = b_{\max} - (b_{\max} - b_{\min}) \frac{V_i}{V_i^0}, \tag{13}$$

with $b_{\min}$ is the minimal semi-width when pedestrian i reaches the desired speed V_i^0 and $b_{\max}$ is the maximum semi-width reached when pedestrian i is not moving [40].

We found in simulations with the CVM that this linear relationship does not provide satisfactory results. Hence we introduce a new non-linear function inspired by the observation that pedestrians often reduce their occupied space in the vertical direction of motion by turning their body to walk faster and pass through narrow gaps that are smaller than the width of their shoulder.

We set

$$b_i = b_{\min} + \frac{b_{\max} - b_{\min}}{1 + e^{\beta \cdot (V_i - \gamma)}}, \tag{14}$$

which is a Sigmoid function, where the maximum semi-width $b_{\max}$ is equal to the half of a static pedestrian's width and $b_{\min}$ is equal to the half of a moving pedestrian's minimum width. Parameters β and γ are used to adjust the shape of the function as shown in figure 4 which shows the curves of the function for different parameter values.

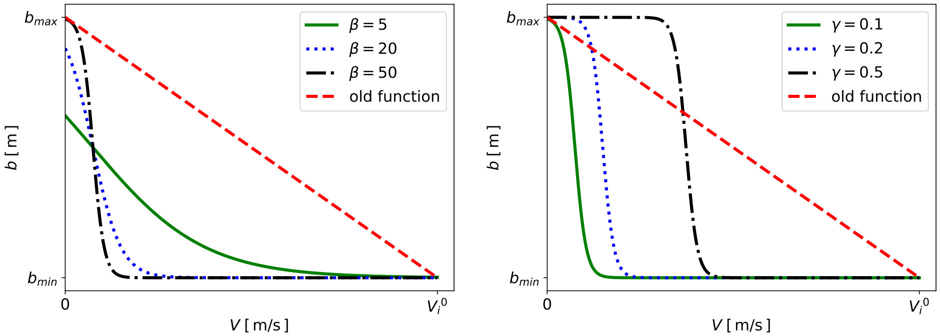

(a) $\gamma = 0.1$ (b) $\beta = 50$

Figure 4. The new function of b with different β and γ, the left figure shows the curves of the function with same $\gamma = 0.1$ but different β while the right figure shows the curves of the function with same $\beta = 50$ but different γ.

After defining the semi-axes of the ellipse, we extend the distance calculations from circle to velocity-based ellipse (figure 5). The ellipses in the full line describe non-moving pedestrians, while the ellipses in the dashed line represent the pedestrians at the desired velocity. $d_{i,j}$ is the distance between ellipses used to represent pedestrian i and j, which is defined as the distance between the borders of ellipses i and j, along a line connecting their centers. $d_{i,v}$ is the distance between the wall v and pedestrian i, which is defined as the distance between the C_v (the closest points in wall v to the center of pedestrian i) and the border of ellipse used to present pedestrian i, along a line connecting the center of pedestrian i and C_v.

In the new equation of motion, the influence of the agents' shape is added as follows: The moving direction $\vec{e}_i$ is calculated by Eq. (7), but the new definition of functions

$$R(d_{i,j}) = k \cdot \exp\left(\frac{d_{i,j}}{D}\right), \quad R_w(d_{i,v}) = k_w \cdot \exp\left(\frac{d_{i,v}}{D_w}\right), \tag{15}$$

are used. Then the speed V_i is obtained by

$$V_i = \min\left\{V_i^0, \max\left\{0, \frac{d_i}{T}\right\}, \max\left\{0, \frac{dw_i}{T}\right\}\right\}, \tag{16}$$

where

$$d_i = \min_{j \in J_i} d_{i,j}, \quad dw_i = \min_{v \in JW_i} \frac{d_{i,v}}{\cos \alpha_v}. \tag{17}$$

Here J_i and JW_i are the sets containing all pedestrians and walls in the direction of movement (i.e. the pedestrians and walls overlap with the grey area in figure 5). We set the width of the grey area to $2b_{\min}$ in the case of a velocity-based ellipse. The comparisons between the models describing agents with different shapes are given in section 3.

2.2 New direction sub-model

After generalizing the model to ellipses, some unrealistic phenomena during simulation become visible. First of all, backward movements occur very often, which is not realistic especially in evacuation scenarios. Second, an unnatural "shaking" appears during simulation, which is due to a strong fluctuation of the ellipse's orientation.

In the original model, the moving direction of pedestrian i is calculated by combining individual desired moving direction $\vec{e}_i^{\,0}$ and the neighbors' influence. Since the direction of neighbor's influence is from the center of pedestrians or closest point on the wall towards the center of the pedestrian i, the influence can be divided into two parts, one is the projection on $\vec{e}_i^{\,0}$ and the other one is perpendicular to the projection part. The direction of the projection part is the reason for backward movements.

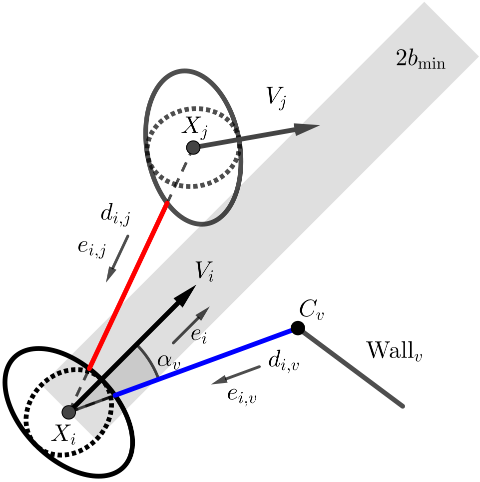

Figure 5. Notations used in the collision-free velocity model after extending the distance calculations between pedestrians from circle to velocity-based ellipse. $d_{i,j}$ is the length of red segment and $d_{i,v}$ is the length of blue segment. X_i and X_j are positions of pedestrians, C_v is the closet point in wall v to X_i, V_i and V_j are moving speeds of pedestrians, $\vec{e}_i$ is the moving direction of pedestrian i, $\vec{e}_{i,j}$ and $\vec{e}_{i,v}$ are the unit vectors from X_j and C_v to X_i, α_v is the angle between $\vec{e}_i$ and $-\vec{e}_{i,v}$.

Pedestrians hardly choose a moving direction whose projection on $\vec{e}_i^{\,0}$ is in the inverse direction of $\vec{e}_i^{\,0}$. And the cause of the "shaking" is that pedestrians turn to $\vec{e}_i$ directly after calculation in the original model (0th order model).

Therefore, our solution has two parts, the projection of neighbors' influence on $\vec{e}_i^{\,0}$ is always equal to zero, and introducing a smoothing process (e.g. a relaxation process) in the direction sub-model. Based on this idea, we propose a new direction sub-model as shown in figure 6, where $\vec{e}_i^{\,0}$ is the desired moving direction of the pedestrian i and $\vec{e}_i$ is the actual moving direction, $\vec{e}_{i,j}^{\,N}$ and $\vec{e}_{i,v}^{\,N}$ are the new directions used to calculate the influence of the pedestrians j and walls v act on pedestrian i respectively.

The new direction sub-model uses two steps to calculate the moving direction of a pedestrian. First, we use

$$\vec{E}_i = u_3 \cdot \left(\vec{e}_i^{\,0} + \sum_{j \in N_i} R(d_{i,j}) \cdot \vec{e}_{i,j}^{\,N} + \sum_{v \in W_i} R_w(d_{i,v}) \cdot \vec{e}_{i,v}^{\,N}\right), \tag{18}$$

to calculate the optimal moving direction of the pedestrian i, u_3 is a normalization constant such that $||\vec{E}_i|| = 1$. The repulsive function $R(d_{i,j})$ and $R_w(d_{i,v})$ are given in Eq. (15) and the definition of $\vec{e}_{i,j}^{\,N}$ and $\vec{e}_{i,v}^{\,N}$ are

$$\vec{e}_{i,j}^{\,N} = \begin{cases} \vec{e}_i^{\,0\perp} & \text{if } C_j > 0, \\ \vec{e}_i^{\,0\perp} \text{ or } -\vec{e}_i^{\,0\perp} & \text{if } C_j = 0, \\ -\vec{e}_i^{\,0\perp} & \text{if } C_j < 0. \end{cases} \qquad \vec{e}_{i,v}^{\,N} = \begin{cases} \vec{e}_i^{\,0\perp} & \text{if } C_v > 0, \\ \vec{e}_i^{\,0\perp} \text{ or } -\vec{e}_i^{\,0\perp} & \text{if } C_v = 0, \\ -\vec{e}_i^{\,0\perp} & \text{if } C_v < 0. \end{cases} \tag{19}$$

where

$$C_j = \vec{e}_{i,j} \cdot \vec{e}_i^{\,0\perp}, \quad C_v = \vec{e}_{i,v} \cdot \vec{e}_i^{\,0\perp}. \tag{20}$$

Here, $\vec{e}_i^{\,0\perp}$ is the vector obtained by rotating desired moving direction $\vec{e}_i^{\,0}$ for 90° counterclockwise. According to Eq. (19), influence from pedestrians and walls are decided not only by their position but also by the desired moving direction of the pedestrian i. If the centers of pedestrians or the closest points in walls to the center of the pedestrian i are located in the left area to $\vec{e}_i^{\,0}$, the direction of influence is defined as right side perpendicular vector of $\vec{e}_i^{\,0}$ and vice versa. It should be noticed that there might be an extremely rare case when C_j or C_v is equal to zero. In this case, the influence direction is decided by multiple factors, e.g. culture, gender. To simplify the model, the direction of influence is randomly chosen from $\vec{e}_i^{\,0\perp}$ and $-\vec{e}_i^{\,0\perp}$ in this case, corresponding to pedestrians avoiding front obstacles from the sides.

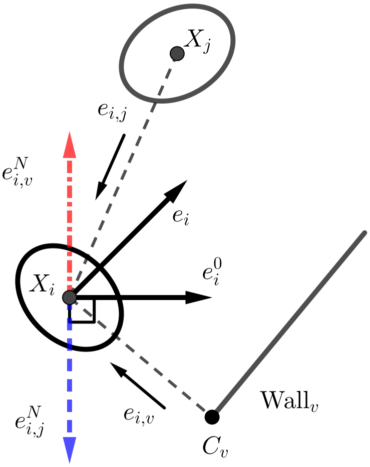

Figure 6. Notations used in the new direction sub-model. the direction of influence from pedestrian j to pedestrian i is vector represented by red chain line and the direction of influence from wall v to pedestrian i is vector represented by the blue dashed line. X_i and X_j are positions of the pedestrians, C_v is the closet point in wall v to X_i, $\vec{e}_i^{\,0}$ and $\vec{e}_i$ are the desired moving direction and the actual moving direction of the pedestrian i, $\vec{e}_{i,j}$ and $\vec{e}_{i,v}$ are the unit vectors from X_j and C_v to X_i, $\vec{e}_{i,j}^{\,N}$ and $\vec{e}_{i,v}^{\,N}$ are the directions used to calculate the influence of the pedestrians j and walls v act on pedestrian i respectively.

Then, we introduce a new relaxation time parameter τ in the direction sub-model, which is represented as

$$\frac{d\vec{e}_i(t)}{dt} = \frac{\vec{E}_i(t) - \vec{e}_i(t)}{\tau}, \tag{21}$$

where $\vec{e}_i$ is the moving direction of the pedestrian i and $\vec{E}_i$ is the optimal moving direction calculated by Eq. (18). In this step, we change the direction sub-module from zero-order to first-order, which does not change the global first-order property of the original CVM. By adjusting τ, a pedestrian can turn to its moving direction smoothly.

Besides, we use a dynamical vision area in this paper, which is the hatching area in figure 7. Only the pedestrians and walls located in Area_i, which is the dynamical vision area of the pedestrian i, influence the moving direction of the pedestrian i. The set contains all neighbors of the pedestrian i in Area_i is

$$N_i^{\text{Area}} = \{j, \vec{e}_i \cdot \vec{e}_{i,j} < 0 \text{ or } \vec{e}_i^{\,0} \cdot \vec{e}_{i,j} < 0\}. \tag{22}$$

Here $\vec{e}_{i,j}$ is the vector from the center of neighbors towards the center of the pedestrian i. As for the walls, only when two vertices of a wall are both in Area_i, this wall influences the moving direction of the pedestrian i. Vision area of the pedestrian i is decided by his desired moving direction $\vec{e}_i^{\,0}$ and his actual moving direction $\vec{e}_i$. This means a pedestrian choose the best moving direction according to the neighbors and walls located in the half area in front of his moving direction and the half area in front of his desired moving direction. The dynamical vision area is based on the idea that pedestrians will turn their heads to obtain the environmental information of the areas in front of their desired moving directions if their actual moving directions deviate from the desired moving directions. Using this dynamical vision area can eliminate some unrealistic block occurred between agents when using fixed vision area in the simulation.

These enhancements can almost eliminate the phenomena of backward movement and “shaking” in the simulation, as shown in figure 8.

ϕ is defined as the angle between the moving direction of a pedestrian and the x-axis. As we can see in figure 8, the blue line (original model) shows a strong fluctuation of the angle over time compared with the red line (our extension).

In the next section, we further show a systematic comparison of both models.

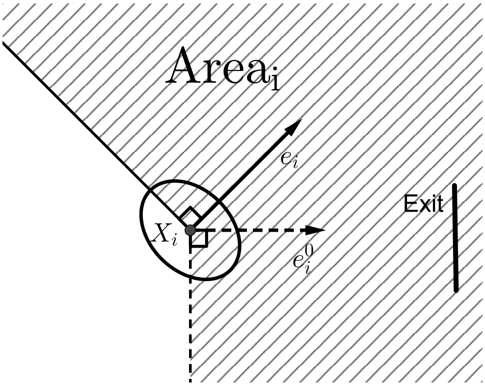

Figure 7. Dynamical vision area. X_i is the position, $\mathrm{Area_i}$ is the hatching area, $\vec{e}_i{}^0$ is the desired moving direction towards the exit, and $\vec{e}_i$ is the actual moving direction of pedestrian i.

3. Simulation results

In this section, the comparisons and analysis of models with different shapes and different direction sub-models are given. Preliminary simulation analysis has shown that the model can satisfy standards addressed in [45, 46] for basic movements of single pedestrians. We aim in this section to extend the validity of the model in regard to fundamental diagrams and collective behaviors in straight corridors and bottlenecks. The simulations in this section are executed with Euler scheme using a time step $\Delta t = 0.05\ s$. The update of the pedestrians is parallel in each step.

First, we perform simulations in a 26 m corridor with periodic boundary condition and measure the 1D fundamental diagram in a two meters long area located in the middle of the corridor. The shape of agents in these simulations, as well as the direction sub-model, are insignificant for the outcome of the simulation since pedestrians can not overtake others walking in front. Hence, we can focus on the validation of the speed sub-model and the relation between the speed and the required spacing in front.

The values of parameters are shown in table 1. The desired speed of the pedestrians is 1.34 m/s. The shape of agents is circular with a constant radius a. The value of a is 0.18 m and the value of T is 1.06 s, which are obtained from the linear relationship of required length and velocity [44].

Table 1. Parameters of CVM in one-dimensional scenario

	V^0 (m/s)	a (m)	T (s)	k	D (m)	k_w	D_w (m)
1D	1.34	0.18	1.06	3.0	0.1	6.0	0.05

The simulation results in the 1D case are shown in figure 9. We realize that the obtained 1D fundamental diagram fit well with the experimental data.

In the second step, we investigate the effect of the agent's shape on the two-dimensional fundamental diagram. The simulation scenario is a 26×1.8 m^2 corridor with periodic boundary conditions. We measure the 2D fundamental diagram of models which describing agent with different shapes. We use three kinds of shapes here, circles with constant radius, ellipses with constant a and variable b as defined in Eq. (13) and ellipses with constant a and variable b as defined in Eq. (14).

The value of V^0, a, T and parameters in direction sub-model are the same as in the one-dimensional case. Table 2 summarizes the value of other parameters.

Table 2. Parameters of CVM in two-dimensional scenario

	$b_{\min}$ (m)	$b_{\max}$ (m)	b function	β	γ
constant circle	\	\	\	\	\
original ellipse	0.15	0.25	(13)	\	\
new ellipse	0.15	0.25	(14)	50	0.1

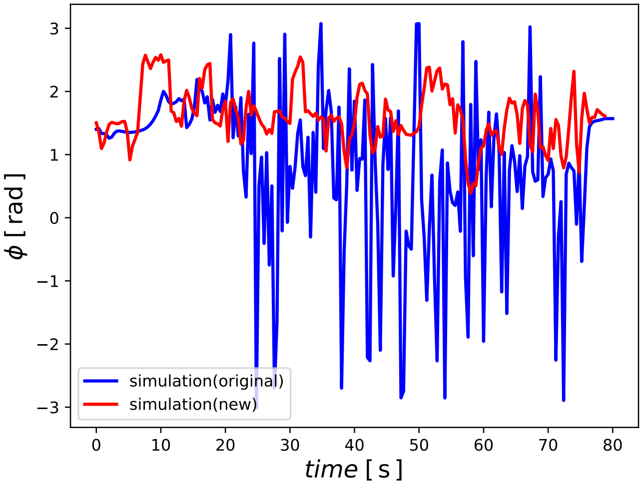

Figure 8. Time series of the angle between the moving direction of a pedestrian and the x-axis (ϕ).

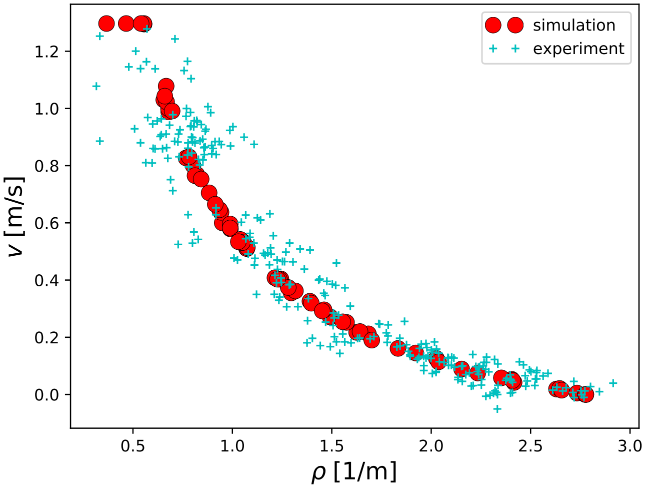

Figure 9. Velocity-density relation (fundamental diagram) in one-dimensional scenario, compared with experimental data [47].

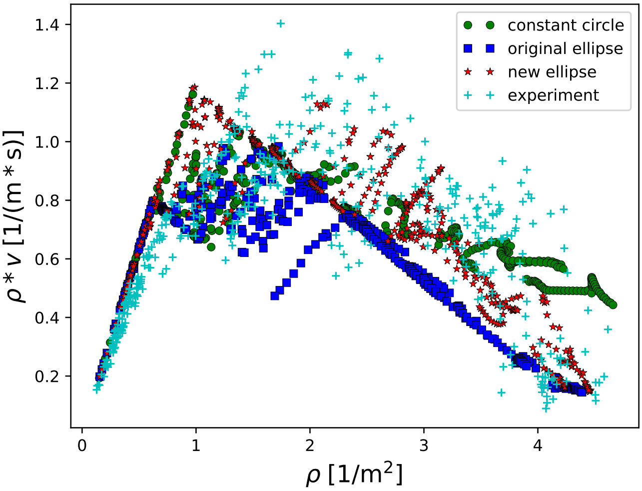

Figure 10. Relation between flow and density (fundamental diagram) in two-dimensional scenario, compared with experimental data obtained in the Hermes-project [48].

The simulation results of the 2D case are shown in figure 10. From figure 10, we can get the result that the shape of agents in the model influence the fundamental diagram in the two-dimensional scenario, especially in the high-density area. The results obtained with constant circle and ellipse with variable b defined as Eq. (13) both have deviation with experimental data in the high-density area while using ellipse with variable b defined as Eq. (14) can obtain 2D fundamental diagram which is closer to the experimental results. That means the new function for b we proposed has a positive impact on the simulation result.

Then, we perform simulations in bottleneck scenarios [47]. We measure the relation between the flow in the middle of the bottleneck and the width of the bottleneck which is adjusted from 1.0 m to 2.5 m in our simulations. As we mentioned before, we can observe some unusual behavior during the simulation. Besides, we observe that the distribution of pedestrians in front of the bottleneck is different from the experiment. The new direction sub-model proposed in the previous section can eliminate these unusual phenomena.

In order to compare the simulation results of original and new direction sub-model fairly, we adjust the value of the parameter T to make the flow-width relation obtained from the simulation results as close to the relation obtained from experimental data as possible. The shape of the pedestrian in original and new model are both the new dynamical ellipse we proposed in previous section, the value of a, $b_{\min}$, $b_{\max}$, β and γ are given in table 2, the value of k, D, k_w, D_w are provided in table 1. The desired speeds of the pedestrians are Gaussian distributed with a mean of 1.34 m/s and a standard deviation of 0.26 m/s [49]. After validation, the value of T in the original model is 0.5 s and in the new model is 0.45 s. The value of new parameter τ introduced in new direction sub-model is 0.3 s. The relations obtained are shown in figure 11 and compared with experimental data. In figure 11 we can find the relation obtained from simulation results of the original and new model both very close to the experimental data.

Since the purpose of our extension is to eliminate backward movement and shaking phenomenon. We compare two indexes to prove that our extensions are useful. The first one is the backward movement proportion

$$O = \frac{\sum_{i=1}^{N}\sum_{k=0}^{M_i} O_i(k \cdot \Delta t)}{\sum_{i=1}^{N} M_i}, \tag{23}$$

where Δt is the time step size in the simulation, $M_i * \Delta t$ is the simulation duration of pedestrian i, N is the number of pedestrians

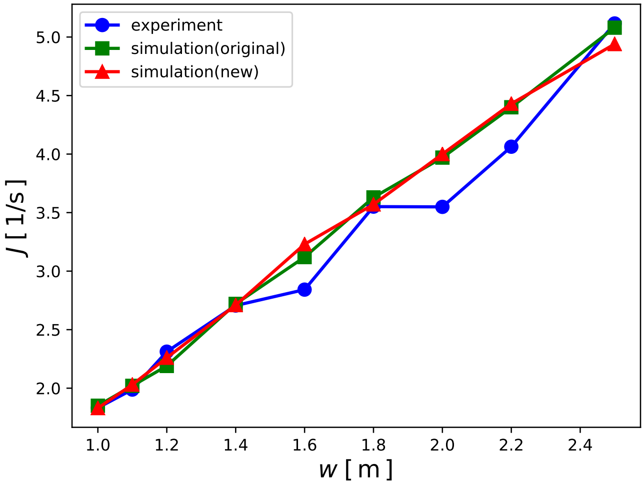

Figure 11. Relation between the flow in the middle of the bottleneck and the width of bottleneck, compared with experimental data[23].

in the simulation and

$$O_i(t) = \begin{cases} 1, & \vec{e}_i(t) \cdot \vec{e}_i^{\,0}(t) < 0 \\ 0, & \text{else} \end{cases}, \tag{24}$$

where $\vec{e}_i(t)$ is the moving direction of pedestrian i. This definition means that when the angle between the actual moving direction and the desired moving direction of a pedestrian is greater than 90 degrees, we regard it as a backward movement.

We calculate the proportion of backward movement from the simulation results of the original model and new model in bottleneck scenarios with different widths from 1.0 m to 2.5 m. The results are shown and compared in figure 12.

From figure 12, we can find that the proportion of backward movement significantly decreases in the new model compared to the original model. Therefore our extension eliminates the unrealistic backward movement.

The second index is the average angular variation in moving direction per pedestrian per frame, which is presented as

$$S_{average} = \frac{\sum_{i=1}^{N}\sum_{k=1}^{M_i} S_i(k \cdot \Delta t)}{\sum_{i=1}^{N}(M_i - 1)} \tag{25}$$

with

$$S_i(t) = \left|\angle\left[\vec{e}_i(t), \vec{e}_i t - \Delta t)\right]\right|, \tag{26}$$

where the definition of $\angle\left[\vec{e}_i(t), \vec{e}_i t - \Delta t)\right]$ is the angle between $\vec{e}_i(t)$ and $\vec{e}_i(t - \Delta t)$. The definition of moving direction $\vec{e}_i(t)$ is the same as before. $S_i(t)$ is the absolute value of the angle between moving direction in the current time step and the previous one. We compare this index for the new model and the original model. The results are presented in figure 13.

It can be observed in figure 13 that in the new model the pedestrians change less their direction than the pedestrians in the original model, which is in line with the fact that pedestrians prefer to keep their direction instead of changing it. Compared within the original model, agents no longer shake frequently.

Finally, we compare the spatiotemporal profile of bottleneck flow when the width is 1.2 m. In simulations, we initialise pedestrians in the same positions and at the same times as in the experiment, in order to eliminate the impact of pedestrians'

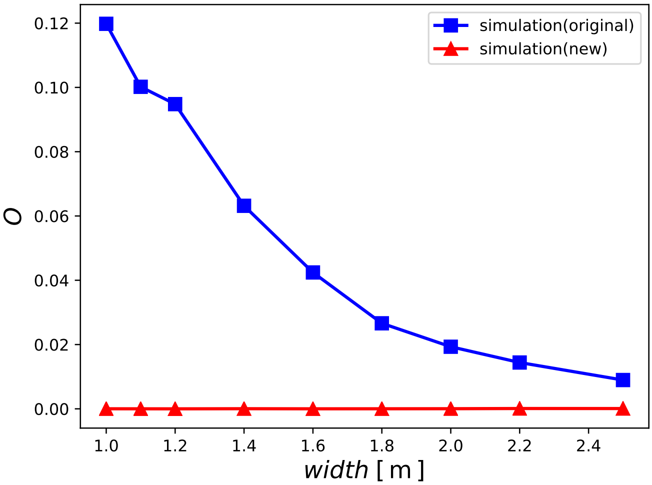

Figure 12. Proportion of backward movement in bottleneck scenarios with different widths from 1.0 m to 2.5 m.

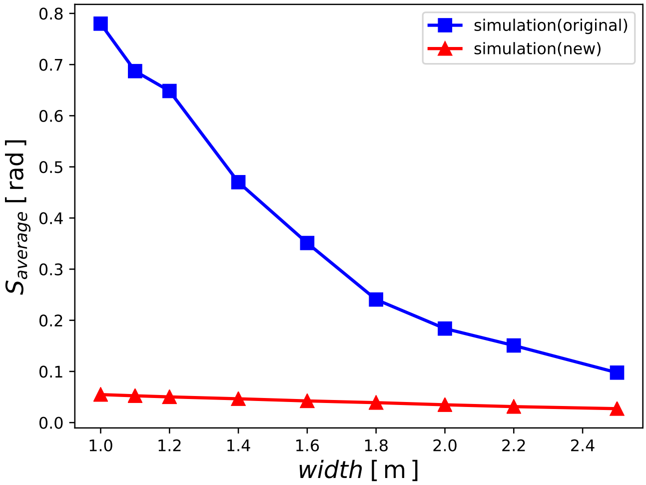

Figure 13. Average angular variation in moving direction per pedestrian per frame in bottleneck scenarios with different widths from 1.0 m to 2.5 m.

initial distribution. The profiles obtained from the experiment, the original speed model as well as the new model are shown in figure 14. Although profiles obtained from new model are still somewhat different from the experimental results, a visible enhancement can be observed. The pedestrians do not deviate strongly from the exit as it can be observed with the original model.

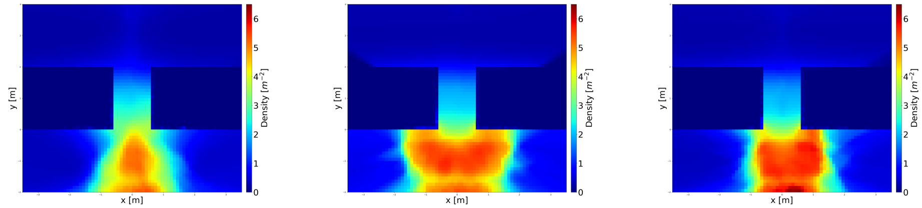

(a) density, experiment (b) density, original model (c) density, new model

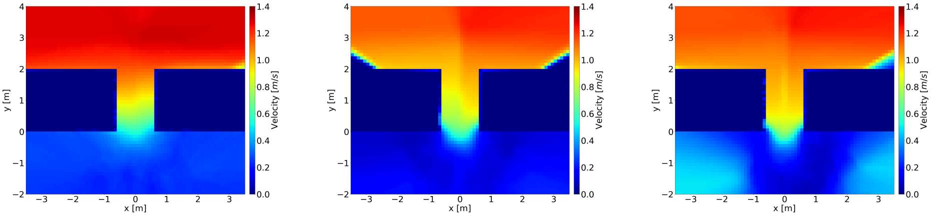

(d) velocity, experiment (e) velocity, original model (f) velocity, new model

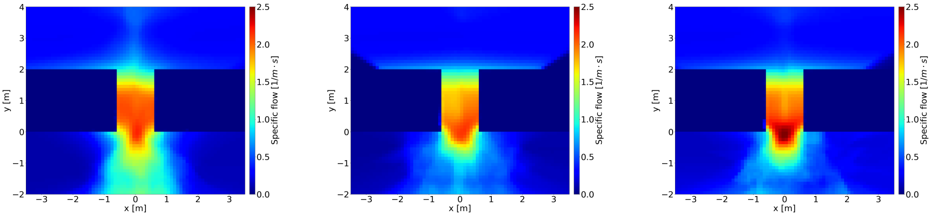

(g) Specific flow, experiment (h) Specific flow, original model (i) Specific flow, new model

Figure 14. Spatiotemporal profile of bottleneck flow, the width of bottleneck is 1.2 m. Pedestrians pass through the bottleneck from bottom to top.

4. Conclusion

In this paper we enhance and generalize the collision-free model [36] by introducing new components that lead to better dynamics. We firstly complete the collision-free velocity model by introducing the influence of walls. Then, we generalize the definition of the model in order to consider dynamical ellipse shapes of pedestrian's projection on the 2D space, instead of the originally used circular shapes. Hereby, we define the semi-axes of the ellipses such that the two-dimensional fundamental diagram is well reproduced with respect to experimental data. After introducing a new direction sub-model, we show quantitatively that the unrealistic behavior of the agents during simulations with the original model could be mitigated. Simulation results show that the new direction sub-model can remove unrealistic backward movement and undesired shaking behaviors without compromising the benefits of the original model.

Our validation of the model was systematic, going from the fundamental diagram in narrow corridors (1D) through fundamental diagrams in wide corridors (2D) to the flow-width relation in bottlenecks. Although the generalized model produces better results, there are still some problems that have not been solved yet. First of all, in bottleneck scenarios with small widths, a jamming arch may arise. Here, the collision-free nature of the model favors excessive blocking of agents in front of the exit. Further investigations are necessary to identify an appropriate mechanism for mitigating the effects of arching. Besides, more detailed validations will be done in future work.

Acknowledgments

Qiancheng Xu thanks the funding support from the China Scholarship Council (Grant NO.201706060186). Mohcine Chraibi thanks the support from the Visiting Professor International Project at the University of Science and Technology of China (2019A VR35).

References

[1] A. Seyfried, O. Passon, B. Steffen, M. Boltes, T. Rupprecht, W. Klingsch, New insights into pedestrian flow through bottlenecks, Transportation Science 43 (3) (2009) 395–406.

[2] D. C. Duives, W. Daamen, S. P. Hoogendoorn, State-of-the-art crowd motion simulation models, Transportation research part C: emerging technologies 37 (2013) 193–209.

[3] R. L. Hughes, A continuum theory for the flow of pedestrians, Transportation Research Part B: Methodological 36 (6) (2002) 507–535.

[4] J. A. Carrillo, S. Martin, M.-T. Wolfram, An improved version of the Hughes model for pedestrian flow, Mathematical Models and Methods in Applied Sciences 26 (04) (2016) 671–697.

[5] B. Piccoli, A. Tosin, Time-evolving measures and macroscopic modeling of pedestrian flow, Archive for Rational Mechanics and Analysis 199 (3) (2011) 707–738.

[6] S. P. Hoogendoorn, F. L. van Wageningen-Kessels, W. Daamen, D. C. Duives, Continuum modelling of pedestrian flows: From microscopic principles to self-organised macroscopic phenomena, Physica A: Statistical Mechanics and its Applications 416 (2014) 684 – 694.

[7] A. Lachapelle, M.-T. Wolfram, On a mean field game approach modeling congestion and aversion in pedestrian crowds, Transportation Research Part B: Methodological 45 (10) (2011) 1572–1589.

[8] M. Burger, M. D. Francesco, P. A. Markowich, M.-T. Wolfram, Mean field games with nonlinear mobilities in pedestrian dynamics, Discrete & Continuous Dynamical Systems - B 19 (2014) 1311.

[9] A. Aurell, B. Djehiche, Mean-field type modeling of nonlocal crowd aversion in pedestrian crowd dynamics, SIAM Journal on Control and Optimization 56 (1) (2018) 434–455.

[10] Y. Achdou, J.-M. Lasry, Contributions to Partial Differential Equations and Applications, Springer International Publishing, Cham, 2019, Ch. Mean Field Games for Modeling Crowd Motion, pp. 17–42.

[11] N. Bellomo, A. Bellouquid, On the modelling of vehicular traffic and crowds by kinetic theory of active particles, in: Mathematical modeling of collective behavior in socio-economic and life sciences, Springer, 2010, pp. 273–296.

[12] C. Dogbe, On the modelling of crowd dynamics by generalized kinetic models, Journal of Mathematical Analysis and Applications 387 (2) (2012) 512–532.

[13] N. Bellomo, D. Clarke, L. Gibelli, P. Townsend, B. Vreugdenhil, Human behaviours in evacuation crowd dynamics: from modelling to “big data” toward crisis management, Physics of life reviews 18 (2016) 1–21.

[14] N. Bellomo, L. Gibelli, N. Outada, On the interplay between behavioral dynamics and social interactions in human crowds, Kinetic & Related Models 12 (2019) 397.

[15] A. Elmoussaoui, P. Argoul, M. E. Rhabi, A. Hakim, Discrete kinetic theory for 2d modeling of a moving crowd: Application to the evacuation of a non-connected bounded domain, Computers & Mathematics with Applications 75 (4) (2018) 1159–1180.

[16] A. Treuille, S. Cooper, Z. Popović, Continuum crowds, ACM Trans. Graph. 25 (3) (2006) 1160–1168.

[17] K. Rahman, N. A. Ghani, A. A. Kamil, A. Mustafa, M. K. Chowdhury, Modelling pedestrian travel time and the design of facilities: A queuing approach, PLoS ONE 8(5) (2013) e63503.

[18] A. Tordeux, G. Lämmel, F. S. Hänseler, B. Steffen, A mesoscopic model for large-scale simulation of pedestrian dynamics, Transportation Research Part C: Emerging Technologies 93 (2018) 128 – 147.

[19] G. Puppo, M. Semplice, A. Tosin, G. Visconti, Fundamental diagrams in traffic flow: The case of heterogeneous kinetic models, Communications in mathematical sciences 14 (2016) 643–669.

[20] G. Visconti, M. Herty, G. Puppo, A. Tosin, Multivalued fundamental diagrams of traffic flow in the kinetic Fokker-Planck limit, Multiscale Modeling & Simulation 15 (2017) 1267–1293.

[21] N. Bellomo, A. Bellouquid, D. Knopoff, From the microscale to collective crowd dynamics, Multiscale Modeling & Simulation 11 (3) (2013) 943–963.

[22] E. Cristiani, B. Piccoli, A. Tosin, Multiscale modeling of pedestrian dynamics, Vol. 12, Springer, 2014.

[23] N. Bellomo, L. Gibelli, Toward a mathematical theory of behavioral-social dynamics for pedestrian crowds, Mathematical Models and Methods in Applied Sciences 25 (13) (2015) 2417–2437.

[24] N. Bellomo, C. Dogbe, On the modeling of traffic and crowds: A survey of models, speculations, and perspectives, SIAM review 53 (3) (2011) 409–463.

[25] N. Bellomo, A. Bellouquid, On multiscale models of pedestrian crowds from mesoscopic to macroscopic, Commun. Math. Sci 13 (7) (2015) 1649–1664.

[26] M. Chraibi, A. Tordeux, A. Schadschneider, A. Seyfried, Modelling of pedestrian and evacuation dynamics, Encyclopedia of Complexity and Systems Science (2018) 1–22.

[27] L. Gibelli, N. Bellomo, Crowd Dynamics – Theory, Models, and Safety Problems, Vol. 1, Springer, 2019.

[28] D. Helbing, I. J. Farkas, P. Molnar, T. Vicsek, Simulation of pedestrian crowds in normal and evacuation situations, Pedestrian and evacuation dynamics 21 (2) (2002) 21–58.

[29] A. Schadschneider, A. Seyfried, Empirical results for pedestrian dynamics and their implications for modeling, Networks & Heterogeneous Media 6 (2011) 545.

[30] V. J. Blue, J. L. Adler, Cellular automata microsimulation for modeling bi-directional pedestrian walkways, Transportation Research Part B: Methodological 35 (3) (2001) 293–312.

[31] C. Burstedde, K. Klauck, A. Schadschneider, J. Zittartz, Simulation of pedestrian dynamics using a two-dimensional cellular automaton, Physica A: Statistical Mechanics and its Applications 295 (3-4) (2001) 507–525.

[32] M. Fukui, Y. Ishibashi, Self-organized phase transitions in cellular automaton models for pedestrians, Journal of the physical society of Japan 68 (8) (1999) 2861–2863.

[33] A. Kirchner, A. Schadschneider, Simulation of evacuation processes using a bionics-inspired cellular automaton model for pedestrian dynamics, Physica A: statistical mechanics and its applications 312 (1-2) (2002) 260–276.

[34] M. Muramatsu, T. Irie, T. Nagatani, Jamming transition in pedestrian counter flow, Physica A: Statistical Mechanics and its Applications 267 (3-4) (1999) 487–498.

[35] A. Tordeux, A. Seyfried, Collision-free nonuniform dynamics within continuous optimal velocity models, Physical Review E 90 (4) (2014) 042812.

[36] A. Tordeux, M. Chraibi, A. Seyfried, Collision-free speed model for pedestrian dynamics, in: Traffic and Granular Flow'15, Springer, 2016, pp. 225–232.

[37] B. Maury, J. Venel, A discrete contact model for crowd motion, ESAIM: Mathematical Modelling and Numerical Analysis 45 (1) (2011) 145–168.

[38] S. Paris, J. Pettré, S. Donikian, Pedestrian reactive navigation for crowd simulation: a predictive approach, in: Computer Graphics Forum, Vol. 26, Wiley Online Library, 2007, pp. 665–674.

[39] D. Helbing, P. Molnar, Social force model for pedestrian dynamics, Physical review E 51 (5) (1995) 4282.

[40] M. Chraibi, A. Seyfried, A. Schadschneider, Generalized centrifugal-force model for pedestrian dynamics, Physical Review E 82 (4) (2010) 046111.

[41] D. R. Parisi, M. Gilman, H. Moldovan, A modification of the social force model can reproduce experimental data of pedestrian flows in normal conditions, Physica A: Statistical Mechanics and its Applications 388 (17) (2009) 3600–3608.

[42] A. Johansson, D. Helbing, P. K. Shukla, Specification of the social force pedestrian model by evolutionary adjustment to video tracking data, Advances in complex systems 10 (supp02) (2007) 271–288.

[43] J. J. Fruin, Pedestrian planning and design, Tech. rep., New York: Elevator World (1971).

[44] A. Seyfried, B. Steffen, W. Klingsch, M. Boltes, The fundamental diagram of pedestrian movement revisited, Journal of Statistical Mechanics: Theory and Experiment 2005 (10) (2005) P10002.

[45] R. e.V., Guideline for microscopic evacuation analysis, URL `https://rimeaweb.files.wordpress.com/2016/06/rimea_richtlinie_3-0-0_-_d-e.pdf` acceded on 01.07.2019 (2016).

[46] E. Ronchi, E. D. Kuligowski, P. A. Reneke, R. D. Peacock, D. Nilsson, The process of verification and validation of building fire evacuation models, US Department of Commerce, National Institute of Standards and Technology, 2013.

[47] A. Seyfried, M. Boltes, J. Kähler, W. Klingsch, A. Portz, T. Rupprecht, A. Schadschneider, B. Steffen, A. Winkens, Enhanced empirical data for the fundamental diagram and the flow through bottlenecks, in: Pedestrian and Evacuation Dynamics 2008, Springer, 2010, pp. 145–156.

[48] S. Holl, A. Seyfried, Hermes-an evacuation assistant for mass events, Inside 7 (1) (2009) 60–61.

[49] S. Buchmüller, U. Weidmann, Parameters of pedestrians, pedestrian traffic and walking facilities, IVT Schriftenreihe 132 (2006).

A.5 ARTICLE IV

A speed-based model for crowd simulation considering walking preferences

S. Zhang, J. Zhang, M. Chraibi, and W. Song.

Communications in Nonlinear Science and Numerical Simulation (**2021**)

Communications in Nonlinear Science and Numerical Simulation, 95, 105624, 2021

10.1016/j.cnsns.2020.105624

A Speed-based Model for Crowd Simulation Considering Individual Preferences

Sainan Zhang[1], Jun Zhang[1], Mohcine Chraibi[2], Weiguo Song[1]

Abstract

To investigate the influence of the individual preferences on pedestrian movements, a modified collision-free speed model is proposed by considering the expectations of comfortable walking for a pedestrian. In the model, the walking directions of pedestrians are determined by taking human perception of comfort and preference for walking straight to their intended destinations into account. The restriction of walls in heading direction on pedestrian's walking is introduced to avoid potential collisions among pedestrians and obstacles. Model validation with respect to experimental data shows that our model performs better than the original model with regards to the trajectory's distribution and the velocity profile, and can effectively alleviate backward movements. Furthermore, the speed-density relation in narrow corridors inferred from the new model fits the experimental data well and the model performs more accurately in simulating the flow-width relation in bottleneck scenario than the original collision-free speed model.

Keywords

Model

[1] *State Key Laboratory of Fire Science, University of Science and Technology of China, Hefei, 230027, China*

[2] *Institute for Advanced Simulation. Forschungszentrum Jülich GmbH, Jülich, 52428, Germany*

Contents

Introduction

Dense crowds formed due to holidays or large scale activities are often related to risks, such as stampede [1, 2]. To improve the safety of events, a variety of pedestrian models have been proposed to uncover the mechanism of individual behaviors and interactions among pedestrians and obstacles [3, 4, 5, 6, 7].

In the force-based models [8], the evolution of pedestrian movement over time is described by the Newtonian dynamics. Several self-organized phenomena like arching at bottlenecks and lane-formation in bidirectional flow [9, 10] can be reproduced fairly well. However, pedestrians in these models are regarded as moving particles under the influence of forces, which often leads to unrealistic backward movement and overlapping when the repulsive forces from neighbors and obstacles are larger than the self-driven force, especially under high densities [11]. Moreover, forces in these models are often defined to be long-ranged, which means that invisible or even pedestrians in a large distance still influence the movement of their neighbors. A usually used remedy is to introduce an artificial cut-off radius. In addition, force-based models require solving second-order differential equations with a small time step, which causes a high computational overhead [12].

Another category of models is velocity-based [13, 14, 15, 16]. Here pedestrian's speed is adjusted based on the relative positions and velocities of their neighbors. Compared to force-based models, they deal with overlapping among pedestrians efficiently with a reduced computational cost. However, these models often depend on a large number of parameters, which causes inherent calibration difficulties. The collision-free speed model [12] realizes collision avoidance solely depending on the minimum headway distance. Despite of its simplicity, it can reproduce many self-organization phenomena with higher efficiency.

In fact, besides the exclusion among people or obstacles, pedestrians are affected by many other factors when deciding the moving directions like their perception of comfort and preference for walking straight to the intended destinations [17, 18, 19]. However, models mentioned above do not take this difference into account. The heuristic model was proposed to predict the walking direction and displacement of pedestrians based on behavioral heuristics [20, 21]. It makes a trade-off between seeking an unobstructed walking direction and minimizing detours from the most direct route. Nevertheless, it does not consider the critical acceptable distance for pedestrians to maintain the desired direction. For example, if there are other people or obstacles in its desired direction, no matter how far away, the pedestrian in this model will immediately react by changing the moving direction to avoid obstacles, which is not in line with reality. In the collision avoidance experiment in [22], the probability of pedestrian changing movement direction decreases exponentially as the headway distance increases when the distance is larger than 1.099 m. Furthermore, the displacement is solved by two integration steps of the acceleration, which results in an increased computational expense.

To overcome these shortcomings, we developed a new microscopic model by integrating subjective preference of pedestrians into the collision-free speed model. Subjective preferences include pedestrians' inclination for a desired direction, demand for a longer walking way than the least comfortable headway distance and tendency to following others' moving behaviors. Whereas from a modelling perspective, it is rather difficult to consider all these factors. In this paper, we only focus on the first two subjective preferences, as we think they have a significant effect on pedestrian's movement.

The remainder of this article is structured as follows. The model is defined in section 1 while the validation and comparison between simulation results of collision-free speed model and proposed model are shown in section 2. In section 3, we discuss parameter's influence on the results and the limitation of the model. Finally, we give a summary of the model in section 4.

1. Model definition

As for the individual preferences, pedestrians' inclination for desired direction and demand for a longer walking way other than the least comfortable headway distance are considered. The proposed model is composed of two parts: a direction submodule and a speed submodule. Within this approach, the actual moving direction is obtained based on two subjective preferences. First, a pedestrian has a strong expectation to maintain its desired direction unless the obstacle in the moving direction makes the walking uncomfortable [23]. Second, in case the direction of motion has to be changed, it is desirable to maintain the deviation from the desired direction as small as possible [24]. Finally, the influence of walls on the pedestrian's walking speed is introduced into the collision-free velocity model to achieve collision avoidance for pedestrians.

The direction submodel

The movement of a pedestrian can be affected by the neighbors nearby. Pedestrians in the front have stronger impact on one's movement than those in the rear and the closed pedestrians have greater influence than those far away. Based on this assumption, only the pedestrians in the desired direction of the movement are regarded as neighbors in the model to maximize the computational efficiency of the model [12]. Here, we define the desired moving direction from the current pedestrian position to the final target point.

Accordingly, the neighbors of pedestrian i are defined as follows:

$$J_i = \{j, \vec{e}_{id} \cdot \vec{e}_{i,j} \leq 0 \text{ and } |\vec{e}_{id}^{\perp} \cdot \vec{e}_{i,j}| \leq l/s_{i,j}\}, \tag{1}$$

where j denotes other pedestrians (except pedestrian i), $\vec{e}_{id}$ represents the desired direction of pedestrian i, $\vec{e}_{id}^{\perp}$ is a vector obtained by rotating $\vec{e}_{id}$ for 90° counterclockwise, $\vec{e}_{i,j}$ is a unit vector from j to i, l denotes the diameter of pedestrians simplified to circles with same size, $s_{i,j}$ represents the Euclidean distance between the centers of pedestrians i and j. As shown in Fig. 1, neighbors of pedestrian i are those who overlap with the grey area.

The closest pedestrian $j_{\min}$ in the desired direction of motion is defined such that

$$s_{i,j_{\min}} = \min_{j \neq i} s_{i,j}. \tag{2}$$

As observed in people's daily behavior in shared places, people prefer to make a detour from their desired

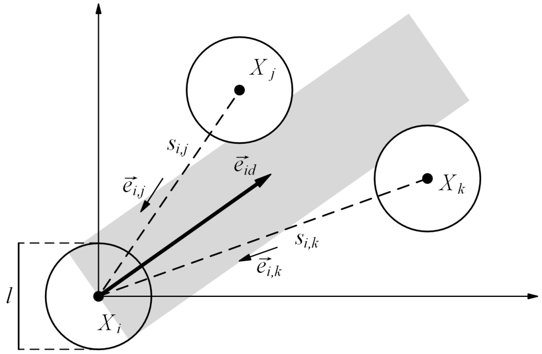

Figure 1. A sketch showing the neighbors of pedestrian i. In this model, X_i, X_j and X_k are positions of pedestrians. $s_{i,j}$ and $s_{i,k}$ are distances between the centers of pedestrians. $\vec{e}_{i,j}$ and $\vec{e}_{i,k}$ are unit vectors from X_j and X_k to X_i.

direction, when the comfortable walking space is occupied by others.

Considering pedestrian's preference for comfort during walking, we define the following condition:

$$s_{i,j_{\min}} < s_c. \tag{3}$$

As shown in Eq. (3), s_c represents the critical headway distance which makes the speed of pedestrian lower than the comfortable speed in different scenarios. That is, if the headway distance $s_{i,j_{\min}}$ for pedestrian i is smaller than s_c, the pedestrian will feel uncomfortable and prefers to pass the one ahead. Whether to take transcendental action or not, it ultimately depends on the size of the free space around. If a pedestrian decides to detour, deflecting minimally from the desired direction will be adopted.

When the condition(3) is met, pedestrian i will deviate from its desired direction and the change is minimized as far as possible. In this sense, two tangent directions $\vec{e}_{io}$ and $\vec{e}_{is}$ shown in Fig. 2 are considered as the best alternative choices. The corresponding deflection angle $\Delta\theta_o$ and $\Delta\theta_s$ can be calculated as:

$$\begin{aligned}\Delta\theta_o &= \left(\arcsin\frac{l}{s_i} - \arccos\left(\vec{e_{id}}\cdot\vec{e_{ji}}\right)\right)\cdot g\left(\vec{e_{id}}^{\perp}\cdot\vec{e_{ij}}\right)\\ \Delta\theta_s &= -\left(\arcsin\frac{l}{s_i} + \arccos\left(\vec{e_{id}}\cdot\vec{e_{ji}}\right)\right)\cdot g\left(\vec{e_{id}}^{\perp}\cdot\vec{e_{ij}}\right),\end{aligned} \tag{4}$$

where subscripts o and s are short for "optimal" and "sub-optimal", respectively. $\Delta\theta_o$ and $\Delta\theta_s$ represent the deflection angles required to turn from the desired direction $\vec{e_{id}}$ to $\vec{e_{io}}$ and $\vec{e_{is}}$. s_i denotes the distance from the center of pedestrian i to that of the nearest neighbor. Function $g(x)$ is 1 if $x > 0$, and otherwise is equal to -1. It is noted that when the conditions of optimal and suboptimal directions are the same, that is, $\vec{e_{id}}^{\perp}\cdot\vec{e_{ij}}$ is equal to 0, $g\left(\vec{e_{id}}^{\perp}\cdot\vec{e_{ij}}\right)$ will be -1, resulting in a negative value of $\Delta\theta_o$. Considering that y-axis is defined along the direction of the exit, x-axis is defined in accordance with the right-hand rule and the desired movement direction of pedestrian corresponds to the angle away from the x-axis, it can be found that the negative deflection angle $\Delta\theta_o$ makes the pedestrian choose the right side of the desired direction, which corresponds to the right-side preference of pedestrian for overtaking [25].

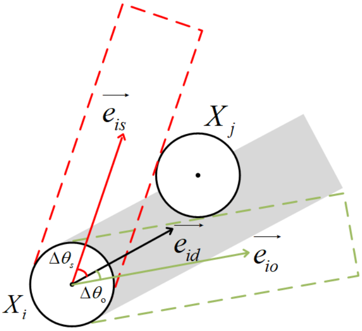

Figure 2. A sketch showing two tangent directions $\vec{e}_{io}$ and $\vec{e}_{is}$. $\vec{e}_{io}$ represents the direction with minimum deflection angle to surpass the pedestrian ahead. $\vec{e}_{is}$ represents the direction with minimum deflection angle in the opposite deflection of $\vec{e}_{io}$.

Based on this idea, we calculate the final deflection angle as defined in Eq. (5). Where k_o and k_s represent the pedestrian's choices of e_{io} and e_{is}. Only two values 0 and 1 can be chosen.

$$\Delta\Theta = k_o \cdot \Delta\theta_o + (1-k_o)\cdot\ k_s \cdot \Delta\theta_s. \tag{5}$$

The value of k_o and k_s is determined by the minimum acceptable distance and actual free space in the new direction. Specifically,

$$\begin{aligned} k_o &= s_r^o(i,j,t) > s_{im} \text{ and } s_r^o(i,w,t) > s_{im} \\ k_s &= s_r^s(i,j,t) > s_{im} \text{ and } s_r^s(i,w,t)) > s_{im}. \end{aligned} \tag{6}$$

Here, j and w indicate the pedestrian and wall, respectively. $s_r^o(i,j,t)$ and $s_r^o(i,w,t)$ are parameters in $\vec{e_{io}}$ direction. Specifically, $s_r^o(i,j,t)$ and $s_r^o(i,w,t)$ represent the movable distance for pedestrian i when there are other pedestrians or walls in its direction. Similarly, $s_r^s(i,j,t)$ and $s_r^s(i,w,t))$ are parameters in the $\vec{e_{is}}$ direction. $s_r^s(i,j,t)$ and $s_r^s(i,w,t))$ represent the movable distance from the nearest pedestrians or walls in $\vec{e_{is}}$ direction. s_{im} denote the minimum acceptable distance for pedestrian i.

Next, we illustrate how a pedestrian makes a detour. Based on the preference for the desired direction, a pedestrian considers the direction with smallest deviation firstly. That corresponds to $\vec{e_{io}}$ direction in Fig. 3. Then, the actual movable distance is compared with the minimum acceptable distance to decide which direction to choose. Only when both conditions $s_r^o(i,j,t) > s_{im}$ and $s_r^o(i,w,t) > s_{im}$ are satisfied, the pedestrian detours to $\vec{e_{io}}$ direction with the angle $\Delta\theta_o$. Otherwise, the other direction $\vec{e_{is}}$ is considered using the same criterion. When both conditions $s_r^s(i,j,t) > s_{im}$ and $s_r^s(i,w,t)) > s_{im}$ are met, it will choose the $\vec{e_{is}}$ direction with the angle $\Delta\theta_s$. If the conditions in both directions do not hold, the original movement direction will be kept without deflection.

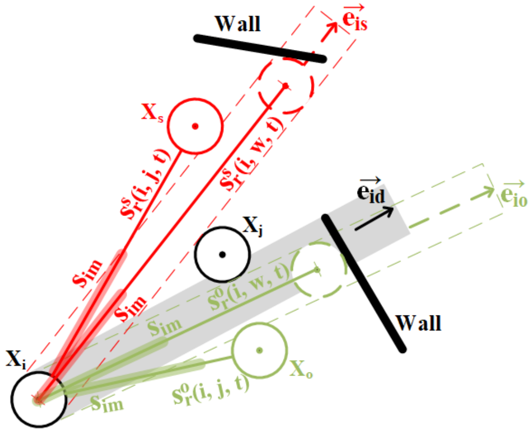

Figure 3. A sketch showing elements in $\vec{e_{io}}$ and $\vec{e_{is}}$ directions. Red and green indicate the elements in $\vec{e_{is}}$ direction and $\vec{e_{io}}$ direction, respectively. The dashed circle represents the furthest position that the pedestrian can reach when there is a wall in the new direction.

The corresponding flow chart of direction model is shown in Fig. 4.

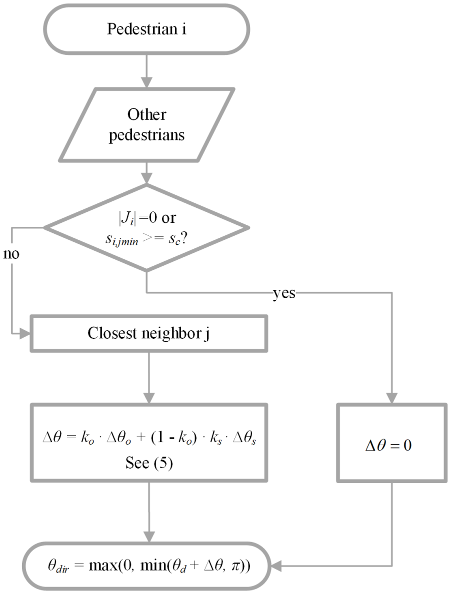

Figure 4. The flow chart of the direction model. θ_{dir} represents the angle between actual movement direction and x-axis. We define that x-axis is the direction perpendicular to the exit direction. θ_d represents the angle between desired direction and x-axis.

The speed submodel

As defined in the collision-free speed model, the speed of pedestrian i is given by

$$v_p = \min\{v_0, \max\{0, (s-l)/T\}\}. \tag{7}$$

Where, v_0 is the free speed. T represents the time gap for pedestrian to accelerate from static to v_0. s denotes the distance from the center of a pedestrian to that of its nearest neighbour.

However, in addition to other pedestrians, there are still some other obstacles and walls affecting the pedestrian's movement state and the magnitude of speed in real environments.

Based on these considerations, we introduce the effect of the wall into the original collision-free speed model. As shown in Fig. 5, s_{iw} represents the maximum distance a pedestrian can move when the movement direction is occupied by the wall. To realize no collisions with walls, a constraint of speed is added as follows:

$$v_w = \min\{v_0, s_{iw}/T\}. \tag{8}$$

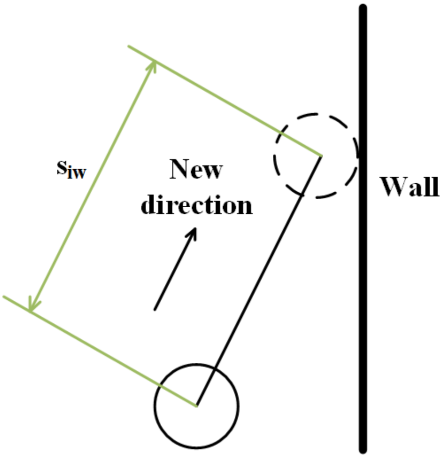

Figure 5. The maximum distance that a pedestrian can move when the front is a wall. The solid circle represents the current position of the pedestrian. The dashed circle represents the furthest position that the pedestrian can reach when there is a wall in the new direction. s_{iw} represents the maximum distance a pedestrian can move with a wall in a new direction.

Combining the above constraints, the final speed model is defined as

$$v_p = \min\left\{v_0, \max\left\{0, (s-l)/T\right\}, s_{iw}/T\right\}. \tag{9}$$

2. Simulation results

In this section, we set up a series of simulations to verify and validate the model by comparing it with the original collision-free speed model and empirical findings. Several scenarios are considered, including narrow corridor, corridor with periodic boundaries and bottleneck. The simulations are executed with JuPedSim[1] using a time step $\Delta t = 0.04s$.

Test in narrow corridor

Firstly, we perform simulations in a narrow corridor as shown in Fig. 6. In this scenario, a pedestrian is set to move straight along the corridor, while another pedestrian is standing on the way. The free speed v_0 of the pedestrian is set as 1.6 m/s. T is equal to 1.0 s in both collision-free speed model (CFM) and the proposed model. The minimum acceptable distance is equal to 0.1 m in $\vec{e_{io}}$ and $\vec{e_{is}}$ direction. s_c is the distance at current speed in a time step.

---

[1] https://jupedsim.org

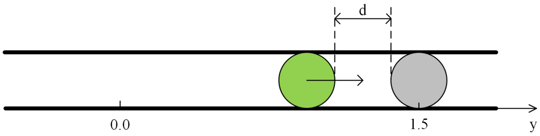

Figure 6. A sketch of the test in narrow corridor. The corridor is very narrow such that only one person can pass at the same time. The green circle denotes the pedestrian who wants to go straight and the grey one indicates the person standing in the corridor.

The positions of the pedestrian during the movement in both models are shown in Fig. 7. It is clear that the moving pedestrian in the CFM starts to oscillate in a certain distance to the pedestrian in front. The occurrence of such oscillations is due to the superpositive nature of its destination sub-model. However, the pedestrian stays close to the static one without oscillations in our model.

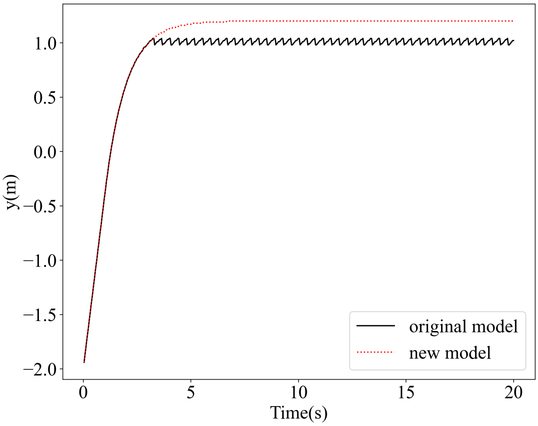

Figure 7. The position of the moving pedestrian versus time. While the original model shows an erroneous oscillatory behavior, the trajectory simulated by our proposed model is smooth and shows no oscillations.

Corridor with periodic boundaries

To further verify and validate the model, we carry out a simulation in a 30 $\times 1.8$ m^2 corridor with periodic boundary conditions and compare the results with the experimental data[2].

Fig. 8 shows the sketch of the experiment scenario, which is composed of two 6 m long straight corridor and two semicircular corridors with the inner radius 2.0 m. The width of the corridor is 1.8 m. Pedestrians were distributed uniformly along the oval corridor at the beginning of the experiment and then they were asked to walk clockwise at a normal speed. In the experiment, different crowd densities were formed by changing the number of the participants in the corridor.

---

[2] https://doi.org/10.34735/ped.2009.13

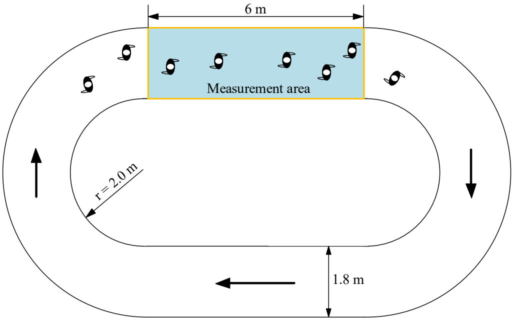

Figure 8. The sketch of the experiment scenario. The measurement area is set in the straight corridor with the length of 6 *m* and width of 1.8 *m*.The pedestrians were asked to move in the direction shown by the arrow in the oval corridor.

Considering that the desired directions of pedestrians in this scenario are parallel to each other and there are little competition among them for side-wise movement space, we make the critical headway distance of the detour s_c consistent with the distance of 0.1 times free velocity in speed model. The parameter setup is shown in table 1. The shape of pedestrian is circular with a constant diameter l, which is determined by the highest density in the experiment. Specifically, we calculate the average area occupied by each pedestrian in the high-density area in the experiment. Then the diameter of the equivalent circle under the same area is calculated as the pedestrian size. Based on the experiment data, we get the value of l 0.36 m. T is the ratio of pedestrian's headway distance to the moving speed defined in Eq. 9 before the one reaches the free velocity. The headway distance and speed under different densities in the experiment are calculated and then we get the value of T 0.86 s. The experimental data with 15 participants (the minimum number of participants) are selected to obtain the free speed of pedestrians with the consideration that the minimum headway distance is 2 m, which is enough for pedestrians to walk at the free speed when the participants are distributed uniformly in the corridor. Based on this, we get the mean value of the free speed 1.186 m/s and a standard deviation of 0.05 m/s.

Table 1. Parameters of pedestrian and model in corridor with periodic boundary scenario. where, $s(x)$ denotes the minimum headway distance when the speed is x, which is consistent with Eq. (9).

l	s_c	s_{im}	T
0.36	$s(0.1v_0)$	$s(v_0)$	0.86

We use method D in [26] to calculate the density and speed of pedestrians in the measurement area. As shown in Fig. 9, with the increase of the crowd density, the movement speed of the crowd decreases. It is worth noting that when the crowd density is greater than 3 m^{-2}, the speed decreases very slowly and is mostly less than 0.2 m/s. These results fit well with the experiment.

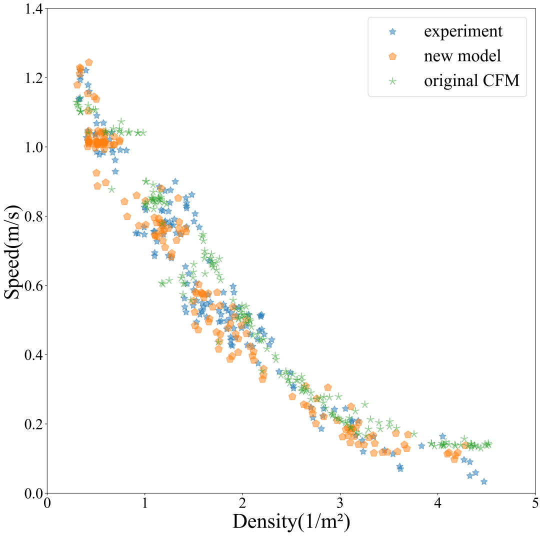

Figure 9. The relationship between speed and density. Blue, orange and green represent the results of experiment, new model and original CFM, respectively.

Bottleneck

In order to test the rationality of the model in the bottleneck scenario, we set up the model's simulation scenario referring to the setting in the experiment [27].

The parameters of the original model(CFM) are from [28] and shown in table 2. The strength coefficient k is 3.0. The distance coefficient D is 0.1 m. The time gap T is 0.5 s. The parameters of the new proposed model are shown in table 3. v_t is the moving speed of pedestrian in current frame. The free speed of pedestrians are obtained from the experiment scenario with the bottleneck length of 0 m where the pedestrians move relatively freely after walking out of the bottleneck. The free speed follows a normal distribution with a mean value of 1.200 m/s and a standard deviation of 0.249 m/s. The time gap T is obtained based on the ratio of headway distance to walking speed in the experiment. The value of T is 0.61 s. Considering the desired directions of pedestrians in this scenario are intersecting so that the competition among them for movement space is more intense than that in corridor scenario, we make the critical headway distance of the detour s_c consistent with the distance of free velocity in speed model.

Table 2. Parameters of pedestrian and CFM in bottleneck scenario.

k	D	T
3.0	0.1	0.5

Table 3. Parameters of pedestrian and new model in bottleneck scenario.

l	s_c	s_{im}	T
0.36	$s(v_0)$	$s(v_t)$	0.61

Trajectories and spatial profiles of velocity and density of pedestrians are shown in Fig. 10 [27]. We can intuitively find that the trajectories follow a cone distribution in the experiment due to the normal walking without pushing in the experiment. Compared with the trajectories distribution from the CFM, which is like an arching shape, the trajectories obtained from our model are more similar to those of the experiment. Moreover, comparing the velocity profiles among the experiment, CFM and new model, we find some common characteristics of them. Firstly, the velocity of pedestrians in front of the bottleneck entrance is relatively uniform. This may because the pedestrians are congested before the narrowing in both models, while in the experiment, according to the recorded video, pedestrians rarely take surpass behavior and they enter the bottleneck with an orderly manner, which leads to the similar moving state of pedestrians. Secondly, pedestrians in the bottleneck are in an accelerated state, which may due to the increase of the exit attraction as the pedestrian approaches the exit. Furthermore, although the bottleneck limits the moving space, the speed in it is higher than in front of it, which is due to the lower density and competition in the bottleneck. Compared with the velocity profile from the CFM, the speed calculated by the new model describes the velocity profile of the experiment better. From the density profiles, it is found that the density in the bottleneck decreases as the distance to exit decreases, since the pedestrians ahead are in an accelerated moving state so that the distance between the agents becomes larger and the density becomes lower. In addition, although the densities in front of the bottleneck entrance obtained from the new model are higher than that of the experiment, a visible enhancement can be observed compared with the density profile from the CFM.

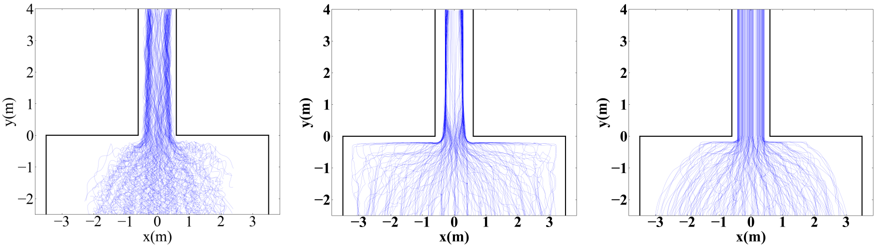

(a) Trajectory, experiment (b) Trajectory, CFM (c) Trajectory, new model

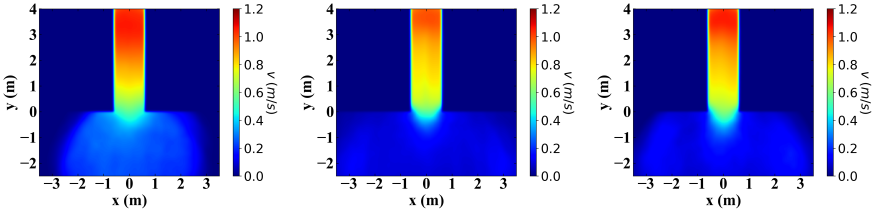

(d) Velocity, experiment (e) Velocity, CFM (f) Velocity, new model

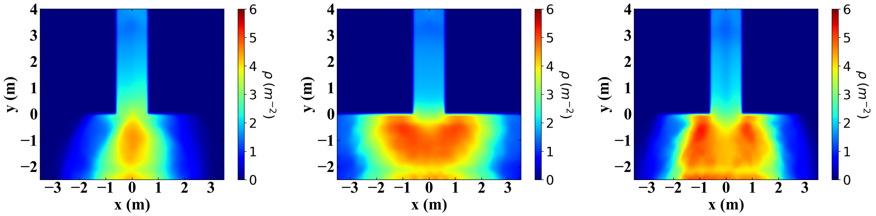

(g) Density, experiment (h) Density, CFM (i) Density, new model

Figure 10. Trajectories and spacial profiles of velocity and density in the experiment and simulations. Pedestrians passed through the bottleneck from the bottom to top. The width of the bottleneck is 1.2 m. Columns from left to right show the data from experiment, CFM and new model, respectively. Rows show the trajectories, velocity profile and density profile from top to bottom, respectively.

To validate the model quantitatively, we further analyze the relationship between the flow and bottleneck width by adjusting the bottleneck width from 1.0 m to 2.5 m in our simulation. Here, we choose the line at the middle of the bottleneck as measurement line to calculate the flow defined in Eq. (10). For each bottleneck width, ten runs are performed and the mean of these results is shown in Table 4.

$$flow = (N-1)/\Delta t. \tag{10}$$

Where, N is the number of participants in the experiment. Δt represents the time interval between the first and the last person passing the measurement line.

Table 4. Pedestrian flow in bottleneck scenario.

$Width/m$	$Flow/\left(s^{-1}\right)$			$Relativeerror\,(e)$	
	Exp	CFM	New	$e\,(CFM)$	$e\,(New)$
1.0	1.791	1.502 (±0.037)	1.701 (±0.046)	16.13	5.02
1.1	1.952	1.793 (±0.048)	1.885 (±0.049)	8.17	3.43
1.2	2.258	1.940 (±0.025)	2.079 (±0.044)	14.07	7.91
1.4	2.644	2.231 (±0.040)	2.407 (±0.084)	15.61	8.98
1.6	2.688	2.724 (±0.049)	2.767 (±0.126)	1.35	2.95
1.8	3.397	3.013 (±0.028)	3.102 (±0.066)	11.31	8.69
2.0	3.375	3.393 (±0.087)	3.434 (±0.096)	0.55	1.73
2.2	3.783	3.773 (±0.103)	3.784 (±0.168)	0.27	0.03
2.5	4.797	4.262 (±0.104)	4.300 (±0.083)	11.16	10.35
average error	/	/	/	8.736	5.454

Values between brackets represent the standard deviation of pedestrian flow.
The relative error is calculated as

$$\frac{|experiment\ flow - simulation\ flow|}{experiment\ flow} \times 100\%$$

As can be seen from Table 4 and Fig. 11, with the increasing bottleneck width, the pedestrian flow increases in the experiment and both models. Further comparing the relative errors between the results of the two models and that of the experiment, it can be found that most of the relative errors from the new model are smaller than those obtained from the CFM.

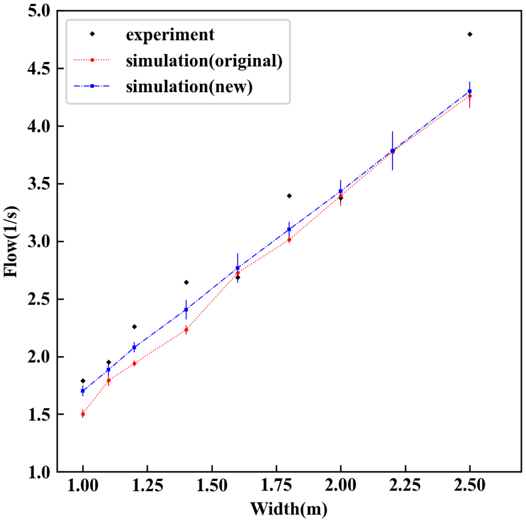

Figure 11. The relationship between flow and bottleneck width. Rhombus, circle and square represent the results of experiment, CFM and new model, respectively.

Next, to test whether our model can effectively alleviate the backward movement of pedestrians in the bottleneck scenario, we calculate the angle between the actual movement direction and the y-axis (We assume that the y-axis direction is consistent with the direction along the exit) during the entire movement in bottleneck scenario. When the angle is larger than $\pi/2$, we regard it as a backward movement. The statistic results of angles in each frame are shown in Fig. 12. As we can observe, there is a part of pedestrians moving backwards in the original model, whereas this backward movement is strongly reduced in the new model which is more consistent with the experimental data. Therefore, the new model alleviates unrealistic backward movement effectively.

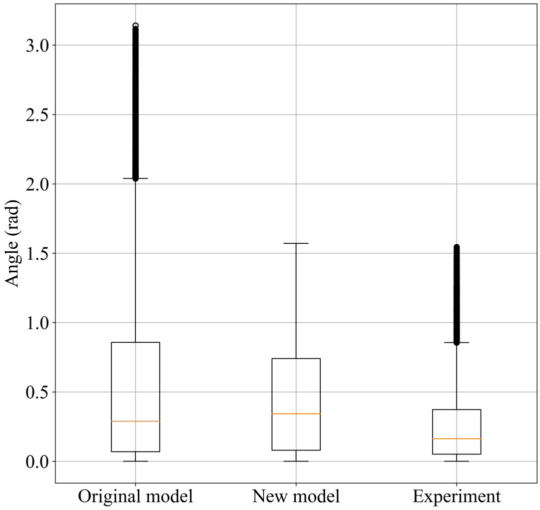

Figure 12. Statistic results of the angle between pedestrians' moving direction and y-axis during the entire movement in bottleneck scenario. The box plots on the left, middle and right are from the CFM, new model and experimental data, respectively.

3. Discussion

The parameters and the limitation of the model are discussed in this section. The values of parameters depend on the situation and they may change in different scenarios. The possible reasons are as follows: In straight corridors with periodic boundary conditions, all pedestrians are expected to move straight. Hence, their desired movement directions are parallel so that there is little competitive behavior during walking. In this case, pedestrian's motion inertia dominates the movement and the intention to turn is not strong. However, in the bottleneck scenario, this behavior changes, since the bottleneck limits the movement space of pedestrian. In the simulation, the desired directions of pedestrians point to the bottleneck entrance. As the crowd gets closer to the bottleneck, the desired directions of pedestrians tend to intersect, so that the competition between pedestrians is intensified. This may lead to a decrease in pedestrians' inertia influence, resulting in more frequent steering maneuvers. In order to increase the probability of obtaining forward space as soon as possible, pedestrians will force themselves to react faster, which leads to the decrease of T. s_c denotes the critical comfortable distance for pedestrian to maintain the desired direction. When there is more competitive behavior during walking, pedestrians will prefer larger value of s_c to make them feel comfortable. Factors affecting s_{im} are similar to that of s_c. That is, the more intense the competition, the smaller the minimum acceptable distances in the new direction. Therefore in straight corridor with periodic boundary, s_{im} and T conditions are larger than in the bottleneck scenario, whereas s_c is the opposite.

While the trajectories and profiles of velocity and density of pedestrians obtained from the new model are qualitatively more consistent with the experimental results than those from the CFM, the distribution of pedestrian and the density before the narrowing obtained from the new model are still divergent to the experiment to some extent. The shape of trajectories in front of the bottleneck entrance from the experiment is more conical. The density obtained from the new model is higher than the experimental results. The possible reasons are as follows: first, the patience and humility of human are not considered in the model, pedestrians are competitive at the entrance of the bottleneck, which results in more pedestrians staying close to each other and waiting at the bottleneck entrance, while under the non-emergency conditions in real life, pedestrians showcase a polite behavior, so they pass through the bottleneck in an orderly manner, hence the density of crowd in front of the bottleneck is lower. It is also confirmed in the experiment video that pedestrians enter the bottleneck continuously, without excessive clustering or long waiting time before the narrowing. Second, to make pedestrians in our model pass through the bottleneck, we set target point for every pedestrian. The target setting which affects the position of high-density area in the CFM and new model are shown in Fig. 13. In the CFM, the target point is set at the center of the bottleneck entrance, so that pedestrians who have not arrived at the bottleneck will compete for the same target position, which contributes to the arch-like shape of crowd distribution. In the new model, the room is divided into three areas. Two target points are set based on the shortest distance between pedestrians and the bottleneck entrance. Pedestrians in area 1 and area 3 try to move towards target 1 and target 2, respectively. Pedestrians in area 2 are expected to walk straight. Compared with the density profiles shown in Fig. 10, it is found that pedestrians in both two models cluster around the target point and lead to high density of nearby areas. In both two models, the target point for each pedestrian is static and never be changed in front of the bottleneck entrance. However, the target point for every pedestrian in real life may be dynamic and related to the surrounding environment, that is conductive to make people walk with less competition. At last, to improve the calculation efficiency, the pedestrians in the model are simplified to circles with equal diameters, which is different from the shape of people in daily life. When a pedestrian is in a stationary state, the shape of the real pedestrian is closer to an ellipse, which may also affect the form of the entire crowd distribution.

The simulation results show that the model can simulate the pedestrians in bottleneck or corridor with periodic boundaries accurately, but it is not suitable for the counter-flow scenario. In reality, pedestrian's preferences in counter-flow are different from those in bottleneck or corridor with periodic boundaries. In the counter-flow scenario, before the formation of the layer, the potential conflict for pedestrians is greater than that in the other two scenarios. In this case, pedestrians are more inclined to avoid people further but moving in the opposite direction to avoid conflict, rather than overtaking the neighbor near but in the same direction ahead. That is, even if the distance factor is not taken into account, pedestrians do not treat their neighbors equally. However, to simply the model, neighbors are treated equally by the pedestrian except for the distance factor. To improve the calculation efficiency, only the nearest neighbor is considered to determine the walking direction of pedestrian, no matter what the moving direction of neighbor is, which causes the congestion in counter-flow scenario. It's the limitation of this model which needs to be improved in the future. Validation of the model is geometry dependent. This is a clear limitation of the model's application and usability in complex evacuation scenarios. However, for understanding of

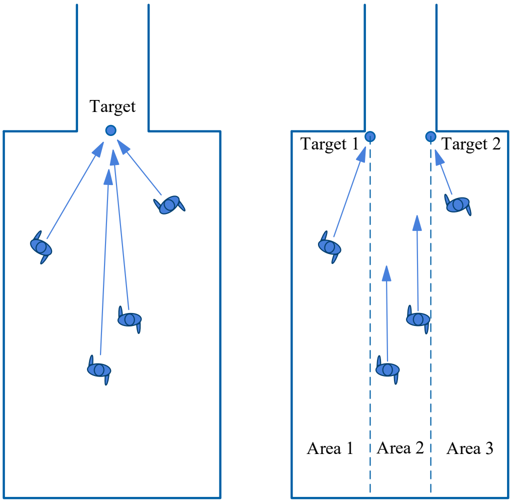

(a) Target setting, CFM (b) Target setting, New model

Figure 13. The target settings in the CFM and the new model are shown in the left and right, respectively. Pedestrians in the CFM aim to walk towards the same target located at the center of the bottleneck entrance. Pedestrians in the new model are expected to move based on the shortest distance between pedestrian and bottleneck entry. The arrows indicate the desired moving direction of pedestrians.

4. Conclusion

In this paper, we propose a microscopic pedestrian model by combining the pedestrian's individual preferences and collision-free speed model. We define the direction submodel by considering subjective factors of crowd, like perception of comfort and preference for walking straight to destination. The effect of walls is introduced in collision-free speed model to calculate the speed of pedestrians in normal motion. Finally, we conduct several simulations in corridor and bottleneck to verify and validate the model.

The results show that the proposed model can effectively eliminate the oscillating phenomenon in the narrow corridor persisting in the collision-free speed model. Moreover, it fits well with the experimental results in simulating the relationship between the density and speed of pedestrians in the corridor with periodic boundaries. It also performs well in the bottleneck scenario. On the one hand, it shows a visible enhancement in predicting the trajectories and velocities of the crowd and mitigates the backward movement of pedestrian effectively when compared with collision-free speed model. On the other hand, the model predicts the pedestrian flow with different bottleneck widths more accurately. In the future, further mechanisms of pedestrian's behavior, like the tendency to following others and the polite behavior (e.g. way giving), can be introduced to the model.

Credit authorship contribution statement

Sainan Zhang: Conceptualization, Methodology, Formal analysis, Investigation, Validation, Writing-Original Draft, Visualization. Jun Zhang: Conceptualization, Resources, Data Curation, Writing-Reviewing & Editing, Supervision, Funding acquisition. Mohcine Chraibi: Conceptualization, Software, Writing-Reviewing & Editing. Weiguo Song: Writing-Reviewing & Editing, Supervision.

Acknowledgement

The authors acknowledge the foundation support from the National Key Research and Development Program of China (Grant No. 2018YFC0808600), the National Natural Science Foundation of China (Grant No. U1933105, 71704168), the Anhui Provincial Natural Science Foundation (Grant No. 1808085MG217), the Fundamental Research Funds for the Central Universities (Grant No. WK2320000040, WK2320000043), the Visiting Professor International project at the University of Science and Technology of China (Grant No. 2019A VR35).

References

[1] Dirk Helbing and Pratik Mukerji. Crowd disasters as systemic failures: analysis of the love parade disaster. *EPJ Data Science*, 1(1):7, 2012.

[2] Yasser A Alaska, Abdulaziz D Aldawas, Nawfal A Aljerian, Ziad A Memish, and Selim Suner. The impact of crowd control measures on the occurrence of stampedes during mass gatherings: The hajj experience. *Travel Medicine and Infectious Disease*, 15:67–70, 2017.

[3] Debashish Chowdhury, Ludger Santen, and Andreas Schadschneider. Statistical physics of vehicular traffic and some related systems. *Physics Reports*, 329(4):199–329, 2000.

[4] P. Degond, C. Appert-Rolland, M. Moussaïd, J. Pettré, and G. Theraulaz. A hierarchy of heuristic-based models of crowd dynamics. *Journal of Statistical Physics*, 152:1033–1068, Sept 2013.

[5] Mohcine Chraibi, Armin Seyfried, and Andreas Schadschneider. Generalized centrifugal-force model for pedestrian dynamics. *Physical Review E*, 82(4):046111, 2010.

[6] Xiaoxia Yang and Qianling Wang. Crowd hybrid model for pedestrian dynamic prediction in a corridor. *IEEE Access*, 7:95252–95261, 2019.

[7] Xiaoxia Yang, Xiaoli Yang, and Qianling Wang. Pedestrian evacuation under guides in a multiple-exit room via the fuzzy logic method. *Communications in Nonlinear Science and Numerical Simulation*, 83:105138, 2020.

[8] Dirk Helbing and Péter Molnár. Social force model for pedestrian dynamics. *Physical Review E*, 51:4282–4286, May 1995.

[9] Dirk Helbing, Illés Farkas, and Tamás Vicsek. Simulating dynamical features of escape panic. *Nature*, 407:487–490, Sept 2000.

[10] Dirk Helbing. Traffic and related self-driven many-particle systems. *Reviews of Modern Physics*, 73:1067–1141, Dec 2001.

[11] Mohcine Chraibi, Ulrich Kemloh, Andreas Schadschneider, and Armin Seyfried. Force-based models of pedestrian dynamics. *Networks and Heterogeneous Media*, 6:425, 2001.

[12] Antoine Tordeux, Mohcine Chraibi, and Armin Seyfried. Collision-free speed model for pedestrian dynamics. In *Traffic and Granular Flow '15*, pages 225–232, 2016.

[13] Felix Dietrich and Gerta Köster. Gradient navigation model for pedestrian dynamics. *Physical Review E*, 89:062801, Jun 2014.

[14] Jur van den Berg, Ming Lin, and Dinesh Manocha. Reciprocal velocity obstacles for real-time multi-agent navigation. *2008 IEEE International Conference on Robotics and Automation*, pages 1928–1935, Jun 2008.

[15] Jan Ondřej, Julien Pettré, Anne-Hélène Olivier, and Stéphane Donikian. A synthetic-vision based steering approach for crowd simulation. *ACM Trans. Graph.*, 29(4), Jul 2010.

[16] Paolo Fiorini and Zvi Shiller. Motion planning in dynamic environments using velocity obstacles. *The International Journal of Robotics Research*, 17(7):760–772, 1998.

[17] Nuria Pelechano, Kevin O'Brien, Barry Silverman, and Norman Badler. Crowd simulation incorporating agent psychological models, roles and communication. Technical report, Pennsylvania Univ Philadelphia Center for Human Modelling and Simulation, 2005.

[18] Cléo Deroo, Angélique Montuwy, Béatrice Degraeve, Jean-Michel Auberlet, Anne-Hélène Olivier, and Marie-Axelle Granié. Pedestrian collision avoidance on narrow sidewalk: A meeting between psychology and virtual reality. Technical report, 2019.

[19] Piet H Bovy and Eliahu Stern. *Route choice: wayfinding in transport networks*, volume 9. Springer Science & Business Media, 2012.

[20] Mehdi Moussaïd, Dirk Helbing, and Guy Theraulaz. How simple rules determine pedestrian behavior and crowd disasters. *Proceedings of the National Academy of Sciences*, 108(17):6884–6888, 2011.

[21] Xiuming Yao, Yue Lian, and Chengjie Wei. A markov jump approach to modeling and analysis of pedestrian dynamics. *IEEE Access*, 7:87808–87815, 2019.

[22] Wei Lv, Weiguo Song, Jian Ma, and Zhi-ming Fang. A two-dimensional optimal velocity model for unidirectional pedestrian flow based on pedestrian's visual hindrance field. *IEEE Transactions on Intelligent Transportation Systems*, 14(4):1753–1763, 2013.

[23] Michael Batty. Predicting where we walk. *Nature*, 388(6637):19–20, 1997.

[24] Alasdair Turner and Alan Penn. Encoding natural movement as an agent-based system: an investigation into human pedestrian behaviour in the built environment. *Environment and Planning B: Planning and Design*, 29(4):473–490, 2002.

[25] Luo, Lin, Fu, Zhijian, Cheng, Han, Yang, and Lizhong. Update schemes of multi-velocity floor field cellular automaton for pedestrian dynamics. *Physica A Statistical Mechanics and Its Applications*, 2018.

[26] Jun Zhang, Wolfram Klingsch, Andreas Schadschneider, and Armin Seyfried. Transitions in pedestrian fundamental diagrams of straight corridors and t-junctions. *Journal of Statistical Mechanics: Theory and Experiment*, 2011(06):P06004, 2011.

[27] Jack Liddle, Armin Seyfried, Wolfram Klingsch, Tobias Rupprecht, Andreas Schadschneider, and Andreas Winkens. An experimental study of pedestrian congestions: influence of bottleneck width and length. *arXiv preprint arXiv:0911.4350*, 2009.

[28] Qiancheng Xu, Mohcine Chraibi, Antoine Tordeux, and Jun Zhang. Generalized collision-free velocity model for pedestrian dynamics. *Physica A-Statistical Mechanics and Its Applications*, 535, DEC 1 2019.

A.6 ARTICLE V

Anticipation in a velocity-based model for pedestrian dynamics

Q. XU, M. CHRAIBI, AND A. SEYFRIED

TRANSPORTATION RESEARCH PART C: EMERGING TECHNOLOGIES (**2021**)

Transportation Research Part C: Emerging Technologies, 133:103464J, 2021
10.1016/j.trc.2021.103464

Anticipation in a velocity-based model for pedestrian dynamics

Qiancheng Xu[1], Mohcine Chraibi[1], Armin Seyfried[1]

Abstract

Lane formation in bidirectional pedestrian streams is based on a stimulus-response mechanism and strategies of navigation in a fast-changing environment. Although microscopic models that only guarantee volume exclusion can qualitatively reproduce this phenomenon, they are not sufficient for a quantitative description. To quantitatively describe this phenomenon, a minimal anticipatory collision-free velocity model is introduced. Compared to the original velocity model, the new model reduces the occurrence of gridlocks and reproduces the movement of pedestrians more realistically. For a quantitative description of the phenomenon, the definition of an order parameter is used to describe the formation of lanes at transient states and to show that the proposed model compares relatively well with experimental data. Furthermore, the model is validated by the experimental fundamental diagrams of bidirectional flows.

Keywords
Model

[1] *Institute for Advanced Simulation,*
Forschungszentrum Jülich, 52425 Jülich, Germany

Contents

Introduction

In bidirectional flow situations, pedestrians self-organize into dynamically varying and separated lanes [1, 2, 3, 4, 5, 6]. Although the mechanisms behind this apparently organized separation of the crowd are not known for certain and in many cases may seem random, we observe that this formation leads to a reduction in collisions and thus increases the speed. Unlike with car traffic, where stable lanes are predetermined by the restrictions established by the infrastructure, in pedestrian dynamics, lanes are formed dynamically and naturally with neither external synchronization nor any prior agreement between pedestrians.

We also see lane formation in systems of inanimate particles [7, 8, 9], where models ensuring volume exclusion are sufficient to reproduce the phenomenon. Therefore, with a simple social force model considering the repulsion between particles, Helbing et al. [10] qualitatively reproduced the lane formation in a corridor with periodic boundary conditions. They attributed two reasons to this phenomenon, the sideways movement, which separates agents moving in opposite directions, and the weak interaction between agents moving in the same lane, which maintains the lanes that have been formed [2].

However, pedestrians usually avoid collisions by using a stimulus-response mechanism to anticipate changes in the environment. In this context, we consider anticipation as the prediction of the path of neighboring pedestrians by perceiving their past or current movement and taking this information into account to avoid collisions. The effect of anticipation on the movement of pedestrians in bidirectional flows has been discussed and addressed in several works to date. For instance, Suma et al. [11] conducted a bidirectional flow experiment where participants are asked to use cell phones (weak anticipation) or move cautiously (excessive anticipation), to study how anticipation affects the movement of pedestrians. They found anticipation significantly affects the time it takes for pedestrians to pass through the corridor, and there is an optimal degree of anticipation to realize the minimum passing time. However, since the scale of the experiment was small, the lane formation was not analyzed quantitatively. Murakami et al. [12] performed the bidirectional experiment in a corridor with open boundary conditions, and they observed that the sideways movement of pedestrians before lane formation can be described in terms of the Lévy walk process. Therefore, the authors suggested that this sideways movement is strongly related to lane formation. Moreover, they assumed the most likely action underlying the sideways movement is anticipation. The relationship between anticipation and lane formation is further studied in [13] through a larger scale bidirectional flow experiment, where pedestrians distracted by cell phones are located at different positions to represent situations with different degrees of anticipation. They found anticipation favors the formation of lanes in bidirectional flow situations. As a part of the anticipation process, the strategy selected by pedestrians in bidirectional flow situations is also related to the formation of lanes. It was observed in experiments that preferring to follow other pedestrians moving in the same direction is a strategy to promote and stable the formation of lanes [14, 15, 16]. In addition, lane formation is also influenced by the effect of various factors, such as flow ratio [17] and heterogeneity of agents [16]. Therefore, models based solely on volume exclusion, such as the one in [10], are oversimplified and not suitable for quantitatively reproducing the lane formation in pedestrian systems.

To give a more realistic picture of the behavior of agents in the bidirectional flow simulation, the process of anticipation was considered in several recent models. Suma et al. [11] proposed an anticipation floor field cellular automata model. The transition probability of agents is calculated by considering the cells occupied by other agents currently, as well as the cells that are expected to be occupied by other agents in the future. The model was analyzed in [18] by using an order parameter, which is originally used to detect lanes of particles in a colloidal suspension [19]. Quantitative analysis showed that the model with anticipation can reproduce lane formation in higher density situations than the model without anticipation, but the model is not calibrated with experimental data. Zanlungo et al. [20] introduced anticipation into the social force model. Instead of using the current distance between agents, the repulsion force from one agent to another is calculated by using their future distance determined by the time to collision. The result of calibration shows that introducing anticipation improves the model's capability to reproduce pedestrian trajectories. However, the influence of anticipation on lane formation was not studied in this work. Through statistical analysis of pedestrian trajectories, Karamouzas et al. [21] found that the time to collision is more suitable to describe the interaction energy between pedestrians than the distance between them. Based on the power law relationship between the interaction energy and the time to collision, a force-based model is developed, which can reproduce several self-organization phenomena including lane formation. However, a quantitative analysis of the lane formation was not conducted using this model. Moreover, although the model was validated with experimental data by comparing the data from [22], the calibration process did not distinguish the uni- and bidirectional flow. Bailo et al. [23] also proposed a microscopic model based on the time to collisions. The model is able to reproduce the lane formation in bidirectional flow situations, but it hasn't been tested in scenarios with different densities. Besides, the model was not calibrated with the experimental data. Seitz [24] proposed four simple cognitive heuristics to describe pedestrian behavior and investigated the possible heuristics related to lane formation. It was found that only the model with "follower" heuristics can reproduce lane formation, which corresponds to the strategy of following other agents moving in the same direction. This work shows that considering the correct cognitive heuristics is significant and maybe also enough for reproducing self-organization phenomena, which provides a direction for developing models in the future.

Besides lane formation, another phenomenon related to bidirectional flow is the jamming transition, also called gridlock, appearing at a critical density. Muramatsu et al. [25] used a lattice gas model without backstepping to study the jamming transition in bidirectional pedestrian flow with open boundary conditions. They found the jamming transition does not depend on the corridor size but it is affected by the strength of the drift (the preference to move in the desired direction) and the traffic rule adopted (such as keep to the right). Fang et al. [26] adopted a cellular automata model with backstepping and the right-hand side rule. They observed the critical density of jamming transition increases with a higher probability of backstepping. Nowak et al. [18] studied the phenomenon with the anticipation floor field cellular automata model proposed in [11]. They discovered the anticipation mechanism in the model suppresses the formation of jamming (facilitating the formation of lanes), which leads to an increase in the critical density of the jamming transition. However, the jamming transition is only observed in computer simulations.

Furthermore, the fundamental diagram is used to analyze bidirectional streams. In some early studies summarized in [15], it is believed that there is no clear or only a small difference between uni- and bidirectional flows. Helbing et al. [27] concluded that bidirectional flows are more efficient than unidirectional flows. The possible reason behind this is better coordination between people in bidirectional situations (lane formation). Kretz et al. [28] also found that pedestrians use space more efficiently in bidirectional situations. Subsequently, Zhang et al. [15] carried out both uni- and bidirectional flow experiments under laboratory conditions. A clear difference between the fundamental diagrams of uni- and bidirectional flows is observed when the density is higher than $1.0\,\mathrm{m}^{-2}$. The specific flow reaches a peak with increasing density in the unidirectional flow, whereas a plateau is formed in the bidirectional flow. However, there are no experimental data for densities higher than $4.5\,\mathrm{m}^{-2}$.

In order to reproduce bidirectional flow quantitatively, the anticipation velocity model (AVM) for pedestrian dynamics is proposed. The action anticipating changes of neighboring pedestrians' positions and the strategy of following others are covered in this model. The new model is compared to two similar models from the literature, the collision-free speed model [29] and generalized collision-free velocity model [30], and we highlight the reasons behind the difference. Moreover, we use the AVM to study the jamming transition, lane formation, and fundamental diagrams in bidirectional flow scenarios. In the following section, the AVM is described.

1. Definition of the anticipation velocity model

In this model, an agent is represented as a disk with a constant radius r. The position and velocity of pedestrian i are denoted by $\vec{x}_i$ and $\vec{v}_i$, respectively, where $\vec{v}_i = \dot{\vec{x}}_i$. Furthermore, $\vec{v}_i = \vec{e}_i \cdot v_i$, where $\vec{e}_i$ and v_i denote the direction of movement and the speed of agent i, respectively. Both variables are modeled differently as explained in the following subsections.

1.1 Submodel for operational navigation

The direction of movement of agent i is determined by its desired direction which is a unit vector denoted by $\vec{e}_i^{\,0}$ pointing towards its target. The determination of the target follows various tactical strategies, which is not the subject of the present study. For operational navigation to avoid collisions and obstructions, in the presence of other agents, the direction of i will deviate from its desired direction $\vec{e}_i^{\,0}$. To consider anticipation, the process can be divided into the following parts: a. perception of the actual situation, b. prediction of a future situation, and c. selection of a strategy leading to an action.

a. Perception of the actual situation: To consider restrictions using visual perception, it is assumed that only agents located in the union of two half-planes, where i is moving or intends to move, affect its direction. The set containing all agents who have an impact on i's direction of movement is

$$N_i(t) = \left\{ j,\ \vec{e}_i(t) \cdot \vec{e}_{i,j}(t) > 0 \text{ or } \vec{e}_i^{\,0}(t) \cdot \vec{e}_{i,j}(t) > 0 \right\}, \tag{1}$$

where $\vec{e}_{i,j}$ denotes the unit vector from i to j.

b. Prediction of a future situation: To consider the prediction, it is assumed that the strength of j's impact on i is a function of the predicted distance between these two agents at a particular time point. Given a time constant t^{a}, which can be interpreted as the prediction time, the predicted distance is defined as

$$s^{\mathrm{a}}_{i,j}(t+t^{\mathrm{a}}) = \max\left\{ 2r,\ \left(\vec{x}_j^{\,\mathrm{a}}(t+t^{\mathrm{a}}) - \vec{x}_i^{\,\mathrm{a}}(t+t^{\mathrm{a}}) \right) \cdot \vec{e}_{i,j}(t) \right\}, \tag{2}$$

where $\vec{x}_i^{\,\mathrm{a}}(t+t^{\mathrm{a}}) = \vec{x}_i(t) + \vec{v}_i(t) \cdot t^{\mathrm{a}}$. See Figure 1.

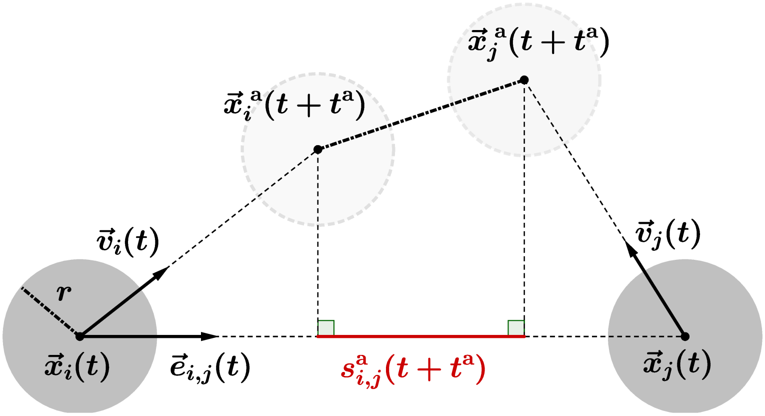

Figure 1. An example of $s^{\mathrm{a}}_{i,j}(t+t^{\mathrm{a}})$, the predicted distance between agents i ($\vec{x}_i$, $\vec{v}_i$) and j ($\vec{x}_j$, $\vec{v}_j$). When pedestrians move towards each other their predicted distance is smaller than the actual distance.

c. Selection of a strategy leading to an action: After the introduction of the predicted distance in Eq. 2, the strength of the impact from agent j on the direction of movement of agent i is defined as

$$R_{i,j}(t) = \alpha_{i,j}(t) \cdot \exp\left(\frac{2r - s^{\mathrm{a}}_{i,j}(t+t^{\mathrm{a}})}{D}\right), \tag{3}$$

where $D > 0$ is a constant parameter used to calibrate the range of the impact from neighbors and $\alpha_{i,j}$ is a directional dependency used to vary the strength of impact from different neighbors (see Eq. 4).

$$\alpha_{i,j}(t) = k\left(1 + \frac{1 - \vec{e}_i^{\,0}(t) \cdot \vec{e}_j(t)}{2}\right),\ k > 0, \tag{4}$$

where $\alpha_{i,j}$ is minimal (k) when both vectors $\vec{e}_i^{\,0}$ and $\vec{e}_j$ are aligned and is maximum ($2k$) when they are anti-aligned, which means that agents influence each other's direction strongly in bidirectional scenarios. Here, $\alpha_{i,j}$ means agents have a high tendency to follow the agents who move in the same direction. When this strategy is used, the probability of further conflicts is reduced.

The direction of the impact from agent j on i's direction of the movement is defined as

$$\vec{n}_{i,j}(t) = -\operatorname{sign}\left(\vec{e}^{\,\mathrm{a}}_{i,j}(t+t^{\mathrm{a}}) \cdot \vec{e}_i^{\,0\perp}(t)\right) \cdot \vec{e}_i^{\,0\perp}(t), \tag{5}$$

where $\vec{e}^{\,\mathrm{a}}_{i,j}(t+t^{\mathrm{a}}) = \vec{x}_j^{\,\mathrm{a}}(t+t^{\mathrm{a}}) - \vec{x}_i(t)$. The direction of $\vec{n}_{i,j}$ depends on the predicted position of agent j after a period of time t^{a}. Note that when this predicted position is aligned with the desired direction of i, the direction of $\vec{n}_{i,j}(t)$ in Eq. 5 is chosen randomly as $\vec{e}_i^{\,0\perp}$ or $-\vec{e}_i^{\,0\perp}$. See Figure 2. This rule prevents agents from moving in the opposite direction to the desired direction.

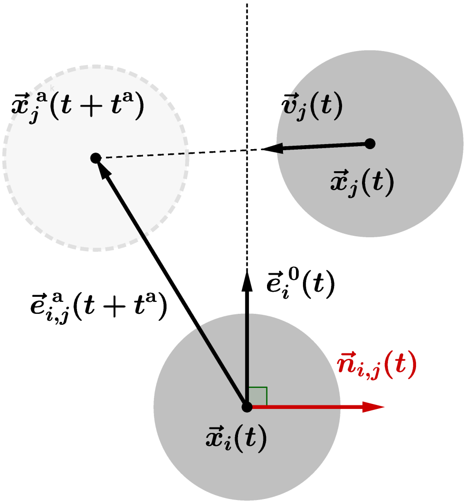

Figure 2. The direction of the impact from j on the direction of movement of i ($\vec{n}_{i,j}$) according to Eq. 5.

Finally, Eq. 3 and Eq. 5 yield the optimal direction of agent i as

$$\vec{e}_i^{\,\mathrm{d}}(t) = u\left(\vec{e}_i^{\,0}(t) + \sum_{j\in N_i(t)} R_{j,i}(t)\cdot\vec{n}_{j,i}(t)\right), \tag{6}$$

where u is a normalization constant such that $\|\vec{e}_i^{\,\mathrm{d}}\| = 1$. Then, the direction of movement of agent i is updated as

$$\frac{d\vec{e}_i(t)}{dt} = \frac{\vec{e}_i^{\,\mathrm{d}}(t) - \vec{e}_i(t)}{\tau}, \tag{7}$$

where τ is a relaxation parameter adjusting the rate of the turning process from the current direction $\vec{e}_i$ to the optimal direction $\vec{e}_i^{\,d}$.

1.2 Submodel for the speed

After obtaining the new direction of the movement according to Eq. 7, the set of neighbors that are imminently colliding with i is defined as

$$J_i = \left\{j,\ \vec{e}_i\cdot\vec{e}_{i,j} \geq 0 \text{ and } \left|\vec{e}_i^{\,\perp}\cdot\vec{e}_{i,j}\right| \leq \frac{2r}{s_{i,j}}\right\}, \tag{8}$$

where $s_{i,j}$ is the current distance between i and j. Therefore, the maximum distance that agent i can move in the direction without overlapping other agents is

$$s_i = \min_{j\in J_i} s_{i,j} - 2r. \tag{9}$$

Finally, the speed of agent i in the new direction is

$$v_i = \min\left\{v_i^0,\ \max\left\{0, \frac{s_i}{T}\right\}\right\}, \tag{10}$$

where v_i^0 is the free speed of agent i, and $T > 0$ is the slope of the speed-headway relationship. The speed submodel used here is the same as in the generalized collision-free velocity model [30].

2. Test with two interacting agents

Binary interaction scenarios with the collision-free speed model (CSM) [29], the generalized collision-free velocity model (GCVM) [30], and the AVM, respectively, are studied to assess the models' ability. The three models adopt the same speed submodel but different submodels for operational navigation. In both the CSM and the GCVM, the strength of the effect from agent j on agent i's direction of movement is a function of the distance between the two agents. As for the direction of this effect, in the CSM it is from j to i, while in the GCVM it is obtained with Eq. 5 ($t_a = 0\,\text{s}$). The parameters of these models are summarized in Table 1.

	r [m]	k Eq. 4	D [m] Eq. 3	T [s] Eq.10	Δt [s]	τ [s] Eq. 7	t^{a} [s]
CSM	0.18	3	0.1	1.06	0.05	\	\
GCVM						0.3	\
AVM							1

Table 1. The parameters of the models in binary interaction simulations. Here, r is the radius of agents, Δt is the time step size, and t_a is the prediction time. The simulation in the present study is conducted using the Euler scheme. Parameter values of the CSM and the GCVM are obtained from [30]. The reason for $t^{\text{a}} = 1\,\text{s}$ in the AVM is discussed in A.

The first scenario is that agent i walks behind agent j, which is shown in Figure 3(a). The agents have the same desired direction, but the free speed of agent i is higher than that of agent j. The trajectory of the agents in the first scenario is shown in Figure 3(b). In the simulation using the GCVM and the AVM, agent i overtakes agent j by adjusting the direction of movement. In the CSM, however, no overtaking is observed. Moreover, compared to the GCVM, the overtaking in the AVM occurs earlier.

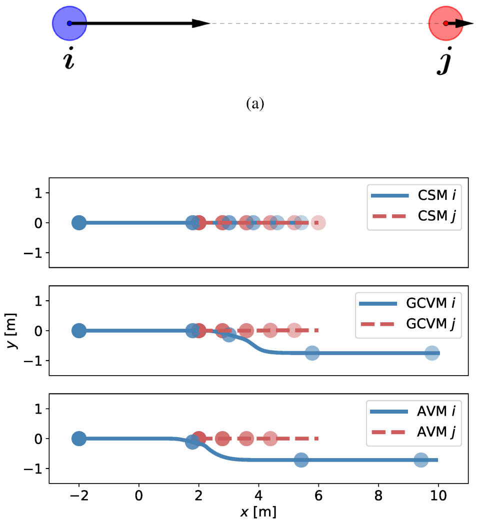

(a)

(b)

Figure 3. (a): Scenario 1, agent i walks behind agent j. The two agents have the same desired direction but the free speed of agent i is higher than that of agent j. (b): The trajectory of agents. The position of agents at different times is represented by the disk, and the transparency of these disks increases with increasing time. When the AVM is used, overtaking starts earlier.

The second scenario, more relevant to bidirectional flow, depicts two agents having the same free speed with opposite desired directions (see Figure 4(a)). The trajectory of the agents in the second scenario is shown in Figure 4(b). Here again, it is observed that with the GCVM and the AVM, agents i and j both change their paths to avoid the imminent conflict, although this maneuver occurs earlier in the AVM than in the GCVM. In the CSM, the two agents are unable to pass each other.

(a)

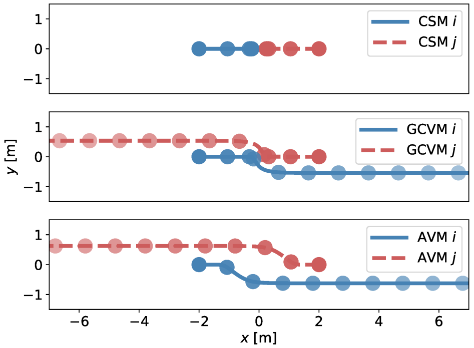

(b)

Figure 4. (a): Scenario 2, agent *i* and agent *j* move toward each other. The two agents have the same free speed but opposite desired directions. (b): The trajectory of agents. The position of agents at different times is represented by the disk, and the transparency of these disks increases with increasing time. Evasive movement starts earlier when the AVM is used.

In the last scenario (see Figure 5(a)), the paths cross at right angles. The free speeds of the two agents are very similar but not quite equal to avoid the symmetric movement of the two agents. The trajectory of the agents in the last scenario is shown in Figure 5(b). When the AVM is used, the agents deviate slightly from the desired direction to the target and avoid collision.

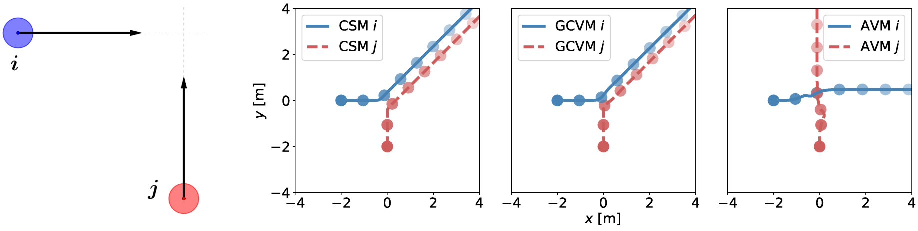

(a) (b)

Figure 5. (a): Scenario 3, agent *i* and agent *j* move across each other's path. The free speeds of the two agents are very close but not equal and their desired directions are perpendicular to each other. (b): The trajectory of agents. The position of agents at different times is represented by the disk, and the transparency of these disks increases with increasing time.

In all cases, it can be concluded that, without introducing noise terms into the models, the movement of agents in the simulation using the AVM is closer to reality than using the CSM and the GCVM, where agents have difficulty overtaking or performing realistic evasive movements.

3. Bidirectional flow simulations with periodic boundary conditions

3.1 States of bidirectional flow

The bidirectional flow simulation is performed for a corridor shown in Figure 6. The width of the corridor is 4 m, which is the same as the experimental setting in [31]. Simulations were also performed in corridors with different widths, and the result is discussed in B. For the initial conditions of a simulation, the gray waiting areas are separated into grids with a specific size, then the agents are randomly distributed in these grids without overlapping. The same number of agents were placed at the left and the right sides of the corridor. After the simulation starts, agents in the left waiting area move toward the right, and vice versa. Different initial conditions of agents' desired direction $\vec{e}^{\,0}$ were compared before performing the simulations in this section. Since no significant difference could be observed between the simulation results of ordered and unordered initial conditions, agents' desired direction $\vec{e}^{\,0}$ were set parallel to the horizontal walls of the corridor. The free speeds of agents are normally distributed $N \sim (1.55, 0.18^2)\ \mathrm{m\,s^{-1}}$ according to [15]. The effect of the free speed distribution on the simulation results is studied in C. All simulations presented in this section are performed with periodic boundary conditions in the walking direction of the agents. Each simulation lasts 400 s, which gives a good compromise between the running time of the simulations and the time needed to develop lane formation.

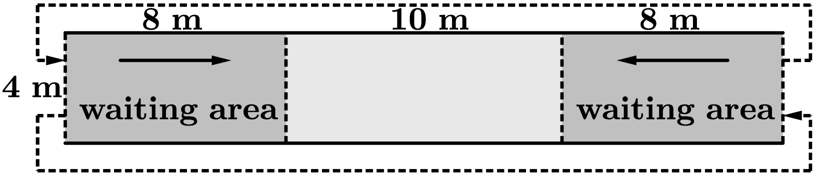

Figure 6. The corridor for bidirectional flow simulations. Dashed arrows outside the corridor represent periodic boundary conditions.

Based on the approach used in [18], the patterns emerging in our simulations are classified into four different states, which are local jamming, global jamming, lane formation, and disorder (see Figure 7). Local jamming and global jamming are both categorized as jamming states, whereas lane formation and disorder are grouped into the moving states. If the average speed of an agent over 10 s is less than $v^0/100$, it is indicated as a static agent. Using this definition, a simulation is considered to be in the jamming state when the number of static agents in the simulation is equal to or greater than 2 ($N_{\text{static}} \geq 2$); otherwise, the simulation is considered to be in a moving state. Note, although 400 s is usually long enough to reach the steady state of the simulation, the jamming or moving state of a simulation still has a certain probability of being transient. The number of static agents in the four simulations in Figure 7 are 29 (local jamming), 80 (global jamming), 0 (lane formation), and 0 (disorder), respectively.

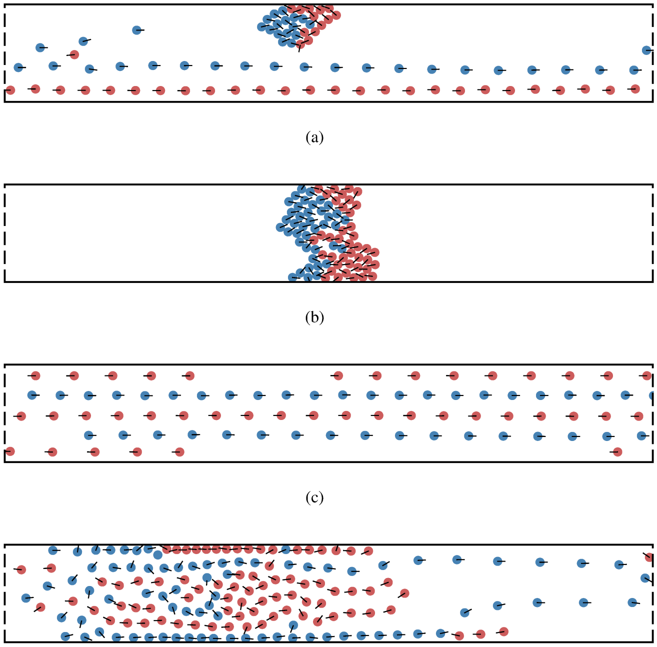

(a)

(b)

(c)

(d)

Figure 7. Different states of bidirectional flow simulations with periodic boundary conditions. (a): Local jamming. (b): Global jamming. (c): Lane formation. (d): Disorder.

In this section (Figures 8, 9, and 10(a)), each simulation is performed for $M = 30$ times with different distributions of agents in the waiting areas, then the jamming probability P_{jam} is calculated as

$$P_{\text{jam}} = S_{\text{jam}}/M, \tag{11}$$

where S_{jam} is the number of simulations leading to a jamming state.

To further distinguish between the states of lane formation and disorder, the quantity Φ defined in [32] is introduced as

$$\Phi = \frac{1}{N}\sum_{i=1}^{N} \phi_i, \tag{12}$$

with

$$\phi_i = \frac{(N_i^{\text{same}} - N_i^{\text{diff}})^2}{(N_i^{\text{same}} + N_i^{\text{diff}})^2} \in [0,1], \tag{13}$$

where N is the total number of agents in the corridor, N_i^{same} is the set of all agents initially in the same waiting area as agent i and currently moving in i's lane, and N_i^{diff} is the set of all agents initially in a different waiting area to agent i and currently moving in i's lane. The expressions of N_i^{same} and N_i^{diff} are

$$N_i^{\text{same}} = \left\{ j, |y_j - y_i| < 3r/2 \text{ and } \vec{e}_i^{\,0} \cdot \vec{e}_j^{\,0} > 0 \right\}, \tag{14}$$

$$N_i^{\text{diff}} = \left\{ j, |y_j - y_i| < 3r/2 \text{ and } \vec{e}_i^{\,0} \cdot \vec{e}_j^{\,0} < 0 \right\}, \tag{15}$$

where y_i is the vertical position of agent i.

Φ is an indicator of how pronounced lanes are formed in a simulation. Knowing that an order parameter is only measured at steady states, Φ is used here to compare models with respect to their performance of describing the transient state of lane formation. The values of Φ in the four simulations in Figure 7 are 0.66 (local jamming), 0.18 (global jamming), 1.00 (lane formation), and 0.31 (disorder), respectively. Nevertheless, there is no specific boundary to clearly distinguish between the states of lane formation and disorder.

3.2 Jamming transition

To study the jamming transition in bidirectional flow, simulations are performed with the AVM, the CSM, and the GCVM, respectively. The parameters of models are shown in Table 1. For each model, simulations are performed with different numbers of agents ranging from 20 to 200 (10 to 100 in each waiting area). The global density of agents in the corridor, ρ_{global}, is defined as the number of agents divided by the area of the whole corridor (including the waiting area). The relationship between P_{jam} and ρ_{global} for different models is shown in Figure 8. With an increase in ρ_{global}, a transition from moving states ($P_{\text{jam}} = 0$) to jamming states ($P_{\text{jam}} = 1$) is observed in the simulation of all three models. However, with the AVM, the transition occurs at a higher value of ρ_{global} compared to the other two models, which indicates the model's ability to reproduce lane formation even at higher density values.

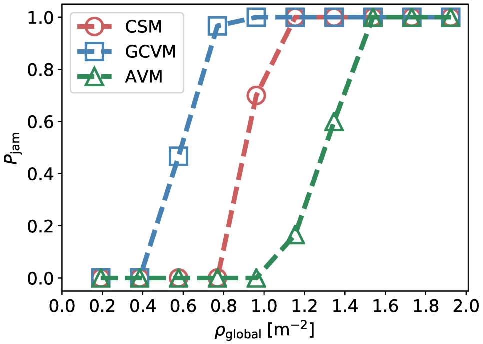

Figure 8. The relationship between P_{jam} and ρ_{global} for different models.

3.3 Parametric study

Parameters k and D are used to calibrate the strength and range of the impact from neighbors to the direction of movement in all three models (the CSM, the GCVM, and the AVM). Although the definitions vary slightly between the three models, higher values of k and larger D always led to agents being more stimulated to deviate from their desired directions. In this section, the effect of k and D on the jamming probability P_{jam} is studied for each of the three models.

For each model, simulations are performed with different values of k (1, 2, 3, 4, 5, and 6) and different values of D (0.01, 0.02, 0.05, 0.10, 0.20 m). To ensure simulations with jamming and moving states, the global density of agents ρ_{global} is set close to the critical density between the moving state and the jamming state (see Figure 8). The number of agents is 100 ($\rho_{\text{global}} \approx 0.96\,\text{m}^{-2}$) for the simulations using the CSM, 60 ($\rho_{\text{global}} \approx 0.58\,\text{m}^{-2}$) for the simulations using the GCVM, and 140 ($\rho_{\text{global}} \approx 1.35\,\text{m}^{-2}$) for the simulations using the AVM. Other parameters of the three models are given in Table 1.

The jamming probability of the simulation using the CSM and the GCVM is shown in Figures 9(a) and 9(b), respectively. The reason of the non-monotonic trend in Figure 9(b) when $D = 0.2\,\text{m}$ is that excessive influence from neighbors will cause agents to be more dispersed in the vertical direction of the corridor. When two groups of agents meet, more dispersed distribution leads to the formation of rows that exceed the maximum number of rows limited by the width of the corridor and ultimately results in the occurrence of jamming. Except for this non-monotonic trend, the value of P_{jam} in the simulation using the CSM and the GCVM decreases with increasing k and D, which means that the jamming probability decreases with increasing impact from neighbors on the direction of movement. However, the value of P_{jam} in the simulation using the AVM shows a different trend (see Figure 9(c)). When the value of D is small (0.01, 0.02, and 0.05 m), the value of P_{jam} changes slightly. With a larger value of D (0.1 m), the value of P_{jam} increases with increasing k. Note that when the value of D is large enough (0.2 m), the value of P_{jam} is close to 1 and the effect of k is marginal again. Generally, in the AVM, with increasing impact from neighbors on the direction of movement, the jamming probability increases.

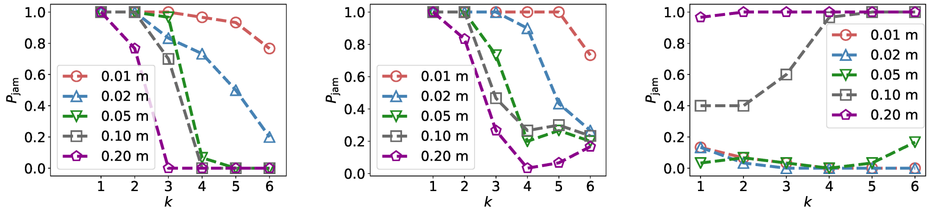

(a)

(b)

(c)

Figure 9. The relationship between P_{jam} and k for different values of D. The mean value of D can be read in the legend. (a): CSM. (b): GCVM. (c): AVM.

On the basis of all combinations of k and D in Figure 9, the set of parameters that leads to the minimal P_{jam} is identified for each model and shown in Table 2.

	CSM	GCVM	AVM
k	6	4	6
D [m]	0.2	0.2	0.01

Table 2. The set of k and D that leads to the minimal P_{jam} in Figure 9.

3.4 Lane formation

The values of k and D from Table 2, together with other parameter values from Table 1, are used for a comparative study of lane formation in the three models. For each model, simulations are performed with different numbers of agents from 20 to 300 (ρ_{global} from 0.19 to $2.8\,\mathrm{m}^{-2}$). The relationship between P_{jam} and ρ_{global} for different models is shown in Figure 10(a). Compared to Figure 8, the jamming probability P_{jam} is significantly reduced in the simulation using the CSM and the AVM by adopting the optimal values of k and D. The GCVM, however, does not show any improvement.

Furthermore, to gain a better insights into the lane formation phenomenon, the average value of Φ in the last 10 s of each simulation is calculated. First, simulations are classified as “jamming” or “moving” according to their states. Then, the mean value and standard deviation of Φ in the simulations with the moving state are calculated for each model and each density. The variations in Φ with respect to the global densities are shown in Figure 10(b). For all the three models, when $\rho_{\mathrm{global}} < 1.0\,\mathrm{m}^{-2}$, the values of Φ in the moving states are always close to 1, which indicates that, in this case, lanes are always formed. When $\rho_{\mathrm{global}} > 1.0\,\mathrm{m}^{-2}$, for the moving states, the value of Φ is unavailable in the GCVM, and the values in the AVM are significantly higher than in the CSM. This indicates that, although both are in the moving states, the AVM reproduces lane formation much better.

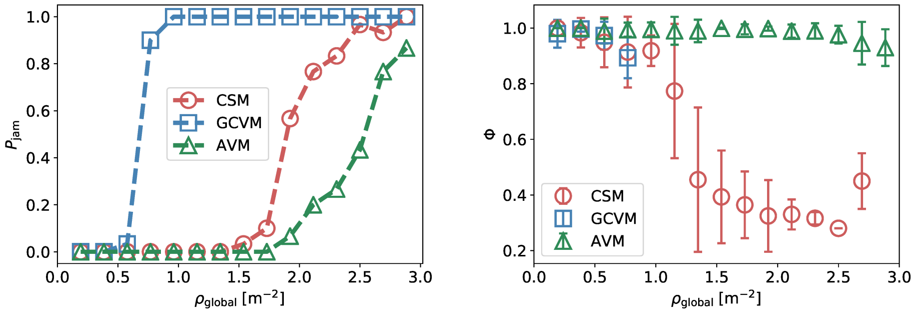

(a) (b)

Figure 10. Using the values of k and D from Table 2. (a): The relationship between P_{jam} and ρ for different models. (b): The mean value and standard deviation of Φ in the simulations with the moving state, for each model and each density.

The quantity Φ is a reliable indicator of the formation of lanes in a simulation. Since it changes in time, an artificial threshold of 0.8 for Φ is introduced to describe how fast lanes are developed. The time when the value of Φ first exceeds the threshold is denoted by t^{lane}. The mean value and standard deviation of t^{lane} in simulations with the moving state are calculated for each model and each density. See Figure 11(a). For all three models, the mean value of t^{lane} increases with increasing ρ_{global}, which is to be expected. Moreover, lanes form much faster in the simulation using the AVM than with the other models.

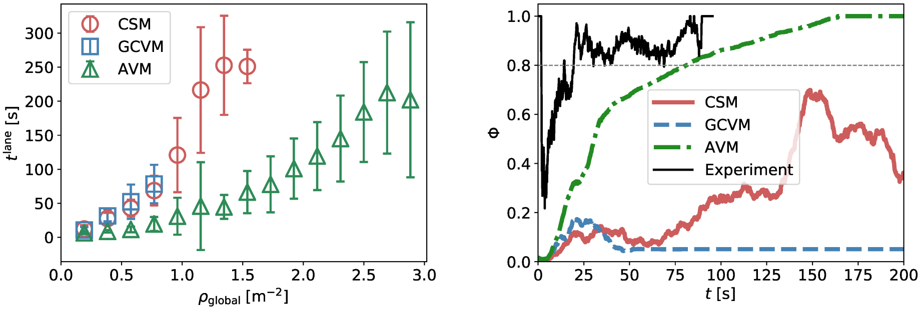

(a) (b)

Figure 11. (a) The mean value and standard deviation of t^{lane} in the simulations with the moving state, for each model and each density. (b):The relationship between the value of Φ and the simulation time t of three simulations using different models (ρ_{global}=1.92 m^{-2}) and an experiment [31].

Three single simulations using different models are further compared with bidirectional flow experiment [31]. Figure 11(b) shows the time series of Φ in the first 200 s. Here, Φ continues to increase to 1 and then remains stable in the simulation using the AVM, while it keeps fluctuating below 0.7 for the CSM. For the GCVM, the quantity Φ is stable at a low value, indicating a lack of any lane formation. The possible reason for the difference between the AVM and the CSM here is that the moving state of the AVM can be attributed to the strategy of following, while the moving state of the CSM is due to agents pushing each other aside. This behavior is also reflected in the snapshots of the three simulations at different times, shown in Figure 12. The experiment compared in Figure 11(b) is performed in a 4 m corridor under open boundary conditions and it records the trajectories of pedestrians in the 10 m length measurement area. The steady density of pedestrians in the measurement area is around 2 m^{-2}. The value Φ for pedestrians in the measurement area is calculated and the lane formation occurs even earlier in the experiment than in the simulation. It could not be excluded that, in the experiment, the formation of lanes starts even outside of the measurement area. Thus, the comparability of experiments and simulations is limited. However, a comparison of the time series of Φ, in particular, the increase in Φ over time, provides a rough estimate whether the time in which the system switches from an unordered state without lanes to an ordered state with lanes has the same order of magnitude.

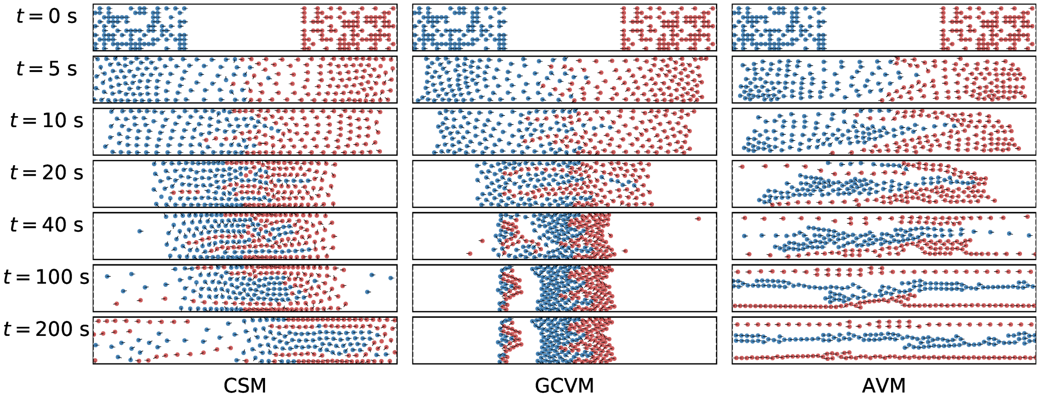

Figure 12. The snapshot of the simulations using the CSM, the GCVM, and the AVM (from left to right). From top to bottom: $t = 0$, 5, 10, 20, 40, 100, and 200 s.

4. Validation of the AVM using the fundamental diagram

After the AVM was compared to two other models and showed its ability to produce lane formation reasonably, the model was then validated with respect to the fundamental diagram. For this purpose, the fundamental diagram (FD) obtained from bidirectional flow experiments in a 3.6 m corridor [15] and a 4.0 m corridor [31] was used to calibrate the parameters of the AVM. Bidirectional flow simulations with open boundary conditions were performed in a corridor shown in Figure 6. The same number of agents were placed at the left and the right side of the corridor. The number of agents is varied in different simulations to realize different local densities in the corridor. Agents in the left waiting area move toward the right, and vice versa. The simulation ends when all agents leave the corridor. The calibration was performed manually. First, simulations were performed with different sets of parameters, and the resulting fundamental diagrams were compared with the experimental data. According to this comparison, the parameters were adjusted repeatedly until the simulated fundamental diagram fits the experimental data. The final set of parameters is listed in Table 3.

Flow types	v^0 [m s^{-1}]	r [m]	k	D [m]	T [s]	τ [s]	t^{a} [s]
Bidirectional	$N \sim (1.55, 0.18^2)$	0.18	6	0.01	0.6	0.3	0.75
Unidirectional					0.5		

Table 3. Validated parameters of the AVM.

The FD obtained by simulations and experiments are compared in Figure 13. The speed v, the local density ρ_{local}, and the specific flow $J_s = \rho_{\mathrm{local}} \cdot v$ in both the simulation and the experiment are measured from trajectories of pedestrians or agents using the same method. The measurement method is proposed in [31], where the local density is measured using the Voronoi method and the measured speed is the projection of the real speed in the horizontal direction. The FD obtained from the simulation is consistent with the FD obtained from the experiment.

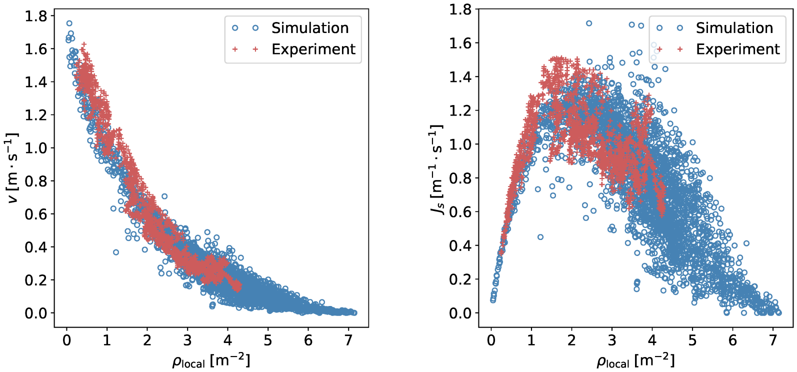

(a) (b)

Figure 13. The fundamental diagram of bidirectional flow from the experiment and the simulation. (a) Density-velocity. (b) Density-specific flow.

As well as the quantitative comparison of the FD, the process of lane formation in the simulation is qualitatively compared to the experiment (see Figure 14). The trajectory snapshots of a simulation and a bidirectional flow experiment in a 4 m wide corridor are compared. Note that the trajectories of the experiment are superimposed by the swaying of the head movement due to the bipedal movement in steps, which is not covered by the model. Moreover, the course of lane formation in the simulation is similar in time to the experiment.

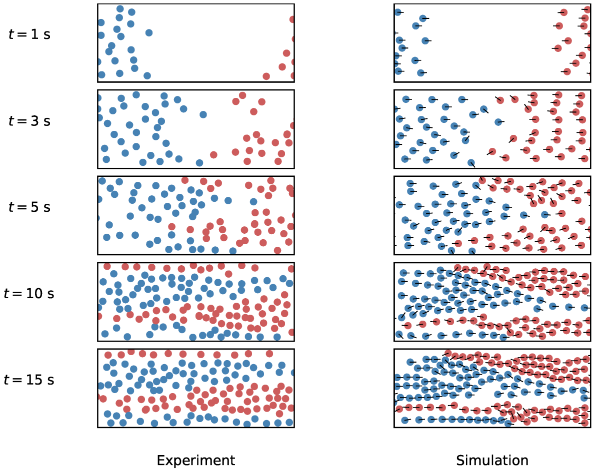

Figure 14. The trajectory snapshots of an experiment (left) and a simulation (right). Top to bottom: t = 1, 3, 5, 10, and 15 s.

The first 50 s trajectories of agents in the simulation and pedestrians in the experiment are shown in Figure 15. Four lanes can be observed in both the experiment and the simulation.

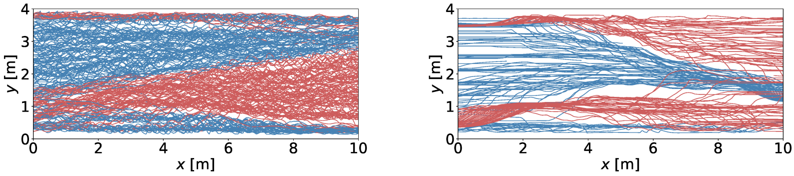

(a)

(b)

Figure 15. The trajectories of pedestrians (agents) in the first 50 s. (a) Experiment. (b) Simulation.

The fundamental diagram of the unidirectional flow was then reproduced with the calibrated parameters listed in Table 3. The value of T is lower from unidirectional flow than bidirectional flow, which means pedestrians keep a larger distance with the person in front in bidirectional flow than in unidirectional flow. It is assumed to be caused by pedestrians move more cautiously in the bidirectional flow. The FD of uni- and bidirectional flow obtained by simulations with the AVM are shown in Figure 16(a). The specific flow reaches a peak with increasing local density ρ_{local} in the unidirectional flow simulation, where a plateau is formed in the bidirectional flow simulation. The difference is in line with the observation in the experiment [15]. See Figure 16(b). A similar result was also reproduced by using an improved cellular automata model in [33]. Note that the experimental data for higher densities than $4.5\,\mathrm{m}^{-2}$ cannot be reached. Data from simulations and experiments show different scatter. The larger scatter at the congested regime indicates that real pedestrians steer more smoothly at high densities than the agents modeled by the AVM. One possible reason for this discrepancy is that the agents in the model always jostle to move further and are apparently unaware of the strategy of simply standing still.

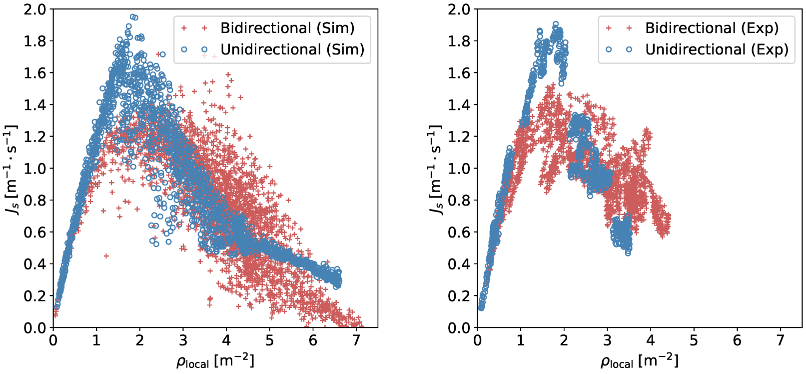

(a)

(b)

Figure 16. The fundamental diagram of uni- and bidirectional flow. (a) The relation between the local density and the specific flow in the simulation. (b) The relation between the local density and the specific flow in the experiment.

5. Conclusion

A new velocity model is proposed to take into consideration anticipation of pedestrians. For this, the process of anticipation is divided into three parts: perception of the actual situation, prediction of a future situation and selection of a strategy leading to an action.

First, the AVM is compared to the two other velocity-based models (the generalized collision-free velocity model (GCVM), and the collision-free speed model (CSM)) in binary interaction scenarios. Even in these simplified situations, the simulated trajectories of agents show that the AVM can reproduce the movement of pedestrians more realistically than the other two models.

In a second step, these models are compared in the bidirectional flow scenario with periodic boundary conditions. Simulations are classified as jamming state or moving state, according to the number of static, or blocked, agents in the simulation. Compared to the other two models, the critical density between the moving states and jamming states is shifted to higher values using the AVM. This indicates that the AVM prevents imminent collisions better than the other models.

The influence of the parameters describing the effect from neighbors in the three models is studied in bidirectional flow scenarios. Only for the AVM does an increase in the impact from neighbors in the direction of movement lead to an increase in the jamming probability. The opposite occurs when the CSM and the GCVM are used. The bidirectional flow simulation with periodic boundary conditions is then performed using the set of parameters that leads to the minimum jamming probability. The jamming probability is significantly reduced in the simulation using the CSM and the AVM by adopting the new parameters but there is little change in the simulation using the GCVM.

After this, the quantity Φ, describing the degree of order given by lanes, is adopted to analyze the formation of lanes quantitatively. In line with experimental results of high-density situations, the AVM leads to the formation of lanes much faster than the CSM. One possible reason for this difference here is that the moving state of the AVM can be attributed to the strategy of following, while the moving state of the CSM could be associated with agents pushing each other aside.

Finally, the AVM is validated using the fundamental diagram (FD). After calibration based on the bidirectional FD, the FD for unidirectional flow is correctly reproduced by simulation using the AVM. The difference between the FD of uni- and bidirectional flow is also well reproduced. Moreover, the course of lane formation in time and the shape of the formed lanes in the simulations with the AVM are similar to those in the experiments.

Additional analyses using the AVM in the bidirectional flow simulation with periodic boundary conditions are conducted. In A, the decisive factors leading to improved performance in the simulation using the AVM are studied. The result shows that the prediction of the future situation and the strategy of following are both significant for reducing the jamming probability, and there is an optimal prediction time to realize the minimum jamming probability. In B, simulations are performed in corridors with different widths. When the corridor is wider than 2 m, the effect of the corridor width on the jamming probability is insignificant. In addition, the heterogeneity of agents' free speed is studied in C, where the jamming probability decreases with increasing heterogeneity of the free speed of agents.

Acknowledgments

The authors are grateful to the HGF for providing funding within the knowledge transfer project under Grant No. WT-0105. Qiancheng Xu wishes to express his thanks for the funding support received from the China Scholarship Council (Grant No. 201706060186). We would also like to thank Antoine Tordeux for his very useful comments and consultations.

A. Decisive factors in the anticipation velocity model

Using the AVM reduces the jamming probability and favors the formation of lanes in bidirectional flow simulations. The possible causes for the improvement are the prediction time t^{a}, and the dynamic $\alpha_{i,j}$ reflecting pedestrians' preference to follow others moving in the same direction. To identify the decisive factor of this improvement, simulations are performed in periodic boundary conditions with dynamic $\alpha_{i,j}$ and constant $\alpha_{i,j}$ ($\alpha_{i,j} = k$), respectively. For each case, different values of t^{a} (0, 0.2, 0.5, 1.0, 1.5, and 2 s) are adopted. The simulation scenario is the corridor shown in Figure 6. The free speeds of agents are normally distributed $N \sim (1.55, 0.18^2)\ \mathrm{m\,s^{-1}}$. The number of agents in each simulation is 140 ($\rho \approx 1.35\,\mathrm{m^{-2}}$). This corresponds to the global density where the transition from moving states ($P_{\mathrm{jam}} = 0$) to jamming states ($P_{\mathrm{jam}} = 1$) occurs in the simulation using the AVM. The other parameters of the AVM are shown in Table 1.

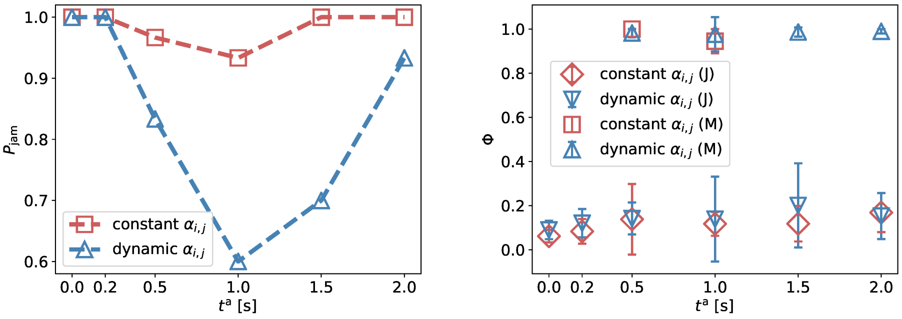

(a) (b)

Figure 17. (a): The relationship between the jamming probability P_{jam} and the prediction time t^{a} for dynamic and constant $\alpha_{i,j}$. (b): Mean value and standard deviation of Φ in the simulation with jamming (J) and moving (M) states for each value of t^{a} and each $\alpha_{i,j}$ (dynamic and constant).

The relationship between the jamming probability P_{jam} and the prediction time t^{a} for dynamic and constant $\alpha_{i,j}$ is shown in Figure 17(a). The same tendency of P_{jam} is observed in the simulation with dynamic and constant $\alpha_{i,j}$. As t^{a} increases, P_{jam} decreases until t^{a} reaches a specific value, then it increases. Moreover, the effect of the prediction time t^{a} on the jamming probability P_{jam} is more significant in the simulation with dynamic $\alpha_{i,j}$ than with constant $\alpha_{i,j}$.

The mean value and standard deviation of Φ in the simulation with jamming and moving states are calculated for each t^{a} and each $\alpha_{i,j}$ (dynamic and constant). See Figure 17(b). The values of Φ are close to 1 in the moving state and less than 0.3 in the jamming state. Neither the prediction time t^{a} nor the coefficient $\alpha_{i,j}$ affects the formation of lanes in the simulation with the moving state.

In conclusion, the prediction time t^{a} and the dynamic $\alpha_{i,j}$ both contribute to reducing the jamming probability in the bidirectional flow simulation. Moreover, a longer prediction time does not mean a lower jamming probability. An appropriate prediction time t^{a} can reduce the jamming probability. A similar conclusion also drawn from [11] is that there is an optimal strength of anticipation to realize the smoothest counterflow.

B. Width of the corridor

A transition from moving states ($P_{\text{jam}} = 0$) to jamming states ($P_{\text{jam}} = 1$) occurs with an increase of ρ_{global} (the global density of agents) in the bidirectional flow simulations. In this appendix, the effect of the corridor width on this transition is studied. Six corridors with different widths (1, 2, 3, 4, 5, and 6 m) are simulated. Apart from the width, these corridors are identical to the corridor shown in Figure 6. For each corridor, simulations are performed in periodic boundary conditions with different values of ρ_{global} (0.31, 0.62, 0.92, 1,23, 1.54, or 1.85 m^{-2}). The simulation is performed with the AVM using the parameters in Table 1. The free speeds of agents are normally distributed $N \sim (1.55, 0.18^2)\ \text{m}\,\text{s}^{-1}$.

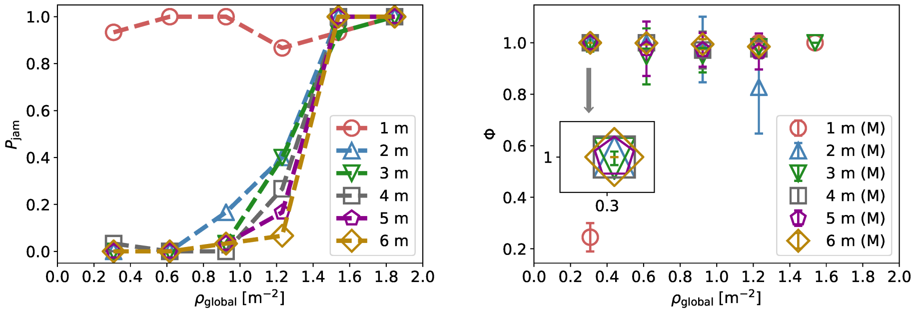

(a) (b)

Figure 18. The numbers in the legend give the width of the corridor. (a): Relationship between the jamming probability P_{jam} and the global density ρ_{global} for corridors with different widths. (b): Mean value and standard deviation of Φ in the simulation with the moving state (M), for each corridor and each global density ρ_{global}.

The relationship between the jamming probability P_{jam} and the global density ρ_{global} for corridors with different widths is shown in Figure 18(a). The transition from moving states to jamming states is observed in the simulation with all corridors except for the corridor of 1 m width. When the width of the corridor is 1 m, the value of P_{jam} is close to 1 even if the global density is very low. One possible reason for this is that the effect of walls prevents agents from using the full width of the corridor.

The mean value and standard deviation of Φ in the simulation with the moving state are calculated for each corridor and each value of ρ_{global}. See Figure 18(b). When the width of the corridor is 1 m and $\rho_{\mathrm{global}} = 0.31\,\mathrm{m}^{-2}$, the value of Φ is lower than in other situations. In addition to this, there is no significant difference between the value of Φ in other simulations with the moving state, which is always close to 1.

C. Heterogeneity of the free speed of the agents

To analyze the influence of the heterogeneity of agents, the free speed is chosen according to a normal distribution. A larger standard deviation of the distribution corresponds to a higher heterogeneity in the free speed of agents. In other sections, the normal distribution $N \sim (1.55, 0.18^2)\ \mathrm{m\,s^{-1}}$ obtained from the experiment in [15] is used. In this subsection, normal distributions with the same mean value ($1.55\,\mathrm{m\,s^{-1}}$) but different standard deviations (0, 0.09, 0.18, 0.36, or $0.54\,\mathrm{m\,s^{-1}}$), which is denoted by σ, are adopted in this analysis. To avoid negative values, the lower limit of the free speed is set as $0.1\,\mathrm{m\,s^{-1}}$. Simulations are performed with periodic boundary conditions in the corridor shown in Figure 6. The number of agents is 140 in each simulation ($\rho \approx 1.35\,\mathrm{m}^{-2}$). It corresponds to the global density, where the transition from moving states ($P_{\mathrm{jam}} = 0$) to jamming states ($P_{\mathrm{jam}} = 1$) occurs in the simulation using the AVM. Other parameters of AVM are shown in Table 1.

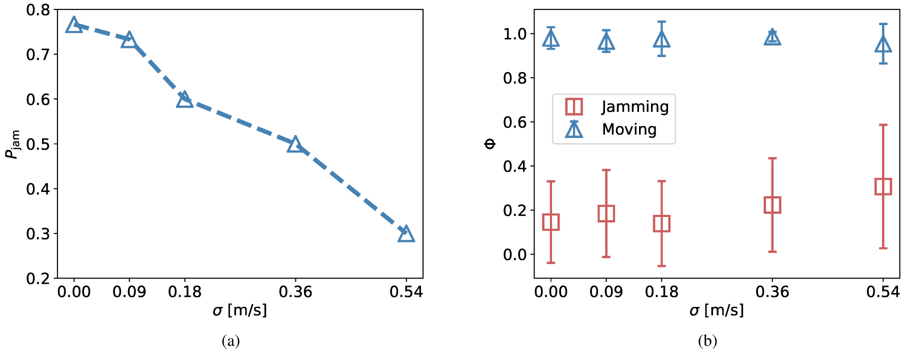

Figure 19. (a): The relationship between the jamming probability P_{jam} and the standard deviation σ. (b): The mean value and standard deviation of Φ in the simulation with jamming and moving states, for each value of σ.

The relationship between the jamming probability P_{jam} and the standard deviation σ is shown in Figure 19(a). The value of P_{jam} decreases as σ increases. The mean value and standard deviation of Φ in the simulation with jamming and moving states are calculated for each value of σ. See Figure 19(b). The value of Φ in the moving state is higher than in the jamming state. Moreover, there is no significant difference between the value of Φ in the simulation with the moving state, which is always all close to 1. In conclusion, with increasing heterogeneity of the free speed of agents, the jamming probability decreases, but the formation of lanes in the simulation with the moving state is not affected.

References

[1] K. Yamori, Going with the flow: Micro–macro dynamics in the macrobehavioral patterns of pedestrian crowds., Psychological review 105 (3) (1998) 530.

[2] D. Helbing, P. Molnár, I. J. Farkas, K. Bolay, Self-organizing pedestrian movement, Environment and planning B: planning and design 28 (3) (2001) 361–383.

[3] S. Hoogendoorn, W. Daamen, Self-organization in pedestrian flow, in: Traffic and Granular Flow'03, Springer, 2005, pp. 373–382.

[4] C. Feliciani, H. Murakami, K. Nishinari, A universal function for capacity of bidirectional pedestrian streams: Filling the gaps in the literature, PloS one 13 (12) (2018) e0208496.

[5] M. Boltes, J. Zhang, A. Tordeux, A. Schadschneider, A. Seyfried, Empirical results of pedestrian and evacuation dynamics, Encyclopedia of complexity and systems science (2018) 1–29.

[6] J. Adrian, M. Amos, M. Baratchi, M. Beermann, N. Bode, M. Boltes, A. Corbetta, G. Dezecache, J. Drury, Z. Fu, et al., A glossary for research on human crowd dynamics, Collective Dynamics 4 (A19) (2019) 1–13.

[7] J. Dzubiella, G. Hoffmann, H. Löwen, Lane formation in colloidal mixtures driven by an external field, Physical Review E 65 (2) (2002) 021402.

[8] M. E. Leunissen, C. G. Christova, A.-P. Hynninen, C. P. Royall, A. I. Campbell, A. Imhof, M. Dijkstra, R. Van Roij, A. Van Blaaderen, Ionic colloidal crystals of oppositely charged particles, Nature 437 (7056) (2005) 235–240.

[9] K. Sütterlin, A. Wysocki, A. Ivlev, C. Räth, H. Thomas, M. Rubin-Zuzic, W. Goedheer, V. Fortov, A. Lipaev, V. Molotkov, et al., Dynamics of lane formation in driven binary complex plasmas, Physical review letters 102 (8) (2009) 085003.

[10] D. Helbing, P. Molnar, Social force model for pedestrian dynamics, Physical review E 51 (5) (1995) 4282.

[11] Y. Suma, D. Yanagisawa, K. Nishinari, Anticipation effect in pedestrian dynamics: Modeling and experiments, Physica A: Statistical Mechanics and its Applications 391 (1-2) (2012) 248–263.

[12] H. Murakami, C. Feliciani, K. Nishinari, Lévy walk process in self-organization of pedestrian crowds, Journal of the Royal Society Interface 16 (153) (2019) 20180939.

[13] H. Murakami, C. Feliciani, Y. Nishiyama, K. Nishinari, Mutual anticipation can contribute to self-organization in human crowds, Science Advances 7 (12) (2021).

[14] M. Isobe, T. Adachi, T. Nagatani, Experiment and simulation of pedestrian counter flow, Physica A: Statistical Mechanics and its Applications 336 (3-4) (2004) 638–650.

[15] J. Zhang, W. Klingsch, A. Schadschneider, A. Seyfried, Ordering in bidirectional pedestrian flows and its influence on the fundamental diagram, Journal of Statistical Mechanics: Theory and Experiment 2012 (02) (2012) P02002.

[16] M. Moussaid, E. G. Guillot, M. Moreau, J. Fehrenbach, O. Chabiron, S. Lemercier, J. Pettré, C. Appert-Rolland, P. Degond, G. Theraulaz, Traffic instabilities in self-organized pedestrian crowds, PLoS Comput Biol 8 (3) (2012) e1002442.

[17] C. Feliciani, K. Nishinari, Empirical analysis of the lane formation process in bidirectional pedestrian flow, Physical Review E 94 (3) (2016) 032304.

[18] S. Nowak, A. Schadschneider, Quantitative analysis of pedestrian counterflow in a cellular automaton model, Physical review E 85 (6) (2012) 066128.

[19] M. Rex, H. Löwen, Lane formation in oppositely charged colloids driven by an electric field: Chaining and two-dimensional crystallization, Physical review E 75 (5) (2007) 051402.

[20] F. Zanlungo, T. Ikeda, T. Kanda, Social force model with explicit collision prediction, EPL (Europhysics Letters) 93 (6) (2011) 68005.

[21] I. Karamouzas, B. Skinner, S. J. Guy, Universal power law governing pedestrian interactions, Physical review letters 113 (23) (2014) 238701.

[22] U. Weidmann, Transporttechnik der fußgänger: transporttechnische eigenschaften des fußgängerverkehrs, literaturauswertung, IVT Schriftenreihe 90 (1993).

[23] R. Bailo, J. A. Carrillo, P. Degond, Pedestrian models based on rational behaviour, in: Crowd Dynamics, Volume 1, Springer, 2018, pp. 259–292.

[24] M. J. Seitz, N. W. Bode, G. Köster, How cognitive heuristics can explain social interactions in spatial movement, Journal of the Royal Society Interface 13 (121) (2016) 20160439.

[25] M. Muramatsu, T. Irie, T. Nagatani, Jamming transition in pedestrian counter flow, Physica A: Statistical Mechanics and its Applications 267 (3-4) (1999) 487–498.

[26] F. Weifeng, Y. Lizhong, F. Weicheng, Simulation of bi-direction pedestrian movement using a cellular automata model, Physica A: Statistical Mechanics and its Applications 321 (3-4) (2003) 633–640.

[27] D. Helbing, L. Buzna, A. Johansson, T. Werner, Self-organized pedestrian crowd dynamics: Experiments, simulations, and design solutions, Transportation science 39 (1) (2005) 1–24.

[28] T. Kretz, A. Grünebohm, M. Kaufman, F. Mazur, M. Schreckenberg, Experimental study of pedestrian counterflow in a corridor, Journal of Statistical Mechanics: Theory and Experiment 2006 (10) (2006) P10001.

[29] A. Tordeux, M. Chraibi, A. Seyfried, Collision-free speed model for pedestrian dynamics, in: Traffic and Granular Flow'15, Springer, 2016, pp. 225–232.

[30] Q. Xu, M. Chraibi, A. Tordeux, J. Zhang, Generalized collision-free velocity model for pedestrian dynamics, Physica A: Statistical Mechanics and its Applications 535 (2019) 122521.

[31] S. Cao, A. Seyfried, J. Zhang, S. Holl, W. Song, Fundamental diagrams for multidirectional pedestrian flows, Journal of Statistical Mechanics: Theory and Experiment 2017 (3) (2017) 033404.

[32] C. von Krüchten, Development of a cognitive and decision-based model for pedestrian dynamics, Ph.D. thesis, Universitäts- und Stadtbibliothek Köln (2019).

[33] C. Feliciani, K. Nishinari, An improved cellular automata model to simulate the behavior of high density crowd and validation by experimental data, Physica A: Statistical Mechanics and its Applications 451 (2016) 135–148.

A.7 ARTICLE VI

Prolonged clogs in bottleneck simulations for pedestrian dynamics

Q. XU, M. CHRAIBI, AND A. SEYFRIED

. PHYSICA A: STATISTICAL MECHANICS AND ITS APPLICATIONS (**2021**)

Physica A: Statistical Mechanics and its Applications, 573:125935, 2021
10.1016/j.physa.2021.125934

Prolonged Clogs in Bottleneck Simulations for Pedestrian Dynamics

Qiancheng Xu[1], Mohcine Chraibi[1], Armin Seyfried[1]

Abstract
This article studies clogging phenomena using a velocity-based model for pedestrian dynamics. First, a method to identify prolonged clogs in simulations was introduced. Then bottleneck simulations were implemented with different initial and boundary conditions. The number of prolonged clogs were analyzed to investigate the decisive factors causing this phenomenon. Moreover, the time lapse between two consecutive agents passing the exit, and the trajectories of agents were analyzed. The influence of three type of factors was studied: parameters of the spatial boundaries, algorithmic factors related to implementation of the model, and the movement model. Parameters of the spatial boundaries include the width and position of the bottleneck exit. Algorithmic factors are the update methods and the size of the time step. Model parameters cover several parameters describing the level of motivation, the strength and range of impact among agents, and the shape of agents. The results show that the occurrence of prolonged clogs is closely linked to parameters of the spatial boundaries and the movement model but has virtually no correlation with algorithmic factors.

Keywords
Model

[1] *Institute for Advanced Simulation,*
Forschungszentrum Jülich, 52425 Jülich, Germany

Contents

Introduction

Clogging is a phenomenon that usually arises when particles pass through narrow bottleneck structures [1]. It is often expressed as the jamming arch formed by several interactive particles in front of the bottleneck, which significantly decreases or even stops the flow through the bottleneck.

The phenomenon occurs in different systems of inert particles such as granular material in the silo [1, 2, 3], dense suspension of colloidal particles [4, 5, 6, 7] or electrons on the surface of liquid helium [8, 9]. This type of clogging is usually stable if there is no external disturbance to break the balance between the particles that form the clogging [1, 10]. Clogging can also be observed in the movement of animals [11] and humans [12] when congestion and high motivation coincide, for instance, when a large number of passengers at a train station enter carriages through a narrow train door with high motivation, or when fans at entrances to a concert hall are all trying to get in and find places near the stage [13].

Unlike with the clogging of inert particles, clogging in systems with humans is temporary. The duration of clogs depends on the motivation level of the pedestrians involved in the clogging [5, 11, 12, 13]. Although the clogging of humans may last a relatively long time in some extreme cases and sometimes even leads to severe injuries [14, 15], in most normal cases, its duration is short even in competitive situations [13]. In the literature, the short-term nature of the clogs is often attributed to the fluctuation in the load to the humans in the clog. This fluctuation, in turn, may be the result of the flexibility and elasticity of the human body. Moreover, some clogs are avoided before forming, through complex steering mechanisms that include cognitive processes and control of the body.

However, microscopic models based on physical principles merely focus on guaranteeing volume exclusion. They do not take the above-mentioned factors sufficiently into account, which could lead to prolonged clogs (clogs interrupting flow for a long time) or even stable clogs similar to inert particles. One study, [16], examined this phenomenon using a cellular automaton (CA) model. A friction parameter was introduced for an improved description of the clogging of pedestrians. In another study, [17], the friction parameter was extended to a function of the number of agents in clogging for a more realistic result of the pedestrian outflow through the exit. The effect of queuing and pushing behavior in front of the bottleneck on the overall dynamics of the crowd is explored using another CA model in [18], where a local pushing mechanism is used [19]. Another global pushing mechanism is proposed in [20]. Furthermore, game theory is combined with CA models in some studies to better reproduce the movement of pedestrians [21, 22]. Prolonged clogs and stable clogs can also be observed in the social force models for pedestrian dynamics by increasing the desired velocity of the agents [23]. Introducing random behavioral variations is important to mitigate these clogs in simulations [24, 25]. Further studies [26, 27] used the social force model to study the effect of desired velocity and the exit door on the duration of clogs. Clogs caused by higher desired velocity in force-based models result in lower flow through bottlenecks, a phenomenon also known as “faster-is-slower” [24, 26, 27, 28, 29].

In this paper, we focus on prolonged clogs occurring in the generalized collision-free velocity model (GCVM) [30], a first-order microscopic model for pedestrian dynamics. It is based on the collision-free speed model [31], and strictly follows the principle of volume exclusion to guarantee that there is no overlap among agents. Therefore, clogs that result in long-term interruption of flow occur frequently in simulations of bottlenecks, particularly in narrow exits. We aim to quantify these prolonged clogs by exploring decisive factors behind their occurrence in the bottleneck scenario, to purposefully improve the GCVM for reproducing pedestrians’ movement more realistically. The effect of three types of factors is examined in this study. The first category includes two parameters of the spatial boundaries, i.e., the width and the position of the bottleneck exit. The second category consists of algorithmic factors related to the implementation of the GCVM, including the time step size and the update scheme (e.g., sequential or parallel update) for the agents in the simulations. Third, several model parameters such as the strength of impact among agents in the GCVM, and the shapes of the agents are analyzed. The results are used to ascertain the relationship between these factors and the occurrence of prolonged clogs.

This paper is organized as follows. Section 1 introduces the bottleneck scenario for the simulations. In section 2, we briefly define the GCVM and introduce the method used for identifying prolonged clogs in numerical simulations. Section 3 compares simulation results obtained with various factors and shows the corresponding analysis. Finally, we conclude with a discussion in section 4.

1. The bottleneck scenario for simulations

The bottleneck scenario for simulations in this study is shown in figure 1. It is composed of three parts separated by red dashed segments. The source area, a $8\,\mathrm{m} \times 8\,\mathrm{m}$ square in gray, the moving area, a rectangular room with an area of $10\,\mathrm{m} \times 8\,\mathrm{m}$, and the exit, a corridor measuring $2\,\mathrm{m} \times w$. In section 3 different values of w and d (the position of the exit with respect to the lower horizontal wall) are used to determine the effect of the structure of the bottleneck has on the occurrence of the prolonged clogs.

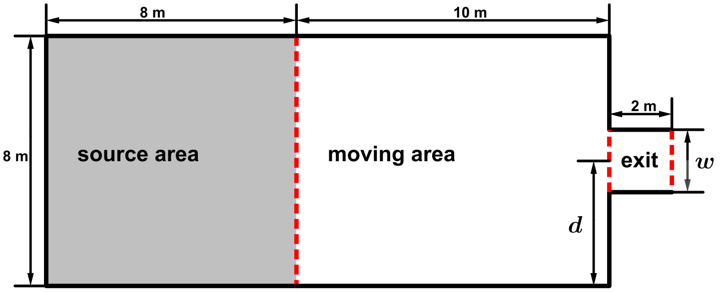

Figure 1. The bottleneck scenario for simulations.

In order to determine the decisive factors behind the appearance of prolonged clogs, simulations are implemented in the bottleneck scenario with different initial and boundary conditions. In each simulation, 400 agents are generated with a constant rate at random positions in the source area and these move through the moving area to leave the scenario by the exit. During this process, clogs may appear, leading to an interruption of the bottleneck flow. A clog interrupting the flow longer than the time threshold T_w is identified as a prolonged clog. Since prolonged clogs can last a long time and so as to ensure that the blockage does not stop the dynamics of the system, resulting in an impractically long simulation time, we manually solve them by moving one of the agents involved in the clog to free space in the source area. The details of this manual clog-solving procedure will be elaborated in the next section. The number of prolonged clogs in each simulation is recorded. Then the results of different simulations are compared to explore the relationship between these factors and the occurrence of prolonged clogs.

The model for pedestrian dynamics and the approach to identify clogs are presented in the following section.

2. Introducing the model and identifying prolonged clogs

We begin this section with a brief introduction to the GCVM, which is the model used in this study. It is defined as

$$\dot{X}_i(X_i, X_j, \dots) = \vec{e}_i(X_i, X_j, \dots) \cdot V_i(X_i, X_j, \dots), \tag{1}$$

where X_i is the position of agent i, V_i is a scalar denoting its speed, and $\vec{e}_i$ is a unit vector representing its direction of movement.

The direction of movement $\vec{e}_i$ is calculated first by using the equation

$$\vec{e}_i = u \cdot \left(\vec{e}_i^{\,0} + \sum_{j \in J_i} k \cdot \exp\left(\frac{-s_{i,j}}{D} \right) \cdot \vec{n}_{i,j} + \vec{w}_i \right). \tag{2}$$

Here, u is a normalization constant such that $\|\vec{e}_i\| = 1$. $\vec{e}_i^{\,0}$ is a unit vector representing the desired direction of the agent. This is calculated according to reference lines indicated by the red dashed segments in figure 1. The vector $\vec{e}_i^{\,0}$ points to the middle of the reference line when agent i is not in the range of the reference line; otherwise, it points to the nearest point on the reference line. More details of the calculation method are given in [32]. J_i is the set of agents that contains all neighbors affecting the moving direction of agent i. The magnitude of the impact from these neighbors is a function of $s_{i,j}$, which is the distance between the edges of agent i and j along the line connecting their centers. Parameters $k > 0$ and $D > 0$ are used to calibrate the strength and range of the impact, respectively. The effect of k and D on the strength of impact is shown in figure 2(a) and a similar analysis for the effect of k and D can be found in [33]. The direction of the impact from agent j to i is denoted by the unit vector $\vec{n}_{i,j}$, which depends on the relative positions of both agents. $\vec{w}_i$ is the effect from walls and obstacles in the room, which is calculated analogously to the effect from neighbors.

Then the speed on the new moving direction is obtained using the equation

$$V_i = \min\left\{ V_i^0, \max\left\{0, \frac{s_i}{T}\right\} \right\}. \tag{3}$$

The speed is a function of s_i, which is the maximum space of agent i in the new direction of movement $\vec{e}_i$ without overlapping with other agents. In equation (3), V_i^0 is the free speed of agent i, the speed that is achieved by moving without interference

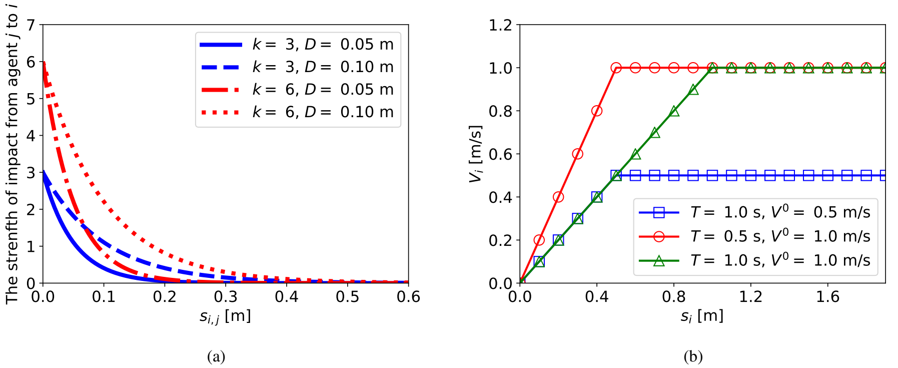

(a)

(b)

Figure 2. (a) The effect of k and D on the strength of impact. (b) The speed functions with different V_i^0 and T.

from other agents. The parameter $T > 0$ is the slope of the speed-headway relationship. The speed functions with different V_i^0 and T are shown in figure 2(b). The value of T could be used to model the level of motivation in simulations. A decrease of T at constant s_i leads to a smaller distance between agent i and the nearest agent in front, which corresponds to behavior with a higher level of motivation. A more detailed introduction to the GCVM can be found in [30].

Since there is no overlapping among agents in the GCVM, the space occupied by one agent is not available to other agents. Therefore, clogging occurs when the direction of movement, $\vec{e}_i$, of two agents point toward each other and the distance $s_{i,j}$ between them is too small for them to move. A representative case is shown in figure 3(a). It could be formalized by

$$\begin{cases} s_{i,j} & \leq \varepsilon, \\ V_i + V_j & \leq \lambda, \\ \vec{e}_{i,j} \cdot \vec{e}_i & < 0, \\ \vec{e}_{i,j} \cdot \vec{e}_j & > 0, \end{cases} \tag{4}$$

where $\vec{e}_{i,j}$ is the unit vector points from the center of agent j to i, ε is a threshold used to determine whether the distance between these two agents is small enough to form a clog, and λ is the threshold of speed to ascertain whether these two agents are almost stationary. The last two conditions in equation (4) denote that these two agents are moving toward each other. In the present study, ε is equal to the radius of agents, and λ is set as $(V_i^0 + V_j^0)/100$. A clog formed by more than two agents contains at least two agents satisfying equation (4).

There could be many pairs of agents that satisfy the definition of clogging in equation (4) at any time and any place in the simulation. We treat clogs that interrupt the flow longer than time period T_w as prolonged clogs. These prolonged clogs occur almost around exits, as the degree of freedom in the direction of movement is limited by the wall. An example of prolonged clogs is shown in figure 3(b), a clog consisting of four red agents is formed in front of the bottleneck and interrupts the flow. After $T_w = 2\,\mathrm{s}$, the clog is solved manually by moving one of the agents in the clog. As for clogs that do not interrupt the flow or last less than T_w seconds, we do not destroy them artificially since these can be solved automatically by agents adjusting their direction of movement. A clog formed by two red agents, which can be automatically solved in $T_w = 2\,\mathrm{s}$, is shown in figure 3(c).

The flowchart in figure 4 illustrates how to count the prolonged clogs in simulations, where t is the current time, t_p is the time at which the last agent enters the exit, t_m is the time of the last manual clog-solving process, N_s is the number of prolonged clogs, Δt is the time step size in the simulation, and t_c is the smaller of $t - t_p$ and $t - t_m$.

For each time step of a simulation, a non-zero flow through the measurement line between moving area and exit is an indicator that no prolonged clogs occur. Otherwise, we will check whether t_c is greater than the threshold T_w, and whether there are agents satisfying the definition of clogging in equation (4). A prolonged clog is identified if these two conditions are met. It is treated as a new clog if t_p, the time when the last agent crossed the bottleneck, is not less than t_m, the time of the last manual removal of an agent. Regardless of whether the clog is new or already existing, one of the two agents forming the closest clog to the exit is moved manually to free space in the source area. It should be noted that breaking up a prolonged clog may require more than one manual clog-solving process, which results in $t_p < t_m$. The number of prolonged clogs is counted from the beginning of the simulation to the last agent leaving the simulation scenario.

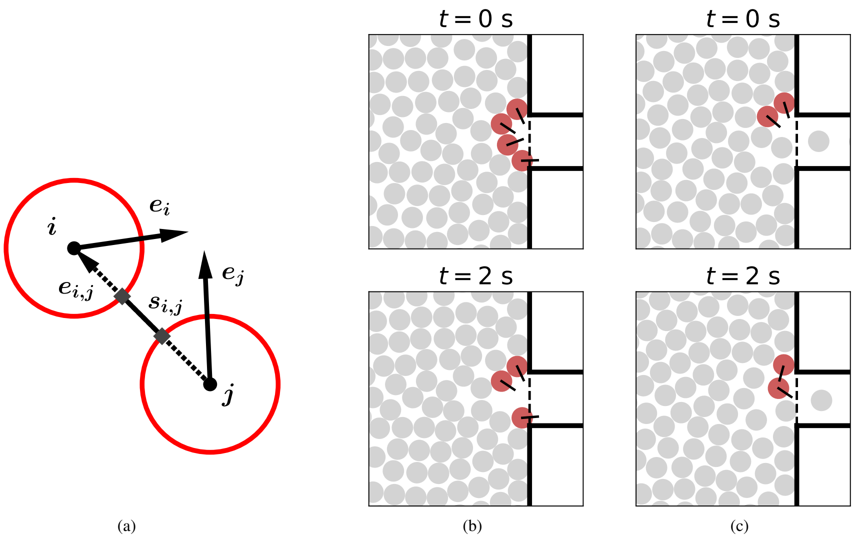

Figure 3. (a): When two agents are about to cause clogging, $\vec{e}_i$ and $\vec{e}_j$ are directions of movement of agent i and j, $\vec{e}_{i,j}$ is the unit vector points from the center of agent j to i, $s_{i,j}$ is the distance between the edges of agent i and j along the line connecting their centers. (b): A prolonged clog is manually solved after interrupting the flow for 2 s. (c): A clog is solved automatically by agents adjusting their direction of movement.

3. Simulation results

In each simulation, one or two factors were selected for variation. The other factors were set to default values as shown in table 1.

To improve the efficiency of simulations, a series of simulations were implemented firstly to select the suitable T_w, the time span between the formation, and artificial termination of a prolonged clog for subsequent simulations. We ran simulations in four bottleneck scenarios, where the value of w was 0.8, 1.0, 1.2, and 1.6 m, respectively. For each scenario, simulations with T_w from 0 s to 4 s were implemented. We ran each simulation four times with different distributions of agents in the source area. The relationship between T_w and the mean values of N_s, the number of prolonged clogs, from the four runs are shown in figure 5, where the error bars indicate the standard deviations. The results in scenarios with a different value of w are represented by different marks and colors. In all four scenarios, N_s dis not change significantly when T_w was longer than 2 s. Therefore, this value for T_w was selected for the following simulations.

In the following, we ran each simulation four times. The mean value of N_s from the four runs reflects the effect of the factors observed on the occurrence of prolonged clogs. Moreover, the time lapse between two consecutive agents entering the exit, and the trajectories of agents were analyzed for the selected factors.

3.1 Parameters of spatial boundaries

The effects of the width and the position of the exit are explored in this subsection. Three exit positions ($d = 4.0$, 2.0, or $w/2$ m) and six widths ($w = 0.8$, 1.0, 1.2, 1.6, 2.0, or 2.5 m) were selected for the simulations. The exit was located in the middle of two lateral walls of the moving area when $d = 4$ m and adjacent to the lower horizontal wall when $d = w/2$.

Figure 6 shows the correlation between N_s and w for different values of d. The position of the exit does not alter the fact that N_s decreases to zero as w increases. Moreover, there is no prolonged clog when the exit is wider than 1.6 m for all three positions. Besides the effect of w, when $d = w/2$ (the exit is adjacent to the lower horizontal wall of the moving area), N_s was significantly less than with the other two locations. We assumed that this difference was caused by the reduced degree of freedom in the possible directions in which agents will move.

In order to quantitatively analyze the influence of the width of the exit (w) on the clogs, we examined the time lapses δ between two consecutive agents passing the exit, for different values of w. The value of δ reflects the sustained time of clogs

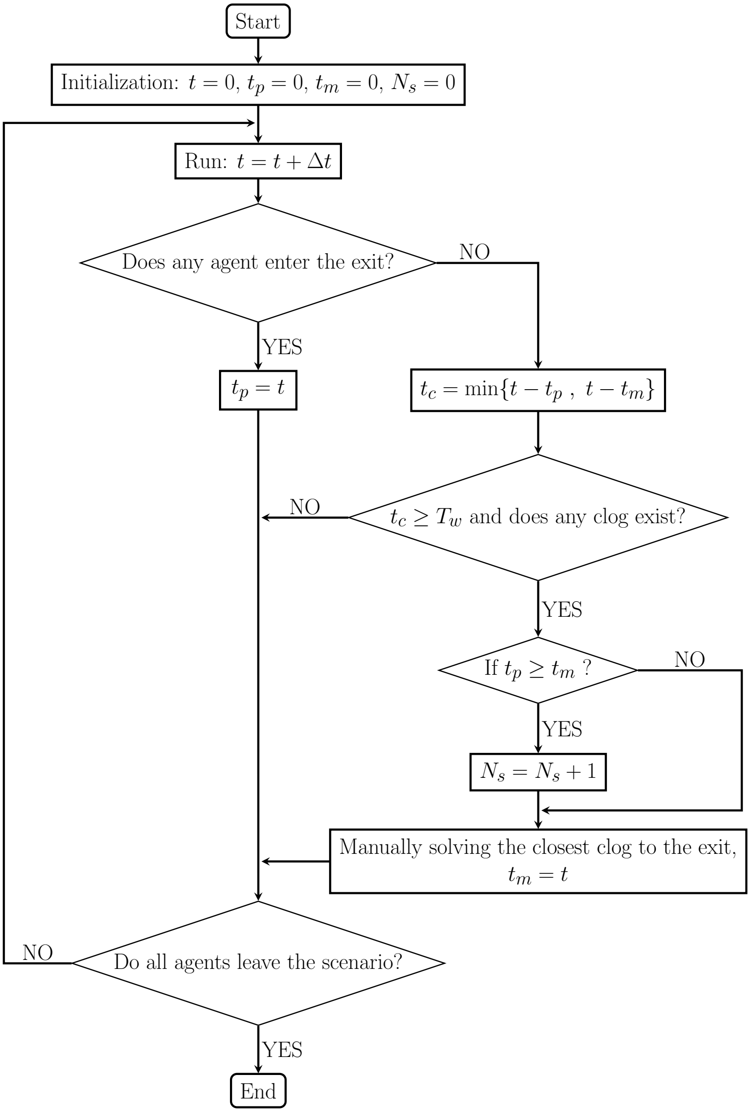

Figure 4. The process of solving and counting prolonged clogs. t is the current time, t_p is the time of the last agent entering the exit, t_m is the time of the last manual clog-solving process, N_s is the number of prolonged clogs, Δt is the time step size in the simulation, t_c is the smaller of $t - t_p$ and $t - t_m$, T_w is the time threshold.

Table 1. Default values of factors in simulations. w is the width of the exit, d is the distance between the center of the exit and the lower horizontal wall of the moving area, k and D are parameters used to calibrate the strength and range, respectively, of the impact from neighbors in the movement direction, V_i^0 is the free speed, and T is the slope of the speed-headway relationship.

Factors	Default values
Agent generation rate	8 Agents/s
Agent shape	circle ($r = 0.2\,\mathrm{m}$)
Update method	parallel update
Time step size Δt	$0.05\,\mathrm{s}$
w (figure 1)	$0.8\,\mathrm{m}$
d (figure 1)	$4\,\mathrm{m}$
k (equation (2))	3
D (equation (2))	$0.1\,\mathrm{m}$
V_i^0 (equation (3))	$1.34\,\mathrm{m\,s^{-1}}$
T (equation (3))	$0.3\,\mathrm{s}$

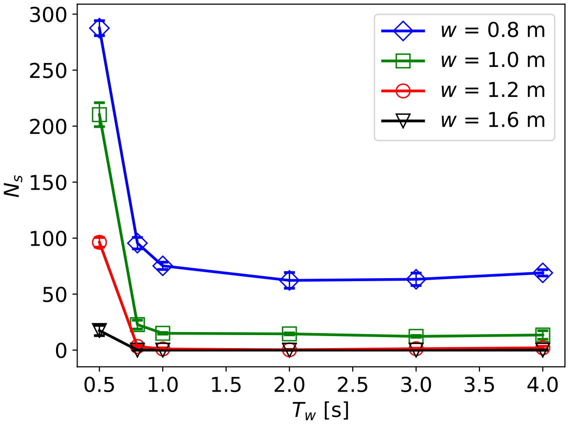

Figure 5. The correlation between N_s (the number of prolonged clogs) and T_w (the time span between the formation and artificial termination of a prolonged clog) for different values of w (the width of the exit). The error bars show the standard deviations.

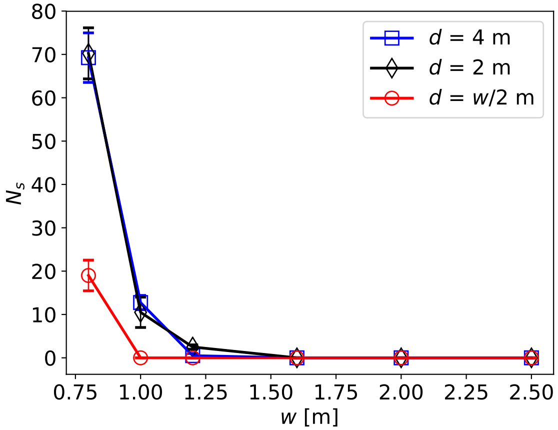

Figure 6. The correlation between N_s (the number of prolonged clogs) and w (the width of the exit) for different values of d (the distance between the center of the exit and the lower horizontal wall of the moving area). The error bars show the standard deviations.

interrupting the flow. The probability distribution function $P(t > \delta)$, also known as the survival function, is sensitive to changes in the spatial boundaries, e.g. the width of the bottleneck [5, 11, 12, 34]. We analyzed the results of simulations when $d = 4\,\mathrm{m}$. The survival functions of different values of w are compared in figure 7(a). It can be observed that the probability of a higher value of δ decreases as w increases. Besides, the occurrence of prolonged clogs leads to plateaus in the survival functions of $w = 0.8$ and $w = 1.0\,\mathrm{m}$. Basically, in these two cases, the actual values of $\langle\delta\rangle$, the mean time lapse, are unknown as clogs lasting longer than 2 s are manually solved. In fact, the actual value of $\langle\delta\rangle$ without manually removal of clogs may probably tend to infinite. Nevertheless, in order to obtain an estimate for the lower bound of $\langle\delta\rangle$ and study its dependence on w, we treated all $\delta > 2\,\mathrm{s}$ as $\delta = 2\,\mathrm{s}$ in the calculation of the mean value of δ. The correlation between the value of $\langle\delta\rangle$ and w is shown in figure 7(b). The mean value and standard deviation of δ both decrease with increasing w.

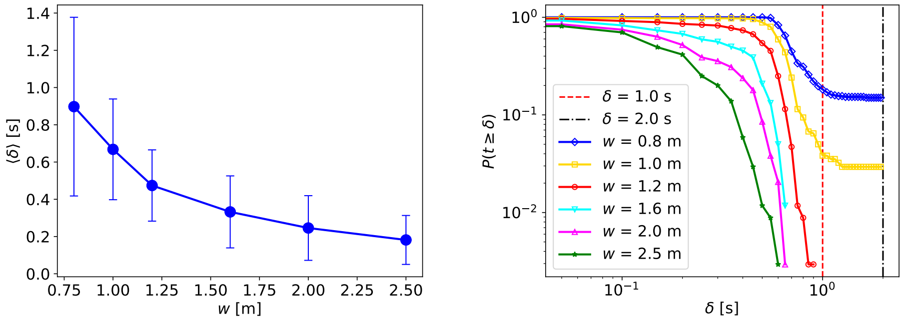

(a)

(b)

Figure 7. (a): The survival functions of δ for simulations with different values of w when $d = 4\,\mathrm{m}$. (b): The correlation between the $\langle\delta\rangle$ (the mean time lapse between two consecutive agents entering the exit) and w when $d = 4\,\mathrm{m}$. The error bars show the standard deviations.

3.2 Algorithmic factors

The effect of update methods and the time step sizes Δt to solve the equation of motion are analyzed in this subsection. Two update methods were adopted: the parallel update and the sequential update. When we used the parallel update, the direction of movement, speed and location of all the agents were updated at the same time. When the sequential update was used, the direction of movement, speed and location of agents were updated one by one according to the distance to the exit. The agents near the exit had more effect on the dynamic of the system than the agents further away from the exit. Therefore, the agent with a greater effect, i.e., the agent closer to the exit, was updated first in the sequential update. For each update method, simulations were performed with different values of Δt from 0.01 s to 0.125 s.

The correlation between N_s and Δt for two update methods is shown in figure 8. The effect of Δt on N_s is marginal for both update methods.

To explain the reason behind the results, an extreme case is considered here where two agents i and j are moving directly toward each other, which means $\vec{e}_i = -\vec{e}_j$. We assume that their direction of movement is fixed, and $s_{i,j} < T \cdot V_i^0$. According to equation (3), their speeds V_i and V_j are both equal to $s_{i,j}/T$. They will not overlap and, consequently, form a clog if their speeds satisfy

$$(V_i + V_j) \cdot \Delta t \leq s_{i,j}, \tag{5}$$

which can be transformed to $2 \cdot \Delta t \leq T$. This example illustrates that adopting a lower value of Δt or substituting the sequential update cannot hinder the occurrence of clogging, since the scarcity of available space is not changed.

Therefore, the occurrence of prolonged clogs in the simulations with the GCVM is not an algorithmic issue.

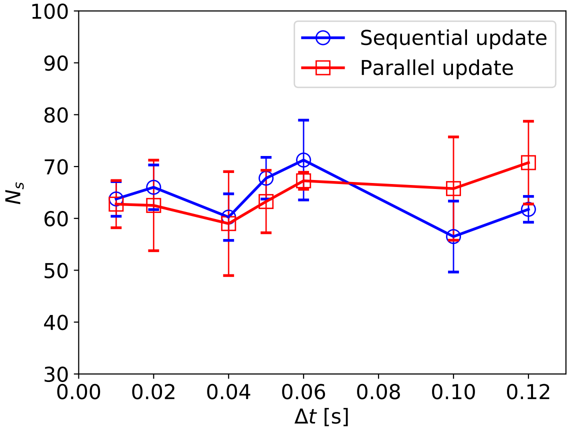

Figure 8. The correlation between N_s (the number of prolonged clogs) and Δt (time step size) for different update methods. The error bars show the standard deviations.

3.3 Parameters of the GCVM

In this subsection, the effect of several parameters in the GCVM is examined, including the slope of the speed-headway relationship T and the free speed V^0 in equation (3). The strength and range of the effect of neighbors in the direction of movement, k and D in equation (2), and the shapes of agents are also studied.

First, we looked at the effect of T and V^0. We ran simulations with different V^0 (1.34, 3.34, or 5.34 $\mathrm{m\,s^{-1}}$) and different T (0.1, 0.3, 0.5, 0.8, or 1.0 s). The correlation between N_s and T for different values of V^0 is shown in figure 9(a). For all three values of V^0, as T increased, N_s decreased initially, then remained relatively stable. A decrease in T led to a smaller slope of the speed-headway function, see equation (3) and figure 2(b). With decreasing T agents move closer, which reduces the space available to resolve clogs. This is in accordance with the finding that clogging is more likely to occur in scenarios with higher level of motivation [12, 25, 28, 34].

The level of motivation has been shown to have an effect on the time lapse δ [12, 25, 28]. Figure 9(b) shows the survival functions of δ in the simulations with $V^0 = 3.34\,\mathrm{m\,s^{-1}}$, which is similar to the result of granular media experiment [28]. These survival functions can be approximately separated into two successive regimes by $\delta = 1.2\,\mathrm{s}$. For $\delta \leq 1.2\,\mathrm{s}$, increasing T leads to a higher value of $P(t > \delta)$, while for $\delta > 1.2\,\mathrm{s}$, increasing T reduces $P(t > \delta)$. The mean time lapse $\langle\delta\rangle$ for each regime is shown in figure 9(c). As we mentioned above, the actual values of $\langle\delta\rangle$ for the region of $\delta > 1.2\,\mathrm{s}$ are unknown as clogs lasting longer than 2 s are manually solved. Therefore, we treated all $\delta > 2\,\mathrm{s}$ as $\delta = 2\,\mathrm{s}$ in the calculation of the mean value of δ. The obtained values are the lower bound of the real ones. Decreasing T can be interpreted as increasing the level of motivation, which results in an increase in the free flow rate ($\delta \leq 1.2\,\mathrm{s}$) as well as an increase in the probability of clogging ($\delta > 1.2\,\mathrm{s}$).

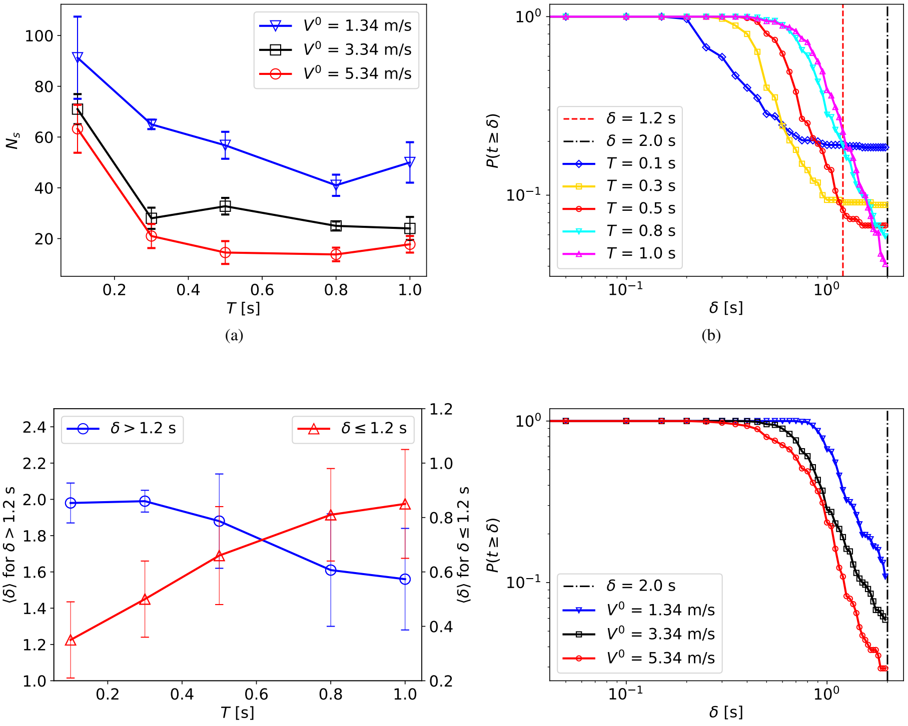

(a) (b)

(c) (d)

Figure 9. (a): The correlation between N_s (the number of prolonged clogs) and T (the slope of the speed-headway relation) for different values of V^0 (the free speed). The error bars show the standard deviations. (b): The survival functions of δ (the time lapse between two consecutive agents entering the exit) in the simulations with different values of T when $V^0 = 3.34\,\mathrm{m\,s^{-1}}$. (c): The mean time lapse $\langle\delta\rangle$ versus T when $V^0 = 3.34\,\mathrm{m\,s^{-1}}$, for $\delta \leq 1.2\,\mathrm{s}$ and $\delta > 1.2\,\mathrm{s}$, respectively. (d): The survival functions of δ (the time lapse between two consecutive agents entering the exit) in the simulations with different values of V^0 when $T = 0.8\,\mathrm{s}$.

However, a higher value of V^0, which can be interpreted as the expression of a higher motivation level, leads to lower values of N_s. We analyzed the results of simulations with $T = 0.8\,\mathrm{s}$. The survival functions of different values of V^0 are compared in figure 9(d). The probability of a higher value of δ decreases as V^0 increases. According to equation (3), the speed of agents in the GCVM depends on the overlapping-free spaces in their directions of movement. Although a higher V^0 increases the maximum possible speed of agents, it has little effect in congested areas due to limited space. Therefore, the effect of V^0 in the GCVM on the motivation level of present simulations is marginal, as most of the investigated situations represent congested conditions. Moreover, a higher V^0 allows agents to move faster in low density situations, which results in the reduction of N_s. Note, that in force-based models [25] the driving force increases with increasing V^0, hence V^0 can have an effect in congested situations as well.

Then we examined the effect of k and D. Higher values of k and larger D led to agents being more stimulated to deviate from their desired directions. We ran simulations with different values of k (0.2, 0.5, 1, 2, 3, 4, 5, or 6) and different values of D (0.01, 0.02, 0.05, or 0.1 m). The correlation between N_s and k for different values of D is shown in figure 10.

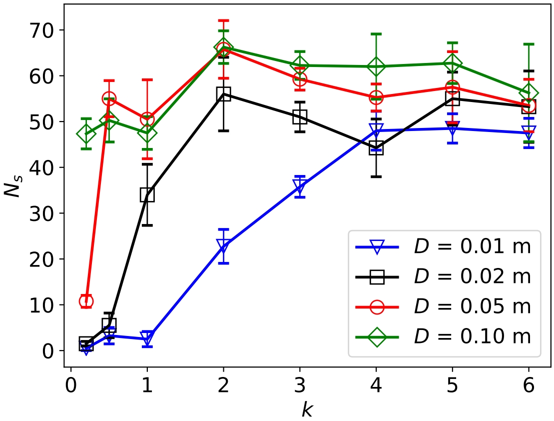

Figure 10. The correlation between N_s (the number of prolonged clogs) and k for different values of D. The error bars show the standard deviations.

It can be seen that N_s increases with increasing k and increasing D. We assume the reason for this is that lower values of k and D decrease the neighbor's impact on agents, which leads to the queuing behavior. We show in figure 11(a) the trajectories of agents in the simulation when k is 0.2 and D is 0.01 m, which shows a strong queuing behavior. When the impact among agents increased consistently, agents began to deviate from their desired direction until the queuing behavior was broken. Figure 11(b) shows the trajectories of agents in the simulation when k is 3 and D is 0.01 m.

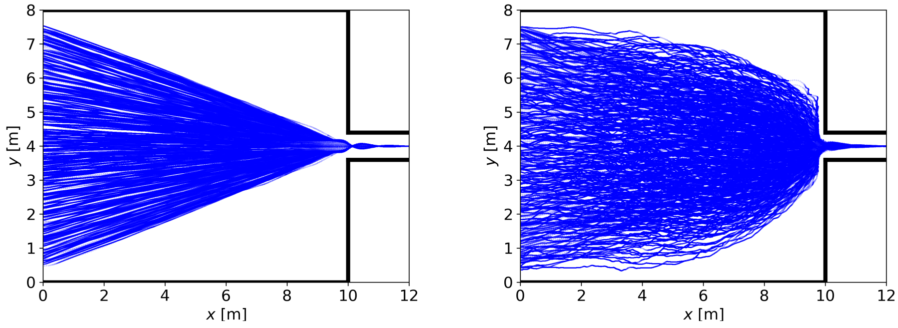

(a)

(b)

Figure 11. (a): Trajectories of agents when k is 0.2 and D is 0.01 m. (b): Trajectories of agents when k is 3.0 and D is 0.01 m.

The final factor analyzed was the shapes of agents. In the previous sections, a pedestrian's shape was modeled as circles with a constant radius. To study the influence of the shape, we also performed simulations where pedestrians were modeled as velocity-based ellipses [30]. The length of the semi-axis along the walking direction is a constant value a. The length of the other semi-axis along the shoulder equals b, which is defined as

$$b = b_{\min} + \frac{b_{\max} - b_{\min}}{1 + e^{\beta \cdot (V - \gamma)}} , \tag{6}$$

where $b_{\max}$ is the maximum value which is equal to half of a static pedestrian's width, $b_{\min}$ is equal to the half of a moving pedestrian's minimum width, V is the speed of the agent, and parameters β and γ are used to adjust the shape of the function.

Simulations in this part are performed with three constant circles with different radius values r (0.15, 0.20, or 0.25 m) and a velocity-based ellipse ($a = 0.20\,\mathrm{m}$, $b_{\min} = 0.15\,\mathrm{m}$, $b_{\max} = 0.25\,\mathrm{m}$, $\beta = 50$, $\gamma = 0.1$). Figure 12(a) shows the correlation between N_s and w for different shapes. The result of the ellipse is close to the result of the circle with $r = 0.20\,\mathrm{m}$, which is between the result of the smallest circle ($r = 0.15\,\mathrm{m}$) and of the biggest circle ($r = 0.25\,\mathrm{m}$). The possible explanation of this result is that the shape of the dynamic ellipse varies with the speed of agents. For example if the speed of an agent is $0.1\,\mathrm{m\,s^{-1}}$, the dynamic ellipse becomes a circle with $r = 0.2\,\mathrm{m}$. Which means that in high density situations the agents tend to have a circular shape instead.

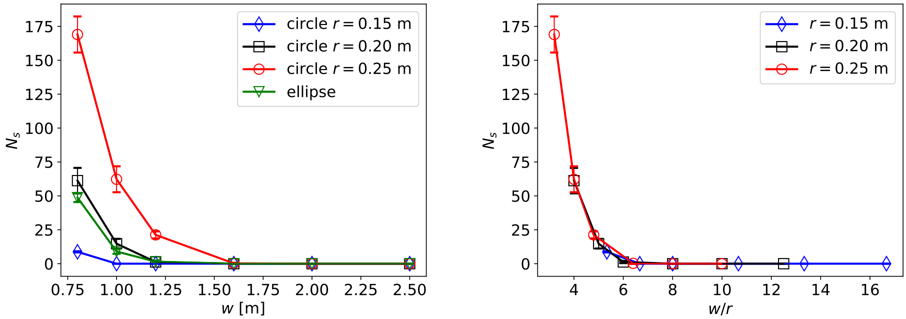

(a) (b)

Figure 12. (a) The correlation between N_s (the number of prolonged clogs) and w (the width of the exit) for different shapes of agents. The error bars show the standard deviations. (b) The correlation between N_s and w/r for different r (the radius of agents). The error bars show the standard deviations.

A finding in [35] is that the probability of clogs stopping the flow decreases with an increasing ratio between the size of the orifice and the size of the beads. Therefore, we plot figure 12(b) with w/r (the ratio between the width of the exit and the radius of the agents) as the horizontal axis. It seems that the number of prolonged clogs is not affected by the absolute values of w and r, provided that w/r remains the same.

4. Conclusion

In the present paper, we focus on prolonged clogs that occur in bottleneck scenarios with the GCVM. A general definition of prolonged clogs has been given. Then a series of simulations in a bottleneck scenario were implemented to analyze the effect of various factors on the occurrence of prolonged clogs.

From the simulation results, the following conclusions can be drawn. First, the number of prolonged clogs decreases as the width of the exit increases. Second, the occurrence of prolonged clogs cannot be eliminated by adopting a smaller time step size or updating the positions of agents sequentially. Third, a decrease in T in the GCVM leads to smaller distance between agents, which corresponds to a behavior with a higher level of motivation. Meanwhile, decreasing T reduces the space available for agents to resolve clogs, which increases the number of prolonged clogs. This is in accordance with the fact that clogging is more likely to occur in scenarios with a higher level of motivation. Fourth, reducing the degree of freedom in the possible directions in which agents will move can reduce or even eliminate the occurrence of prolonged clogs. For instance, this can be facilitated by the queuing behavior in figure. 11(a) as well as by locating the exit adjacent to the lower horizontal wall of the moving area. Finally, when the ratio between the width of the exit and the radius of agents increases, the number of prolonged clogs decreases.

Acknowledgments

The authors are grateful to the HGF Knowledge-transfer project under Grant No. WT-0105. Qiancheng Xu thanks the funding support from the China Scholarship Council (Grant NO. 201706060186).

References

[1] Iker Zuriguel. Invited review: Clogging of granular materials in bottlenecks. *Papers in Physics*, 6:060014–060014, 2014.

[2] Roberto Arévalo and Iker Zuriguel. Clogging of granular materials in silos: effect of gravity and outlet size. *Soft Matter*, 12(1):123–130, 2016.

[3] RC Hidalgo, C Lozano, I Zuriguel, and A Garcimartín. Force analysis of clogging arches in a silo. *Granular Matter*, 15(6):841–848, 2013.

[4] Martin van Hecke. Jamming of soft particles: geometry, mechanics, scaling and isostaticity. *Journal of Physics: Condensed Matter*, 22(3):033101, 2009.

[5] Iker Zuriguel, Daniel Ricardo Parisi, Raúl Cruz Hidalgo, Celia Lozano, Alvaro Janda, Paula Alejandra Gago, Juan Pablo Peralta, Luis Miguel Ferrer, Luis Ariel Pugnaloni, Eric Clément, et al. Clogging transition of many-particle systems flowing through bottlenecks. *Scientific reports*, 4:7324, 2014.

[6] Alfredo Guariguata, Masika A Pascall, Matthew W Gilmer, Amadeu K Sum, E Dendy Sloan, Carolyn A Koh, and David T Wu. Jamming of particles in a two-dimensional fluid-driven flow. *Physical review E*, 86(6):061311, 2012.

[7] Damiano Genovese and Joris Sprakel. Crystallization and intermittent dynamics in constricted microfluidic flows of dense suspensions. *Soft Matter*, 7(8):3889–3896, 2011.

[8] David G Rees, Isao Kuroda, Claire A Marrache-Kikuchi, Moritz Höfer, Paul Leiderer, and Kimitoshi Kono. Point-contact transport properties of strongly correlated electrons on liquid helium. *Physical review letters*, 106(2):026803, 2011.

[9] DG Rees, H Totsuji, and K Kono. Commensurability-dependent transport of a wigner crystal in a nanoconstriction. *Physical review letters*, 108(17):176801, 2012.

[10] Celia Lozano, Geoffroy Lumay, Iker Zuriguel, RC Hidalgo, and Angel Garcimartín. Breaking arches with vibrations: the role of defects. *Physical review letters*, 109(6):068001, 2012.

[11] A Garcimartín, JM Pastor, LM Ferrer, JJ Ramos, C Martín-Gómez, and I Zuriguel. Flow and clogging of a sheep herd passing through a bottleneck. *Physical Review E*, 91(2):022808, 2015.

[12] Angel Garcimartín, Daniel Ricardo Parisi, José M Pastor, C Martín-Gómez, and Iker Zuriguel. Flow of pedestrians through narrow doors with different competitiveness. *Journal of Statistical Mechanics: Theory and Experiment*, 2016(4):043402, 2016.

[13] Juliane Adrian, Armin Seyfried, and Anna Sieben. Crowds in front of bottlenecks at entrances from the perspective of physics and social psychology. *Journal of the Royal Society Interface*, 17(165):20190871, 2020.

[14] Peter Sir Taylor. *The Hillsborough Stadium Disaster: 15 April 1989; Inquiry by the Rt Hon Lord Justice Taylor; Final Report; Presented to Parliament by the Secretary of State for the Home Department by Command of Her Majesty January 1990*. HM Stationery Office, 1990.

[15] Barbara Krausz and Christian Bauckhage. Loveparade 2010: Automatic video analysis of a crowd disaster. *Computer Vision and Image Understanding*, 116(3):307–319, 2012.

[16] Ansgar Kirchner, Katsuhiro Nishinari, and Andreas Schadschneider. Friction effects and clogging in a cellular automaton model for pedestrian dynamics. *Physical review E*, 67(5):056122, 2003.

[17] Daichi Yanagisawa, Ayako Kimura, Akiyasu Tomoeda, Ryosuke Nishi, Yushi Suma, Kazumichi Ohtsuka, and Katsuhiro Nishinari. Introduction of frictional and turning function for pedestrian outflow with an obstacle. *Physical Review E*, 80(3):036110, 2009.

[18] Michael Fischer, Gaspard Jankowiak, and Marie-Therese Wolfram. Micro-and macroscopic modeling of crowding and pushing in corridors. *Networks & Heterogeneous Media*, 15(3):405, 2020.

[19] Christian A Yates, Andrew Parker, and Ruth E Baker. Incorporating pushing in exclusion-process models of cell migration. *Physical Review E*, 91(5):052711, 2015.

[20] Axel A Almet, Michael Pan, Barry D Hughes, and Kerry A Landman. When push comes to shove: exclusion processes with nonlocal consequences. *Physica A: Statistical Mechanics and its Applications*, 437:119–129, 2015.

[21] Anton von Schantz and Harri Ehtamo. Spatial game in cellular automaton evacuation model. *Physical Review E*, 92(5):052805, 2015.

[22] Xiaoping Zheng and Yuan Cheng. Conflict game in evacuation process: A study combining cellular automata model. *Physica A: Statistical Mechanics and its Applications*, 390(6):1042–1050, 2011.

[23] Dirk Helbing, Illés Farkas, and Tamas Vicsek. Simulating dynamical features of escape panic. *Nature*, 407(6803):487, 2000.

[24] Dirk Helbing, Lubos Buzna, Anders Johansson, and Torsten Werner. Self-organized pedestrian crowd dynamics: Experiments, simulations, and design solutions. *Transportation science*, 39(1):1–24, 2005.

[25] R Cruz Hidalgo, Daniel Ricardo Parisi, and Iker Zuriguel. Simulating competitive egress of noncircular pedestrians. *Physical Review E*, 95(4):042319, 2017.

[26] Daniel Ricardo Parisi and Claudio Oscar Dorso. Microscopic dynamics of pedestrian evacuation. *Physica A: Statistical Mechanics and its Applications*, 354:606–618, 2005.

[27] Daniel Ricardo Parisi and Claudio Oscar Dorso. Morphological and dynamical aspects of the room evacuation process. *Physica A: Statistical Mechanics and its Applications*, 385(1):343–355, 2007.

[28] José M Pastor, Angel Garcimartín, Paula A Gago, Juan P Peralta, César Martín-Gómez, Luis M Ferrer, Diego Maza, Daniel R Parisi, Luis A Pugnaloni, and Iker Zuriguel. Experimental proof of faster-is-slower in systems of frictional particles flowing through constrictions. *Physical Review E*, 92(6):062817, 2015.

[29] Germán Agustín Patterson, Pablo Ignacio Fierens, F Sangiuliano Jimka, PG König, A Garcimartín, Iker Zuriguel, Luis Ariel Pugnaloni, and Daniel R Parisi. Clogging transition of vibration-driven vehicles passing through constrictions. *Physical review letters*, 119(24):248301, 2017.

[30] Qiancheng Xu, Mohcine Chraibi, Antoine Tordeux, and Jun Zhang. Generalized collision-free velocity model for pedestrian dynamics. *Physica A: Statistical Mechanics and its Applications*, page 122521, 2019.

[31] Antoine Tordeux, Mohcine Chraibi, and Armin Seyfried. Collision-free speed model for pedestrian dynamics. In *Traffic and Granular Flow'15*, pages 225–232. Springer, 2016.

[32] Mohcine Chraibi. *Validated force-based modeling of pedestrian dynamics*, volume 13. Forschungszentrum Jülich, 2012. Chapter 5.2.3.

[33] B Hein. Agent-based modelling for crowding and queuing in front of bottlenecks. Master's thesis, University of Wuppertal, 2019. Chapter 3.4.2.

[34] A Garcimartín, I Zuriguel, JM Pastor, C Martín-Gómez, and DR Parisi. Experimental evidence of the "faster is slower" effect. *Transportation Research Procedia*, 2:760–767, 2014.

[35] Iker Zuriguel, Angel Garcimartín, Diego Maza, Luis A Pugnaloni, and JM Pastor. Jamming during the discharge of granular matter from a silo. *Physical Review E*, 71(5):051303, 2005.

A.8 ARTICLE VII

Simulation of pedestrian single-lane movement by a biped model

Z. HUANG, M. CHRAIBI, AND W. SONG

PHYSICAL REVIEW E (**2018**)

Physical Review E, 98, 4, 042309, 2018
10.1103/PhysRevE.98.042309

Simulation of pedestrian single lane movement by a biped model

Zhongyi Huang[1], Mohcine Chraibi[2], Weiguo Song[1]

Abstract

In most existing pedestrian dynamic models, agents are modeled as sliding or jumping objects. As a kind of bipedal creature, however, this assumption makes it difficult to include some important human walking characteristics in the models, such as the periodicity of stepping, the adjustment of step frequency and step length, and the change of personal space within the same step cycle. To take these characteristics into consideration, a "Biped Model" is developed to simulate pedestrian locomotion by physical step rather than by time step. The model consists of two components: the stepping simulator and the adjustment of velocity for each step. Simulation results show that the velocity-density relations are consistent with the empirical data. Stable stop-and-go waves are simulated with a critical density. Furthermore, with the considering of biped movement, the lock-step phenomenon is reproduced. The model provides new possibilities to study crowd behavior while considering personal bipedal mechanics. stop-and-go waves, lock-step phenomenon

Keywords

Shape; pedestrian dynamics; Biped Model; foot movement

[1] *State key Laboratory of Fire Science, University of Science and Technology of China, Hefei 230027, China*
[2] *Institute for Advanced Simulation, Forschungszentrum Jülich, 52425 Jülich, Germany*

Contents

Introduction

Simulation of pedestrian movement has been a hot topic in recent years, because of its extensive application in safety, building design, traffic facilities design, and robotics. Many two-dimensional (2D) models have been developed to simulate the movement with different approximations of the projection of pedestrian's shape. A circle is the most commonly used shape [1–4]. The diameter of the circle is of the same width as the shoulders. In cellular atuomata (CA) models, an agent is assigned a grid of the cell. Shapes of the cell are usually square [5–7] or hexagonal [8, 9]. To make the space in CA more flexible, multigrid models [10, 11] are developed by assigning pedestrians in small 3×3 grids.

For the sake of more "accuracy", several researchers opted for different shapes to model pedestrian's volume exclusion. In Ref. [12], a pedestrian is represented by three intersecting circles. In Ref. [13], a spherocylindrical particle is adopted to naturally reproduce evacuations through narrow doors. Marroquin et al. [14] approximate the shape of a chest cross section of a human thorax by the concept of Minkowski's sum of a polygon with a disk. The "body ellipse" was suggested to be the best two-dimensional approximation of the human body [15, 16]. Based on this idea, a generalized centrifugal-force model which included an elliptical volume exclusion of humans was proposed by Chraibi et. al [17].

Although the above-mentioned models differ in precision and updating strategy, they still have something in common: pedestrians are integral and their movements are nonperiodic. Integral means a whole without elements have relative motions. Nonperiodic means no biomechanical cycles are included. In this paper, we refer to these integral and nonperiodic models as “particle models”.

As a kind of bipedal creature, humans move forward by stepping alternately with the left and right foot. This kind of movement pattern results in some unique phenomena that can hardly be investigated by particle models: lock-step phenomenon in high density crowd, tumble and stampede, the effect of music and rhythm on individual or crowd behavior, and pedestrians can still move when there is no spare space for their bodies from the top view. We think the above phenomena mainly result from the following three characteristics of biped movement: At first, walking is a periodic movement, and the expected velocity is always stable within a step cycle. If the actual velocity differs largely from the expected velocity, i.e. pushed by others, stepping on others’ feet or stepping with an unexpected drop, a pedestrian may fall down and a stampede accident may follow. Furthermore, pedestrians adjust their velocity by both step length and frequency. The walking behavior can be affected if one of them is influenced by external environment, e.g. rhythm [18]. Finally, volume exclusion of a pedestrian changes during a step because of the stretching of legs. This could be one reason for the lock-step phenomenon [19]: pedestrians squeeze the front leg into the hole left by the leg of the preceding pedestrian. For the same reason, pedestrians can still move even when there is no spare space for bodies while there is still room for feet. The former two features are also noticed by the works related to the optimal step model (OSM) [20, 21], in which pedestrians are simulated by periodically moving particles. Pedestrian movement in the OSM is natural because they have similar movement cycle and step length adaption behavior as humans. However, the model is rather simple since it does not consider the space change caused by bipedal movement during one step cycle.

To take these characteristics into consideration, a biped model is developed in this paper to simulate pedestrians by natural movements of two feet. A schematic of the model will be introduced in Section 1. Two parts in the schematic, the stepping simulator and the step level velocity adjustment will be developed in Secs. 2 and 3 respectively. Then results of the model are compared with experimental results in Section 4. Finally, the conclusion is given in Sec. 5.

1. Model Schematic

In our model, the spatial state of pedestrian i at time t is denoted by the heels and toes of both feet:

$$P_i(t) = [L_i^h(t), L_i^t(t), R_i^h(t), R_i^t(t)], \tag{1}$$

where $L_i^h = [x,y]^T$ and $L_i^t = [x',y']^T$ are the coordinates of the heel and toe of the left foot. Based on P_i, the physical space (s_i) of a pedestrian is defined as the polygon whose vertexes are the four points. Head position is the middle point of the two heels. Headway distance (d_i) is the distance between head positions of two adjacent pedestrians (see Fig. 1(a)).

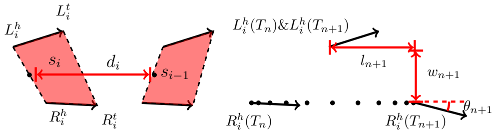

(a) (b)

Fig. 1. Spatial structure of walking. (a)Definitions of spatial state(P_i), head position and physical space (s_i). (b)Definition of step width (w), step length (l) and foot open angle (θ).

According to Boulic et al. [22], a pedestrian has two states while walking: the duration of double support (both feet in contact with the ground) and the duration of balance (one foot in contact with the ground). In our model, we assume that one foot leaves the ground and the other foot touches the ground happen at the same time. That means that, during each step, there is only one moment at which both feet are on the ground. We refer to this moment as the stand moment. The n-th stand moment is labeled T_n. Based on this assumption, the temporal structure of the model is shown in Fig. 2, in which time is discretized by the time step (δ). Stand moments are rounded to the nearest time step. The time between T_n and T_{n+1} is the duration of a step (Δ_{n+1}). Except for stand moments, all the other time steps are balance moments.

Then spatial states of a step can be visualized in Fig. 1 (b). The black arrows are the feet at stand moments and the black points are the heels at balance moments. According to the definition of a stand moment, the black arrows are also footprints. To describe the relative position relationship between footprints, three spatial quantities are defined. Supposing pedestrians are walking along the x-axis in the single lane scenario discussed in this paper, the step length (l_{n+1}) of the (n+1)-th step is the distance between heels along the x-axis, step width (w_{n+1}) is the distance between heels along the y-axis, and foot open angle (θ_{n+1}) is the angle between the front footprint and the x-axis.

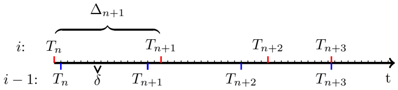

Fig. 2. Temporal structure of walking of the model.

The main idea of the model is that pedestrians plan their movement by physical steps rather than by time steps. In the biped model, velocity is only planned when a step is finished (stand moments). While at balance moments, pedestrians just execute the planned step. If two adjacent pedestrians finish a step at the same time ($t = T_{n+3}$ for both pedestrians in Fig. 2), the front pedestrian (referred to as "leader") will decide at first.

A schematic of the model is shown in Fig. 3, in which time increases in nature with the time step ($t = t + \delta$). When a step of a pedestrian is finished ($t = T_n$), velocity of the next step (v_{n+1}) will be planned by the three updating processes proposed in Section 3. With v_{n+1} we can solve the spatial states of the next step ($P_i(t), t \in (T_n, T_{n+1}]$) by the stepping simulator developed in Section 2. Note that the "Stepping simulator" is called by"Collision avoidance" in the process of velocity updating, as a result Section 2 (Stepping simulator) will be introduced before Section 3 (Updating of velocity).

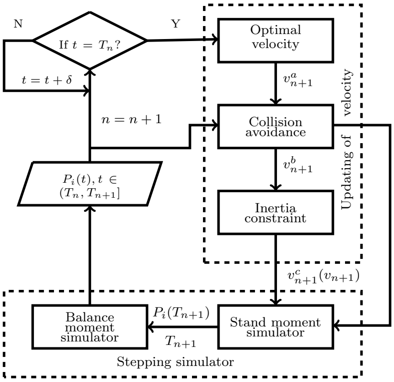

Fig. 3. Schematic of the biped model. The stand moment simulator refers to the generation of spatial state at stand moment described in Section 2. The balance moment simulator refers to the generation of a spatial state at the balance moment described in Section 2.

2. Stepping simulator

Generation of spatial state at stand moment

According to the temporal structure shown in Fig. 2, time of the new stand moment is:

$$T_{n+1} = T_n + \Delta_{n+1}. \tag{2}$$

As the spatial structure shown in Fig 1 (b), spatial state of the new stand moment is [1]:

$$P_i(T_{n+1}) = [L^h_i(T_n), L^t_i(T_n), R^h_i(T_{n+1}), R^t_i(T_{n+1})], \tag{3}$$

where

$$\begin{aligned} R^h_i(T_{n+1}) &= L^h_i(T_n) + [l_{n+1}, -w_{n+1}]^T, \\ R^t_i(T_{n+1}) &= R^h_i(T_{n+1}) + f[\cos\theta_{n+1}, -\sin\theta_{n+1}]^T. \end{aligned} \tag{4}$$

f is the foot length of the pedestrian. According to Ilayperuma et. al [23], there is the following linear dependence between f and human's height (H):

---

[1] $P_i(T_{n+1})$ can be solved in a similar manner when the left foot is stepping forward from T_n to T_{n+1}.

$$f(H) = (H - 0.79)/3.59. \tag{5}$$

In Eqs. (3) and (4) we see that the left foot is static from T_n to T_{n+1}. The heel position of the right foot $R_i^h(T_{n+1})$ is calculated by l_{n+1} and w_{n+1} at first, then the toe position is solved by $R_i^h(T_{n+1})$ and θ_{n+1}. To summarize, Δ, l, w and θ are needed to generate the movement of a new stand moment. A global human walking model was proposed by Boulic et. al [22], in which the values of l_{n+1}, w_{n+1} and θ_{n+1} are functions of the velocity (v_{n+1}) of a step[2]:

$$l(v)/g = 0.637\sqrt{v/g}, \tag{6}$$
$$w(v)/g = 0.02v/g + 0.05, \tag{7}$$
$$\theta(v) = -1.4v/g + 8.5, \tag{8}$$

where g is the thigh height. According to Kreighbaum et al. [24] g is about 53% of a pedestrian's height:

$$g(H) = 0.53H. \tag{9}$$

In the single lane scenario, the step duration (Δ) is determined when l and v are known:

$$\Delta(v) = l(v)/v = 0.637\sqrt{g/v} \tag{10}$$

In Ref. [22], the applicable velocity of Eqs. (6)-(10) is from 0.6 m/s to 2.0 m/s when $g = 1$ m. Therefore these functions can not be applied in low velocity situations (such as v = 0.17 m/s when ρ=1.97 ped/m [19]). To validate these functions, especially in low velocity situation, controlled experiments were conducted. The schematic of the experimental set up is shown in Fig. 4 (a).

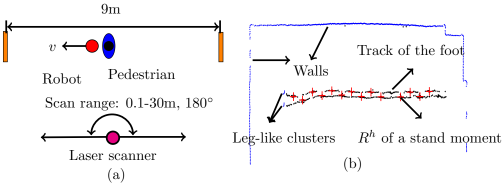

Fig. 4. (a) Schematic of experiments. (b) Results extracted from one experiment.

In each experiment, a pedestrian kept following a straight moving robot for about 9m at a constant velocity. Velocities of the robot were 0.2, 0.4, 0.6, 0.8, 1.0 and 1.2 m/s respectively. Finally, the pedestrian walked at a normal velocity without following the robot. The experiment at each velocity was repeated four times. Six male and four female university students took part in the experiments. A laser range scanner (type: HOKUYO UTM-30LX) was set at a height of 0.15 m to record the ankle movement. With the method described in Appendix A, the heel positions and the time of all stand moments could be extracted (see 4 (b)). With these data, Eqs. (6), (7) can be validated. The results are shown in Fig. 5.

According to Fig. 5 , Eq. (6) has a good agreement with the experiments, while Eq. (7) shows a trend opposite that of the experiments. We refit the relation between w and v as follows:

$$w(v)/g = -0.04v/g + 0.17. \tag{11}$$

The above relations are applicable when $v > 0.2$ m/s. Nevertheless in high density situations, some extreme slow steps may be adopted by pedestrians. According to Ref. [25], pedestrians continue to sway and shift their body weight from one leg to the other when the density is too high to force them almost to stop. Comparing to the dependence between velocity and step length, the increase in step duration is much more gradual with the decrease of velocity, and the largest duration of a step is about 1.2 s. But with Eq. (10), a step has a duration of 6.37 s when an extreme low velocity (v = 0.01 m/s) is planned. It is much larger than the maximum duration in experiments. To make the simulator more realistic at low velocity, we controlled the duration of a step by setting a cutoff time C for Δ:

---

[2] For simplicity, the subscripts of Δ, l, w, θ and v are omitted in the following discussion.

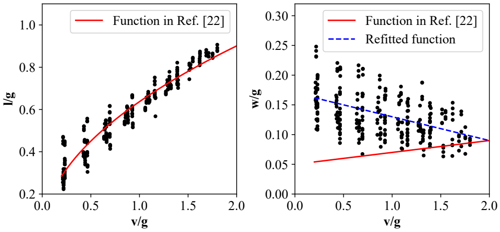

(a) (b)

Fig. 5. Relationships obtained from robot following experiments. (a) Normalized step length (l/g) as a function of normalized velocity (v/g). (b) Normalized step width (w/g) as a function of normalized velocity (v/g).

$$\Delta(v) = \begin{cases} 0.637\sqrt{g/v} & 0.637\sqrt{g/v} \le C, \\ C & 0.637\sqrt{g/v} > C. \end{cases} \tag{12}$$

Then the step-length function Eq. (6) should be adjusted accordingly to guarantee the velocity after the cut-off:

$$l(v) = v\Delta(v). \tag{13}$$

Based on the discussion above, the time and spatial state of the next stand moment can be generated by the velocity with a wide range from 0 to about 2 m/s. Equations (8), (11) and (12) should first be computed to obtain θ, w and Δ, then we calculate l with Δ obtained from Eq. (13). Finally, we solve the new stand moment by using Eqs. (2)-(4).

Generation of spatial state at balance moment

At balance moments, the space occupied by a pedestrian is changing because of the swing of the foot. Hence spatial states at balance moments are necessary in the collision avoidance process which is introduced in Section 3. The uniform accelerating model in Ref. [26] is adopted to solve for the heel position at balance moments, in which the swing foot first accelerates uniformly and then decelerates uniformly between two stand moments. In addition, we suppose that the foot opening angle changes uniformly at the same time. Based on the two assumptions, spatial states of the feet at balance moments between $P_i(T_n)$ and $P_i(T_{n+1})$ in Fig. 1 (b) can be solved by [3]:

$$P_i(t) = [L_i^h(T_n), L_i^t(T_n), R_i^h(t), R_i^t(t)], t \in (T_n, T_{n+1}), \tag{14}$$

where

$$\begin{aligned} R_i^h(t) &= \begin{cases} R_i^h(T_n) + 2t'^2(R_i^h(T_{n+1}) - R_i^h(T_n)), \\ \qquad\qquad 0 < t' \le 1/2 \\ R_i^h(T_{n+1}) - 2(1-t')^2(R_i^h(T_{n+1}) - R_i^h(T_n)), \\ \qquad\qquad 1/2 < t' \le 1 \end{cases} \\ t' &= (t - T_n)/(T_{n+1} - T_n) \\ R_i^t(t) &= R_i^h(t) + f[\cos\theta', -\sin\theta'] \\ \theta' &= \theta_n + (\theta_{n+1} - \theta_n)t'. \end{aligned} \tag{15}$$

3. Updating of velocity

With the stepping simulator developed in Section 2, the foot movement of a new step ($P_i(t), t \in (T_n, T_{n+1}]$) can be simulated with a given velocity v_{n+1}. In this section, we discuss how to update v_{n+1} according to the bipedal movements.

---

[3] By analogy it can be solved in a similar manner when the left foot is stepping forward.

Optimal velocity

At first, a pedestrian makes a temporary decision considering the headway distance (d), which is called an optimal velocity process. In the experiment presented by Jelić et al [27], the instantaneous individual measurements were adopted: Measuring the instantaneous velocity and the headway distance at each frame. When a pedestrian in our model makes a decision, she faces a similar situation with the instantaneous measurement: Determining the velocity of next step by the instantaneous headway distance. Instantaneous velocity as a function of headway distance in Ref. [27] is shown in Fig. 6.

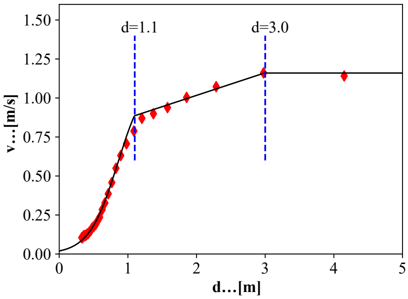

Fig. 6. Velocity as a function of headway distance. Red diamonds are data from Ref. [27], and the black lines are the fitting results.

In Ref. [27] the authors distinguished the dependence into three regimes: a free regime ($d > 3$ m), a weakly constrained regime (1.1 m $< d \leq 3$ m) and a strongly constrained regime ($d \leq 1.1$ m). Therefore, we fit the relation with a piecewise function:

$$v^a_{n+1}(d) = \begin{cases} \tanh(2.4 * (d - 0.85)/2 + 0.5) * 1.16, \\ \qquad\qquad\qquad\qquad d \leq 1.1 \\ F(0.53d - 0.58) - 0.47d + 1.41, \\ \qquad\qquad\qquad\qquad 1.1 < d \leq 3 \\ F, d > 3, \end{cases} \tag{16}$$

where F is the free walking velocity of the pedestrian.

Collision avoidance

According to Ref. [3], an optimal velocity function based model with a high updating frequency (100 Hz in Ref. [3]) is collision free if velocity is 0 m/s when the minimal spacing in front is 0 m. However, according to the definition of headway distance, d in Eq. (16) is larger than the minimal space, i.e. the distance between the backward heel of the leader and forward toe of the follower. Besides, in the biped model the updating frequency is uncertain, and could be quite low when a slow step is adopted (0.83 Hz when $\Delta = 1.2$ s). Furthermore the space of a pedestrian is dynamic for all time steps in the biped model, which also increases the possibility of collision. As a result, with the velocity obtained by Eq. (16), a collision in the next step can not be excluded. Collision avoidance is necessary after the optimal velocity process.

In Section 1 we describe the 2D space occupied by a pedestrian as a physical space s (see Fig. 1(a)). However, if we use s to conduct collision avoidance directly, pedestrians will be aggressive: Stepping close to the leader's feet as long as no collision happens. If the leader decelerates during this period, the follower may step on the leader's foot. An extension coefficient E is introduced to guarantee a safety margin. Space for collision avoidance is obtained by extending s along the x and the y axis by E. We outline the collision avoidance process in Algorithm 1, where we see that the spatial states of the next step of pedestrian i are first generated by the stepping simulator with the result of the optimal velocity function. Next, a while loop is conducted to find a velocity which can pass the collision test. The collision test process is shown in Fig. 7, in which the model checks if the two polygons of the follower and the leader overlap during the oncoming step (from T_n to T_{n+1}) with the method described in Appendix B. If a collision happens ($t = T_n + 8\delta$ in Fig. 7(a)), the velocity is rejected in the test. We reduce the velocity by 0.05 m/s each time until we obtain a velocity that can pass the test. In Fig. 7(b), no collision happens when the velocity is reduced to 0.27 m/s, which is the result of the collision avoidance process: v^b_{n+1} = 0.27 m/s.

Algorithm 1 Collision avoidance process

```
Input: spatial states of the leader $P_{i-1}$, result of the optimal velocity $v^a_{n+1}$
Output: result of collision avoidance $v^b_{n+1}$
function CollisionAvoidance($P_{i-1}$, $v^a_{n+1}$)
    $v^b_{n+1} \leftarrow v^a_{n+1}$
    $P_i \leftarrow$ SteppingSimulator($v^b_{n+1}$)
    while CollisionTest($P_i, P_{i-1}$)==Failed do
        $v^b_{n+1} \leftarrow v^b_{n+1}$ - 0.05
        $P_i \leftarrow$ SteppingSimulator($v^b_{n+1}$)
    end while
    return $v^b_{n+1}$
end function
```

(a):v_{n+1}=0.32m/s, failure

(b):v_{n+1}=0.27m/s, success

Fig. 7. Collision test process. Black core is s, filled and empty red polygons are the extended space of the follower and the leader respectively. (a) When v_{n+1} = 0.32 m/s, collision happens at $t = T_n + 8\delta$. (b) When v_{n+1} = 0.27 m/s, no collision happens in the new step.

Inertia constraint

Due to inertia, there is a limitation of velocity change (L) between two steps. We estimate the value of L by free accelerated walking. For example, when $L = 0.4$ m/s, $F = 1.29$ m/s four steps are needed to accelerate to F, i.e. v_1 = 0.4 m/s, v_2 = 0.8 m/s, v_3 = 1.2 m/s, v_4 = 1.29 m/s. The trajectory of the head position within the four steps is the free acceleration trajectory of the the biped model. According to the experimental study in Ref. [28], the acceleration process can be described as a nonuniformly accelerating movement. The acceleration at a specific v is $a = (F - v)/\tau$, where $\tau = 0.5$ s is the relaxation time. With the function, we can obtain the free acceleration trajectory of experiment. Five trajectories are simulated in the biped model by setting L = 0.4, 0.6, 0.8, 1.0 and 1.2 m/s respectively. By comparing the length of the five trajectories with the length of experiment trajectory, we find that the deviation of length is minimal when L = 0.8 m/s. As a result, 0.8 m/s is the value of L in the Biped Model. Restricting the result of collision avoidance by L is the final velocity of the new step:

$$v_{n+1} = v^c_{n+1} = \begin{cases} v_n - L & v^b_{n+1} - v_n < -L \\ v^b_{n+1} & |v^b_{n+1} - v_n| \leq L \\ v_n + L & v^b_{n+1} - v_n > L. \end{cases} \tag{17}$$

4. Results

With the stepping simulator and the velocity updating method, biped movement can be simulated in the single lane scenario. In this section, we evaluate the model by comparing the simulation results with experiments. Descriptions and values of the parameters used in the model are listed in Table 1. To simulate the differences between individuals, the parameters are normally distributed. The values of C, F and L are already specified in Secs. 2 and 3. The value of E is discussed later. Except for the five parameters listed in the table, all other definitions are dependent variables.

Table 1. Descriptions and values of parameters in Biped Model. N(μ, σ) indicates that the parameter is normally distributed in a crowd with mean value (μ) and standard deviation (σ).

Parameter	Description	Value	Unit
H	height of pedestrian	N(1.70, 0.05)	m
C	max duration of a step	N(1.20, 0.05)	-
F	free walking velocity	N(1.29, 0.05)	m/s
E	extension coefficient of s	To be determined	-
L	limitation of velocity change	N(0.80, 0.03)	m/s

The scenario of the following simulations consists of uniformly distributed pedestrians walking in a 10 m corridor with periodic boundary conditions. The time step δ is 0.04 s. All pedestrians stand still at the beginning and a pedestrian is chosen randomly to make the first step with a random foot. Others make the first step by trying with two feet, and choosing the foot to make velocity of the first step larger. If the velocities are the same in the two trails, the foot to conduct the first step is chosen randomly. Each simulation lasts 4000 time steps (160 s). Nineteen simulations with densities ranging from 0.2 to 2.0 ped/m are conducted five times each.

Fundamental diagram

During the simulation we find that the velocity is not stable at the beginning of a simulation. Hence the average velocity of each simulation is computed after 80 s. The average value (μ) and standard deviation (σ) of the five repeated simulations at each density are compared in Fig. 8 with the experimental results of Ref. [27] .

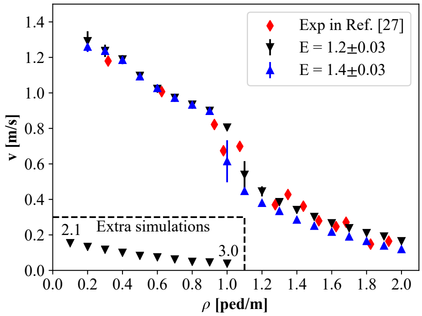

Fig. 8. Fundamental diagram of experiments and simulations. The points are μ of velocities in five repeated simulations, and the vertical lines are σ of velocities.

From the figure we see that velocities with different E are nearly the same when density is < 1.0 ped/m. However, when density grows, $E = 1.2 \pm 0.03$ leads to a better fit. Velocities with $E = 1.4 \pm 0.03$ in the simulation are always less than in experiments. This can be explained by the fact that, with larger E, pedestrians need a larger walking space. Considering the good agreements between experiments and simulations, 1.2 ± 0.03 is set as the value of E. Benefiting from the accurate description of space, pedestrian movement can be simulated at quite a high density in the biped model. Extra simulations are conducted with $E = 1.2 \pm 0.03$ to test the maximal applicable density of the model. As the black points shown in left bottom of Fig. 8, the average velocity declines gradually and keeps a nonzero value until 3.0 ped/m. In most particle models, the diameter of a pedestrian is usually between 0.4m and 0.5m. This means that, at this density, pedestrians already overlap with each other. Additionally, we find that there is a fast decline region (density from 1.0 to 1.2 ped/m) in both experiments and simulations.

Stop-and-go wave

Stop-and-go waves have been observed in a lot of pedestrian dynamic experiments [25, 29, 30]. By analyzing these experiments, some researchers find that there is a critical density for this phenomenon in the single-lane scenario. In data of German soldiers [30], stopping was first observed during runs with 45 pedestrians in a 26m corridor (1.73 ped/m). In French experiments [25], stop-and-go waves arise when the density is larger than 1.20 ped/m. To investigate the ability of the biped model to reproduce realistic stop-and-go waves, pedestrians' positions as a function of time in three simulations are shown in Fig. 9. At the same time, μ and σ of all pedestrians' velocities are also recorded every two seconds.

As shown in Fig. 9, stable stop-and-go waves appear when density ≥ 1.1 ped/m. The critical density in the simulation is close to that in Ref. [25]. Furthermore, we observe that small fluctuations are magnified over time at the beginning. At the

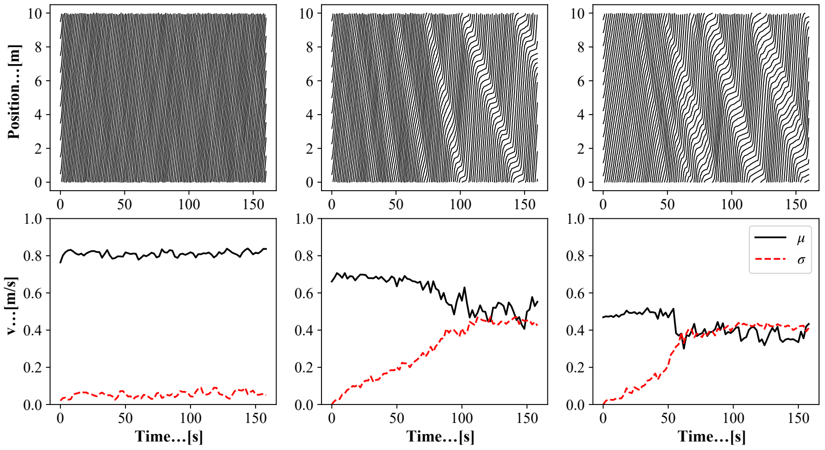

(a) (b) (c)

Fig. 9. Position, μ and σ of velocity at different densities. (a) 1.0 ped/m. (b) 1.1 ped/m. (c) 1.3 ped/m.

same time, μ decreases and σ increases. After a period of time, a stable jam emerges, and both μ and σ of velocity become stable. Generally speaking, shorter time is needed to reach the stable state in higher density. Then the findings mentioned in Section 4 can be explained: The formation of stop-and-go waves give rise to the fast decline zone.

Lock-step phenomenon

The lock-step phenomenon was noticed in Ref. [19], which can be described as pedestrians squeezing the front leg at the gap left by the leg of the leader for the full use of space at high density. This phenomenon indicates that the space a pedestrian takes up changes not only with velocity, but also with time within a step, and pedestrians can optimize their use of the space. To investigate if this phenomenon can be reproduced in our model, we use a quantitative method proposed in Ref. [25]. Φ is defined in this method to measure the synchronization among pedestrians:

$$\Phi = 2\pi(t_i - t_{i-1})/\Gamma_{i-1}, \tag{18}$$

where t_i is the start time of the follower's walking cycle (a walking cycle contains two steps), and Γ_{i-1} is the duration of the leader's walking cycle. According to the definition, if $\Phi = 0$, the two adjacent pedestrians take the same foot at the same time (synchronization). In Ref. [25], Φ was grouped by instantaneous density (ρ, inverse of the instantaneous headway distance). They observed that at large densities (beyond 1.25 ped/m), there was a peak around the phase $\Phi = 0$, which indicated the existence of the lock-step phenomenon (see Fig. 10, black dots). By using the same measurement, the result of simulations are also shown in Fig. 10.

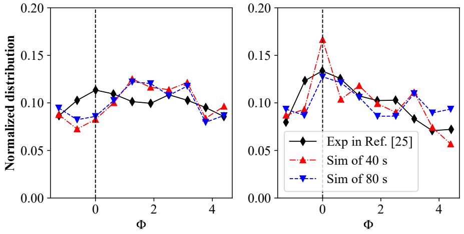

(a) (b)

Fig. 10. Normalized distributions of Φ. (a) 1.25 ped/m $< \rho \leq$ 1.50 ped/m . (b) $\rho >$ 1.50 ped/m.

According to the figure, a peak at $\Phi = 0$ only appears when $\rho > 1.5$ ped/m in simulation. With increasing simulation time, the distributions of Φ are stable in Fig. 10(a), while the peak becomes lower in Fig. 10(b). This means that, in the biped model, the lock-step phenomenon only appears when $\rho > 1.5$ ped/m and the phenomenon disappears gradually with increasing simulation time. The fading of lock steps in a simulation can also be observed in Fig. 11, in which the first steps of most pedestrians are lock steps. As the simulation time increases, less lock steps are observed. This can be explained by the fact that, in the biped model, step level interactions are simulated by collision avoidance, and collisions seldom happen when $\rho \leq 1.5$ ped/m. As time passes, stop-and-go waves arise, which affects the lock-step mechanism. Pedestrians in the model are unable to adjust their step frequency to catch the leader's step while leaving a jam. As a result, the peak at $\Phi = 0$ becomes lower.

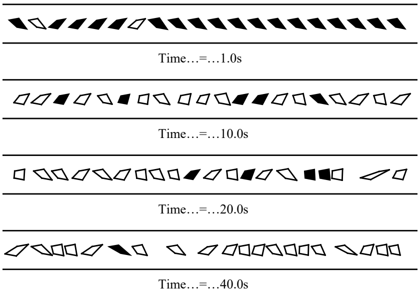

Fig. 11. Evolution of lock-step when density=2.0 ped/m. Filled polygons are lock-steps and empty polygons are non-lock steps.

5. Discussion and outlook

Modeling of pedestrian movement was divided by a top-down approach into strategic, tactical and operational levels [31]. Seitz et. al [21] pointed out that an inaccurate model of lower level corrupted the results on higher levels. In this paper we provide a realistic model at the underlying level. To guarantee the accuracy, most processes in the biped model are based on experiments data: Generating of stand moment movement is based on the empirical equations in Ref. [22], studies of step frequency in Ref. [25], and our robot following experiments. The swing movement model [26] is also derived from experiments. Updating of velocity is based on the instantaneous fundamental diagram in Ref. [27] and the accelerating studies in Ref. [28].

With these experimental data, natural foot movements are simulated and the characteristics mentioned in Sec. are included: Pedestrian movement is periodic, pedestrians adjust both step frequency and step length, physical space varies during a step cycle. With the collision avoidance process, the possibility of overlap is low even when pedestrians make decisions at low frequency. If overlap still happens after the collision avoidance, that indicates that the leader may slow down sharply. The follower can not react in time, and finally step on the leader's heel. That could induce a tumble during evacuation. Meanwhile, pedestrians in the biped model can move at quite high densities (3 ped/m described in Sec. 4) as long as there is space for a foot.

Although several phenomena has been reproduced, some discrepancies with experiments can be observed: no lock-steps appear when the density is between 1.25 and 1.50 ped/m, and stop-and-go waves arise earlier than that observed in some experiments. A possible explanation is that pedestrians in this density regime may have other step level considerations, e.g. the adjustment of step frequency according to the phase of the leader, which could have a deep impact on the lock-step phenomenon and stop-and-go waves. This consideration can be clarified through further experiments in future works. Furthermore, we strive to generalize the biped model to 2D scenarios.

Acknowledgments

The authors would like to thank the Key Research and Development Program (2016YFC0802500) for support. Zhongyi Huang acknowledges funding support from the China Scholarship Council . Mohcine Chraibi acknowledges funding support from the Visiting Professor International project at the University of Science and Technology of China (Grant No. 2017B VR40).

Appendix A: Extracting bottom points from laser radar data

In each scan of the laser scanner, the raw data of both moving objects (e.g. pedestrians) and static objects (e.g. walls) can be collected (see blue points in Fig. 3 (b). At first, the static points are removed based on the distance histogram at each scanning angle [32]. Second, moving points are clustered: If the distance between two neighboring sample points is less than the threshold (5 cm), they will be classified as the same cluster. If the maximal distance between points in the cluster is similar to the diameter of the leg (10-18 cm), it will be regarded as a leg-like cluster. Centers of all leg-like clusters during the whole experiment are demonstrated by black points in the figure, according to which the black points are dense when the leg is during the support duration. Computing the local density around each black point, the point with the maximal local density is marked by the red crosses, which is also the approximate position of the heel.

Appendix B: Detecting overlap between two polygons

If any vertex in either polygon is inside the other one, the two polygons overlap. The judgment of whether a point is in a polygon is based on Franklin's PNPLOY algorithm [33]: Making a ray from the point to any direction, if the number of intersections between the ray and the edges of the polygon is even, the point is inside the polygon. Otherwise it is outside.

References

[1] Dirk Helbing and Peter Molnar. Social force model for pedestrian dynamics. *Physical review E*, 51(5):4282, 1995.

[2] WJ Yu, R Chen, LY Dong, and SQ Dai. Centrifugal force model for pedestrian dynamics. *Physical Review E*, 72(2):026112, 2005.

[3] Antoine Tordeux, Mohcine Chraibi, and Armin Seyfried. Collision-free speed model for pedestrian dynamics. In *Traffic and Granular Flow'15*, pages 225–232. Springer, Cham, 2016.

[4] Yao Xiao, Ziyou Gao, Yunchao Qu, and Xingang Li. A pedestrian flow model considering the impact of local density: Voronoi diagram based heuristics approach. *Transportation research part C: emerging technologies*, 68:566–580, 2016.

[5] Jian Ma, Wei-guo Song, Jun Zhang, Siu-ming Lo, and Guang-xuan Liao. k-nearest-neighbor interaction induced self-organized pedestrian counter flow. *Physica A: Statistical Mechanics and its Applications*, 389(10):2101–2117, 2010.

[6] Victor J Blue and Jeffrey L Adler. Cellular automata microsimulation for modeling bi-directional pedestrian walkways. *Transportation Research Part B: Methodological*, 35(3):293–312, 2001.

[7] Katsuhiro Nishinari, Ansgar Kirchner, Alireza Namazi, and Andreas Schadschneider. Extended floor field ca model for evacuation dynamics. *IEICE Transactions on information and systems*, 87(3):726–732, 2004.

[8] Biao Leng, Jianyuan Wang, Wenyuan Zhao, and Zhang Xiong. An extended floor field model based on regular hexagonal cells for pedestrian simulation. *Physica A: Statistical Mechanics and its Applications*, 402:119–133, 2014.

[9] Maria Davidich, Florian Geiss, Hermann Georg Mayer, Alexander Pfaffinger, and Christian Royer. Waiting zones for realistic modelling of pedestrian dynamics: A case study using two major german railway stations as examples. *Transportation Research Part C: Emerging Technologies*, 37:210–222, 2013.

[10] Weiguo Song, Xuan Xu, Bing-Hong Wang, and Shunjiang Ni. Simulation of evacuation processes using a multi-grid model for pedestrian dynamics. *Physica A: Statistical Mechanics and its Applications*, 363(2):492–500, 2006.

[11] Shuchao Cao, Weiguo Song, Wei Lv, and Zhiming Fang. A multi-grid model for pedestrian evacuation in a room without visibility. *Physica A: Statistical Mechanics and its Applications*, 436:45–61, 2015.

[12] Paul A Langston, Robert Masling, and Basel N Asmar. Crowd dynamics discrete element multi-circle model. *Safety Science*, 44(5):395–417, 2006.

[13] RC Hidalgo, DR Parisi, and I Zuriguel. Simulating competitive egress of noncircular pedestrians. *Physical Review E*, 95(4):042319, 2017.

[14] Fernando Alonso-Marroquin, Jonathan Busch, Coraline Chiew, Celia Lozano, and Álvaro Ramírez-Gómez. Simulation of counterflow pedestrian dynamics using spheropolygons. *Physical Review E*, 90(6):063305, 2014.

[15] John J Fruin. *Pedestrian planning and design*. New York: Metropolitan Association of Urban Designers and Environmental Planners, New York, 1971.

[16] Jake L Pauls. Suggestions on evacuation models and research questions. In *Conference Proceedings of the 3rd International Symposium on Human Behaviour in Fire*, London, 2004.

[17] Mohcine Chraibi, Armin Seyfried, and Andreas Schadschneider. Generalized centrifugal-force model for pedestrian dynamics. *Physical Review E*, 82(4):046111, 2010.

[18] Daichi Yanagisawa, Akiyasu Tomoeda, and Katsuhiro Nishinari. Improvement of pedestrian flow by slow rhythm. *Physical Review E*, 85(1):016111, 2012.

[19] Armin Seyfried, Bernhard Steffen, Wolfram Klingsch, and Maik Boltes. The fundamental diagram of pedestrian movement revisited. *Journal of Statistical Mechanics: Theory and Experiment*, 2005(10):P10002, 2005.

[20] Isabella von Sivers and Gerta Köster. Dynamic stride length adaptation according to utility and personal space. *Transportation Research Part B: Methodological*, 74:104–117, 2015.

[21] Michael J Seitz and Gerta Köster. Natural discretization of pedestrian movement in continuous space. *Physical Review E*, 86(4):046108, 2012.

[22] Ronan Boulic, Nadia Magnenat Thalmann, and Daniel Thalmann. A global human walking model with real-time kinematic personification. *The visual computer*, 6(6):344–358, 1990.

[23] I Ilayperuma, BG Nanayakkara, and KN Palahepitiya. A model for reconstruction of personal stature based on the measurements of foot length. *Galle Medical Journal*, 13(1):6–9, 2008.

[24] E Kreighbaum and KM Barthels. Biomechanics-a qualitative approach for studying human movement, 1996.

[25] Asja Jelić, Cécile Appert-Rolland, Samuel Lemercier, and Julien Pettré. Properties of pedestrians walking in line. ii. stepping behavior. *Physical Review E*, 86(4):046111, 2012.

[26] Woojin Chung, Hoyeon Kim, Yoonkyu Yoo, Chang-Bae Moon, and Jooyoung Park. The detection and following of human legs through inductive approaches for a mobile robot with a single laser range finder. *IEEE transactions on industrial electronics*, 59(8):3156–3166, 2012.

[27] Asja Jelić, Cécile Appert-Rolland, Samuel Lemercier, and Julien Pettré. Properties of pedestrians walking in line: Fundamental diagrams. *Physical Review E*, 85(3):036111, 2012.

[28] Mehdi Moussaïd, Dirk Helbing, Simon Garnier, Anders Johansson, Maud Combe, and Guy Theraulaz. Experimental study of the behavioural mechanisms underlying self-organization in human crowds. *Proceedings of the Royal Society of London B: Biological Sciences*, 276(1668):2755–2762, 2009.

[29] Andreas Schadschneider, Wolfram Klingsch, Hubert Klüpfel, Tobias Kretz, Christian Rogsch, and Armin Seyfried. Evacuation dynamics: Empirical results, modeling and applications. In *Extreme Environmental Events*, pages 517–550. Springer, New York, NK, 2011.

[30] Armin Seyfried, Maik Boltes, Jens Kähler, Wolfram Klingsch, Andrea Portz, Tobias Rupprecht, Andreas Schadschneider, Bernhard Steffen, and Andreas Winkens. Enhanced empirical data for the fundamental diagram and the flow through bottlenecks. In *Pedestrian and Evacuation Dynamics 2008*, pages 145–156. Springer, Berlin, Heidelberg, 2010.

[31] Serge P Hoogendoorn and Piet HL Bovy. Pedestrian route-choice and activity scheduling theory and models. *Transportation Research Part B: Methodological*, 38(2):169–190, 2004.

[32] Xiaowei Shao, Huijing Zhao, Katsuyuki Nakamura, Kyoichiro Katabira, Ryosuke Shibasaki, and Yuri Nakagawa. Detection and tracking of multiple pedestrians by using laser range scanners. In *Intelligent Robots and Systems, 2007. IROS 2007. IEEE/RSJ International Conference on*, pages 2174–2179. IEEE, 2007.

[33] W Randolph Franklin. Pnpoly-point inclusion in polygon test. *Web site: http://www. ecse. rpi. edu/Homepages/wrf/Research/Short_Notes/pnpoly. html*, 2006.

A.9 ARTICLE VIII

Investigation of Voronoi diagram based direction choices using uni- and bi-directional trajectory data

---

Y. XIAO, M. CHRAIBI, Y. QU, A. TORDEUX, AND Z. GAO

PHYSICAL REVIEW E (**2018**)

Physical Review E, 97(5):052127, 2018
10.1103/PhysRevE.97.052127

Investigation of Voronoi diagram based Direction Choices Using Uni- and Bi-directional Trajectory Data

Yao Xiao[1], Mohcine Chraibi[2], Yunchao Qu[1], Antoine Tordeux[3], Ziyou Gao[1]

Abstract
In a crowd, individuals make different motion choices such as "moving to destination", "following other pedestrians", and "making a detour". For the sake of convenience, the three direction choices are called destination direction, following direction and detour direction, respectively. In this work it is found that the shape characteristics of Voronoi diagrams are used to define these featured direction choices. More specifically, the direction to a neighboring Voronoi node could be considered as a potential "detour" direction, whereas the direction perpendicular to a Voronoi link could be regarded as a potential "following" direction. A pedestrian's cell is generally surrounded by several alternative nodes and links, therefore the optimal detour and following direction are determined by considering related factors such as e.g. deviation. The last direction we define is the destination direction, which is directly pointing to the goal at every time step. In order to assess the above-defined directions, the empirical trajectory data in both uni- and bi-directional flow experiments are extracted. A time series method considering the step frequency is used to reduce the "swaying" in the original trajectories, which might disturb the recognition of the actual forward direction. The deviations between the empirical velocity direction and the basic directions are investigated, and each velocity direction is classified into a basic direction or regarded as an "inexplicable" direction according to the degree of deviation. The analysis results show that each basic direction could be a potential direction choice for pedestrian. The combination of the three basic directions could cover most empirical velocity direction choices in both uni- and bi-directional flow experiments.

Keywords
Model

[1] *School of Traffic and Transportation, Beijing Jiaotong University, 100044 Beijing, China*
[2] *Jülich Supercomputing Centre, Forschungszentrum Jülich, 52425 Jülich, Germany*
[3] *School of Mechanical Engineering and Safety Engineering, University of Wuppertal, 42119 Wuppertal, Germany*

Contents

Introduction

With the growing frequency of crowd activities, the investigation of pedestrian dynamics is attracting more attention. Understanding the principles of pedestrian motion is beneficial to the planning and designing of public facilities, as well as the

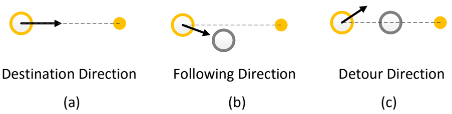

Figure 1. Illustration of pedestrian motion direction choices. The dashed circles represent the pedestrian, and the solid dots represent the target of pedestrian.

schedule and organization of pedestrian crowds. Data analysis and simulation [1] are important methods for the understanding of pedestrian dynamics, and among them, the simulation method is considered to have many advantages such as low cost and high safety.

Typical crowd motion modeling methods include force based models [2, 3] and cellular automata models [4, 5]. In force based models, pedestrians are regarded as physical particles, and the Newton's second law is applied. The sum of driving force and interaction force lead to the reaction of pedestrian motion. In cellular automata models, space is divided into discrete cells, and each cell would be occupied by one or several pedestrians. Based on specific rules, the pedestrian jumps from one cell to another to simulate the motion of crowd dynamics.

Another modeling approach is the cognitive behavior method [6, 7, 8]. The idea of this approach is to recognize the potential motion strategies in velocity choices and formulate the reasonable motion heuristics. A pedestrian normally has several different motion strategies such as maintaining the current velocity or making a turn. In [7], a discrete choice framework for pedestrian walking behaviors is proposed. The velocity direction choice has been divided into several radial cones according to the deviation. Three speed choices, i.e., "keep the same speed",“ slow down", and "acceleration" are proposed. In [8], the motion strategies are classified into four kinds, step or wait heuristic, tangential evasion heuristic, sideways evasion heuristic, and follower heuristic. The pedestrian will follow different heuristics depending on exact situations. On one hand, an advantage of these models is the convenience for considering the intelligent behaviors of a pedestrian. On the other hand a core problem for this approach is the definition and cognition of the different pedestrian behaviors.

Voronoi diagram [9, 10] is considered to have potential in both understanding pedestrian behavior [11, 12] and modeling pedestrian dynamics [13]. The Voronoi diagram is a partitioning of a plane into regions based on distance to points in a specific subset of the plane. Each region contains all the points closer to the related particle than to others. Due to its special geometric features, the Voronoi diagram has been applied in many fields, e.g., networking [14, 15] and biology [16]. Also, motion planning is also a wide-used area for Voronoi diagram. In autonomous robot navigation [17, 18, 19], the Voronoi diagram is used to find feasible routes among obstacles. In pedestrian crowd experiments [12, 11, 20], the geometry features of Voronoi cell is used to calculate the local density of pedestrian. The method is capable of obtaining a fundamental diagram with fewer fluctuations. Concerning the modeling of pedestrian dynamics [13], the Voronoi diagram of pedestrians is also introduced. According to three characteristic directions, i.e., destination direction, detour direction, and fine-tuning direction, a pedestrian recognition process is formulated for pedestrian motion. The simulation results show good agreement with the empirical fundamental diagram.

In this work, based on the features of Voronoi diagram, three basic direction choices are introduced and defined. It is noted that the three basic direction choices proposed in this paper are a little bit different from the formal definitions [13], mainly the following direction takes place of the fine-tuning direction. The combination of destination direction, following direction and detour direction is believed to have a better performance in realizing the pedestrian behaviors. To investigate the effects of the basic directions, the empirical trajectory data in both uni- and bi-directional flow experiments are introduced and smoothed. Analyses from different aspects are presented in the text to explore the potential of the single basic direction, as well as the combination of the basic directions.

The rest of the paper is organized as follows. Section 2 presents the definitions of the basic directions and an assessment method based on empirical data. In section 3, the setting of the trajectory experiments is introduced, and a smooth method is used to reduce the swaying in original trajectories. In section 4, the effects of the basic directions are investigated with the smoothed trajectories. Section 5 gives the conclusion and the prospect.

1. Basic direction choice and assessment method

In pedestrian crowds, three kinds of directions choices could be observed, which are "moving to the destination" "following another pedestrian" and "making a detour". For the sake of convenience, the three direction choices are called ‘ destination direction’, ‘ following direction’ and ‘ detour direction’, respectively (Fig.1).

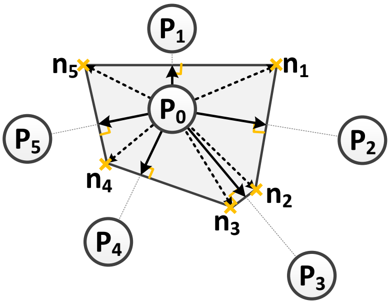

Figure 2. Potential following directions and potential detour directions.

A pedestrian normally strives for a most efficient route to the destination, and the shortest route in geometry usually corresponds to the most efficient route. Since the destination direction points to the destination and indicates the shortest route, it is defined to be the default direction choice for motion [21, 22, 23]. The following direction indicates the behavior along a neighboring pedestrian who has a similar motion pattern. The following direction might deviate from the shortest route, but most conflicts and collisions will be undertaken by the leader pedestrian while the follower is going to own a more comfortable walking environment. The detour direction generally deviates from the shortest route and points to an intermediate area between neighboring pedestrians. Usually, it is regarded as a regular option for the avoidance of conflicting/congestion area and the achievement of an overall efficient route.

1.1 Voronoi diagram based directions

The shape characteristics of Voronoi diagram inspires two kinds of basic direction choices for a pedestrian. Fig.2 shows a Voronoi cell of pedestrians to indicate the two kinds of directions. First, the direction pointing to the Voronoi node (dashed arrow) corresponds to the intermediate space between two neighboring pedestrians. Thus, it is defined as a potential detour direction. In this case, the pedestrian P_0 has five potential detour directions which are pointing to the five Voronoi nodes, n_1, n_2, n_3, n_4, n_5, respectively. Second, the direction perpendicular to the Voronoi links (solid arrow) corresponds to the neighboring pedestrians. Thus, it is defined as a potential following direction. In this case, the pedestrian P_0 has five potential following directions which are perpendicular to the Voronoi links. It is noted that these directions also point to the five neighboring pedestrians P_1, P_2, P_3, P_4, P_5 according to the properties of Voronoi diagram.

In this section, an evaluation function with respect to the pedestrian states is proposed to determine the optimal following and detour direction. The optimal following target is determined by, $P^*_{\text{following}} = \underset{P_j \in M_i}{\operatorname{argmax}}((\vec{e}_i \cdot \vec{e}_j) \times (\vec{e}_i \cdot \vec{e}_{ij}))$, where M_i represents the set of neighbors of pedestrian P_i, $\vec{e}_i$ and $\vec{e}_j$ are the unit vector of velocity of pedestrian P_i and its following target P_j, respectively. $\vec{e}_{ij}$ is the unit vector of the direction from pedestrian P_i to pedestrian P_j. Similarly, the optimal detour objective is determined by, $n^*_{\text{detour}} = \underset{n_j \in N_i}{\operatorname{argmax}}(\vec{e}_i \cdot \vec{e}_{ij}/\rho_j)$, where N_i represents the set of the Voronoi nodes of pedestrian P_i. ρ_{n_j} is the local density of Voronoi node n_j. In this paper, the local density of a Voronoi node is defined as the average value of the densities of its related pedestrians, and the detailed definition of local density could be found in Appendix.A.

The determination of destination may be a difficult problem in pedestrian simulation [7]. In some cases, the destination is changing with time and events. For example, in a shopping mall, the destination is easy to make a change along with the newfound attractors. In some cases, a pedestrian might lack a specific destination. For instance, some pedestrians might lose mind about the destination in an emergent evacuation situation. In this work, the destination is known and set up at first. As a result, the three basic direction choices, i.e. destination direction, following direction, and detour direction, are indicated in Fig.3. The destination of pedestrian P_i points to the target D_i, so the destination direction for pedestrian P_i is given as, $\vec{e}^*_{\text{dest}} = \overrightarrow{P_iD_i}/||\overrightarrow{P_iD_i}||$. The optimal following objective is obtained as P^*_{follow} with the method introduced in the last part, so the following direction is given as $\vec{e}^*_{\text{follow}} = \overrightarrow{P_iP^*_{\text{follow}}}/||\overrightarrow{P_iP^*_{\text{follow}}}||$. The optimal detour Voronoi node is obtained as n^*_{detour} with the method just introduced, so the detour direction is given as $\vec{e}^*_{\text{detour}} = \overrightarrow{P_in^*_{\text{detour}}}/||\overrightarrow{P_in^*_{\text{detour}}}||$.

1.2 Direction judgment method

A direction judgment method is proposed in this section to classify the empirical velocity data. The empirical velocity direction data is determined as a basic direction or an inexplicable direction based on the deviation between them. The deviation from the

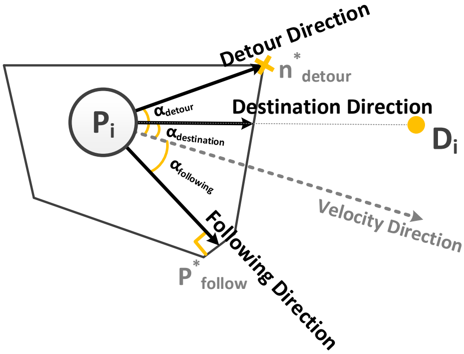

Figure 3. Voronoi diagram based direction choices.

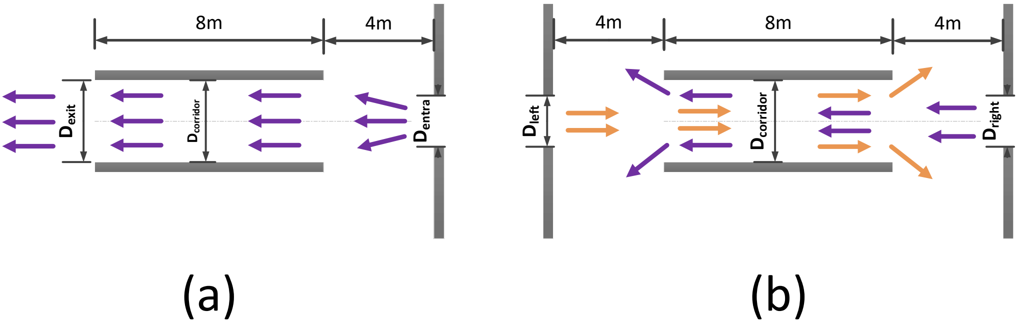

Figure 4. (a)Sketch map of the uni-directional flow experiment. (b)Sketch map of the bi-directional flow experiment.

velocity direction to the destination direction, following direction and detour direction, are calculated and called as destination deviation, $\alpha_{\text{destination}}$, following deviation, $\alpha_{\text{following}}$ and detour deviation α_{detour}, respectively (Fig.3). α_0 is a threshold value for the judgment of a basic direction, and $\alpha_{\text{min}} = \min_(\alpha_{\text{destination}}, \alpha_{\text{following}}, \alpha_{\text{detour}}, \alpha_0)$. As a result, the classification of the velocity direction is given as,

$$C = \begin{cases} \text{Destination} & \text{direction}, \quad \alpha_{\text{min}} = \alpha_{\text{destination}} \\ \text{Following} & \text{direction}, \quad \alpha_{\text{min}} = \alpha_{\text{following}} \\ \text{Detour} & \text{direction}, \quad \alpha_{\text{min}} = \alpha_{\text{detour}} \\ \text{Inexplicable} & \text{direction}, \quad \alpha_{\text{min}} = \alpha_0 \end{cases} .$$

Note that α_0 is critical for the classification, and it should not be too large or too small. With a strict value, for instance, $\alpha_0 = \pi/180$, very few empirical data could be classified as a basic direction. With a loose value, for instance, $\alpha_0 = \pi/3$, some deflecting data might be classified as basic directions. A more detailed analysis could be found in Appendix.B, and in this case, α_0 is set to $\pi/18$.

2. Experimental data

In this section, the data from uni- and bi-directional flow experiments [12, 24] were used for the investigation of Voronoi diagram based direction choices.

The geometry configurations of the uni- and bi-directional flow experiments are shown in Fig.4. In the uni-directional flow experiments (Fig.4(a)), the length of corridor is 8m (constant), and the width of the corridor, i.e., D_{corridor}, is changing among 1.8m, 2.4m and 3m. In these experiments, the width of the exit D_{exit} is equal to the width of corridor D_{corridor}, so there is no

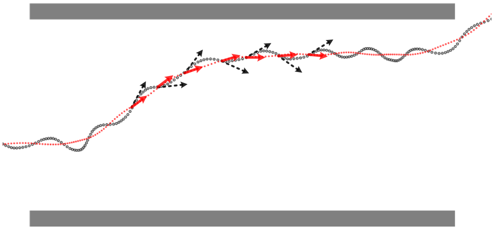

Figure 5. An example of the original trajectories and the smoothed trajectories (color). The black points represent the original trajectory data and the red points represent the smooth trajectory data. The red and black arrows represent the direction based on the original and smoothed trajectories.

bottleneck in the corridor and the destination of pedestrian is easy to be obtained. According to the specific features of corridor experiments, the destination direction is defined to be parallel to the wall of corridor and points to the opposite end of the corridor. At the initial stage, the pedestrians are waiting outside the entrance. Through the adjustment of entrance width D_{entra}, the uni-directional pedestrian flow into the corridor can be controlled. In the bi-directional flow experiments (Fig.4(b)), the length of corridor is 8m (constant), and there are two values for the corridor width D_{corridor} which are 3m and 3.6m, respectively. The pedestrians are waiting outside the entrance at the two sides, and the bi-directional pedestrian flow into the corridor is able to be controlled by the width of entrance D_{left} and D_{right}. It is noted that there is a buffer zone (length = 4m) between the entrance and the corridor in both uni- and bi-directional flow experiments. The buffer zone is used to minimize the effect of entrance bottleneck so that the pedestrians could be homogeneously distributed on the total width of the corridor.

In the experiments, the crowd motions are recorded by the cameras mounted on the ceiling, and the location of the head of a pedestrian is obtained at each frame step. An example of the original trajectories is shown as the black points in Fig.5. The trajectories pattern is similar to an oscillation curve, and the zigzag feature in the trajectories is usually called swaying phenomenon [25, 26, 27]. The phenomenon is caused by the step walking behaviors of the pedestrian. A pedestrian naturally needs to shift the body to maintain balance during walking. Thus, the body especially the head has to sway left and right with different foot striking the ground, and it leads to the zigzag trajectories. Here, the velocity direction is determined as the direction from its current location to the location of the next time step, and the original trajectories based velocity directions (dashed arrow) fluctuate frequently and highly in Fig.5. As a result, due to the swaying phenomenon, the real forward direction of a pedestrian is likely to be covered in the original trajectories and it might terribly affect the judgment of the direction choice classification. To exclude the influence of swaying phenomenon, a time series method is introduced. The original location of pedestrian at time step t is assumed as $\vec{l_t} = (x_t, y_t)$, and the smoothed location is given as,

$$\vec{l'_t} = (\sum_{i=t-k}^{t+k} x_i/(2k+1), \sum_{i=t-k}^{t+k} y_i/(2k+1)),$$

where k is a free parameter, and it is found work best when corresponds to the step length (Appendix.B). To efficiently reduce the swaying effect, the step frequency is considered and k is given by, $k = f_c/f_s + 1$. Where f_c is the frames per second of the camera, and f_c = 16 (1/s) in our uni- and bi-directional flow experiments. The step frequency f_s is estimated by [27], $f_s = 1.72 \cdot bv^p/h$, where h is the height of pedestrian, v is the value of current speed, b and p are two dimensionless parameters, b = 1.57 and p = 0.5.

Based on the smoothed trajectories, the specific velocity direction (solid arrow) is determined as shown in Fig.5. The fluctuations of the velocity direction caused by the swaying trajectories are reduced significantly. The set of velocity direction data in uni- and bi-directional flow experiments formulate the basis of analysis in the work.

3. Results Analysis

In this section, the empirical pedestrian velocity data in both uni- and bi- directional flow experiments are used for the investigation of the Voronoi diagram based basic direction. According to the direction judgment method, the empirical direction data have been classified into four classes, the three basic directions (destination direction, following direction, detour direction) and the inexplicable direction. In Fig.6, the trajectories are shown with different colors to represent the direction classification, and the qualitative direction pattern in corridor is found. Among them, the blue color represents the defined destination direction, the green color represents the defined following direction, the red color represents the defined detour direction and the black color represents the inexplicable direction.

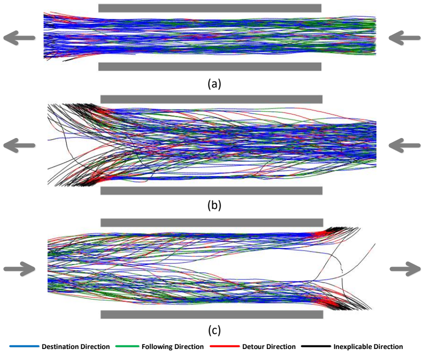

Figure 6. Featured trajectories in uni and bi-directional flow (color). The trajectories are colored with blue, green, red and black to represent destination, following, detour and inexplicable direction, respectively. (a) Pedestrian trajectories of uni-directional flow experiment. (b) Pedestrian trajectories from right to left in bi-directional flow experiment. (c) Pedestrian trajectories from left to right in bi-directional flow experiment.

Fig.6(a) shows the featured pedestrian trajectories in uni-directional flow experiment. In the experiment, entrance width equals to 0.7m and 111 pedestrians enter the corridor from the right end to the left end. In general, the destination direction and following direction play the dominant roles, and the detour direction and inexplicable direction are limited to a small percentage. Both the destination direction and following direction are found at the entrance(right) side of corridor, while the destination direction plays a much more significant role at the exit(left) side and very few directions are still obtained as the following direction. It is noted that the pedestrians have spread to a wide width at the buffer zone. Thus, the entrance(right) side of corridor plays as a kind of bottleneck for the pedestrians, and the pedestrians are likely to prefer the following behavior to enter the bottleneck. After the entering, conflicts and obstacles are very rare in the corridor. The pedestrian just needs to move forward with the shortest route which responds to the destination direction, and the following behavior is not so required. As a result, the following directions are gradually reduced from the entrance side to the exit side.

Fig.6(b) and Fig.6(c) show the featured pedestrian trajectories to the right side and to the left side, respectively. The entrance width equals to 0.5 m and 130 pedestrians taking part in the bi-directional flow experiment. The pedestrian motion pattern to the left side and to the right side are generally not identical. In this experiment, the pedestrian flow to the left side separate quite late in the corridor, while the pedestrian flow to the right side separate early. However, the separation pattern is not so stable and it may vary among different experiments. In addition, the constitution of basic directions in the bi-directional flow experiment is more complicated than the uni-directional flow experiment, but the destination direction and following direction also play important roles especially in the center part of the corridor. At the corner of the corridor, the inexplicable direction and detour direction rises due to a special requirement of the experiment. The pedestrians are required to leave the corridor from the corner, and the required direction is usually deviating from the default destination which is parallel to the wall in our method. To maintain the simplicity of the destination setting and the validity of the data, the trajectory data at the end of the corridor are removed from our analyses.

For the quantitative features of the three basic directions, base data contains 19 uni-directional flow experiments and 18 bi-directional flow experiments which own different corridor width or entrance width [12, 24]. Angular deviation is the most direct quantitative way to measure the differences between directions. Therefore, the angular deviation between defined basic directions and empirical direction data are firstly explored. In Fig.7, the deviation distribution of the three basic directions in uni- and bi-directional flow experiments are obtained. In general, all kinds of distributions in both experiments are symmetrical and range between around -60 to 60 degrees. In the uni-directional flow experiments, the distribution of destination deviation is centered over 0 degree and spreads from about -20 to 20 degrees in the uni-directional flow experiments. The pedestrian rarely deviates a lot from the destination direction since almost no serious conflicts and obstacles exist in the uni-directional flow. Although overtaking the slow pedestrian might take place in the uni-directional flow, the pedestrian prefers to chooses a soft and gradual way to achieve it. In bi-directional flow experiments, the distribution of destination deviation is also centered over 0 degree, but the distribution spreads in a wider range, about -40 to 40 degrees. It is known that the conflicts are more common

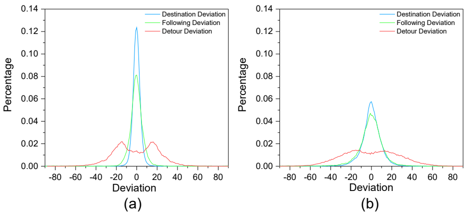

Figure 7. Distribution of deviation between current velocity direction and basic directions. (a) unidirectional flow experiment data (b)bidirectional flow experiment data.

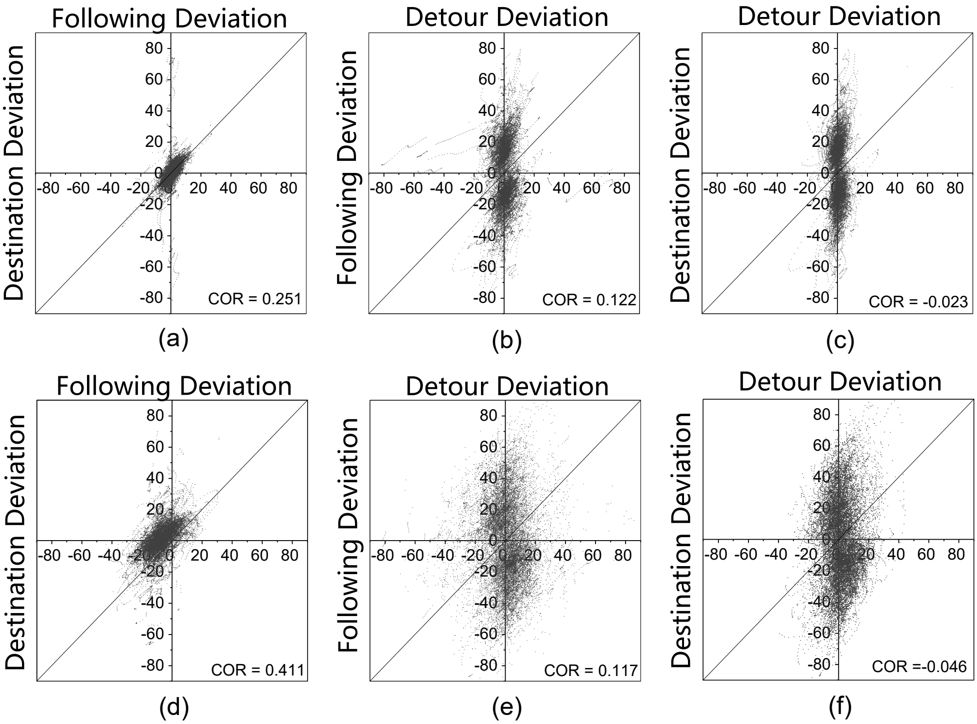

Figure 8. Correlation of deviation between basic directions. (a) and (d) are destination deviation-following deviation relation in uni- and bi-directional flow experiments, respectively. (b) and (e) are following deviation-detour deviation in uni- and bi-directional flow experiments, respectively. (c) and (f) are destination deviation-detour deviation in uni- and bi-directional flow experiments, respectively.

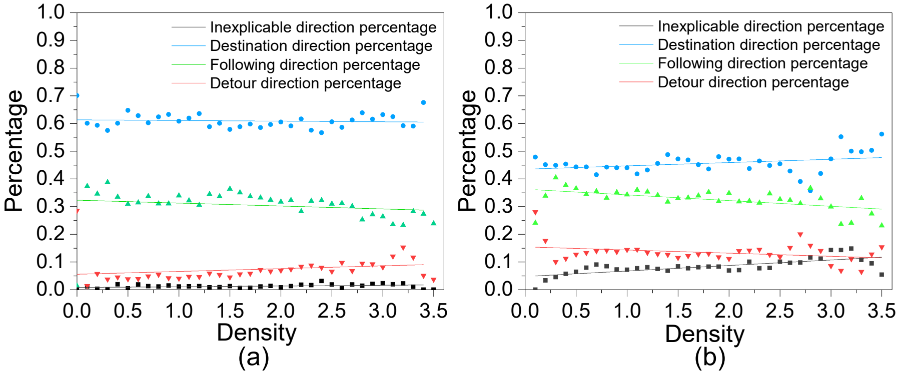

Figure 9. Percentage of basic directions in different densities (a) Basic direction percentage for uni-directional flow. (b) Basic direction percentage for bi-directional flow. Note that the density of pedestrian is obtained by a Voronoi method which is able to calculate the local density of single pedestrian, the detail definition could be found in AppendixA.

and frequent in the bi-directional flow, especially that the pedestrian has to face the oncoming pedestrian from the other side. Hence, the pedestrian has to make urgent and sharp adjustments to the current velocity to avoid these conflicts. The central tendency of destination deviation in the experiments implies that the destination direction is an significant direction choice. The distributions of following deviation are similar to the distributions of destination deviation, which are also centered over 0 degree in both uni- and bi-directional flow experiments. The following direction is also likely to be an important direction choice. The distributions of detour deviation get two peak values at about -15 and 15 degrees in both uni-directional flow and bi-directional flow. According to the characteristics of Voronoi based detour direction, its deviation to the destination direction is likely to be around 15 degrees. Meanwhile, the destination direction and following direction are the main choices by most pedestrians most of the time in corridor experiments. In conclusion, the choices for the frequently used basic directions lead to the peak values in the distribution of the detour deviation.

Table 1. Correlation coefficient between basic directions

	Dest-Following	Dest-Detour	Following-Detour
Uni-	0.251	0.122	-0.023
Bi-	0.411	0.117	-0.046

As found in Fig.7, the distributions of destination direction and following direction are quite similar. In order to investigate the correlation of basic directions, the deviation from the current velocity direction to the basic directions in uni- and bi-directional flow experiments are compared in Fig.8. Here, the Pearson correlation coefficient is introduced and applied as, $COR_{X,Y} = \sum_{i=1}^{n}(x_i - \bar{x})(y_i - \bar{y}) / \sqrt[2]{\sum_{i=1}^{n}(x_i - \bar{x})^2}\sqrt[2]{\sum_{i=1}^{n}(y_i - \bar{y})^2}$ where data set $X = (x_1, x_2, \cdots, x_n)$ and $Y = (y_1, y_2, \cdots, y_n)$ are the deviation data set of a basic direction, respectively. $\bar{x}$ and $\bar{y}$ are the mean deviation of the data set X and Y. First, the absolute value of correlation coefficient between destination deviation and detour deviation, as well as the correlation coefficient between following deviation and detour deviation are less than 0.15. It indicates that these two sets of deviations of basic directions are not strongly correlated in both uni- and bi-directional flow experiments. The absolute value of correlation coefficient between destination direction and following direction, especially in bi-directional flow, is remarkably larger than the other two kinds of coefficients. The specific value in bi-directional flow could be explained by the lane formation phenomenon. In bi-directional flow, most pedestrians would walk within a lane to obtain a comfortable walking environment, hence the destination direction is naturally agree with the following direction in the case. Therefore, there is an idea that these two directions might have no difference in the case. To test it, the null hypothesis H_0 is given as that the destination direction and following direction in bi-directional flow have no difference. A paired t-test is presented here, and the significance level is set as 0.05 and two tailed. The calculation results of 108164 pairs data show that $t = 16.781 > t_{critcal} = 1.959$, that is to say, the p-value is almost zero. Therefore, the null hypothesis H_0 is rejected. The conclusion should be the alternative hypothesis H_1 that these two kinds of direction choices have some differences in bi-directional flow.

Next, the performance of the combination of basic directions is investigated, and the percentage of different basic directions are given as Fig.9. In uni-directional flow (Fig.9(a)), more than 95% direction data are explained as the three basic directions. Among them, the destination direction plays a dominant role (around 60%). Since the motion conflicts rarely occur in uni-directional flow, pedestrians are not likely to deviate from the shortest route. Following and detour direction take up around 30% and 7% of the total data, respectively. With increasing densities, it is observed that the following percentage tends to decrease while the detour percentage tends to increase. The reduction of the personal space leads to the rising desire to obtain a more comfortable personal space, so the pedestrian is more likely to make a detour to change the current position instead of following in a more crowded situation.

In bi-directional flow (Fig.9(b)), around 90% percent direction data are explained as the three basic directions. The destination direction also plays a most important role (around 45%) in the total direction data, but the percentage is less dominating compared with the uni-directional flow data. The main reason is that the conflicts are much more frequent in the bi-directional flow compared with the uni-directional flow experiment. Thus, the detour direction grows to be a more important choice for directly dealing with the frequent conflicts. At the same time, adopting the following direction is another effective method to avoid the conflicts, and that is a critical reason for the appearance of lane formation phenomenon in the bi-directional flow. As a result, the percentage of detour direction and following direction increase in the bi-directional flow. There are two reasons for the growing of inexplicable direction percentage in the bi-directional flow. First, the pedestrian dynamics are richer in the bi-directional flow. Second, the pedestrians are required to leave the corridor from a specific corner in the bi-directional flow experiment, so the actual destination direction might differ from the original destination direction which is parallel to the wall. Adjusting the definition of destination in corridor might reduce the inexplicable percentage, but maintaining a simple definition of the destination is also useful. With increasing densities, the following direction percentage decreases and the inexplicable direction percentage increases. Similar to the uni-directional flow, the reduction of personal space is considered to be the reason for this change.

4. Conclusion and prospect

Three kinds of direction choices are found to describe the different pedestrian motion patterns. They are destination direction, i.e., the direction moving to the destination, following direction, i.e., the direction following another pedestrian, and detour direction, i.e., the direction for making a detour. The three basic directions are considered to be important direction choices in the crowd motion. Inspired by the characteristics of Voronoi diagram of pedestrians, the three kinds of basic directions are determined for each pedestrian at each time step. The empirical trajectory data in uni- and bi-directional flow experiments are used here to investigate the effects of the three directions. A time averaging method is introduced to smooth the original trajectories and obtain a reasonable forward velocity. Based on the smoothed trajectory data, the velocity direction is determined and classified into a specific basic direction whenever possible.

Based on the smoothed trajectories in uni- and bi-directional flow experiments, the features of the three basic directions are qualitatively and quantitatively investigated, including the direction pattern, the deviation distribution, the correlation between basic directions, and the percentage of different basic direction choices. It is found that the direction choice patterns in the corridor experiments are able to be recognized by the basic directions. First, different proportions of basic directions are obtained in different parts of the corridor. Second, the motion direction patterns are significantly different between uni- and bi-directional flow experiments.

The results also show that the general velocity directions could be reduced into the three kinds of basic direction choices. In addition to the three basic directions, more direction choices are still possible. For example, the detour direction is able to be classified into two categories, one for the avoidance of local collisions and another for the planning of a global optimal route. The two kinds of detour direction might point to a similar direction, but the motivations varies. Another problem for our work is the simplicity of corridor experiments. With only two kinds of destinations in the corridor, the crowd motion patterns could be quite simple. For instance, the destination and following directions are quite similar in these cases. Although these two kinds of choices are proved to be different, it raises an idea that the two kinds of directions might be merged in pedestrian motion. To completely deal with the problem, further analyses in even more complicated scenarios, e.g., bottleneck[28, 29] and evacuation situation[30, 31], are scheduled for the next-step investigation of the basic directions. A further concern is regarding the pedestrian behaviors in different density situations. A pedestrian is able to make intelligent motion choice in a low-density environment, but it would be much more difficult for the pedestrian to determine the movement in a crowded situation since the passive collision force between the pedestrians might dominate the motion. In this case, these defined direction choices might lose their effectiveness. These different combinations of basic direction choices need further empirical investigations and analyses. Besides, simulations based on the basic direction choices could be presented to explore the potentials of the different combinations, and it would be our next-step work.

The introduction of the three basic directions could inspire the modeling of pedestrian dynamics. An important problem for the pedestrian dynamics is to determine the velocity at the next time step, and the velocity determination could be divided into two procedures, velocity direction determination and speed determination [32, 33]. The three basic directions are inspired from the pedestrian cognitive heuristics, and they have the potential to summarize the general pedestrian direction choices. Based on it, determining the direction choice based on the cognitive process of a pedestrian is a promising modeling method. In [8], four

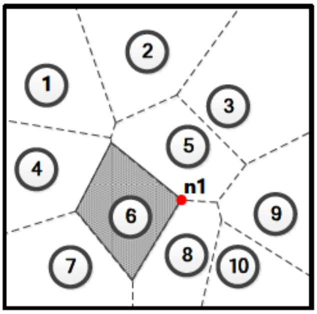

Figure 10. Voronoi diagram of pedestrians.

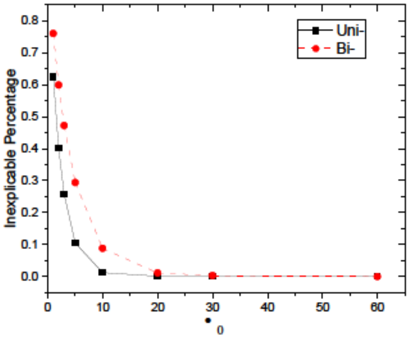

Figure 11. Relationship between α_0 and percentage of inexplicable direction. Note that α_0 is measured in degrees in the figure.

kinds of heuristics, i.e., step or wait heuristics, tangential evasion heuristic, sideways evasion heuristic, and follower heuristic are proposed to represent the different pedestrian behaviors. Similarly, a simple logit based model could be given based on the three basic direction choices. Many factors such as velocity, density and deviation could be considered into the utility function and support the choice of the logit method.

In conclusion, the investigation with Voronoi diagram based directions is a meaningful work for the pedestrian motion research. The understanding of pedestrian motion is promoted by the Voronoi diagram based directions. Also, it inspires the work for lots of fields such as the modeling of pedestrian dynamics.

Acknowledgment

A. Local density

This section contains the definitions of local density for both pedestrian and Voronoi node in the Voronoi digram of pedestrians. In Fig.10, a Voronoi digram of pedestrians is shown. There are ten pedestrian represented by the dashed circles and the Voronoi diagram is drawn based on them. The area of the Voronoi cell of pedestrian P_i is given as a_i. For instance, the Voronoi cell area of pedestrian P_6 is the shadow area which equals to a_6. In our method, the local density of pedestrian P_6 is defined as the reciprocal of the area of its corresponding Voronoi cell, $\rho_{P_6} = 1/a_6$. It makes sense since the Voronoi cell actually contains all the closest space of the pedestrian. Moreover, the local density of Voronoi node is defined as the average density of its related pedestrians, $\rho_{n_j} = \Sigma_{i=1}^{m}(\rho_{P_i})/m$. Note that the related pedestrians are those pedestrians who own this Voronoi node. For Voronoi node n_1(Fig10), its local density $\rho_{n_1} = (\rho_{P_5} + \rho_{P_6} + \rho_{P_8})/3$.

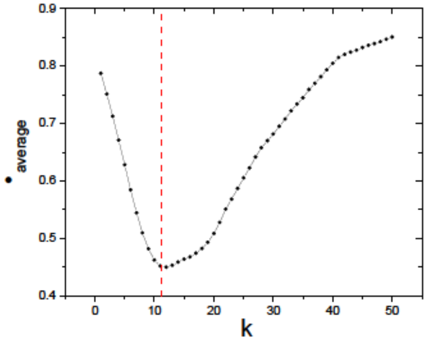

Figure 12. Relationship between smoothing steps and average direction deviation. The average step length is marked by the red dashed line

B. Sensitivity Analysis

This section contains the sensitivity analyses of both α_0 and k. The threshold value α_0 is critical for the classifications of basic directions. Fig.11 shows the relationship between α_0 and the percentage of inexplicable direction in basic direction classifications for both uni- and bi-directional flow experiments. In both experiments, the percentages of inexplicable direction decrease with the growing of α_0. Apparently, α_0 can not be limited to be too strict. A mass of empirical trajectory data might be ignored due to the swaying phenomenon and other errors. In the case of $\alpha_0 = \pi/180 = 1 degree$, only 20-30 percent trajectory data are able to be distinguished as basic directions. Also, α_0 can not be too loose. In the case of $\alpha_0 = \pi/3 = 60 degrees$, those deflecting trajectory data might be classified as basic directions, and almost 100 percent empirical trajectory data are explained. Therefore, based on the limitations of both sides, α_0 is set to $\pi/18$ in this paper.

Qualitatively, the shape of the original pedestrian trajectories is similar to a sine function due to the swaying phenomenon. The real motion direction is difficult to be obtained based on the oscillating trajectories, so a time-averaging method is proposed for the smoothness. k is a core parameter in the time-averaging method, and it represents the smooth time step. In order to achieve the smoothness of trajectories and keep the necessary velocity tendency, k is best to correspond to the period of trajectories for the smoothness. To perform the sensitivity analysis of k, a parameter δ_i is introduced. δ_i is the maximum angular deviation between current velocity direction and its adjacent velocity direction data on the set of trajectories of a pedestrian,

$$\delta_i = \{\max_x \langle \vec{v}_x, \vec{v}_i \rangle, i - j \leq x \leq i + j, x \in \mathbb{N}\}.$$

Where the adjacent velocity data parameter $j = 25$ in this section. δ_i could be used to investigate the deviation level of trajectories, in other words, the smoothing effect. $\delta_{average}$ is the average value of δ_i for all trajectory data, $\delta_{average} = \sum_{i=1}^{n} (\delta_i)/n$. $\delta_{average}$ could be used to measure the effect of different smooth parameters. As shown in Fig.12, $\delta_{average}$ firstly decreases with the growing of smooth steps and reaches a minimum value around $k = 12$. It's found that $k = 12$ basically corresponds to the calculated average step length (Fig.12) [27]. As a result, match the smoothing steps to the step length has the potential to make the results smoother.

References

[1] Andreas Schadschneider, Wolfram Klingsch, Hubert Klüpfel, Tobias Kretz, Christian Rogsch, and Armin Seyfried. *Evacuation dynamics: Empirical results, modeling and applications*, pages 3142–3176. Springer, 2009.

[2] D. Helbing and P. Molnar. Social force model for pedestrian dynamics. *Physical Review E*, 51(5):4282–4286, 1995.

[3] M. Chraibi, A. Seyfried, and A. Schadschneider. Generalized centrifugal-force model for pedestrian dynamics. *Physical Review E*, 82(4 Pt 2):046111, 2010.

[4] Victor J Blue and Jeffrey L Adler. Cellular automata microsimulation for modeling bi-directional pedestrian walkways. *Transportation Research Part B: Methodological*, 35(3):293–312, 2001.

[5] S. Nowak and A. Schadschneider. Quantitative analysis of pedestrian counterflow in a cellular automaton model. *Physical Review E*, 85(6 Pt 2):066128, 2012.

[6] Gerd Gigerenzer and Peter M Todd. *Simple heuristics that make us smart*. Oxford University Press, USA, 1999.

[7] Gianluca Antonini, Michel Bierlaire, and Mats Weber. Discrete choice models of pedestrian walking behavior. *Transportation Research Part B: Methodological*, 40(8):667–687, 2006.

[8] Michael J Seitz, Nikolai WF Bode, and Gerta Köster. How cognitive heuristics can explain social interactions in spatial movement. *Journal of The Royal Society Interface*, 13(121):20160439, 2016.

[9] Georges Voronoï. Nouvelles applications des paramètres continus à la théorie des formes quadratiques. deuxième mémoire. recherches sur les parallélloèdres primitifs. *Journal für die reine und angewandte Mathematik*, 1908.

[10] Franz Aurenhammer. Voronoi diagrams—a survey of a fundamental geometric data structure. *ACM Computing Surveys (CSUR)*, 23(3):345–405, 1991.

[11] B. Steffen and A. Seyfried. Methods for measuring pedestrian density, flow, speed and direction with minimal scatter. *Physica A-Statistical Mechanics and Its Applications*, 389(9):1902–1910, 2010.

[12] J. Zhang, W. Klingsch, A. Schadschneider, and A. Seyfried. Transitions in pedestrian fundamental diagrams of straight corridors and t-junctions. *Journal of Statistical Mechanics-Theory and Experiment*, 2011(06):P06004, 2011.

[13] Yao Xiao, Ziyou Gao, Yunchao Qu, and Xingang Li. A pedestrian flow model considering the impact of local density: Voronoi diagram based heuristics approach. *Transportation Research Part C: Emerging Technologies*, 68:566–580, 2016.

[14] Ivan Stojmenovic, Anand Prakash Ruhil, and DK Lobiyal. Voronoi diagram and convex hull based geocasting and routing in wireless networks. *Wireless communications and mobile computing*, 6(2):247–258, 2006.

[15] Nor Azlina Bt Ab Aziz, Ammar W Mohemmed, and Mohammad Yusoff Alias. A wireless sensor network coverage optimization algorithm based on particle swarm optimization and voronoi diagram. In *Networking, Sensing and Control, 2009. ICNSC'09. International Conference on*, pages 602–607. IEEE, 2009.

[16] Martin Bock, Amit Kumar Tyagi, Jan-Ulrich Kreft, and Wolfgang Alt. Generalized voronoi tessellation as a model of two-dimensional cell tissue dynamics. *Bulletin of mathematical biology*, 72(7):1696–1731, 2010.

[17] Lin Liao, Dieter Fox, Jeffrey Hightower, Henry Kautz, and Dirk Schulz. Voronoi tracking: Location estimation using sparse and noisy sensor data. In *Intelligent Robots and Systems, 2003.(IROS 2003). Proceedings. 2003 IEEE/RSJ International Conference on*, volume 1, pages 723–728. IEEE, 2003.

[18] Priyadarshi Bhattacharya and Marina L Gavrilova. Roadmap-based path planning-using the voronoi diagram for a clearance-based shortest path. *IEEE Robotics and Automation Magazine*, 15(2):58–66, 2008.

[19] Santiago Garrido, Luis Moreno, Mohamed Abderrahim, and Fernando Martin. Path planning for mobile robot navigation using voronoi diagram and fast marching. In *Intelligent Robots and Systems, 2006 IEEE/RSJ International Conference on*, pages 2376–2381. IEEE, 2006.

[20] Takahiro Ezaki, Kazumichi Ohtsuka, Mohcine Chraibi, Maik Boltes, Daichi Yanagisawa, Armin Seyfried, Andreas Schadschneider, and Katsuhiro Nishinari. Inflow process of pedestrians to a confined space. *arXiv preprint arXiv:1609.07884*, 2016.

[21] Michael Batty. Predicting where we walk. *Nature*, 388(6637):19–20, 1997.

[22] Alasdair Turner and Alan Penn. Encoding natural movement as an agent-based system: an investigation into human pedestrian behaviour in the built environment. *Environment and planning B: Planning and Design*, 29(4):473–490, 2002.

[23] Paul A Warren and Simon K Rushton. Optic flow processing for the assessment of object movement during ego movement. *Current Biology*, 19(18):1555–1560, 2009.

[24] Jun Zhang, Wolfram Klingsch, Andreas Schadschneider, and Armin Seyfried. Ordering in bidirectional pedestrian flows and its influence on the fundamental diagram. *Journal of Statistical Mechanics: Theory and Experiment*, 2012(02):P02002, 2012.

[25] S. P. Hoogendoorn and W. Daamen. Pedestrian behavior at bottlenecks. *Transportation Science*, 39(2):147–159, 2005.

[26] Jeong Won Kim, Han Jin Jang, Dong-Hwan Hwang, and Chansik Park. A step, stride and heading determination for the pedestrian navigation system. *Positioning*, 1(08):0, 2004.

[27] DW Grieve and Ruth J Gear. The relationships between length of stride, step frequency, time of swing and speed of walking for children and adults. *Ergonomics*, 9(5):379–399, 1966.

[28] Iker Zuriguel, Daniel Ricardo Parisi, Raúl Cruz Hidalgo, Celia Lozano, Alvaro Janda, Paula Alejandra Gago, Juan Pablo Peralta, Luis Miguel Ferrer, Luis Ariel Pugnaloni, Eric Clément, Diego Maza, Ignacio Pagonabarraga, and Angel Garcimartín. Clogging transition of many-particle systems flowing through bottlenecks. *Scientific Reports*, 4:7324, 2014.

[29] Takahiro Ezaki, Daichi Yanagisawa, and Katsuhiro Nishinari. Pedestrian flow through multiple bottlenecks. *Physical Review E*, 86(2):026118, 2012.

[30] Ren-Yong Guo, Hai-Jun Huang, and S. C. Wong. Route choice in pedestrian evacuation under conditions of good and zero visibility: Experimental and simulation results. *Transportation Research Part B: Methodological*, 46(6):669–686, 2012.

[31] Tie-Qiao Tang, Liang Chen, Ren-Yong Guo, and Hua-Yan Shang. An evacuation model accounting for elementary students? individual properties. *Physica A: Statistical Mechanics and its Applications*, 440(Supplement C):49–56, 2015.

[32] Antoine Tordeux, Mohcine Chraibi, and Armin Seyfried. *Collision-free speed model for pedestrian dynamics*, pages 225–232. Springer, 2016.

[33] M. Moussaid, D. Helbing, and G. Theraulaz. How simple rules determine pedestrian behavior and crowd disasters. *Proceedings of the National Academy of Sciences*, 108(17):6884–8, 2011.

A.10 ARTICLE IX

Assessment of models for pedestrian dynamics with functional principal component analysis

M. CHRAIBI, T. ENSSLEN, H. GOTTSCHALK, M. SAADI, AND A. SEYFRIED

PHYSICA A (**2016**)

Physica A, Vol. 451, 2016
10.1016/j.physa.2016.01.058

Assessment of Models for Pedestrian Dynamics with Functional Principal Component Analysis

Mohcine Chraibi[1], Tim Ensslen[2], Hanno Gottschalk[2], Mohamed Saadi[2], Armin Seyfried[1,3]

Abstract
Many agent based simulation approaches have been proposed for pedestrian flow. As such models are applied e.g. in evacuation studies, the quality and reliability of such models is of vital interest. Pedestrian trajectories are functional data and thus functional principal component analysis is a natural tool to asses the quality of pedestrian flow models beyond average properties. In this article we conduct functional PCA for the trajectories of pedestrians passing through a bottleneck. In this way it is possible to asses the quality of the models not only on basis of average values but also by considering its fluctuations. We benchmark two agent based models of pedestrian flow against the experimental data using PCA average and stochastic features. Functional PCA proves to be an efficient tool to detect deviation between simulation and experiment and to asses quality of pedestrian models.

Keywords
Model Validation

[1] *Jülich Supercomputing Centre, Forschungszentrum Jülich, Jülich, 52428 Germany¨*
[2] *Department of Mathematics and Computer Science, Bergische Universität Wuppertal, 42119 Wuppertal, Germany*
[3] *Department of Civil Engineering, Bergische Universität Wuppertal, Pauluskirche 7, 42285 Wuppertal, Germany*

Contents

Introduction

Most of force-based models *qualitatively* describe the movement of crowds of pedestrians. Self-organization phenomena e.g., lane formations [7, 6, 29], oscillations at bottlenecks [7, 6], clogging at exit doors [6, 29] etc., are reproduced. From a physical point of view it is of interest how simple model reproduce qualitatively self-organization phenomena of driven multi-particle systems. That contributes to a better understanding of the investigated systems and the essential interactions. In addition numerical simulations basing of these models are used to address safety related issues, concerning e.g. design and conception of escape routes in buildings [26, 28] or optimal organization of mass events or public transport facilities (VISWalk [31], Legion [32],). For such utilization a thorough *quantitative* validation of the models is obligatory to ensure a reliable layout, dimensioning or evaluation of pedestrian facilities. In most known cases this is fulfilled by reproducing the fundamental diagram [24, 15, 2, 9] or measuring the flow through bottlenecks [8, 2, 13]. An overview of quantitative validation of models by means of the fundamental diagram is given in [21]. On one hand, the common point between these quantitative methods is the fact that they are based on calculating specific traffic quantities, e.g. density, flow and velocity. On the other hand, these measurements are performed based on locally averaged values over time or space. [30] and [22] provide examples how the measurement methods could influence the resulting empirical relations of such granular and heterogeneous systems of finite size. The differences between the measurement methods suggest that important information on the system may be lost during the measurement process. Moreover state of the art models describe pedestrian dynamics on a more detailed level by simulating trajectories of every single pedestrian allowing in principle a validation method assessing average pedestrian or traffic flow behavior, but also accounting for the amount and typical nature of fluctuation around this average.

A first methodology based on exploiting information of individual trajectories was introduced in [10] to calibrate the social force model. While one pedestrian was moved according to the model the others were moved according to real trajectories. By means of an evolutionary algorithm the deviations of the resulting trajectories from the experimental ones was used to calibrate the parameters of the model. But this approach doesn't allow an assessment of the quality of a model.

While an abundance of agent-based models in the field of pedestrian and traffic dynamics were developed in the last years [3, 17] the question of systematic comparison of experimental evidence and model generated results has not caught the same attention. This would however be important for the ranking of models into more or less adequate ones. As argued above methodology of the evaluation should provide a comparison of model results and empirical data corresponding to the level of detail of the model. It is desirable that such a validation method should not only be able to asses average pedestrian or traffic flow behavior, but also account for the amount and typical nature of fluctuation around this average.

Among the difficulties in this validation process is the fact that in agent-based pedestrian or traffic flow data is functional, i.e. to each individual we associate data in the infinite dimensional space of trajectories $x\ t$. The adequate statistical approach for the study of pedestrian or traffic flow data is thus the well established method of functional data analysis [20]. In this method, the variation in the trajectories of different agents is interpreted as random fluctuations. Thus, the measured or simulated trajectories are interpreted as realizations of some stochastic process $X\ t \qquad ^2$, where t stands for a time parameter and $X\ t \quad X\ t$ tacitly depends on some random parameter from a probability space P . For more details the reader is conferred to [1]. Although there are infinitely many trajectories available for an agent to move from point A to point B, it often turns out that a few typical modes of variation around the average movement are responsible for the bulk of fluctuation of trajectories between different individuals. As a classical method in the analysis of functional data, the functional principal component analysis (PCA) is the standard method to find and analyze these typical variations.

The scope of this article is to use functional PCA analysis to study the performance of agent-based models of pedestrian motion with respect to experimental data. In order to demonstrate the methodological approach, two models – social force model (SFM) [14] and generalized centrifugal force model (GCFM) [2] – are used to simulate pedestrian movement through a bottleneck of the same dimensions. In the following we apply functional PCA using the open source extension `fda` by Ramsey, Hooker and Graves [19] to conduct the analysis. We present the results and give a detailed comparison of average values for locations and velocities and their respective principal components. For the latter we separately compare strength, distribution of total variation, and morphology of principal components.

We show that functional PCA in fact can be used to make statistically significant statements about model quality. Functional PCA reveals significant deviation between both models and the experiment already on the level of average values. While the morphology of principal components for locations is more or less adequately represented by both models, there are significant deviations in the strength of fluctuations around the mean behavior with the GCFM model underestimating the experimentally observed fluctuations while the SFM mostly overestimates fluctuation strength. These empirical observations can be confirmed with statistical testing for significance using the PCA-bootstrap methodology [4, 5].

In this article, for the fist time we combine functional PCA in the sense of [20] with the bootstrapping of scores in order to calculate the fluctuations of specific statistics that describe and distinguish characteristic features of fluctuations of individual pedestrian behavior in a crowd. Also on the PCA-side, benchmarking and testing with specific statistics evaluated in functional PCA is a new strategy, to the best of our knowledge.

The article is organized as follows. In section 1 we review the pedestrian flow experiment [23] as the benchmark case for this study. Section 2 gives a brief account on the SFM and the GCFM model. In Section 3 reviews the functional PCA and its numerical implementation. Section 4 is the main part of this article. After some introductory remarks on data formatting and smoothing (Subsection 4), we compare average data for x and y position data (Subsection 4) and velocities directed in the main direction of motion, which is the x-direction. We then compare fluctuations strength via PCA eigenvalues (Subsection 4) and morphology for the first PCA harmonics for x- and y- positions and x-velocities (Subsection 4). Section 5 presents the PCA-bootstrap approach in the context of spline-based PCA (Subsection 5) and applies this to total variation and Gini index (Subsection 5) as well as the L^2-distance of the average trajectories and the Hilbert Schmid distance of the empirical correlation functions (Subsection 5). In Section 6 we summarize or findings and give some conclusions on model quality in the specific case and general applicability of functional PCA in the given context.

1. Experiment

In this work we use as a reference the experimental data extracted from the experiment [23], that was performed in 2006 in the wardroom of the “Bergische Kaserne Düsseldorf”. See Fig. 1.

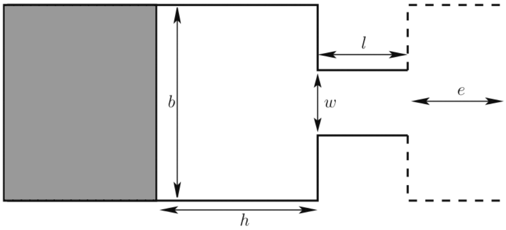

Figure 1. The simulation set-up: pedestrians start from the shaded area and move through the bottleneck ($l \quad 4$ m, $h \quad 4\ 5$ m, $b \quad 6$ m and $w \quad 0\ 9$ m). An adjacent area of length $e \quad 2\ 5$ m is added to consider the backward effect of leaving pedestrians on those still in the bottleneck.

A waiting area was used to distribute the attendees before the start of each run of the experiment. For simulation purposes we enlarge the area of the set-up by an extra room of length e. This is necessary to take into consideration the effects of pedestrians that leaved the bottleneck on the pedestrians still in the system.

The flow through the bottleneck is measured as follows:

$$J \quad \frac{N}{t} \tag{1}$$

with N the number of pedestrians and $t \quad t_{\text{last}} \quad t_{\text{first}}$ the time gap between the first and the last pedestrian passing the bottleneck at the measurement line.

2. Models

Force-based models describe the movement of pedestrians as a superposition of forces. Given the state variables of pedestrian i at time $t \quad x_i \quad t \quad v_i \quad t$ and considering Newton’s second law of dynamics the state of each pedestrian i is defined by:

$$m_i a_i \quad t \qquad \underset{i \quad j}{f_{ij}^r} \qquad \underset{W}{f_{iw}^r} \quad f_i^d \tag{2}$$

and

$$v_i \quad t \qquad \frac{dx_i \quad t}{dt} \tag{3}$$

where f_{ij}^r denotes a repulsive force acting from the j^{th}-pedestrian on the i^{th}-pedestrian, f_{iw}^r is a repulsive force emerging from borders, walls etc. and f_i^d is a driven force. m_i is the mass of pedestrian i.

The superposition of the forces reflect the fact that pedestrians move towards a certain point in space (e.g. an exit) and meanwhile try to avoid collisions with each other or with walls and objects.

The driving force f_{ij}^r models, at low densities, an exponential acceleration towards a desired speed v_0: The following expression [18] is used:

$$f_i^d \quad m_i \frac{v_0 e_i^0 \quad v_i}{} \tag{4}$$

with a relaxation time typically equal to 0.5 s, and a desired direction e_i^0 of pedestrian i.

The repulsive force between pedestrians f_{ij}^r is defined differently from one model to another [7, 24, 29, 2, 25, 11].

In this work we study a variation of the SFM and the GCFM. Both models are microscopic and continuous in space. In the GCFM the agents have an elliptical form with velocity-dependent semi-axes, whereas the shape of agents in the SFM is circular. In the general case, the distance d_{ij} is defined as the distance between the borders of the ellipses i and j along a line connecting their centers. See Fig. 2. For the SFM the semi-axis orthogonal to the movement direction is equal to the other semi-axis in the direction of movement. For simplicity we write d_{ij} to denote the norm of the vector d_{ij}.

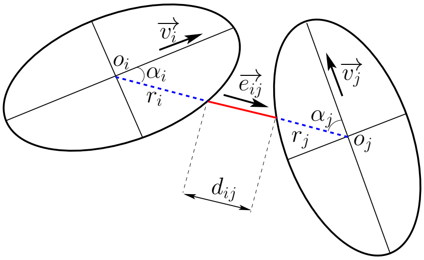

Figure 2. The effective distance d_{ij} of two pedestrians represented by two ellipses.

The social force model (SFM)

The SFM as originally published by Molnár [14] describes the movement of circular agents as superposition of different factors e.g. influence of neighboring pedestrians, walls, attractions and groups. In this work we reduce the complexity of the model to a minimum, considering only the influence of pedestrians and walls and assuming only circular potentials.

The repulsive force in the SFM between agent i and j is defined as

$$f_{ij}^{r} \qquad m_i k_{ij} A \exp \frac{d_{ij}}{B} \; e_{ij} \tag{5}$$

with

$$d_{ij} \qquad x_j \quad x_i \qquad r_i \quad r_j \tag{6}$$

and

$$e_{ij} \qquad \frac{x_j \quad x_i}{x_j \quad x_i} \tag{7}$$

with the parameters A and B the strength and the range of the force are adjusted. The limited vision of pedestrians (180) is modeled by the coefficient k_{ij}:

$$k_{ij} \qquad v_i \; e_{ij} \tag{8}$$

is the Heaviside function. The repulsive force between pedestrians and static objects is defined similarly to (5).

The generalized centrifugal force model (GCFM)

The repulsive force in the GCFM is inversely proportional to the distance of two ellipses representing moving pedestrians i and j and depends on their relative velocity:

$$f_{ij}^{r} \qquad m_i \frac{\quad v_0 \quad v_{ij} \quad ^{2}}{d_{ij}} \tag{9}$$

where v_{ij} $\qquad v_i \quad v_j \quad e_{ij}$ is the relative velocity. The use of the Heaviside function ensures, that faster pedestrians are not effected by slower pedestrians. By means of the parameter the strength of the force can be adjusted. As mentioned earlier in the GCFM the space requirement in the direction of movement is modeled by the semi-axis

$$a \quad a_{\min} \quad {}_{a} v_i \tag{10}$$

with two parameters $a_{\min}$ and ${}_{a}$, whereas the lateral swaying of pedestrians is modeled by the semi-axis

$$b \quad b_{\max} \quad b_{\max} \quad b_{\min} \; \frac{v_i}{v_0} \tag{11}$$

Model parameters

As mentioned earlier the original SFM includes several forces e.g. physical contact forces and attractive forces. For our purpose we use a simplified version of the SFM as presented in Sec. 2. We choose A 5 N for pedestrian-pedestrian interactions (5) and A 7 N for pedestrian-wall interactions. The range of the function defined by the parameter B in (5) was chosen to be 0 08 m for pedestrian-pedestrian interactions and 0 05 m for pedestrian-wall interactions. The parameter in (9) is set to 0.2 for pedestrian-pedestrian interactions and 0.33 for pedestrian-wall interactions. The desired speed v_0 is set to 1 1 m/s. For simplicity we set for both models m_i 1 Kg. Table 1 gives a resume of the parameters used.

Parameter	Equation	Value
A_{ped}	(5)	5 N
A_{wall}	Similar to (5)	7 N
B_{ped}	(5)	0.08 m
B_{wall}	Similar to (5)	0.05 m
$_{\text{ped}}$	(9)	0.2
$_{\text{wall}}$	Similar to (9)	0.33
	(4)	0.5 s
v_0	(4)	1.1 m/s
m	(4)	1 Kg
a	(10)	0.12 s
a_{min}	(10)	0.15 m
b_{min}	(11)	0.15 m
b_{max}	(11)	0.2 m

Table 1. Parameter values in simulations with both GCFM and SFM.

The values chosen in Tab. 1 differ from the values published in other works [12, 2]. Our choice of the above mentioned values is supported by qualitative reasons, ensuring minimal overlapping among pedestrians, as well by quantitative consideration of the flow through the bottleneck. See Fig. 3. For safety relevant simulations a careful calibration of the used models is needed.

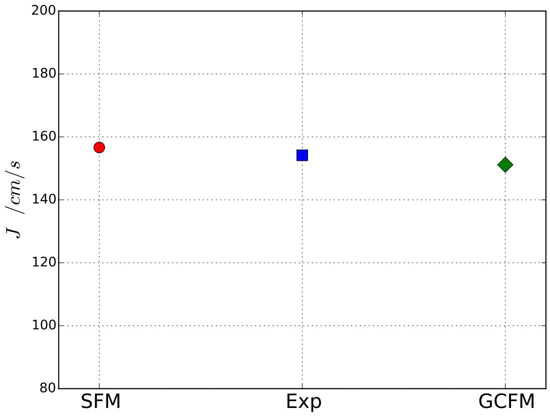

Figure 3. The flow through the bottleneck measured at the middle of the corridor after the entrance to the bottleneck. The empirical value is a reference value for the calibration of the GCFM and the SFM.

Having calibrated two different models based on usual qualitative and quantitative criteria, we strive to apply a new technique to assert the goodness of the investigated models and verify whether the aforementioned validation is sufficient to ensure a trustworthy and safe use of the produced simulations.

3. Functional PCA: Foundations

What is functional PCA?

In this section we give some details of functional PCA following [20]. The principal component analysis uses the principal axis transformation for multivariate, correlated numerical data using the (empirical) covariance information between the single random variables. Eigenvalues then sort the importance of the single eigenvectors (also called harmonics or modes) according to the variance.

This concept needs to be adapted to the case where the observed data from n individuals are functions – as it is the case with the trajectories of pedestrians. The variability of the data can still be described in with the eigenvalues and eigenvectors of the covariance function seen as an operator on the function space of square integrable functions. Given the stochastic process of random trajectories $X\ t$, with $t \quad 0\ L$, the covariance function is defined as

$$C\ s\ t \qquad X\ s \qquad X\ s \quad X\ t \qquad X\ t \tag{12}$$

with the expected value with respect to the underlying probability space. This covariance function needs to be estimated out of the data $x_j\ t$

$$\hat{C}\ s\ t \qquad \frac{1}{n \quad 1}\ {}_{j\ 1}^{n}\ x_j\ s \quad \bar{x}\ s \quad x_j\ t \quad \bar{x}\ t \tag{13}$$

with $x_j\ t$ the j-th observation is one realization of the random process $X\ t$ and $\bar{x}\ t \quad \frac{1}{n}\ {}_{j\ 1}^{n} x_j\ t$.

In the following we assume that average values have already been removed from the stochastic signal, i.e. we consider transformed random quantities $X\ t \quad X\ t \qquad X\ t$ with estimated observations $x_i\ t \quad \bar{x}\ t$. The eigenvalues of $C\ s\ t$ can then be calculated after solving the follow eigenvalue equation

$${}_{0}^{L}\ C\ s\ t \quad t\ dt \qquad s \tag{14}$$

This results in a set of eigenvalues $_1 \quad _2 \qquad 0$ and corresponding eigenfunctions $_i\ s$. These eigenfunctions are orthonormal ${}_0^L\ _i\ t \quad _j\ t\ dt \quad _{ij}$, where $_{ij}$ 1 for i j and zero otherwise. The eigenfunctions and eigenvalues can now approximately be determined from the observations $x_j\ t$ by replacing $C\ s\ t$ by its empirical counterpart $\hat{C}\ s\ t$.

Numerical approximation

The problem (14) is an infinite dimensional eigenvalue problem and its empirical counter part is potentially very high dimensional (of dimension n). A frequently used method to make this problem numerically tractable is to project the covariance matrix on the space spanned by some finite basis, - e.g. a sufficiently fine B-spline or Fourier basis. Then one solves for the eigenvalues and functions in the given finite dimensional space of basis functions. Therefore we approximate the observed functions $x_i\ t$ with a suitable linear combination of basis functions

$$x_i\ t \qquad {}_{k\ 1}^{K}\ c_{ik}\ \ _k\ t \qquad x_i\ t \qquad \mathbf{C}\blacksquare\ \mathbf{t} \tag{15}$$

with basis function vector $t \qquad _1\ t \qquad _K\ t\ ^T$ and coefficient matrix $\mathbf{C} \quad c_{jk}\ {}_{k\ 1}^{j\ 1}\ {}_{K}^{n}$ obtained e.g. by orthogonal projection of $x_i\ t$ to the space spanned by the basis functions and a subsequent basis decomposition, in which case $\mathbf{C} \quad \mathbf{W}\ ^1\mathbf{v}_j$ with $W_{ij} \qquad _i \quad _j \quad {}_0^L\ _i\ t \quad _j\ t\ ds$ and $c_{jk} \quad x_j \quad _k \quad {}_0^L x_j\ t \quad _k\ t\ dt$. Here some numerical quadrature may be employed for the integrals involved in the definition of v_{jk}, whereas in most cases analytic formulae are available for W_{ij}. This projection method implies that the covariance function can be approximated by

$$\hat{C}\ s\ t \qquad \frac{1}{n \quad 1} \quad s\ ^T\bar{\mathbf{C}}^T\bar{\mathbf{C}} \quad t \tag{16}$$

Here we use $\bar{C}$ for the matrix of coefficients of $x_j\ t \quad \bar{x}\ t$ with respect to the basis t , namely $\bar{c}_{jk} \quad c_{jk} \quad \frac{1}{n}\ {}_{j\ 1}^{n}\ c_{jk}$. Now we expand the eigenfunction with the same basis functions to a good approximation:

$$t \qquad {}_{k\ 1}^{K}\ b_k\ \ _k\ t \qquad t\ ^T\mathbf{b} \tag{17}$$

The approximate eigen value equation can be written as

$$ {}_{0}^{L} \hat{C}\; s\; t \quad t\; dt \quad \frac{1}{n} \quad s^{\;T}\bar{\mathbf{C}}^T\bar{\mathbf{C}}\mathbf{W}\mathbf{b} \qquad s^{\;T}\mathbf{b} \qquad s \tag{18}$$

leading to the eigenvalue equation $\bar{\mathbf{C}}^T\bar{\mathbf{C}}\mathbf{W}\mathbf{b} \quad \mathbf{b} \quad \mathbf{W}^{1\;\;2}\bar{\mathbf{C}}^T\bar{\mathbf{C}}\mathbf{W}^{1\;\;2}\mathbf{u} \quad \mathbf{u}\;\; \mathbf{b} \quad \mathbf{W}^{\;\;1\;\;2}\mathbf{u}$, which can be solved numerically. The result is a number of eigenvalues ${}_1 \quad {}_2 \qquad 0$ and coefficient vectors $\mathbf{b}_i$ for approximate principal components ${}_i\; t \qquad t^{\;T}\mathbf{b}_i$, for $i \quad 1\; 2 \qquad n \quad 1$, which is the maximal rank of $\bar{\mathbf{C}}$.

Statistics of the eigenvalues

In this subsection, we discuss how to reduce the information from the set of eigenvalues to a few significant characteristics. In particular we will focus on code figures that measure the strength of fluctuations and their concentration to a few, active modes.

The eigenvalue ${}_i$ represents the strength of fluctuations in the respective mode of characteristic shape ${}_i\; t$. The relative strength ${}_i$ of the variation in the mode ${}_i\; t$ and the cumulative relative strength L_j up to the j-th mode ${}_j\; t$ is given by

$$ {}_i \quad \frac{{}_i}{{}_{j\;\;1}^{\;n}\;\;{}_j} \text{ and } L_j \quad {}_{i\;\;1}^{\;j}\;\;{}_i \tag{19}$$

Two quantities that can be derived form the eigenvalues of the PCA are of special interest: First, the total variation strength is simply the sum of all eigenvalues $\quad {}_{j\;\;1}^{\;n}\;\;{}_j$ whereas the Gini index is a measure of concentration that is build from the Lorenz curve quantities L_j via $G \quad \frac{2}{n\;\;1}\;\;{}_{j\;\;1}^{\;n}\; L_j \quad j\;\; n$. Geometrically, the Gini index measures the area between the diagonal and the Lorentz curve, cf. e.g. Figure 8 in the right panel. It is normalized such that it takes the value one if only one mode is active and takes the value zero when all modes are equally activated ${}_1 \quad {}_2 \qquad {}_n$. Note that the order of ${}_j$ is descending in contrast to the usual definition of the Gini index, where the order is ascending. As an alternative, one could also consider the entropy of the distribution of the total activity to the single modes. The result of the observation however remain largely unchanged.

Deviation measures

In this section we derive some quantities that can be used to measure the distance between one set of functional data and another such data set. In particular we will utilize these distances for benchmarking models with respect to their distance to the experiment. Two distance measures will be employed in the following: First, the mean quadratic deviation between the average trajectories of the model on the one hand and the experimental data on the other. Secondly, we consider the Hilbert-Schmidt norm between the respective empirical covariance functions as a measure of the distance of the fluctuation behavior of the experiment and the simulation. In the following we work with the data after projection to a finite spline basis ${}_k\; t$.

We start with the mean quadratic difference in the average behavior. The mean of the observed function $x_i\; t$ is:

$$ \bar{x}\; t \quad \frac{1}{n}\;{}_{j\;\;1}^{\;n}\; x_j\; t \qquad {}_{k\;\;1}^{\;K}\; \underbrace{\frac{1}{n}\;{}_{j\;\;1}^{\;n}\; c_{jk}}_{C_k} \quad {}_k\; t \qquad {}_{k\;\;1}^{\;K}\; C_k \quad {}_k\; t \tag{20}$$

The mean quadratic distance, the squared L^2 norm, of the difference between $\bar{x}\; t \qquad {}_{k\;\;1}^{\;K}\,C_k \quad {}_k\; t$ and $\bar{y}\; t \qquad {}_{k\;\;1}^{\;K}\,C_k \quad {}_k\; t$ is:

$$ \bar{x}\; t \quad \bar{y}\; t\;\; {}_2^2 \qquad {}_{k\;\;1}^{\;K}\; C_k \quad C_k \quad {}_k\; t \qquad {}_{k\;\;1}^{\;K}\; C_k \quad C_k \quad {}_k\; t \qquad \mathbf{C} \quad \mathbf{C}^{\;\;T}\mathbf{W}\;\mathbf{C} \quad \mathbf{C} \tag{21}$$

We now derive formulae for measuring the distance between experiment and simulation in the covariance structure. Let $\hat{D}\; s\; t \quad \hat{C}\; s\; t \quad \hat{C}\;\; s\; t \qquad {}_{k\;\;1}^{\;K}\;{}_{l\;\;1}^{\;K}\; \underbrace{\bar{c}_{k\,l} \quad \bar{c}_{k\,l}}_{d_{k\,l}} \quad {}_k\; t \quad {}_l\; s$ be the difference of covariance functions. The Hilbert-Schmidt norm of $\hat{D}\; s\; t$ is:

$$ \hat{D}\;{}_{HS}^{2} \qquad {}_{0}^{L}\;{}_{0}^{L}\;\; \hat{D}\; s\; t \quad {}^{2} dsdt \quad \mathrm{Tr} \quad \mathbf{DW}\;{}^{\mathbf{T}}\mathbf{DW} \tag{22}$$

Here Tr A stands for the trace of the matrix A and $\mathbf{D}$ is the matrix with entries $d_{j\,k}$.

4. PCA Results

In this section we show that functional PCA is a useful tool for detailed validation of models for pedestrian dynamics. Ideally, the variability in the data can be described with the help of the PCA with a few principal components. These main components can be interpreted as the schemes for the deviation of individual trajectories from the mean flow. This allows a comparison of simulated and experimental data beyond averaged flow features. Therefore, we apply the PCA to the experimental and simulated data from two models SFM and GCFM and compare the results. Here we apply the PCA for x and y coordinates over time separately, as this approach is somewhat more accessible to the interpretation. For the alternative approach of jointly analysing x and y trajectories and a discussion of the pros and cons of both approaches, see [20, 19].

The analysis of the data is based on the `R` package `fda` developed by J.O. Ramsay et al. [19] with some minor extensions by the authors.

Preparation of the Data

The pedestrian trajectory data in the experiment is recorded electronically with video tracking at the rate of 25 frames per second. A total number of 149 trajectories has been recorded. Likewise, the SFM and GCFM models have been simulated with 25 time steps per second using Euler integration with a time step t 0 01 s. For both models, a total of 149 trajectories have been simulated. See the trajectories in Figure 4.

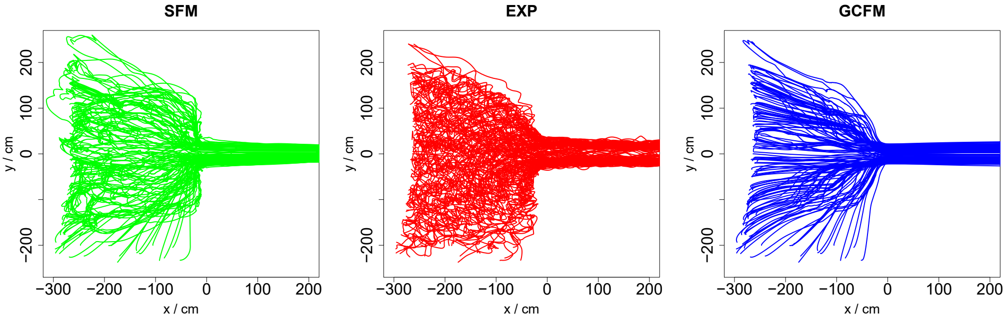

Figure 4. XY plots of pedestrian trajectories generated by the SFM model (left), experiment (middle) and GCFM model (right).

For the analysis, the pedestrian motion has to be stationary, i.e. all agents move under the same conditions.

Furthermore, the considered time interval has to be the same for all agents. Therefore we account only to the pedestrians, who need more than 12 seconds to reach the exit. Furthermore, the trajectory is tracked only two seconds after the passage of the bottleneck entrance. The analysis of the experimental data and the models thus is based on trajectories in individual time intervals that range from 12 s before passage through the bottleneck by the individual to 2 s afterwards. This makes a total time of 14 s. In order to avoid negative time values, we start each pedestrian trajectory at time t 0 s such that passage through the door for each individual occurs at t 12 s, exactly. From now on we work with this time scale. Figure 5 visualizes the formatting steps. After reformatting, a total of 118 pedestrian trajectories were available for the experiment, 121 for the SFM and also 121 for the GCFM model, respectively.

The experimental data contain the swaying caused by the bipedal locomotion of pedestrians in combination with the tracking of markers on the head. But the SFM as well as the GCFM model the movement of the centre of mass neglecting the bipedal locomotion, which produce swaying-free trajectories. Therefore, we smooth the data before the analysis in order to filter out the lateral swaying. It turns out that the regression with a B-spline basis containing 10 elements with nodes equally distributed over the underlying time interval 0 14 effectively removes swaying while properly reproducing the other features of the individual's trajectories, see Figure 6.

Average trajectories

As PCA components describe variation around some mean value, it is essential to analyse average functions $\bar{x}$ t and $\bar{y}$ t .

Figure 7 shows the mean functions $\bar{x}$ t and $\bar{y}$ t of the x- and y-components for the experiment and the models.

When we examine the x-component, we identify clearly discrepancies between the experiment and both models. The average pedestrian in the experiment shows a nearly linear progress to reach the exit. The acceleration after passing the bottleneck, i.e. the increase in the slope, is modest. In contrast, both SFM and GCFM show a slower progress of the average pedestrian through the crowd and a much more pronounced acceleration after the passage of the bottleneck. While the latter

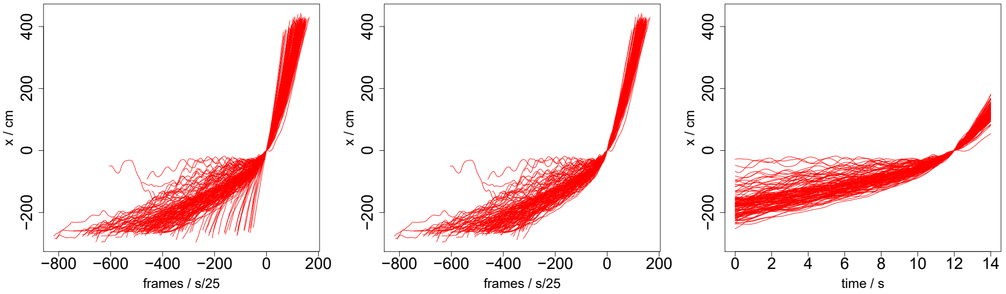

Figure 5. Plots of x-coordinates of pedestrians (experimental data): raw data (left), stationary data (middle) and with individual time in the interval [0,14] s (right). One Frame in the first two panels corresponds to 1/25 s.

deviation from experiment is about the same for both models, the underestimation in the slope from the experimentally observed value is bigger for the GCFM model. Thus both models overestimate the dwell time indicating a missing anticipation and cooperation of the modelled pedestrians. However the SFM produces this effect by a lesser amount.

The y-component is described by both models in a satisfactory manner, as trend lines only move at a scale of a few centimeters from the center of the bottleneck. At least for the simulated data this is due to the left hand - right hand reflection symmetry of the agents in both models and the (approximate) symmetry of initial positions with respect to the y 0 axis, i.e. the center line through the bottleneck. In the experiment, a certain asymmetric behavior is visible for the mean y-position of the trajectories over time. In average, the pedestrians approach the bottleneck coming slightly from the left seen from the direction of progress. Interestingly, this asymmetry can not be traced back to the initial conditions, as these are the same for the experimental and the simulated trajectories.

This behavior is absent in both models, which have left-right symmetries in their respective constituting equations.

PCA eigenvalues

Having analyzed the average behavior, we now turn to the question, how well the models describe fluctuations in pedestrian data around the averages. We start with the absolute strength of PCA variability, which is represented by the PCA eigenvalues $_i$, i 1 10, as we are using a 10 dimensional spline basis. At the same time, we also consider the cumulative relative strength $_j$ in order to measure the concentration or dispersion of variability in experimental or the simulated data. We first consider PCA mode strength for x-position over time as given in Figure 8. These modes describe typical patterns of pedestrians lagging behind and being in front of the trajectory of the average pedestrian. The SFM overestimates the total amount of statistical deviation in x-position from the average x-position by approximately 12% as compared with the experiment. Also, concentration of variability in the first mode is slightly lower than in the experiment. In the GCFM, the total level of x-position variation is underestimated by 37% of the total variation. The relative concentration in the fist mode is higher as in the experimental data by an amount comparable to the SFM, but in the opposite direction. For the values of total variation and Gini indices confer Table 2.

In Figure 9 the PCA-modes for the statistical y-fluctuation around the average y-position (essentially y 0) is displayed. The experiment and both simulations all show that basically only one mode is active representing the axially symmetric shape of the jammed area in front of the bottleneck. The size of this area is underestimated by both models. The GCFM predicts a pronouncedly reduced area in the y-direction covered by trajectories passing the bottleneck in the next 12 seconds, showing a total y-variation of 1 3 33 6% of the experimental data. The same figure of underestimation of y-variation for the SFM compared with experiment is 57%. Total variations and Gini indices can again be found in Table 2.

Tot.Var	SFM	Experiment	GCFM
x-position	10863	9550	6835
y-position	35469	61619	20749

Gini	SFM	Experiment	GCFM
x-position	0.83	0.85	0.87
y-position	0.89	0.89	0.89

Table 2. Total variation (left) and Gini indices (right) for the eigenvalues of the PCA.

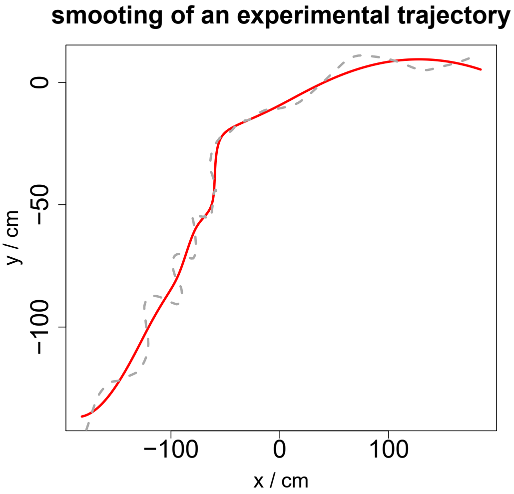

Figure 6. Smoothing of a experimental trajectory (dotted blue) with a B-spline basis of dimension 10 (solid red).

PCA modes

Figure 10 shows the principal fluctuation components of the x-position for the experiment and the models. From the aforementioned eigenvalue analysis (Figure 8) we can conclude that fluctuations can be mainly described by the first three principal components.

Let us now give an interpretation to the morphology of the PCA components. The first principal component describes the tolerance between the initial positions of the pedestrians 12 seconds before passing the bottleneck. Two pedestrians reach the bottleneck at the same reference time $t = 12$. Due to the fact that some pedestrian starts with a higher or lower x-distance to the bottleneck than the the others, at $t = 0$, a statistical variation in x-positions occurs. This could be called “slipping-through-effect” because faster pedestrians find more favorable configurations of fellow pedestrians ahead which allows a faster passage through the crowd.

The second and third principal component describe an effect which we can associate to long stop and go behavior in different lanes in a traffic jam: One trajectory is temporary faster than the other, but afterwards it is the other way round. In the case of the experiment and the GCFM, the third principal component also shows different velocity patterns after the bottleneck.

The morphological comparison of the experimental data with the SFM and GCFM shows that the points of intersection

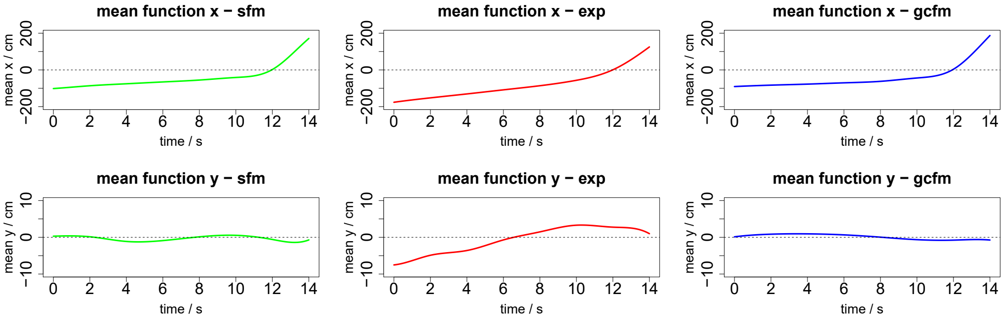

Figure 7. Average curves for position vs time for the SFM (left), experiment (middle) and GCFM (right): x-ccordinate (top) and y-coordinate (right).

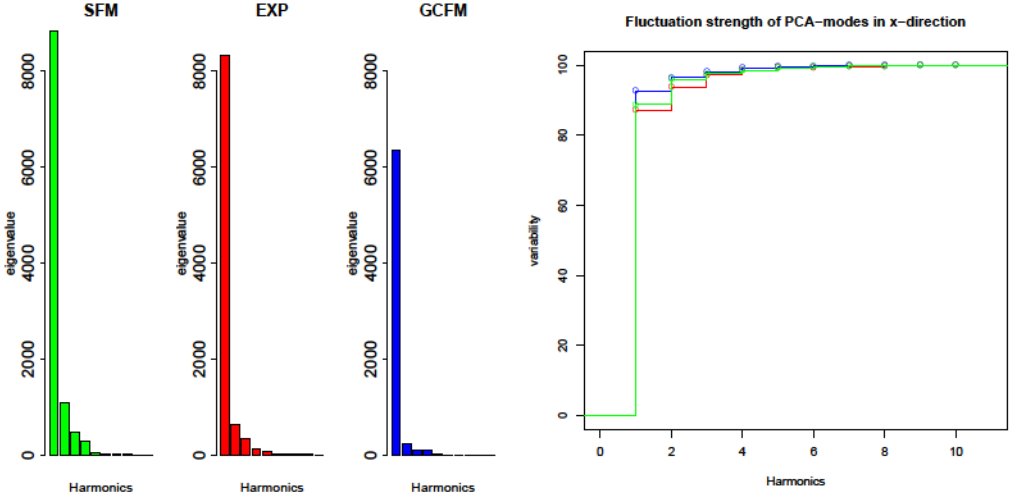

Figure 8. Left: Barplot of absolute fluctuation strength (eigenvalues) of the 10 PCA-modes (harmonics) for x-position over time for the SFM-model, Experiment and GCFM-model. Right: Cumulative relative strength of PCA-modes over all 10 harmonics.

of the first two principal components are nearly at the same times. Thus both models reproduce the qualitative behavior of statistical fluctuations in the pedestrians x-positions over time quite well. The main difference thus lies in the different activation strength of the “slipping-through” mode.

Figure 11 shows the PCA of the y-components for the experiment and the models. We observe that the variability of the data can be mainly described by the first principal component which represents the shape of the crowd in front of the door. The first principal component of both models describe the experiential data acceptably well. Also the higher modes are of quite similar shape, although they should be neglected since they hardly contribute to the total variation.

Evaluation of deviation measures

Lastly in this section, we want to compare the deviation measures of the respective simulation model with the experiment. The results are summarised in 3.

L^2-norm	EXP-GCFM	EXP-SFM
x-position	169.8	166.0
y-position	15.34	13.20

HS-norm	EXP-GCFM	EXP-SFM
x-position	2291	1282
y-position	4449	2880

Table 3. Deviations between experimental data and models data using the L^2-norm (left) Hilbert-Schmidt norm (right).

The average squared distance of x- and y- coordinates of the trajectories as function over time is of the same order of magnitude for both models.

A slight advantage can however be attributed to the SFM-model. This effect is even more pronounced in the Hilbert-Schmidt norm that measures the distance to the experiment in the fluctuation structure of measured and simulated data.

5. Statistical inference based on the bootstrap

In the previous section, we evaluated the total variation and the Gini coefficient or deviation measures for the average behavior and the fluctuation structure (L^2- and HS-norms, respectively) in order to compare simulated and experimental data. This descriptive approach however leaves open the question, to which extent these findings depend on the intrinsic stochastic nature of pedestrian trajectories and to which extent they are due to structural differences between simulated agents in the models and real pedestrians observed in the experiment. In the present section, we describe and apply a simulation-based test procedure in order to clarify, to what extent the observed differences between models and experiment are statistically significant.

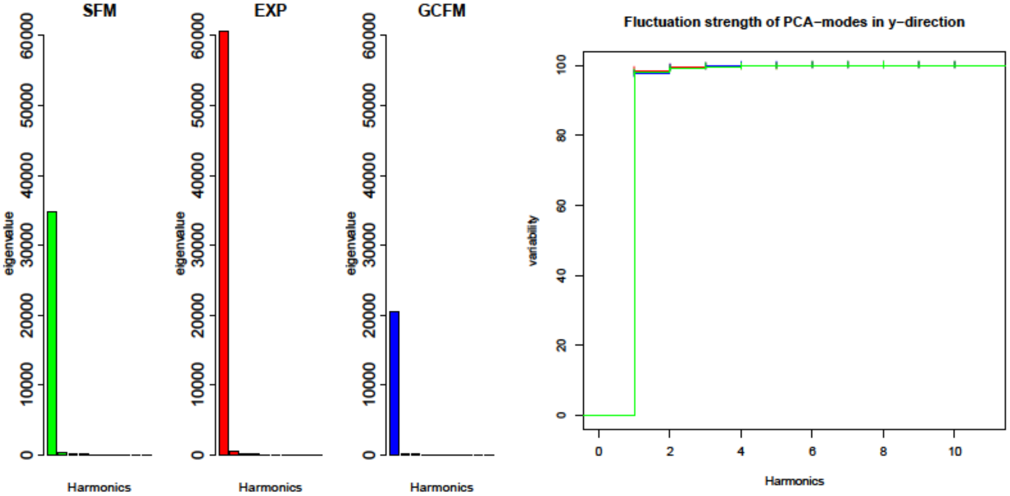

Figure 9. Left: Barplot of absolute fluctuation strength (eigenvalues) of the 10 PCA-modes (harmonics) for y-position over time for the SFM-model, Experiment and GCFM-model. Right: Cumulative relative strength of PCA-modes over all 10 harmonics.

Bootstrapping PCA scores

As the basis of our statistical testing procedure, we use the bootstrap over the matrix of principal components from [4, 5]. We now shortly describe the bootstrap approach. Given, e.g., the i-th x-value of the trajectory over time, $x_i(t)$, the score of this trajectory with respect to the principal component $\xi_j(t)$ is

$$\begin{aligned} s_{ij}^{(x)} &= \langle x_i(t) - \bar{x}(t), \xi_j(t) \rangle \\ &= \left\langle \sum_{l=1}^{K} \underbrace{(c_{i,l} - C_l)}_{\blacksquare_{i,l}} \Phi_l(t), \sum_{k=1}^{K} \mathbf{b}_{jk} \Phi_k(t) \right\rangle \\ &= (\blacksquare^T \mathbf{W} \mathbf{b}^T)_{i,j} \, . \end{aligned} \tag{23}$$

By construction, the scores $s_{ij}^{(x)}$ and $s_{i,j'}^{(x)}$ are (linearly) uncorrelated for $j \neq j'$. Neglecting potential higher order correlations, we construct a virtual bootstrap sample from the scores of the experimental data by drawing with replacement, for i, j fixed, $s_{i,j}^{(x,\text{boot})}$

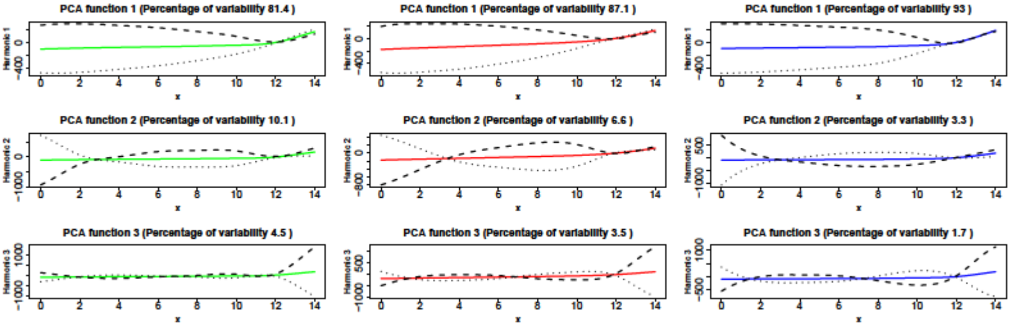

Figure 10. PCA components in for x-position over time for the SFM model (left), experiment (middle) and GCFM model (right). The first three harmonics are displayed.

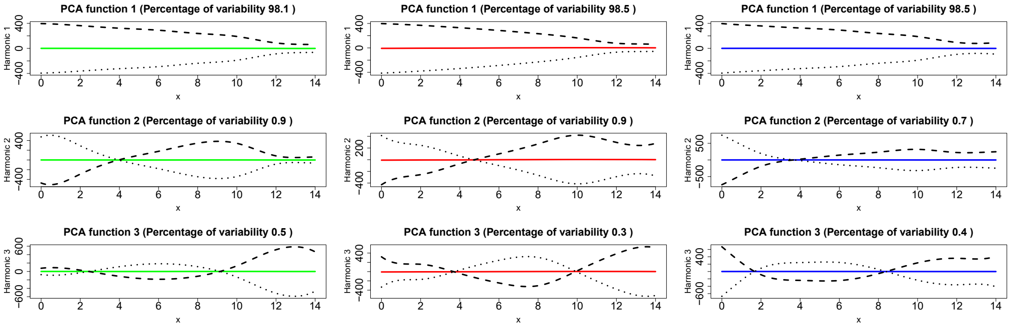

Figure 11. PCA components in the y direction for the SFM model (left), experiment (middle) and GCFM model (right). The first three harmonics are displayed.

from the N samples $s_{i\,j}^{x}$ of the original scores with respect to the j-the principal component $\ _j\ t$. Doing this independently for $i \quad 1 \quad N$ and $j \quad 1 \quad K$ (remember, in our case $N \quad 110$ is the number of experimental pedestrian trajectories and $K \quad 10$ the number of principal components) we obtain the $N \quad K$ bootstrap score matrix $\mathbf{s}^{x\ \text{boot}}$. The corresponding bootstrapped trajectories then are

$$x_i^{\text{boot}}\ t \qquad \mathbf{s}^{x\ \text{boot}} \qquad t\ _i \quad \bar{x}\ t \qquad i \quad 1 \qquad N \tag{24}$$

Figure 12 shows the x-coordinates plots of pedestrian trajectories by bootstrapped and experimental data.

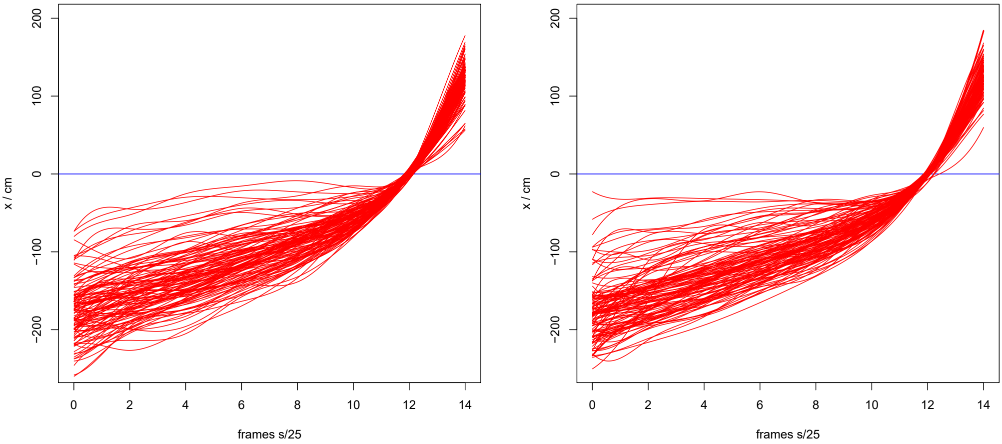

Figure 12. Plots of x-coordinates of pedestrians by bootstrapped data (left) and experimental data (right).

With this virtual data set, the PCA analysis is then repeated. In particular, we obtain bootstrapped quantities for total variation and Gini index, as well as distance measures for the average behavior of the actual experiment and its virtual bootstrap replica. This entire process is then repeated a sufficiently high number of times, such that p-values in the range of usual significance levels $\quad 1 \quad 5\%$ can safely be determined. Here we generate 10^4 bootstrap samples, each containing $N \quad 118$ virtual trajectories, and thereby obtain a simulated distribution for each of the aforementioned quantities.

The same iteration is repeated for the y-coordinate and the x-coordinate of the velocity v_x.

For statistical testing, we generate two-sided confidence intervals for the total variation and the Gini coefficient and left open confidence intervals for the distance measures based on the empirical distributions of the respective quantities. If the related quantities for the SFM and GCFM model are not contained in these confidence regions, we consider this as a positive test result for a deviation between experiment and model.

Testing Gini indices and total variations

One of the advantages of using this bootstrap technique is to have the opportunity to examine the distributions of Gini indices and the total variations. We compute for every bootstrap sample the Gini indices and total variations by the experimental data for x-coordinates, y-coordinates and x-velocities. Afterwards, we are able to compute their empirical cumulative distribution functions (ECDF). Figure 13 shows the ECDF of Gini indices and total variations of x-coordinates by bootstrapped experimental data. The blue lines show the values of Gini index and total variation by original experimental data. The corresponding p-values, i.e. the critical level of statistical significance where the difference between model and experiment becomes significant, are calculated on the basis of two-sided confidence regions of the bootstrapped distribution. The p-values are summarized in Table 4. Note that p-values below 10^{-3} become numerically unreliable for 10^4 bootstrap samples and are set to zero.

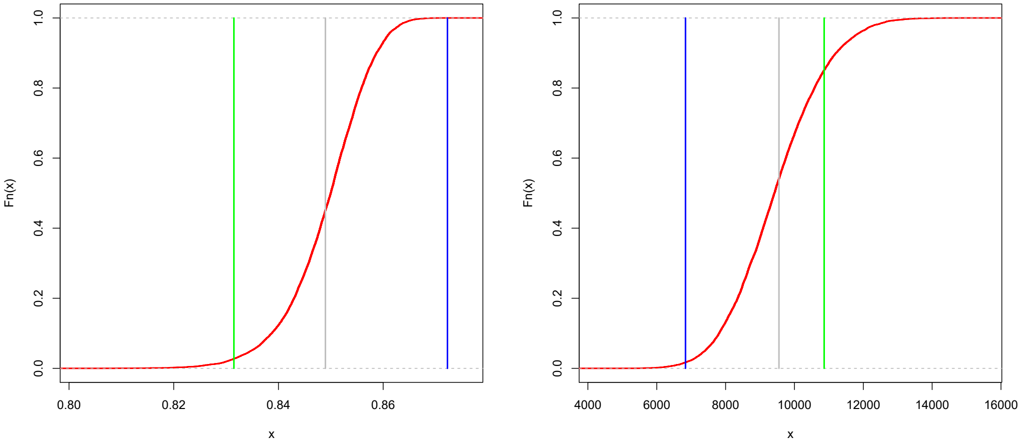

Figure 13. ECDF of Gini indices (left) and ECDF of total variation (right) from bootstrapped experimental data. Green, grey and blue vertical lines mark the values for the SFM, experiment and GCFM, respectively.

p-values for Gini index		
	EXP/GCFM	EXP/SFM
x-position	0	0.055
y-position	0.610	0.007

p-values for TotalVar		
	EXP/GCFM	EXP/SFM
x-position	0.034	0.297
y-position	0	0

Table 4. The p-value of Gini index and total variations by bootstrapped experimental data.

The p-values in Table 4 show that statistical testing reveals significant differences between experiment and model with respect to several Gini indices and total variations. Only the Gini index of the GCFM and the total variation of the SFM do not produce significant differences (significance level 5%).

Tests based on deviation measures

We are now interested to measure the deviations between bootstrapped and experimental data. Firstly we compute for every bootstrap sample the L^2 norm of the difference between the mean trajectory of the bootstrap sample based on the virtual experimental data and the mean trajectory of the experiment. In this way we obtain an empirical distribution of the L^2-norm distance due to natural fluctuation inside the experiment. This is then compared with the L^2-norm distance of average trajectories between the experiment and the SFM and GCFM model. The same procedure is also carries through for the Hilbert-Schmidt distance between the estimated correlation functions, see Figure 14.

Again, p-values are calculated as in the previous subsection, however this time we have to use one-sided regions of confidence for statistical testing. The p-values are displayed in Table 5.

p-values for L^2 norm		
	EXP/GCFM	EXP/SFM
x-position	0	0
y-position	0.512	0.576

p-values for HS norm		
	EXP/GCFM	EXP/SFM
x-position	0.122	0.434
y-position	0	0

Table 5. The p-values for L^2 norm and Hilbert-Schmidt norm .

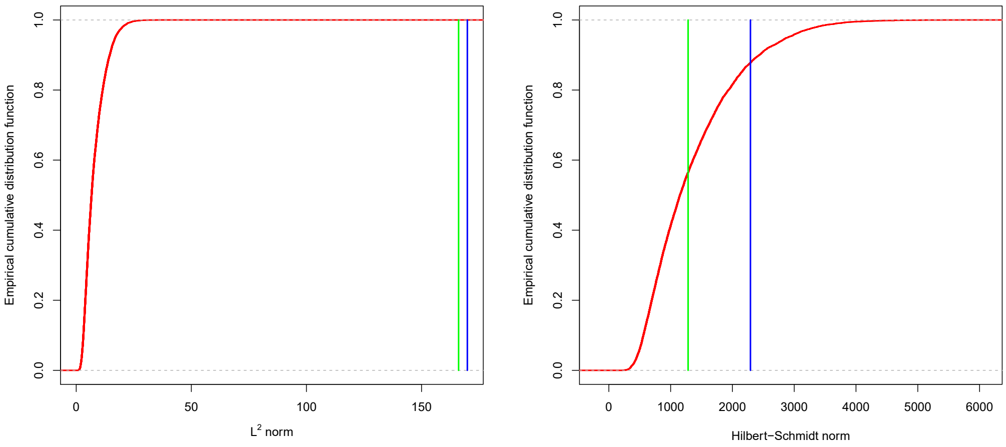

Figure 14. The ECDF of the L^2-norm difference of average x t values (left) and the Hilbert Schmidt (HS) norm difference between covariance functions of x t fluctuations of experimental and bootstrapped data. Green and blue vertical lines show L^2- and HS-norm distance between the experiment SFM and GCFM models respectively.

All statistical tests of the L^2-norm distance between the average x-values and v_x-values of the experiments and the models are highly significant. We find thus a clear indication that model and experiment are statistically distinguished. Not unexpectedly, the situation is different for the average of the y-values over time. Here, due to the axial symmetry of the experimental set up, no major differences of the average y-trajectory can be observed. This also shows that the slight asymmetry in the average y-trajectory in the experimental data is not statistically significant.

With regard to the fluctuation structure, the x-position fluctuations encoded by the empirical correlation function can not be easily distinguished between the SFM model and the experiment. The difference between the fluctuation of the x-trajectories of the GCFM and the experiment also shows a very marginal p-value of 12%, which is not significant when compared to the usual 5%-level of significance. All other fluctuation structures significantly differ between the experiment and the models.

6. Summary

The functional PCA has been applied as a diagnostic tool to assess model quality for agent-based simulations of pedestrian flows with respect to average behavior and beyond. Here we applied it to experimentally measured pedestrian trajectories passing through a bottleneck and agent trajectories simulated by two different force-based models. Both models are a-priori calibrated to satisfy qualitative and quantitative criteria.

Already in the analysis of mean flow behavior, the PCA reveals considerable and statistically significant deviation of both models from the experiment. In the x-direction, the SFM and the GCFM predict slower progress and lower velocities leading to a longer dwell time before the bottle neck, as experimentally observed, although total through flow is being produced correctly. This effect is more pronounced for the GCFM average behavior so that the SFM model reproduces the average behavior of the experiment – for the given set of parameters – in a relatively better way.

Coming to the statistical variations simulated in the SFM for x-position, we find a quite reasonable match in the qualitative behavior (the PCA mode shapes) of the x- and y-position over time. A certain deviation in the quantitative variation strength is observed as well. Again the SFM predictions are a little closer, when measured in terms of the deviation in the total variation. Also, the concentration of variability to dominating modes is under estimated by the SFM and over estimated by the GCFM for the x-variations, while in the velocity variations both models show a higher degree of concentration as compared with the experiment.

Summarizing the PCA gives none of the models a clear "pass", as the SFM and the GCFM both significantly differ from the experiment, although both models were validated quantitatively with respect to the experimental flow through the bottleneck. The SFM however performs relatively better than the GCFM, which is mostly due to a gradually better prediction of the average x-positions and x-velocities.

Caution is needed when applying these (and presumably also other) models to evacuation studies, as the evidently do not capture all features of real life pedestrian flows, as has been shown by our functional data analysis. The overall picture of all the qualitative metrics derived from the PCA however slightly favours the SFM as the more accurate model over the GCFM, given our set of model parameters.

In this case study, applying functional PCA for the first time to pedestrian flows, we have thus shown that it is in fact a useful tool to benchmark and statistically test agent based pedestrian flow models. Given the amount of deviation between experiment and model, it is certainly of interest to use this methodology for the future refinement of pedestrian flow models and for the critical assessment of models used by practitioners.

Acknowledgments

We would like to thank Stefan Rosbach for his preparatory work on the functional PCA analysis for pedestrian data.

References

[1] Bauer, H., Probability Theory, de Gruyter 1995.

[2] Chraibi, M., Seyfried, A., and Schadschneider, A., The generalized centrifugal force model for pedestrian dynamics, *Phys. Rev. E* **82** (2010) 046111.

[3] Traffic and Granular Flow '13, Eds. M. Chraibi, M. Boltes, A. Schadschneider and A. Seyfried, Springer (2015)

[4] Diaconis, P. and Efron, B., Computer-intensive methods in statistics. Scientific American, **248** No. 5 (1983) 116–130.

[5] Fisher, A., Caffo, B., Schwartz, B. and Zipunnikov, V., Fast, Exact Bootstrap Principal Component Analysis for p 1 million, arXiv:1405.0922v3.

[6] Helbing, D., Collective phenomena and states in traffic and self-driven many-particle systems, *Comp. Mater. Sci.* **30** (2004) 180–187.

[7] Helbing, D. and Molnár, P., Social force model for pedestrian dynamics, *Phys. Rev. E* **51** (1995) 4282–4286.

[8] Hoogendoorn, S. P. and Daamen, W., Microscopic Parameter Identification of Pedestrian Models and its Implications to Pedestrian Flow Modeling (Transporttation Research Board Annual Meeting, 2006).

[9] Jian, M., Weiguo, S., Jun, Z., Siuming, L., and Guahgxuan, L., k-Nearest-Neighbor interaction induced self-organized pedestrian counter flow, *Physica A: Statistical Mechanics and its Applications* **389** (2010) 2101–2117.

[10] Johansson, A., Helbing, D., and Shukla, P. K. Specification of the social force pedestrian model by evolutionary adjustment to video tracking data, *Advances in Complex Systems* **10** (2007) 271–288.

[11] Karamouzas, I., Skinner, B., Guy, S. J, A universal power law governing pedestrian interactions, *Phys. Rev. Lett.* **113** (2014) 238701

[12] Lakoba, T. I., Kaup, D. J., and Finkelstein, N. M., Modifications of the Helbing-Molnár-Farkas-Vicsek social force model for pedestrian evolution, *Simulation* **81** (2005) 339–352.

[13] Liao, W., Chraibi, M., Seyfried, A., Zhang, J., Zheng, X. and Zhao, Y. Validation of FDS+Evac for pedestrian simulations in wide bottlenecks, *Intelligent Transportation Systems (ITSC), 2014 IEEE 17th International Conference*, (2014) 554–559.

[14] Molnár, P., Modellierung und Simulation der Dynamik von Fußgängerströmen, Ph.D. Thesis. University Stuttgart 1996.

[15] Nishinari, K., Sugawara, K., and Kaza, Modelling of self-driven particles: Foraging ants and pedestrians, *Physica A* **372** (2006) 132–141.

[16] Parisi, D. R. and Dorso, C. O., Morphological and dynamical aspects of the room evacuation process, *Physica A* **385** (2007) 343–355.

[17] Daamen, W., Duives, C. and Hoogendoorn, S. P. (eds.) *The Conference on Pedestrian and Evacuation Dynamics 2014 (PED 2014)*

[18] Pipes, L. A., An operational analysis of traffic dynamics, *J. Appl. Phys.* **24** (1953) 274 – 281.

[19] Ramsay, J., Hooker, G. and Graves, S. , Functional Data Analysis with R and Matlab, UseR! Series, Springer Dortrecht Heidelberg London New York, 2009.

[20] Ramsay, J. and Silverman, B., Functional Data Analysis, Springer Verlag New York, 2005.

[21] Seyfried, A. and Schadschneider, A., Fundamental Diagram and Validation of Crowd Models, in *Cellular Automata*, eds. Umeo, H., Morishita, S., Nishinari, K., Komatsuzaki, T., and Bandini, S., *Lecture Notes in Computer Science*, Vol. 5191/2008 (Springer, Berlin Heidelberg, 2008), pp. 563–566, doi:10.1007/978-3-540-79992-4.

[22] Seyfried, A.; Boltes, M.; Kähler, J.; Klingsch, W.; Portz, A.; Rupprecht, T.; Schadschneider, A.; Steffen, B. and Winkens,A. Klingsch, W. W. F.; Rogsch, C.; Schadschneider, A. and Schreckenberg, M. (Eds.)Enhanced empirical data for the fundamental diagram and the flow through bottlenecks *Pedestrian and Evacuation Dynamics* Springer Berlin Heidelberg (2010) 145-156

[23] Seyfried, A. and Schadschneider, A., Empirical results for pedestrian dynamics at bottlenecks, in *Parallel Processing and Applied Mathematics*, eds. Wyrzykowski, R., Dongarra, J., Karczewski, K., and Wasniewski, J., *Lecture Notes in Computer Science*, Vol. 6068 (Springer, Berlin Heidelberg, 2010), pp. 575–584, `http://dx.doi.org/10.1007/978-3-642-14403-5_62`.

[24] Seyfried, A., Steffen, B., and Lippert, T., Basics of modelling the pedestrian flow, *Physica A* **368** (2006) 232–238.

[25] Shiwakoti, N., Sarvi, M., Rose, G., and Burd, M., Animal dynamics based approach for modelling pedestrian crowd egress under panic conditions, *Transportation and Traffic Theory* **17** (2011) 438–461.

[26] Schneider, V. and Könnecke, R. Simulating evacuation processes with ASERI, *Pedestrian and Evacuation Dynamics* Springer (2002) 303–314

[27] Steffen, B. and Seyfried, A., Methods for measuring pedestrian density, flow, speed and direction with minimal scatter, *Physica A* **389** (2010) 1902–1910.

[28] TraffGo HT GmbH, Handbuch PedGo 2, PedGo Editor 2, `www.evacuation-simulation.com` (2005)

[29] W. J. Yu, R. Chen, L. Y. Dong and S. Q. Dai, Centrifugal force model for pedestrian dynamics, *Phys. Rev. E*, **72** (2005) p. 026112.

[30] Zhang, J., Klingsch, W., Schadschneider, A., and Seyfried, A., Transitions in pedestrian fundamental diagrams of straight corridors and t-junctions, *J. Stat. Mech.* (2011).

[31] `http://vision-traffic.ptvgroup.com/de/produkte/ptv-viswalk/`

[32] `http://www.legion.com/`

A.11 Article X

Automated Quality Assessment of Space-Continuous Models for Pedestrian Dynamics

V. Kurtc, M. Chraibi, and A. Tordeux

Traffic and Granular Flow '17 (**2017**)

Traffic and Granular Flow ’17, 317-325, Springer, 2019
10.1007/978-3-030-11440-4_35

Automated Quality Assessment of Space-Continuous Models for Pedestrian Dynamics

Valentina Kurtc[1], Mohcine Chraibi[2], Antoine Tordeux[3]

Abstract

In this work we propose a methodology for assessment of pedestrian models continuous in space. With respect to the Kolmogorov-Smirnov distance between two data clouds, representing for instance simulated and the corresponding empirical data, we calculate an evaluation factor between zero and one. Based on the value of the herein developed factor, we make a statement about the goodness of the model under evaluation. Moreover this process can be repeated in an automatic way in order to maximize the above mentioned factor and hence determine the optimal set of model parameters.

Keywords
Validation

[1] *Peter the Great St. Petersburg Polytechnic University, Russia*
[2] *Supercomputing centre, Forschungszentrum Jülich GmbH, 52425 Jülich, Germany*
[3] *School of Mechanical Engineering and Safety Engineering, University of Wuppertal, 42119 Wuppertal, Germany*

Contents

Introduction

Mathematical models have been developed to describe and simulate the dynamics of complex systems. For pedestrian dynamics several kinds of models have been built with different intentions. For an overview of the existing models the reader is referred to [1]. In order to develop and use mathematical models for pedestrian dynamics with high fidelity level, the verification and validation process should be considered as key part in the development cycle.

According to conventional terminology [2] **verification** is the process of assuring if the computer programming and implementation of a mathematical model is correct. The verification process does not assess the quality of mathematical models nor does it allow to make any conclusions related to its realism. In the literature some verification-driven works regarding the goodness-of-fit of a pedestrian model have been published. In [3] several verification tests were recommended to assess the quality of simulations of ships. In the RiMEA project [4] verification tests were proposed to evaluate the quality of pedestrian simulations. Based on the above-mentioned works Ronchi et al. [5] suggested some modified and new verification tests with the aim to additionally consider the movement of pedestrians in case of fire.

Having verified the numerical implementation of the given model, the question that should be of concern is “does the implemented model show sufficient accuracy in emulating the targeted system?” In order to answer this question reliably, an iterative **validation** process is required, that is, comparing the model/simulation results with empirical findings and evaluating their discrepancies to enhance the behavior of the model. Repeating this process leads to a better description of the targeted system (pedestrian dynamics). The process of validation in pedestrian dynamics can benefit from the tremendous development of empirical research. Several experiments were conducted to investigate crowd performances and to build a well-documented database. Empirical research does not only contain data of controlled experiments [6, 7, 8, 9, 10, 11, 12, 13, 14, 15], but also data issued from field studies [16, 17, 18]. These empirical works capture relevant properties of the crowd in *normal* situations and for basic geometries. Examples are unidirectional flows (fundamental diagram), bottleneck (jam formation), counter-flow (lane formation), intersection (e.g. T-junction).

The goal of this paper is to develop an automatic assessment of the predictive capability of pedestrian models. We introduce new quantities, in order to quantify the degree of success (or failure) of a model/simulation with respect to a given set of empirical data. The introduced "validity factor" is a measure for the verification *and* the validation process of a given implementation of a model. In the first stage of the model's assessment (verification) we use tests mostly based on the RiMEA guideline [4]. While in the second stage (validation) we compare the model with experimental data issued from six different experiments: Uni-directional flow (1D and 2D), bi-directional flow, corners, bottlenecks and T-junctions. Comparing the model results with empirical findings and automatically evaluating their discrepancies is important for the validation process as well as for making a precise estimation of its goodness. 1

1. Verification and Validation Tests

We implement two different kinds of tests: verification and validation tests. In the first stage of the pedestrian model assessment, the verification step, we use tests based on the RiMEA guideline [4]. During the validation process we propose to compare the simulation results with experimental data issued from six different experiments: Uni-directional flow (1D and 2D), bi-directional flow, corners, bottlenecks and T-junctions (Fig. 1). The proposed geometries are different in order to cover various dynamics of pedestrians and hence, the validation results may show more significance with respect to empirical findings.

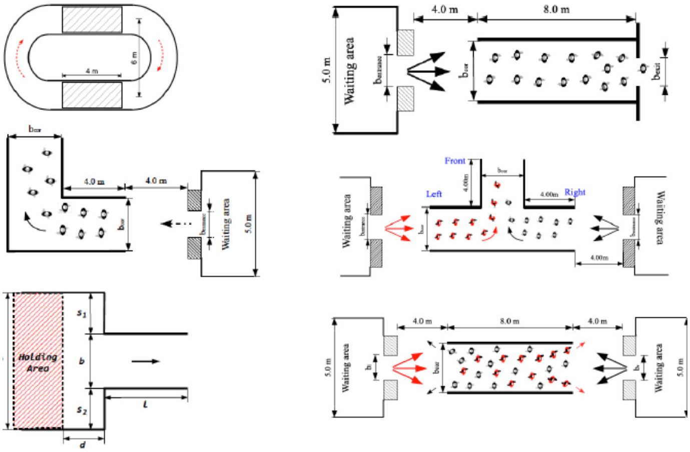

Figure 1. Validation tests: six different experimental set-ups suggested to validate a model.

Considering the pedestrian model and specifying area geometry and initial conditions, which are speed and position of pedestrians, one can compute trajectories of all pedestrians. The simulations are performed with JuPedSim [19, 20], using models [21, 22].

Afterwards, both for simulated and empirical trajectories the fundamental diagram is calculated using one of the measurement methods implemented in the JPSreport module of JuPedSim. For an accurate comparison it is important to use the same measurement method for both the experimental as well as the simulation data.

2. Methodology

This section presents the methodology for quantitative comparison of results obtained from experiments and simulations on basis of the verification and validation tests introduced earlier. Firstly, we suggest the approach for similarity assessment of two fundamental diagrams (speed-density relations), which are the main outcome of the validation tests. This approach exploits the data-binning and cumulative distribution functions calculation. Secondly, the quantitative quality assessment metric is formulated, which aggregates the comparison results of experiments and simulations both for verification and validation tests.

2.1 Comparison of two data clouds

Assessment of validation results is made by means of comparison of two fundamental diagrams (FD), i.e. the speed-density relation. Given observation points of speed and density from experiments $\{\ \rho_i^{\mathrm{data}}, v_i^{\mathrm{data}}\ \}$ and simulations $\{\ \rho_i^{\mathrm{model}}, v_i^{\mathrm{model}}\ \}$, our goal is to quantify the degree of similarity among these two point clouds. Therefore, we create a partitioning of the data points by filtering them according to N equally-spaced density intervals (Fig. 2),

$$V_j^{\mathrm{src}} \quad \{v_i^{\mathrm{src}} : \rho_i^{\mathrm{src}} \in \ \rho_j, \rho_{j\ 1}\ , i \quad 1, \dots, N^{\mathrm{src}}\}, \tag{1}$$

where $j \quad 1, \dots, N, \mathrm{src} \quad \{\mathrm{data},\ \mathrm{model}\}$ and N^{src} is the number of observations. The key idea here is to interpret V_j^{src} as a one-dimensional random variable. Now we calculate the cumulative distribution functions (CDFs) both for the experiment, $F_{V_j^{\mathrm{data}}}\ x$ as well as for the simulations, $F_{V_j^{\mathrm{model}}}\ x$, and calculate the Kolmogorov-Smirnov distance

$$D_j \quad \sup_x |F_{V_j^{\mathrm{data}}}\ x\ - F_{V_j^{\mathrm{model}}}\ x\ |, j \quad 1, \dots, N. \tag{2}$$

Finally, the weighted arithmetic mean of distances D_j is used as a quantitative metric estimating the similarity of two

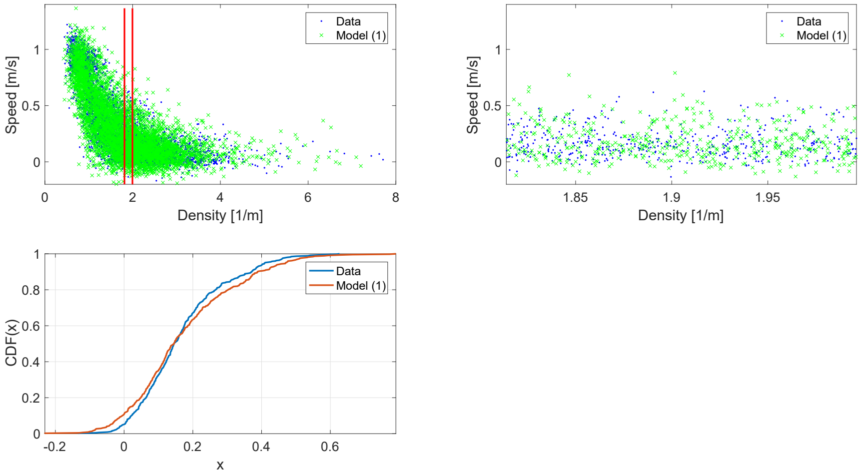

Figure 2. Comparison of simulated (green) and empirical (blue) speed-density relations with data-binning method (upper plots). Cumulative distribution functions for specific bin (bottom plot).

data-clouds

$$D^* \quad \frac{\sum_{j\ 1}^{N} N_j^{\mathrm{data}} \quad N_j^{\mathrm{model}}\ D_j}{N^{\mathrm{data}} \quad N^{\mathrm{mode}l}}, \tag{3}$$

where N_j^{data} and N_j^{model} are the number of observations in the jth bin for data and model respectively. In other words, metric D^* quantifies the degree of success (or failure) of the validation process.

2.2 Validity factor

Verification tests are considered to be relatively simple and are expected to be fulfilled. For each verification test there are only two possible outputs which are 0 (failure) and 1 (success). The quantitative metric for N_{ver} verification tests is

$$\delta_{\mathrm{ver}} \quad \prod_{k\ 1}^{N_{\mathrm{ver}}} v_k^{\mathrm{ver}}, \tag{4}$$

where v_k^{ver} is the outcome of the kth verification test.

We quantify the degree of success of the considered pedestrian model for the k-th validation test with $v_k^{\text{val}} \in [0,1]$. 0 and 1 corresponds to complete failure and absolute success respectively. The value v_k^{val} is computed according to the methodology described in Section 2.1, that is $v_k^{\text{val}} = 1 - D^*$. To quantify the degree of success for N_{val} validation tests we write

$$\delta_{\text{val}} = \frac{\sum_{k=1}^{N_{\text{val}}} w_k \cdot v_k^{\text{val}}}{N_{\text{val}}}, \tag{5}$$

with a weight w_k equal to 1.

However, in general the parameter values of the model are obtained after a calibration process involving several scenarios simultaneously [23]. In this case we calculate w_k as follows

$$w_k = \frac{N_{\text{cal}}}{N_{\text{val}}}, \tag{6}$$

where $N_{\text{cal}} \in [0, N_{\text{val}}]$ is a number of scenarios used simultaneously in the calibration procedure. Eq. (6) expresses the following assumption: it is less beneficial to get the value v_k^{val} by calibration obtained on the basis of one scenario, that is $w_k = \frac{1}{N_{\text{val}}}$, than if we get the same value v_k^{val} with the parameter set from calibration with all scenarios simultaneously ($w_k = 1$).

Finally the success estimator of the considered model on the basis of verification and validation tests is as follows

$$\delta = \delta_{\text{ver}} \times \delta_{\text{val}}. \tag{7}$$

3. Results

We tested this methodology on two continuous pedestrian speed models based on optimal velocity function and specific stochastic additive noises. The noise is white for the first model (Model (1)) [21], while it is determined by the inertial Ornstein-Uhlenbeck process for the second model (Model (2)) [22]. x"In this section we show only results of one of the validation tests – uni-directional 1D flow. In other validation test (except bottleneck scenario) the fundamental diagram is produced by the measurement module (Jpsreport) using Voronoi diagrams (method D). Figure 3 shows the results. The first row represents speed-density relations calculated on the basis of real trajectories and obtained from simulations of Model (1) and Model (2).

We consider 20 bins for the density partitioning of the validation test and limit the observations for densities not higher than $4\,m^{-2}$. For both models and each density bin the Kolmogorov-Smirnov distance is calculated (lower-left subplot of Fig. 3), the mean value of which (Eq. 3) is equal to 0.13 and 0.11 for Model (1) and Model (2) respectively.

Moreover, we investigated how the number of density bins N influences the final value D^*. Considering values of N from 20 to 470 we calculated corresponding values of D^* (bottom-right subplot of Fig. 3). Firstly, one can conclude that Model (2) is always better than Model (1), which is conform with the results in [22]. Secondly, for both models the value of D^* is increasing when the number of bins N is increasing. This can be explained by the fact that, with increasing number of bins, the number of points each bin contains, becomes more scarce. For example, if a bin contains only two points from each compared data set it is obvious that the Kolmogorov-Smirnov distance (Eq. 2) will be large.

4. Discussion and Conclusions

In this paper we present a methodology for quantitative assessment of pedestrian models exploiting results of verification and validation tests. However, this procedure can be applied to any space-continuous model describing pedestrian dynamics. Two stochastic pedestrian models were compared using the results of 1D uni-directional flow test. We investigated stability properties of the proposed metric (3) by considering different number of bins for density partitioning. According to the results, the metric for quantitative assessment shows a monotonic increasing behavior.

More generally, the method of quantitative comparison of two data-clouds (here, two fundamental diagrams) using an averaged Kolmogorov-Smirnov distance D^* (Section 3) can be interpreted as a separate result. In other words, this method can be used for comparison of two data-clouds of any nature.

The approach for comparison of two data-clouds allows a detailed analysis for different density ranges (lower densities, higher densities) by means of Kolmogorov-Smirnov distances per density interval D_j, $j = 1, \ldots, N$. Analyzing values of D_j, it is possible to determine for which density ranges the underlying model performs better wrt. to experimental data.

Finally, the proposed metric (3) can be used in calibration procedure as the minimized objective function. We suggest to use the introduced quantity D^* (3) as a goodness of fit function in calibration procedure.

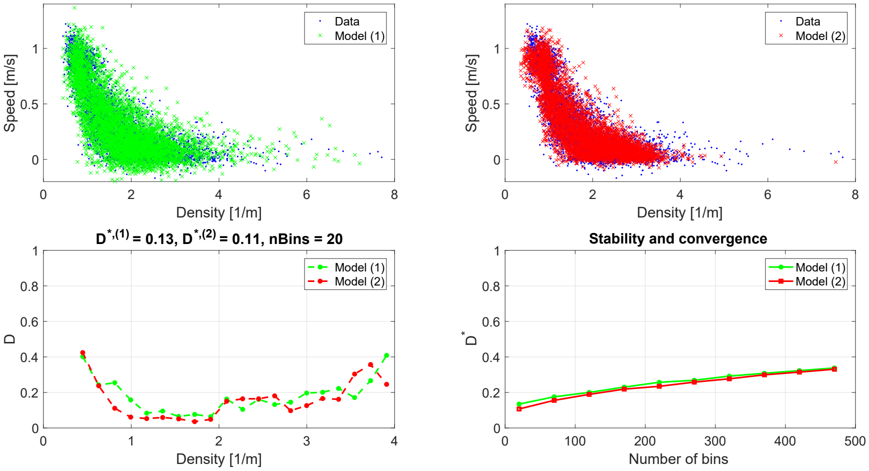

Figure 3. Uni-directional 1D flow. Fundamental diagrams calculated on the basis of real trajectories and trajectories produced with Model (1) (upper-left) and Model (2) (upper-right). The Kolmogorov-Smirnov distance (2) for each density bin (lower-left). The dependence of the value D^* (3) on the number of density bins N.

References

[1] Andreas Schadschneider and Armin Seyfried. Empirical Results for Pedestrian Dynamics and their Implications for Cellular Automata Models. In Harry Timmermans, editor, Pedestrian Behavior, pages 27–43. Emerald Group Publishing Limited, November 2009.

[2] R G Sargent. Verification and validation of simulation models. Journal of Simulation, 7(1):12–24, February 2013.

[3] IMO. REVISED GUIDELINES ON EVACUATION ANALYSIS FOR NEW AND EXISTING PASSENGER SHIPS. Technical report, 2016.

[4] RiMEA. Guideline for Microscopic Evacuation Analysis. Technical Report 3.0, 2009.

[5] E. Ronchi, S. M. V. Gwynne, D. A. Purser, and P. Colonna. Representation of the Impact of Smoke on Agent Walking Speeds in Evacuation Models. Fire Technology, 49(2):411–431, April 2013.

[6] Serge P. Hoogendoorn and Piet H. L. Bovy. Pedestrian Travel Behavior Modeling. Networks and Spatial Economics, 5(2):193–216, June 2005.

[7] Tobias Kretz and Michael Schreckenberg. The F.A.S.T.-Model. In Samira El Yacoubi, Bastien Chopard, and Stefania Bandini, editors, Cellular Automata, pages 712–715, Berlin, Heidelberg, 2006. Springer.

[8] Tobias Kretz, Marko Wölki, and Michael Schreckenberg. Characterizing correlations of flow oscillations at bottlenecks. Journal of Statistical Mechanics: Theory and Experiment, 2006(02):P02005–P02005, February 2006.

[9] Xuan Liu, Weiguo Song, and Jun Zhang. Extraction and quantitative analysis of microscopic evacuation characteristics based on digital image processing. Physica A: Statistical Mechanics and its Applications, 388(13):2717–2726, July 2009.

[10] Ujjal Chattaraj, Armin Seyfried, and Partha Chakroborty. COMPARISON OF PEDESTRIAN FUNDAMENTAL DIAGRAM ACROSS CULTURES. Advances in Complex Systems, 12(03):393–405, June 2009.

[11] Mehdi Moussaïd, Dirk Helbing, Simon Garnier, Anders Johansson, Maud Combe, and Guy Theraulaz. Experimental study of the behavioural mechanisms underlying self-organization in human crowds. Proceedings of the Royal Society B: Biological Sciences, 276(1668):2755–2762, August 2009.

[12] Maik Boltes, Jun Zhang, Armin Seyfried, and Bernhard Steffen. T-junction: Experiments, trajectory collection, and analysis. In 2011 IEEE International Conference on Computer Vision Workshops (ICCV Workshops), pages 158–165, Barcelona, Spain, November 2011. IEEE.

[13] Asja Jelić, Cécile Appert-Rolland, Samuel Lemercier, and Julien Pettré. Properties of pedestrians walking in line. II. Stepping behavior. Physical Review E, 86(4):046111, 2012.

[14] Stefan Holl and Armin Seyfried. Laboratory experiments on crowd dynamics. inSiDE (Innovatives Supercomputing in Deutschland), 11(2), 2013.

[15] Sebastian Burghardt, Armin Seyfried, and Wolfram Klingsch. Fundamental Diagram of Stairs: Critical Review and Topographical Measurements. In Ulrich Weidmann, Uwe Kirsch, and Michael Schreckenberg, editors, Pedestrian and Evacuation Dynamics 2012, pages 329–344, Cham, 2014. Springer International Publishing.

[16] S Burghardt, A Seyfried, and W Klingsch. Improving egress design through measurement and correct interpretation of the fundamental diagram for stairs. Developments in Road Transportation, pages 181–187, 2010.

[17] Sebastian Burghardt. Dynamik von Personenströmen in Sportstadien. PhD thesis, Bergische Universität Wuppertal, June 2013.

[18] Stefan Seer, Norbert Brändle, and Carlo Ratti. Kinects and human kinetics: A new approach for studying pedestrian behavior. Transportation Research Part C: Emerging Technologies, 48:212–228, November 2014.

[19] Armel Ulrich Kemloh Wagoum, Mohcine Chraibi, and Jun Zhang. JuPedSim: An open framework for simulating and analyzing the dynamics of pedestrians. In 3rd Conference of Transportation Research Group of India. SUMO Conference 2016, Berlin (Germany), 23 May 2016 - 25 May 2016, 2015.

[20] Development Core Team. JuPedSim.

[21] Antoine Tordeux, Mohcine Chraibi, and Armin Seyfried. Collision-Free Speed Model for Pedestrian Dynamics. In Victor L. Knoop and Winnie Daamen, editors, Traffic and Granular Flow ’15, pages 225–232, Cham, 2016. Springer International Publishing.

[22] Antoine Tordeux and Andreas Schadschneider. White and relaxed noises in optimal velocity models for pedestrian flow with stop-and-go waves. Journal of Physics A: Mathematical and Theoretical, 49(18):185101, May 2016.

[23] Mario Campanella, Serge Hoogendoorn, and Winnie Daamen. Quantitative and Qualitative Validation Procedure for General Use of Pedestrian Models. In Ulrich Weidmann, Uwe Kirsch, and Michael Schreckenberg, editors, Pedestrian and Evacuation Dynamics 2012, pages 891–905, Cham, 2014. Springer International Publishing.

A.12 Article XI

A microscopic method for the evaluating of continuous pedestrian dynamic models

---

Z Huang, M. Chraibi, S. Cao, C. Huang, Z. Fang, and W. Song

Physica A: Statistical Mechanics and its Applications (2019)

Physica A: Statistical Mechanics and its Applications, 536, 122461, 2019
10.1016/j.physa.2019.122461

A microscopic method for the evaluating of continuous pedestrian dynamic models

Zhongyi Huang[1]*, Mohcine Chraibi[2], Shuchao Cao[3], Chuanli Huang[1], Zhiming Fang[4], Weiguo Song[1]

Abstract
In this paper, we propose a microscopic method to evaluate continuous pedestrian dynamic models at the trajectory level. By comparing the experimental and the simulated trajectory in four directions, the evaluation of the model can be described by a radar chart, with which both qualitative and quantitative conclusions can be obtained. In order to demonstrate our method, we evaluate a social force model by 1,936 trajectories with graded densities in three different scenarios. Three qualitative conclusions are obtained by observing radar charts of the simulation of the unidirectional experiments. All of them are verified by the comparison of the macroscopic parameters. Besides, we find that a model with smaller error in our method always has a better performance at the macroscopic level. At last, the possible quantitative descriptions of the method are discussed. Compared to the evaluations by comparing collective features like fundamental diagram, our method is general, comprehensive and quantitative. The method provides a new possibility to evaluate any continuous pedestrian dynamic model in any scenario with a standard process.

Keywords
Validation

[1] *State key Laboratory of Fire Science, University of Science and Technology of China, Hefei 230027, China*
[2] *Institute for Advanced Simulation, Forschungszentrum Jülich, Jülich 52425, Germany*
[3] *School of Automotive and Traffic Engineering, Jiangsu University, Zhenjiang 212013, China*
[4] *Business School, University of Shanghai for Science and Technology, Shanghai 200093, China*

Contents

Introduction

The modeling of pedestrian movements has been a hot topic in the past decades for its wide application in architecture [1], safety engineering [2, 3], urban planning [4], robotics and animation [5]. A large number of models, such as cellular automata (CA) [6, 7, 8], force-based models [9, 10, 11], velocity based models [12], Goal-oriented models [13, 14, 15], and the optimal step model (OSM) [16, 17] have been developed. To make the models more realistic, calibrating and validating processes are necessary before applying the modeling results into practice.

In the process of calibrating and validating, a generalized evaluating method and a diverse experimental database are important. In this paper, we divide the existing evaluating methods into macroscopic and microscopic with respect to the level of the data they use. Collective characteristics such as flow rate [18, 19], movement time [20], the relation between velocity and density (known as fundamental diagram) [11] or their combinations [21] are often used in the macroscopic methods. Macroscopic methods are straightforward, for the reason that some characteristics are the main focus for the application of the model. Besides, there are some well-know collective benchmarks [22, 23]. Nevertheless, there are some common problems in the macroscopic methods. At fist, macroscopic evaluating methods are always qualitative, which is a barrier when a comparison between different models has to be made. In [24], the shape of the curve plotted from pedestrian number inside the corridor as a function of time is compared between simulations and experiments. In [21], experimental and simulation trajectories are compared by the overlap of the trajectories. Although from these comparisons it is possible to draw some conclusions with respect to experimental data, it is however difficult to perform evaluations and ratings when a lot of models, which have different shapes of curves and distributions of trajectories, have to be compared with each other. Secondly, the applicability of the macroscopic methods in different scenarios is limited and can be scenario specific. For example, the movement time is always used in the bottleneck scenario, while it could be meaningless when describing pedestrian movements in a corridor. Finally, it is possible that a model has considerable accuracy when evaluated with a macroscopic feature while has big error when evaluated with another feature. This phenomenon has been described in [21], in which the simulation flow matches the experimental flow well by adjusting parameters, while the time series of density still show obvious discrepancies with respect to experiments. The reason is summarized as that the coincident flow through bottleneck is actually achieved by the discrepant density and velocity [21].

The microscopic method is usually defined at the trajectory level. Simulating the movement of one pedestrian with a spacial continuous model while the other pedestrians are moving according to the experimental trajectories, we can get a simulated trajectory of a specific participant. In [25, 26], error (e) is defined based on acceleration difference between simulated and experimental trajectories:

$$e = \sum_{i} \sum_{t=t_i^{start}}^{t_i^{end}} [(\tilde{f}_i^x(t) - f_i^x(t))^2 + (\tilde{f}_i^y(t) - f_i^y(t))^2], \tag{1}$$

where i is a pedestrian, t is the time stamp, $[\tilde{f}_i^x(t), \tilde{f}_i^y(t)]$ is the acceleration at time t obtained from experimental trajectory, and $[f_i^x(t), f_i^y(t)]$ is the acceleration simulated by a social-force-based model at time t. According to the definition, the comparison is based on the second derivation of a trajectory. This method has been criticized by the authors of Ref. [25] themselves in their another work [27], in which they think the body sway affects the acceleration obtained from head trajectories, while the effect is not considered in the social force model. Besides, the acceleration is sensitive to small noises of a trajectory. In our opinion, it is also a limitation of the model if it can only be used in the evaluating of the force-based models. Hence in [27, 28], e is based on the position rather than the acceleration of pedestrians:

$$e = \sum_{i} \sum_{t=t_i^{start}}^{t_i^{end}} D(p_i(t), \tilde{p}_i(t))^2 / (t_i^{out} - t_i^{in}) / A, \tag{2}$$

where $p_i(t)$ is the measured position of pedestrian i at time t. $\tilde{p}_i(t)$ is the simulated position. The function $D()$ is to solve the distance between two points. Because of trajectories in the simulation and in the experiment are only synchronized when a pedestrian entering a scenario, e in this method will be sensitive to the direction discrepancy and the length of the trajectory. Imagining that if a small direction discrepancy happens at the beginning of the simulation, the error obtained by Eq. 2 will be amplified with the increasing of the trajectory length. This problem is improved in [29], in which the pedestrians in the simulation and in the experiment are synchronized every 1.5 s. Although the existing microscopic evaluating methods are able to optimize parameters of a model, there are some problems when applying them to evaluate a model. The main problem is that the errors in existing microscopic methods are one dimensional, from which we can only know the performance of a model is better or worse than another model. However, what results in the performance difference can not be speculated from the results described by numbers.

Besides, trajectory data used in existing microscopic estimation methods are singular: bidirectional trajectories in corridors [28] or several observation scenarios [27, 29]. Comprehensive evaluation in different densities and scenarios are still rare. In this paper, we evaluate a continuous model with a directional microscopic method. The method is proposed in Section 1. Based on the method a model introduced in Section 2 is evaluated in Section 3. At last, we discuss the results in Section 4.

1. Methods

To avoid the problems mentioned in Section , a generalized method is designed to include the following features:

- Independent of the used scenario,
- able to get rich information from one trajectory,
- insensitive to the length of trajectory,
- and the evaluated results have a directional physical meaning.

The original trajectory of a pedestrian i (j_i^{ori}) used in the method is the positions at continuous time steps:

$$j_i^{ori} = \{\boldsymbol{r}_{i,n}^{ori} | n = 0, 1, 2, ...\}, \tag{3}$$

where $\boldsymbol{r}_{i,n}^{ori}$ is the pedestrian position at the n-th time step. Extracting head positions from top-view videos could be the most common used method to obtain a trajectory. To reduce the influence of the swing of the head, the trajectory should be smoothed before solving the velocity. The smoothing method and the velocity solving method are introduced in Appendix A. If the evaluation is conducted on each time step, the result of the model will be sensitive to small errors, especially the angular error defined in Eq. 6. So the trajectory is resmapled after smoothing. The resampling method is also introduced in Appendix A. Furthermore, an area selection technique is provided to conduct an evaluation in a specific area A. A point in j_i^{res} (a trajectory after the resampling) belongs to j_i^{slc} (the trajectory after the selection) if it is inside A:

$$j_i^{slc} = \{\boldsymbol{r}_{i,k}^{smt} | \boldsymbol{r}_{i,k}^{smt} \in A, k \in \{0, N, 2N, ...\}\}.\tag{4}$$ [1]

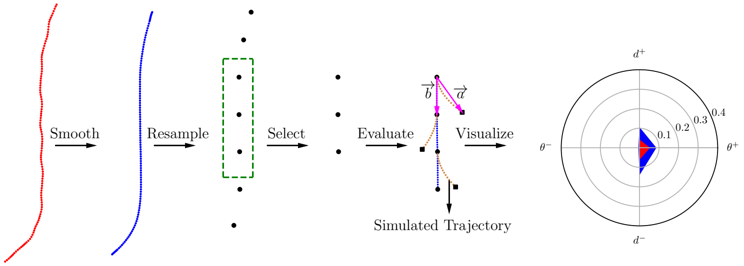

(a) j^{ori} (b) j^{smt} (c) j^{res} (d) j^{slc} (e) $\vec{a}, \vec{b}$ (f) $e_{exp}(x_i)$

Fig. 1. The procedures of the trajectory processing and the evaluation.

The procedures of the trajectory processing are shown in Fig. 1 (a)-(d). In the following, we define the microscopic error by comparing trajectories in the simulation and in the experiment. At time step k in j_i^{slc}, all agents in the simulation have the same position and velocity with the pedestrians in the experiment. The movement of pedestrian i is simulated with a continuous model until $k+N$, while the other pedestrians are moved exactly as their smoothed trajectories in the experiment. The distance error d and the angular error θ are

$$\begin{aligned} d(k) &= (||\boldsymbol{a}|| - ||\boldsymbol{b}||)/D, \\ \theta(k) &= \arcsin\left(\frac{\boldsymbol{a} \times \boldsymbol{b}}{||\boldsymbol{a}||||\boldsymbol{b}||}\right)/\Theta, \\ \boldsymbol{a} &= \mathrm{r}_i^{sim}(k+N) - \mathrm{r}_i^{smt}(k), \\ \boldsymbol{b} &= \mathrm{r}_i^{smt}(k+N) - \mathrm{r}_i^{smt}(k), \end{aligned} \tag{5}$$

where $\mathrm{r}_i^{sim}(k)$ is the pedestrian position at the k-th time step in the simulation. $D = 1$ m and $\Theta = 1$ rad are the normalized parameters. According to the definition and Fig. 1 (e), $\boldsymbol{a}$ is the motion vector of the pedestrian in the simulation, and $\boldsymbol{b}$ is the motion vector in the experiment. Therefore, when $d(k) > 0$, the mean speed in the simulation is larger than that in the experiment. When $\theta(k) > 0$, the direction of the velocity has a bias to right when comparing to that in the experiment. Based on d and θ, the error of the frame $e_{fra}(k)$ is

$$e_{fra}(k) = \{d^+(k), d^-(k), \theta^+(k), \theta^-(k)\}, \tag{6}$$

where $d^+ = ||d||$, $d^- = 0$ when $d \geq 0$. $d^+ = 0$, $d^- = ||d||$ when $d < 0$. θ^+ and θ^- are obtained with a similar manner. The four elements describe the error of the speed and the direction in positive and negative respectively. The error of the trajectory $e_{trj}(j_i)$ is

$$e_{trj}(j_i) = \{\mu_{d^+}(j_i), \mu_{d^-}(j_i), \mu_{\theta^+}(j_i), \mu_{\theta^-}(j_i)\}, \tag{7}$$

where $\mu_{d^+}(j_i) = \frac{1}{n_k}\sum d^+(k)$ is the mean value of all frames in the direction of d^+ (n_k is the number of frame in j_i^{slc}). $\mu_{d^-}(j_i)$, $\mu_{\theta^+}(j_i)$, and $\mu_{\theta^-}(j_i)$ can be solved analogically. According to the definition, $e_{trj}(j_i)$ describes the mean errors of a trajectory in the four directions. At last, the error of the experiment $e_{exp}(x_i)$ is

$$e_{exp}(x_i) = \{\{\mu_{d^+}(x_i), \sigma_{d^+}(x_i)\}, \{\mu_{d^-}(x_i), \sigma_{d^-}(x_i)\}, \{\mu_{\theta^+}(x_i), \sigma_{\theta^+}(x_i)\}, \{\mu_{\theta^-}(x_i), \sigma_{\theta^-}(x_i)\}. \tag{8}$$

Each item of $e_{exp}(x_i)$ is composed of the mean value and the standard deviation of all trajectories in the specific direction:

$$\begin{aligned} \mu_{d^+}(x_i) &= \frac{1}{n_j}\sum d^+(j_i), \\ \sigma_{d^+}(x_i) &= \sqrt{\frac{1}{n_j}\sum (d^+(j_i) - \mu_{d^+}(x_i))^2}, \end{aligned} \tag{9}$$

where n_j is the number of trajectories in the experiment. $e_{exp}(x_i)$ can be visualized with a radar chart (also referred as a error chart of an experiment). As shown in Fig. 1 (f), the vertex of inside polygon is the mean value. The vertex of the outside polygon is the sum of mean value and the standard deviation. Synthesizing the mean values, the standard deviations and the symmetry of the chart, the evaluation result can be described with a number $E(x_i)$:

$$E(x_i) = \exp\left(P(x_i) + S(x_i) + Y(x_i)\right), \tag{10}$$

where

$$P = \mu_{d^+} + \mu_{d^-} + \mu_{\theta^+} + \mu_{\theta^-}$$

is the sum of the mean values (referred as the precision of the model),

$$S = \sigma_{d^+} + \sigma_{d^-} + \sigma_{\theta^+} + \sigma_{\theta^-}$$

is the sum of the standard deviations (referred as the stability of the model), and

$$Y = \left(\frac{|(\mu_{d^+} + \sigma_{d^+}) - (\mu_{d^-} + \sigma_{d^-})|}{|(\mu_{d^+} + \sigma_{d^+}) + (\mu_{d^-} + \sigma_{d^-})|} + \frac{|(\mu_{\theta^+} + \sigma_{\theta^+}) - (\mu_{\theta^-} + \sigma_{\theta^-})|}{|(\mu_{\theta^+} + \sigma_{\theta^+}) + (\mu_{\theta^-} + \sigma_{\theta^-})|}\right)/2$$

is the symmetric factor of the outside polygon in the radar chart (referred as the symmetry of the model).

2. Materials

Specification of the Social Force Model

The circular specification of the social force model [29, 30] is selected to demonstrate the evaluation process of the method. In this model, velocity is calculated with an acceleration equation when no physical contact happens between pedestrians:

$$\frac{d\mathrm{v}_i}{dt} = \frac{v_i^0\mathrm{e}_i - \mathrm{v}_i}{\tau_i} + \sum_{j(\neq i)} \boldsymbol{f}_{ij}(t) + \sum_w \boldsymbol{f}_{iw}(t). \tag{11}$$

The first term is the desire force, which describes the pedestrian is willing to move to a desire direction $\boldsymbol{e}_i$ with a desire speed v_i^0. $\boldsymbol{v}_i$ is the velocity. τ_i is the relaxation time (the time needed to accelerate to desire velocity). $\boldsymbol{f}_{ij}$ is the repulsive force between pedestrian i and pedestrian j:

$$\boldsymbol{f}_{ij}(t) = \sum_j A_i e^{(R_i+R_j-||\mathrm{d}_{ij}||)/B_i} \frac{\mathrm{d}_{ij}}{||\mathrm{d}_{ij}||} \cdot w(\varphi_{ij}), \tag{12}$$

where d_{ij} is the vector point from j to i. R_i and R_j are the radius of the pedestrian. In our evaluation, $R = 0.25$ m. A_i reflects the strength of interaction, and B_i corresponds to the interaction range. $w(\varphi_{ij})$ is the anisotropy factor describing the different reactions of a pedestrian to what happens in front and behind:

$$w(\varphi_{ij}) = \lambda + (1-\lambda)\frac{1+\cos(\varphi_{ij})}{2}, \tag{13}$$

$$\cos(\varphi_{ij}) = \frac{\mathrm{v}_i}{||\mathrm{v}_i||} \cdot \frac{-\mathrm{d}_{ij}}{||\mathrm{d}_{ij}||}. \tag{14}$$

The repulsive force of wall has a similar form with Eq. (12):

$$\boldsymbol{f}_{wi}(t) = A_w e^{(R_i - ||\mathrm{d}_{iw}||)/B_w} \frac{\mathrm{d}_{iw}}{||\mathrm{d}_{iw}||}, \tag{15}$$

in which d_{iw} is the vector points from the pedestrian to the point on the wall which has the minimal distance to the pedestrian. Parameters listed in Table 1 are the calibration results of the evolutionary adjustment from three observation experiments [29]. P_1 is the calibration results without considering the anisotropy ($\lambda = 1$), and P_2 is the optimal parameters with an appropriate anisotropy factor ($\lambda = 0.12$). Note that in [30], the parameters of the repulsive forces of the wall and the pedestrians are not distinguished. So A_w and B_w are the same with A_i and B_i in P_1 and P_2. P_3 is the adjusting result of this paper.

Table 1. Parameter sets in Ref. [29] and in this paper.

Parameters	A_w	B_w	A_i	B_i	λ	τ
P_1	0.11	0.84	0.11	0.84	1	0.5
P_2	0.42	1.65	0.42	1.65	0.12	0.5
P_3	0.80	0.30	0.42	1.25	0.12	0.5

Trajectory Database

Trajectories used in the evaluation come from PED Data Archive [2], which are extracted automatically from video recordings of controlled experiments by using the software PeTrack [31]. Experiments of unidirectional, bottleneck, bidirectional scenarios are involved in the evaluation. Sketches of these scenarios are shown in Fig. 2, in which pedestrians start from the waiting area (blue rectangle in Fig. 2), then cross the corridor with an expected exit (red dashed line in Fig. 2). Density in the corridor is controlled by the width of entrance b_{in} and the number of pedestrians in the waiting area.

All participants walk from the left to the right to cross the corridor in unidirectional and bottleneck experiments(more details of the experiments can be found in [32]). In bidirectional experiments, participants are asked to leave the corridor by left or right side according to a number given to them in advance. We simulate the process by setting four virtual exits. As shown in Fig. 2 (c), the width of each exit is 1/3 of the total width. The desire exit is assigned the one which is more close to the pedestrian when he or she leaves the corridor. More information about the bidirectional experiments can be found in [33]. To reduce the influence of the entrance and the exit, investigation areas are selected as the middle part in the corridor (yellow areas in Fig. 2). Parameters of the experiments are shown in Table 2. According to [32, 33], the desire speed is $v_0 = 1.5$ m/s in the experiments.

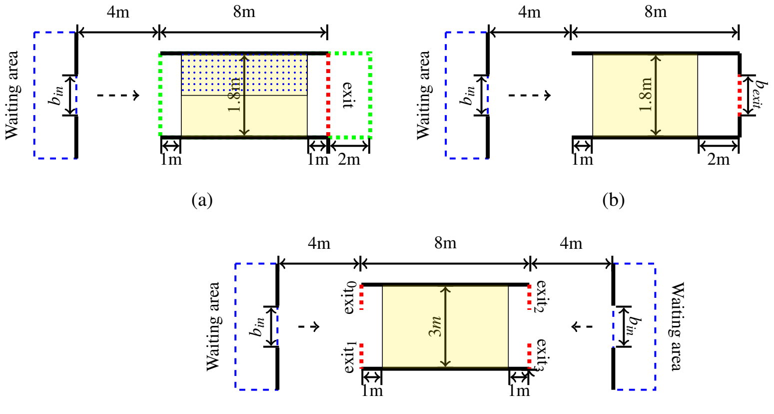

(a) (b)

(c)

Fig. 2. Sketch of experiments in different scenarios. (a) Unidirectional scenario. (b) Bottleneck scenario. (c) Bidirectional scenario.

3. Results

---

[2] http://ped.fz-juelich.de/db

Table 2. Experiment parameters. In bidirectional experiments, the two numbers of "Participant number" are the pedestrians in the left and right waiting area respectively. $\overline{\rho}$ is the mean density in the investigation area.

Scenario	Experiment	Participant number	b_{in}(m)	b_{exit}(m)	$\overline{\rho}$(ped/m^2 or m)
Unidirectional	U_1	61	0.50	-	0.40
	U_2	66	0.60	-	0.46
	U_3	111	0.70	-	0.57
	U_4	121	1.00	-	0.93
	U_5	175	1.45	-	1.30
	U_6	220	1.80	-	1.38
Bottleneck	T_1	170	1.80	1.20	1.63
	T_2	159	1.80	0.95	1.93
	T_3	148	1.80	0.70	2.24
Bidirectional	B_1	54/71	0.50	-	0.42
	B_2	61/86	0.75	-	0.65
	B_3	119/97	0.85	-	0.97
	B_4	125/105	1.00	-	1.33

microscopic evaluation in unidirectional scenario

By observing the error charts of the parameter set P_1, we find that the speed in the simulation is much larger than that in the experiment, especially in high density situations. The radar chart of $e_{exp}(U_5)$ with P_1 is shown in Fig. 3(a), in which the simulated speed is much larger than the actual speed in experiment. The possible reason could be that the repulsive force between pedestrians is too weak. We adjust the force by increasing A_i to 0.50. However, according to Fig. 3(b), the symmetry has no improvement while the stability becomes even worse. The reason should be that when $\lambda = 1$, repulsive forces from front and back pedestrians are similar in most cases when the pedestrian is walking in the controlled experiments. The forces will be counteracted by each other along the walking direction. Further increasing A_i does not slow down the pedestrian. While after considering the anisotropy ($\lambda = 0.12$), the speed becomes smaller (see Fig. 3(C)), and there is a significant improvement of the symmetry. In summary, a systematic error (bias to d^+) will be caused when using isotropous repulsive force between pedestrians.

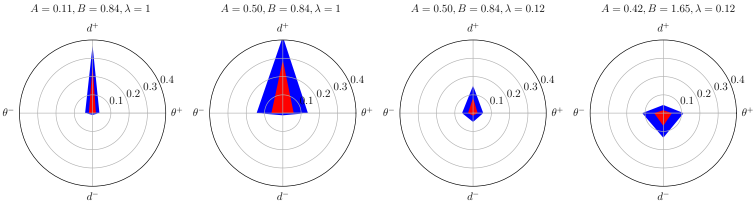
$A = 0.11, B = 0.84, \lambda = 1$ $A = 0.50, B = 0.84, \lambda = 1$ $A = 0.50, B = 0.84, \lambda = 0.12$ $A = 0.42, B = 1.65, \lambda = 0.12$

(a) (b) (c) (d)

Fig. 3. Radar chart of $e_{exp}(U_5)$ with different A, B and λ

The error chart of $e_{exp}(U_5)$ with P_2 is shown in Fig. 3 (d). Compared to the Fig. 3 (c), the speed becomes smaller, while the error of direction (θ^+ and θ^-) becomes larger. Considering the strength factor A_i in Fig. 3 (c) is smaller than that in Fig. 3 (d), but the speed is much slower, we suspect that the effective range factor B_i is too large in P_2, since with a large B_i, more neighbors will have significant influence to the pedestrian. Sequentially, the speed will be smaller. If a pedestrian is close to the wall, the crowd around her will be asymmetric. As a result, the direction error (θ^+ and θ^-) will be large in such a case.

Furthermore, the performance of the wall repulsive force (Eq. 15) can be evaluated with the error chart of the dot area in Fig. 2(a), which is the upper half of the yellow area. According to Fig. 4, the simulated trajectories drift away from the wall in low density, while drift toward the wall in high density. It means that the repulsive force is too strong in low density and too weak in high density. This is due to the fact that a wall acts like a static pedestrian, if the repulsive forces of wall-pedestrians and pedestrian-pedestrian have the same strength parameter. In low density, there are less lateral agents around the pedestrian. In addition to the anisotropy is not considered in Eq. 15, the lateral force exerted by the wall will be larger than the repulsive force of pedestrians in most cases. In high density, however, the lateral force of pedestrians increases significantly while the force of wall remains unchanged. We think this problem can be improved by increasing A_w and decreasing B_w to obtain a stronger wall repulsive force near the wall, and a weaker wall repulsive force far from the wall.

In summary, three conclusions are obtained with the microscopic evaluation:

1. The simulated speed is too large in high density situations with P_1.

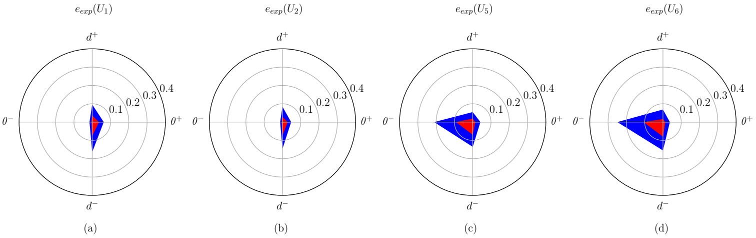

Fig. 4. Evaluations of dot area in unidirectional experiments.

2. The simulated speed is too small in high density situations with P_2.
3. The pedestrians are too close to the wall in high density situations with P_2.

macroscopic verification in unidirectional scenario

To verify the conclusions in Sec. 3, we simulate the movements of all pedestrian with the following rules:

1. Pedestrians move as in the experiments before they enter the simulation field.
2. Pedestrians are driven by the model when they are in the simulation field.
3. Pedestrians are removed when they are outside the simulation field.

The simulation field of the unidirectional scenario is the green box in Fig. 2 (a). In experiments, pedestrians still move to leave the scenario after they walk out of the corridor. Hence, simulation field is two meters longer than the corridor. Then we can make a comparison with some macroscopic features. At first, the trajectories of U_6 in the experiment and the simulations are shown in Fig 5. For clarity, ten percent of trajectories are displayed.

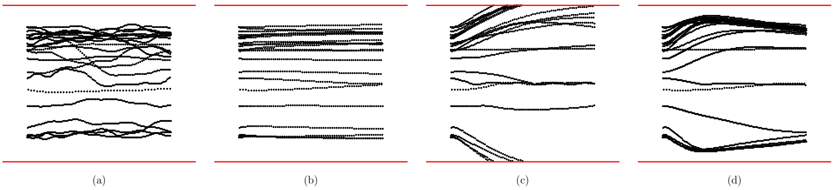

Fig. 5. Experimental and simulated trajectories of U_6. (a) Experimental trajectories. (b) Simulated with P_1. (c) Simulated with P_2. (d) Simulated with $A_w = 0.80$, $B_w = 0.30$.

As shown in Fig. 5 (c), some trajectories near the wall intersect with the wall. It indicates that the wall repulsive force is too small with P_2 and some pedestrians are pushed outside the wall in high density. Therefore, conclusion (3) is correct.

Then we verify the conclusions (1) and (2) by comparing the mean speed. According to Fig. 6 (a), the mean speed of all pedestrians in the simulation with P_1 is close to the free speed 1.5 m/s in the whole simulation. While in the experiment, the speed decreases clearly with more pedestrians entering the investigation area. It indicates that the isotropous social force between pedestrians is unable to slow down the pedestrians in U_6. Therefore, conclusion (1) is correct.

However, according to Fig. 6 (a), in most time steps the mean speed with P_2 is also larger than that in the experiment, rather than smaller as shown in Fig. 3 (d). We think the main reason is that in the simulation of the macroscopic evaluation, some pedestrians are removed when they cross the wall, so that it is irrational to verify conclusion (2) by comparing the speed of the crowd directly. Considering no pedestrian crosses the wall with P_1 (see Fig. 5 (a)), we think that conclusion (1) still holds. Hence, the wall repulsive force should be adjusted first before verifying conclusion (2).

According to the fact mentioned in Sec. 3, A_w should be increased and B_w should be decreased. The trajectories simulated with $A_w = 0.80$, $B_w = 0.30$ (the other parameters are the same with the values in P_2) are shown in Fig. 5 (d), in which all pedestrians move inside the investigation area. Then we compare the mean speed in Fig. 6 (b). In most time steps, the speed in the simulation is smaller than that in the experiment. The conclusion (2) is verified. Furthermore, we follow the fact mentioned in Sec. 3 to decrease B_i in P_2. The error chart with $B_i = 1.25$ is shown in Fig. 7. Both the inner

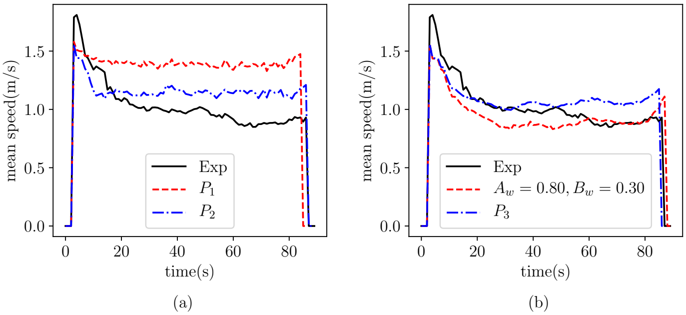

Fig. 6. The comparison of the speed in the experiment and the simulations.

polygon and the outer polygon are small and symmetrical. As it is shown in Fig. 6 (b), the macroscopic parameter (mean speed) also shows a good agreement with the experiment.

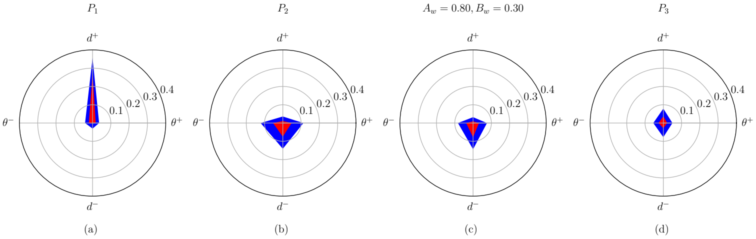

Fig. 7. The error charts of $e_{exp}(U_6)$ with different parameter sets.

In summary, all of the three conclusions deduced from the error charts of the microscopic evaluation method are verified by the macroscopic comparisons. The directions of the bias in the error charts have good agreements with the macroscopic evaluations. Most of all, according to Fig. 6 and 7, a parameter set with a smaller error at the microscopic level always has a better performance at the macroscopic level.

Quantitative results of the microscopic evaluation

Evaluating all experiments with the microscopic method, we get a comprehensive and quantitative assessment of the investigated model. The evaluation results of P_2 and P_3 are shown in Table. 3. From the table we can see that from P_2 to P_3, the improvement is significant in unidirectional and bidirectional experiments, especially in high density situations. While the improvement is not significant in bottleneck experiments. When focusing on P_2 and P_3 respectively, we find that P_2 has a better performance in low density, unidirectional and bottle neck scenarios. P_3 has a better performance in high density, unidirectional and bidirectional scenarios. This implies the parameter are “optimal” only with respect to a specific scenario and density . If a threshold ($E = 1.55$) is set for the applicability, we can obtain a quantitative description of P_3. Based on the evaluation results of trajectories database of this paper, P_3 is applicable in unidirectional scenario with a mean density ranges from 0.93 to 1.38 ped/m^2. However, the threshold may be different when applying the model to different scenarios.

4. Conclusion

In this paper, we propose a microscopic method to evaluate a continuous model by means of the trajectories. The microscopic error of a trajectory is defined in four directions, which corresponds to the positive and the negative deviations of the speed and the direction respectively. The microscopic error of an experiment, which can be visualized by a radar chart, is then defined as the mean values and standard deviations of all trajectories in the experiment. Qualitative conclusions can be deduced from the radar chart. Synthesizing the vertex values and the shape of the radar chart, the evaluation result is finally described by a quantitative value.

With the microscopic method, a social force model is evaluated with 1,936 trajectories in three different scenarios. Based on the error charts of unidirectional experiments, three qualitative conclusions are summarized. Some suggestions

Table 3. Quantitative evaluation results of P_2 and P_3.

x_i	$\exp(P(x_i))$		$\exp(S(x_i))$		$\exp(Y(x_i))$		$E(x_i)$	
	P_2	P_3	P_2	P_3	P_2	P_3	P_2	P_3
U_1	1.18	1.16	1.22	1.21	1.25	1.21	1.80	1.70
U_2	1.16	1.15	1.19	1.20	1.31	1.20	1.81	1.70
U_3	1.12	1.23	1.18	1.17	1.37	1.20	1.85	1.58
U_4	1.17	1.11	1.16	1.14	1.48	1.23	2.01	1.55
U_5	1.20	1.13	1.25	1.16	1.37	1.11	1.95	1.46
U_6	1.21	1.12	1.25	1.16	1.37	1.03	2.07	1.34
T_1	1.30	1.22	1.40	1.25	1.08	1.22	1.96	1.87
T_2	1.41	1.33	1.51	1.29	1.22	1.45	2.59	2.51
T_3	1.54	1.36	1.71	1.42	1.05	1.18	2.77	2.29
B_1	1.23	1.18	1.18	1.17	1.62	1.55	2.36	2.14
B_2	1.22	1.14	1.27	1.15	1.46	1.39	2.37	1.81
B_3	1.22	1.16	1.27	1.19	1.46	1.14	2.37	1.58
B_4	1.40	1.22	1.41	1.26	1.66	1.19	3.28	1.83

on how to modify the parameters are also made from the error charts. In the following we verify the conclusions with the macroscopic level comparison. The verification results show that all conclusions deduced from the microscopic method are reasonable. Most of all, a parameter set with smaller error in the microscopic evaluation always has a better performance at the macroscopic level. Finally, we discuss the possible quantitative descriptions of a model with the microscopic method.

The method is defined at the trajectory level, therefore its effectiveness is the same in different scenarios. The evaluation is conducted many times along one trajectory, hence, we can get rich information from one trajectory. Because of the simulation and the experiment is synchronized at the beginning of each evaluation, the result is insensitive to the length of a trajectory. The result has four directions, based on which qualitative conclusions can be obtained from the trajectory level comparison. Moreover, the final result E is a comprehensive evaluation of the precision, the stability and the symmetry of a model.

We suggest that the microscopic method and the trajectory database can be used as a standard criterion to give qualitative and quantitative evaluations of a model. In the future, we will try to establish an evaluation database of continuous pedestrian dynamic models based on the method. The database will be composed of experimental trajectories with graded densities and various scenarios, and evaluations results of different models with these trajectories.

A. Methods of the trajectory smoothing, resampling and the velocity solving

A trajectory is smoothed by averaging the positions of adjacent time steps:

$$j_i^{smt} = \{\boldsymbol{r}_{i,n}^{smt} | \boldsymbol{r}_{i,n}^{smt} = \frac{1}{K_1} \sum_{n-K_1/2}^{n+K_1/2} \boldsymbol{r}_{i,n}^{ori}, n = 0, 1, 2, ...\}, \tag{16}$$

where K_1 is the number of the time step for the smoothing. The sampling result of the trajectory i is:

$$j_i^{res} = \{\boldsymbol{r}_{i,n}^{smt} | n = 0, N, 2N, ...\}, \tag{17}$$

where N is the interval between two resamplings. The velocity of a time step ($v(n)$) depends on the future movement of the pedestrian:

$$\boldsymbol{v}_i(n) = \frac{\boldsymbol{r}_{i,n+K_2}^{smt} - \boldsymbol{r}_{i,n}^{smt}}{K_2 \delta}, \tag{18}$$

where δ is the duration of the time step in the original trajectory.

In this paper, $K_1 = N = K_2 = 1/\delta$. It means that all of the intervals (the smooth interval, the resampling interval and the velocity solving interval) are 1 s.

Acknowledgement

This research was supported by Key Research and Development Program (2018YFC0807000), and Fundamental Research Funds for the Central Universities (WK2320000036).

References

[1] S. Okazaki, A study of pedestrian movement in architectural space, part 1: Pedestrian movement by the application on of magnetic models, Trans. AIJ 283 (1979) 111–119.

[2] T. Korhonen, S. Hostikka, O. Keski-Rahkonen, A proposal for the goals and new techniques of modelling pedestrian evacuation in fires, Fire Safety Science 8 (2005) 557–567.

[3] S. Cao, L. Fu, P. Wang, G. Zeng, W. Song, Experimental and modeling study on evacuation under good and limited visibility in a supermarket, Fire Safety Journal 102 (2018) 27–36.

[4] B. Jiang, Simped: simulating pedestrian flows in a virtual urban environment, Journal of geographic information and decision analysis 3 (1) (1999) 21–30.

[5] W. Shao, D. Terzopoulos, Autonomous pedestrians, in: Proceedings of the 2005 ACM SIGGRAPH/Eurographics symposium on Computer animation, ACM, 2005, pp. 19–28.

[6] J. Ma, W.-g. Song, J. Zhang, S.-m. Lo, G.-x. Liao, k-nearest-neighbor interaction induced self-organized pedestrian counter flow, Physica A: Statistical Mechanics and its Applications 389 (10) (2010) 2101–2117.

[7] W. Song, X. Xu, B.-H. Wang, S. Ni, Simulation of evacuation processes using a multi-grid model for pedestrian dynamics, Physica A: Statistical Mechanics and its Applications 363 (2) (2006) 492–500.

[8] S. Cao, W. Song, W. Lv, Z. Fang, A multi-grid model for pedestrian evacuation in a room without visibility, Physica A: Statistical Mechanics and its Applications 436 (2015) 45–61.

[9] D. Helbing, P. Molnar, Social force model for pedestrian dynamics, Physical review E 51 (5) (1995) 4282.

[10] W. Yu, R. Chen, L. Dong, S. Dai, Centrifugal force model for pedestrian dynamics, Physical Review E 72 (2) (2005) 026112.

[11] M. Chraibi, A. Seyfried, A. Schadschneider, Generalized centrifugal-force model for pedestrian dynamics, Physical Review E 82 (4) (2010) 046111.

[12] A. Tordeux, M. Chraibi, A. Seyfried, Collision-free speed model for pedestrian dynamics, in: Traffic and Granular Flow'15, Springer, 2016, pp. 225–232.

[13] F. Chittaro, F. Jean, P. Mason, On the inverse optimal control problems of the human locomotion: stability and robustness of the minimizers, Journal of Mathematical Sciences 195 (3) (2013) 269–287.

[14] A. V. Papadopoulos, L. Bascetta, G. Ferretti, A comparative evaluation of human motion planning policies, IFAC Proceedings Volumes 47 (3) (2014) 12299–12304.

[15] G. Arechavaleta, J.-P. Laumond, H. Hicheur, A. Berthoz, Optimizing principles underlying the shape of trajectories in goal oriented locomotion for humans, in: Humanoid Robots, 2006 6th IEEE-RAS International Conference on, IEEE, 2006, pp. 131–136.

[16] M. J. Seitz, G. Köster, Natural discretization of pedestrian movement in continuous space, Physical Review E 86 (4) (2012) 046108.

[17] I. von Sivers, G. Köster, Dynamic stride length adaptation according to utility and personal space, Transportation Research Part B: Methodological 74 (2015) 104–117.

[18] S. Heliövaara, T. Korhonen, S. Hostikka, H. Ehtamo, Counterflow model for agent-based simulation of crowd dynamics, Building and Environment 48 (2012) 89–100.

[19] D. R. Parisi, M. Gilman, H. Moldovan, A modification of the social force model can reproduce experimental data of pedestrian flows in normal conditions, Physica A: Statistical Mechanics and its Applications 388 (17) (2009) 3600–3608.

[20] T. I. Lakoba, D. J. Kaup, N. M. Finkelstein, Modifications of the helbing-molnar-farkas-vicsek social force model for pedestrian evolution, Simulation 81 (5) (2005) 339–352.

[21] W. Liao, J. Zhang, X. Zheng, Y. Zhao, A generalized validation procedure for pedestrian models, Simulation Modelling Practice and Theory 77 (2017) 20 – 31.

[22] A. Seyfried, M. Boltes, J. Kähler, W. Klingsch, A. Portz, T. Rupprecht, A. Schadschneider, B. Steffen, A. Winkens, Enhanced empirical data for the fundamental diagram and the flow through bottlenecks, in: Pedestrian and Evacuation Dynamics 2008, Springer, 2010, pp. 145–156.

[23] U. Weidmann, Transporttechnik der fussgänger, Schriftenreihe/Institut für Verkehrsplanung, Transporttechnik, Strassen- und Eisenbahnbau 90.

[24] H. Benner, J. Lohmiller, P. Sukennik, Is calibration a straight-forward task if detailed trajectory data is available?, Tech. rep. (2017).

[25] S. Seer, C. Rudloff, T. Matyus, N. Brändle, Validating social force based models with comprehensive real world motion data, Transportation Research Procedia 2 (2014) 724–732.

[26] S. P. Hoogendoorn, W. Daamen, Microscopic parameter identification of pedestrian models and its implications to pedestrian flow modeling, Transporttation Research Board Annual Meeting, 2006.

[27] C. Rudloff, T. Matyus, S. Seer, D. Bauer, Can walking behavior be predicted? analysis of calibration and fit of pedestrian models, Transportation Research Record: Journal of the Transportation Research Board (2264) (2011) 101–109.

[28] S. Seer, N. Brändle, C. Ratti, Kinects and human kinetics: A new approach for studying pedestrian behavior, Transportation research part C: emerging technologies 48 (2014) 212–228.

[29] A. Johansson, D. Helbing, P. K. Shukla, Specification of the social force pedestrian model by evolutionary adjustment to video tracking data, Advances in complex systems 10 (supp02) (2007) 271–288.

[30] D. Helbing, A. Johansson, Pedestrian, crowd and evacuation dynamics, in: Encyclopedia of complexity and systems science, Springer, 2009, pp. 6476–6495.

[31] M. Boltes, A. Seyfried, B. Steffen, A. Schadschneider, Automatic extraction of pedestrian trajectories from video recordings, in: Pedestrian and Evacuation Dynamics 2008, Springer, 2010, pp. 43–54.

[32] J. Zhang, W. Klingsch, A. Schadschneider, A. Seyfried, Transitions in pedestrian fundamental diagrams of straight corridors and t-junctions, Journal of Statistical Mechanics: Theory and Experiment 2011 (06) (2011) P06004.

[33] J. Zhang, W. Klingsch, A. Schadschneider, A. Seyfried, Ordering in bidirectional pedestrian flows and its influence on the fundamental diagram, Journal of Statistical Mechanics: Theory and Experiment 2012 (02) (2012) P02002.

A.13 Article XII

A generalized trajectories-based evaluation approach for pedestrian evacuation models

---

Y. Xiao, J. Xu, M. Chraibi, J. Zhang, and C. Gou.

Safety Science (**2020**)

Safety science 147, 105574, 2022
10.1016/j.ssci.2021.105574

A generalized trajectories-based evaluation approach for pedestrian evacuation models

Yao Xiao[1], Mohcine Chraibi[2],Jun Zhang[3], Chao Gou[1]

Abstract
The fundamental diagram and self-organized phenomena in crowds are widely used to test the applicability of evacuation models. These benchmarks are good indicators for the validity of a model, whereas they are insufficient descriptors for the realistic microscopic behaviors of pedestrians. In recent years, the rapid increase of the trajectory datasets which benefits from the development of recognition technologies open the door to new possibilities for an extensive quantitative validation of the models. In this work, a trajectories-based analysis approach which contains types of indexes is proposed. The indexes are a mix of macroscopic type (fundamental diagram index, speed choice index, and direction choice index) and microscopic type (trajectories pattern index), distribution type (route length distribution index, travel time distribution index) and time-series type (starting position distance time-series index, destnation position distance time-series index.) Moreover, the Kolmogorov-Smirnov (K-S) test as well as the dynamic time warping (DTW) method are introduced to quantify the similarities of results on different types of indexes. In brief, by comparing experimental and simulation trajectories, we can measure a set of performance scores in different perspectives. Here, the Social Force Model (SFM) and Heuristics Model (HM) are respectively introduced and evaluated. According to the proposed evaluation approach, we show that the HM performs better than the SFM. Our analysis approach is model agnostic and is defined in a general way, such that it can be applied for trajectory sets from different experiment settings. This work can help to improve the accuracy of simulation models, and the pedestrian safety in crowd activities and autonomous vehicle navigation will be benefited.

Keywords
Validation; Evaluation; Pedestrian evacuation models; Trajectories; K-S test; DTW method

[1] *School of Intelligent System Engineering, Sun Yat-Sen University, Shenzhen, Guangdong, China*
[2] *Institute for Advanced Simulation, Forschungszentrum Jülich, Jülich, Germany*
[3] *State Key Laboratory of Fire Science, University of Science and Technology of China, Hefei, China*

Contents

Introduction

In recent decades, the prediction and reproduction of movement behaviors is growing to be a hot topic in the field of evacuation dynamics, pedestrian dynamics and autonomous vehicle navigation. To support the development, plenty of microscopic models such as the social force model

(Qu et al., 2014; Helbing et al., 2000; Helbing and Molnar, 1995), cellular automata model (Burstedde et al., 2001), velocity obstacle models (Douthwaite et al., 2019; Van den Berg et al., 2008), heuristics model(Moussaid et al., 2011), Voronoi model (Xiao et al., 2016) and deep learning models (Sadeghian et al., 2019; Alexandre et al., 2016) have been proposed. Generally, the simulation results of the models such as the fundamental diagrams and the self-organized phenomena would be compared with the empirical results to investigate the capacity of pedestrian models. Currently, the fundamental diagram is a widely-used approach to evaluate the model(Dong et al., 2020) (Schadschneider et al., 2018; Vanumu et al., 2017). It makes use of the relationship between macroscopic indexes including density, velocity and flow to illustrate the similarities between simulation results and empirical results. In fact, the fundamental diagram whether speed-density relation or flow-density relation mainly reflects the speed determination mechanism, and it is a well-studied module in pedestrian models (Moussaid et al., 2011; Helbing and Molnar, 1995). It is not that hard for many pedestrian models to reproduce well-agreed fundamental diagrams. Relatively, some microscopic pedestrian behaviors (e.g., direction choice), which also play important roles in pedestrian dynamics, cannot be reflected by the fundamental diagrams. Another model evaluation approach is regarding the reproduction of self-organized phenomena such as lane formation and stop-and-go wave. Even without considering the subjectively defined self-organized phenomenon, it is hard to ignore that most self-organized phenomena only occur in some specific situations, and it can lead to feasibility problems for the universal model evaluation. By far, the current quantitative methods are not enough for a comprehensive evaluation of the pedestrian models, and the researches on the evaluation of pedestrian models are still not sufficiently studied. It is still fuzzy about how to evaluate the overall performance of a pedestrian model no matter in a scenario or in a series of scenarios. As a result, developing a systematic and quantitative mathematical approach to evaluate the pedestrian model is imperative.

Trajectory pattern is considered to be a significant and critical symbol of pedestrian behaviors (Hidaka et al., 2019; Do et al., 2016). The recent development of trajectory recognition and extraction technologies (Boltes and Seyfried, 2013; Boltes et al., 2010) benefits a rapid increase of the trajectory datasets. In this paper, we developed a pedestrian model evaluation approach through the quantitative comparison of pedestrian behaviors between simulation results and empirical results, and proposed four kinds of indexes (i.e., macroscopic indexes, microscopic index, distribution indexes and time-series indexes) to quantitatively measure the model performance in simulations.

The rest of the paper is organized as follows. Section 2 gives a comprehensive analysis of the related literature of the pedestrian calibration and validation. In Section 3, the model evaluation framework is formulated, and each type of index is illustrated. In Section 4, the empirical and simulation trajectories of the circle antipode experiments are applied for investigation, and the simulation results of the SFM and the HM are compared and evaluated through the proposed trajectories-based approach. Section 5 summarizes the advantages and disadvantages of the evaluation approach and gives a further investigation prospect.

1. Literature review

Current pedestrian model evaluation approaches mainly include macroscopic approaches and microscopic approaches.

The macroscopic pedestrian model evaluation approaches mainly make use of the fundamental diagrams, self-organized phenomena, and other macroscopic indexes. The fundamental diagrams mainly reflect the relationship between macroscopic parameters such as density, velocity and flow. Researchers have gathered plenty of fundamental diagrams data in different scenarios, uni-directional flow, bi-directional flow, and multi-directional flow. Weidmann (1993) summarized the existing empirical data and fitted a widely-used velocity-density relation with a non-linear function. Seyfried et al. (2005) revisited the related velocity-density relation in a single-file movement and found a linear relation. Four different measurement methods are defined in (Zhang et al., 2011) to explore their influence on the fundamental diagram. It is shown that they have a minor impact for the low-density situation, but the Voronoi method is able to resolve the fine structure of the fundamental diagram. Zhang et al. (2012) further investigated the fundamental diagrams with different forms of ordering and found that the specific flow in uni-directional flow is significantly larger than that in all bi-directional flow. Cao et al. (2020) found and classified three types of headway-velocity relation in uni-directional, bi-directional and multi-directional flow situations, respectively. The fundamental diagram is generally regarded as the most basic model indicator for traditional pedestrian models (Sticco et al., 2020; Zhang et al., 2020; Xiao et al., 2016; Moussaid et al., 2011; Chraibi et al., 2010).

The self-organized phenomenon usually reflects the collective dynamics of pedestrian crowds. Lane formation (Helbing et al., 2005) indicates the formulation of several walking lanes in bi-directional flow, and it generally benefits the crowd movement efficiency. In the original SFM research (Helbing and Molnar, 1995), the reproduction of lane formation in walkways as well as the change of passing direction in bottleneck are applied to verify the model simulation results. A Yamori's index which reflects segregation of opposite flow direction is proposed in (Moussaid et al., 2011) to demonstrate the rapid transition from disorder to order in the pedestrian model. In the improved SFM (Helbing et al., 2000), the reproduction of self-organized phenomena such as arching phenomenon and faster-is-slower effect is regarded as the symbols of validation. A pedestrian dynamics model with two heuristics mechanisms of anticipation and attraction is formulated in (Lü et al., 2020), and the reproduction of phenomena such as the lane formation, stop-and-go waves and the vortexlike pattern supported its reliability.

Other frequently-used approaches include the bottleneck flow and the evacuation time from a room. Gao et al. (2014) took use of the experimental evacuation time of different exits in a supermarket to validate the effect of their macro-micro integrated mathematical model. Hanseler et al. (2014) made a comparison between the models and pedestrian tracking data, and found a good performance with respect to the prediction of travel time and density. Galea et al. (2014) collected passenger validation datasets including response times, starting locations and arrival times, and three objective measures are applied to assess the goodness of fit between model and measured data. Poulos et al. (2018) proposed an agent-based evacuation model to simulate the evacuation of approximately 1500 children and staff from the school during a global evacuation drill carried out for the entire city, while both practical flow rates and evacuation times were applied for the model validation. Ronchi et al. (2013) evaluated the building evacuation models by their five main components including pre-evacuation time, movement and navigation, exit usage, route availability, and flow constraints. Ronchi (2021) further focused on the smoke issues and discussed the potential of a standardized verification and validation document. Currently, a verification and validation protocol (ISO, 2020) for building fire evacuation models is proposed, and it considers modules including basic components, behavioral components, fire-people interaction components and building-specific components.

In recent years, different types of pedestrian recognition and extraction technologies, such as video (Boltes and Seyfried, 2013; Boltes et al., 2010), Kinect sensor (Corbetta et al., 2014; Seer et al., 2014), Bluetooth (Abedi et al., 2015), and LIDAR (He et al., 2015) significantly promoted the development of behavior researches. As a result, more pedestrian-related empirical movement data are obtained, and types of microscopic pedestrian behaviors (e.g., trajectories) can be further applied for model evaluation.

Johansson et al. (2007) proposed an evolutionary optimization algorithm to determine the simulation model parameter specification with the relative distance error. Alexandre et al. (2016) formulated an LSTM model for trajectory prediction and demonstrated the performance of trajectories by public datasets with metrics including average displacement error (ADE), final displacement error (FDE), and average linear displacement error (FLDE). These trajectory metrics, e.g., ADE and FDE are applied by modified LSTM models (Zhang et al., 2019; Xue et al., 2018) to illustrate their model performance. A critical limitation for these displacement errors is that the previous minor disturbance from common heterogenous and indeterminacy behaviors could cause remarkable result deviation. Generally, the disturbance as well as the remarkable result deviation are considered to be normal phenomena for a qualified pedestrian model.

An integrated modeling framework (Porter et al., 2018) with SFM, behavioral heuristics, and material science is developed, and trajectory data from narrow bottleneck and bi-directional flow experiments are used for calibration. Chraibi et al. (2016) applied functional principal component analysis to assess the quality of models in a bottleneck scenario, and it is proved to be an efficient approach to detect the differences between simulation and experiment results. Huang et al. (2019) developed an evaluation approach between the experimental and simulated trajectories in four directions, and the approach is demonstrated using empirical trajectories in three kinds of scenarios. Basically, it is a general and quantitative method for the evaluation of continuous pedestrian models compared with the fundamental diagram. Ma et al. (2019) proposed an intelligence-based approach for pedestrian walking behavior prediction and evaluated the pedestrian model with direction displacement and speed error based on trajectory sets. The trajectory-based methods provide further microscopic-level insights into the pedestrian models, and these models can be therewith quantitatively evaluated. However, current evaluation methods of pedestrian models are still not that systematic and appropriate for different types of scenarios as well as different levels of model properties. As a result, it is necessary to formulate a general evaluation approach for pedestrian models.

2. Trajectories-based approach

Considering the practical needs in the areas of pedestrian dynamics, a generic and quantitative evaluation approach for different walking models is developed. In the section, the approach is illustrated with three parts, i.e., framework, indexes and processes. Briefly, the framework part mainly introduces the overall design of the evaluation approach, namely, how to organize the indexes extracted from the trajectories. In the index part, the different types of indexes are respectively introduced and defined in detail. The process part mainly describes how to evaluate the pedestrian models, and the procedures are specifically provided.

2.1 Framework

The approach introduced in the section is demonstrated on basis of the recognized pedestrian trajectory sets as follows.

$$S_i\ t \quad i,t,x \ \mid i \in I,\ t \in\ T^{\text{start}},\ T^{\text{dest}}\ ,\ t \in Z, \tag{1}$$

where i indicates the pedestrian index in the pedestrian set **I**, t indicates the time step, and x represents the corresponding coordinates of the pedestrian location. T^{start} and T^{dest} represent the valid time leaving the starting point and reaching the destination point, respectively. Considering the realistic trajectory recognition process, the pedestrian trajectories applied in the approach are represented by some discrete points. Generally, the pedestrian trajectory would be mapped to the ground space and represented as a two-dimensional vector. The ground trajectories are the original data of the pedestrian behaviors, and the other evaluation indexes should be a reduced dimensional representation of the trajectory data. The framework here is to organize the different perspectives of the trajectory data. To determine which type of perspectives are needed, getting back to the original intention is helpful. The intention of the approach here is to evaluate different pedestrian models and find out both the advantages and disadvantages of the model. Therefore, finding the implicit meaning of the index and connecting it with the specified model component is critical. Further model optimization direction can be determined according to the specified model problem.

Basically, the framework of our approach based on trajectory sets can be divided into three levels, operational level, tactical level (Hoogendoorn and Bovy, 2004) and hybrid level.

Symbol	Description
I	The pedestrian set
N	The number of individuals in the set I
T^{start}	The valid time leaving the starting point for pedestrians.
T^{dest}	The valid time reaching the destination point for pedestrians.
T_i^{start}	The valid time leaving the starting point for pedestrian i.
T_i^{end}	The valid time reaching the destination point for pedestrian i.

Table 1. List of Main Notations.

At the operational level, the fundamental dynamics mechanism of the pedestrian walking model is evaluated. For a pedestrian walking model, the core outputs can be summarized as the determination of the next time-step velocity direction and speed for each individual pedestrian. Comparing the aggregated pattern of the core dynamics outputs (i.e., velocity direction and speed) between the empirical results and the simulation results shall be the most essential part for the evaluation of pedestrian walking models.

At the tactical level, the primary behavior choice mechanism of the pedestrian walking model is evaluated. Compared with the fundamental direction and speed choices, the behavior choice is more related to the intelligence reproduction abilities of a pedestrian model. Considering the format of the trajectory sets, the behavioral results are analyzed by comparing different pedestrians and different time-steps, respectively. Regarding the former part, the distribution index is proposed for evaluation, and the time-series index is proposed to evaluate the latter one. The evaluation of the behavior choices shall be a significant indicator for the agent-based walking model of intelligent pedestrians.

At the hybrid level, the detailed trajectory performances of the pedestrian model are evaluated, and it is considered to be an evaluation for both operational level and tactical level. With the evaluation, the differences between empirical and simulation results can be quantified. Here, the differences are directly quantified based on the empirical and simulation trajectory sets, and it is the most specified indicator for the model evaluation.

2.2 Transformed sets for indexes

In brief, the three levels of trajectory-based approach evaluate the operational level, the tactical level, and hybrid level, respectively. In this subsection, the evaluation indexes in each level are specifically introduced.

(1) Operational level. In this level, the speed choice as well as the direction choice mechanisms are respectively analyzed in the section, and the related indexes include the fundamental diagram index, the speed choice index and the direction choice index.

Fundamental diagram index. The index reflects the speed reaction mechanism differences between empirical and simulation results, and the density-speed relation is applied here. The density-speed relation is considered to be an important indicator for the calibration and validation of models in the researches of pedestrian dynamics. Here, the local density is calculated through a Voronoi method using the trajectories (Xiao et al., 2016), and the density-speed relation sets are accordingly obtained as follows.

$$v_i\ t \quad \|x_i\ \ t \quad 1\ - x_i\ \ t\ \|/\Delta t, \tag{2}$$

where $x_i\ t$ indicates the coordinate of pedestrian i at time-step t. Δt is the practical time duration between two time-steps. Base on it, the sets of density and speed are obtained,

$$C_{\mathrm{FD}} \qquad \rho_i\ t\ , v_i\ t \quad — \mathrm{i} \in I, t \in\ T_i^{\mathrm{start}},\ T_i^{\mathrm{dest}}\ .t \in Z, \tag{3}$$

where $\rho_i\ t$ indicates the local density of pedestrian i at time-step t. Based on the density-speed relation sets C_{fd}, the speed element in the set for fundamental diagram index is obtained as follows.

$$\bar{v}_{\mathrm{FD}}\ n \qquad \frac{\sum_{k\ \ 1}^{K} v_k}{K},\ \text{if}\ \frac{n}{N_\rho}\cdot\rho_{\max} < \rho_k \le \frac{n\quad 1}{N_\rho}\cdot\rho_{\max}\ ,\quad \rho_k, v_k\ \in C_{\mathrm{fd}}. \tag{4}$$

Where K indicates the number of elements in the density scope, N_ρ is the number of density blocks, and $\rho_{\max}$ is a given value of the maximum density. The sets for fundamental diagram index are obtained as follows.

$$\mathbf{S}_{\mathrm{FD}} \quad \{\bar{v}_{\mathrm{fd}}\ n\ —1 \le n \le N_\rho,\ n \in Z\} \tag{5}$$

Speed choice index. The index indicates the aggregated speed choice performance differences between empirical and simulation results. The overall distribution of the speed choice during the movements is calculated, and the set of speed choices can be determined with the trajectory sets as follows.

$$\mathbf{S}_{\mathrm{SC}} \quad \left\{v_i\ t\ \ — \mathrm{i}\in \mathbf{I}, t \in \left[T_i^{\mathrm{start}},\ T_i^{\mathrm{dest}}\right], t \in \mathbf{Z}\ \right\}, \tag{6}$$

Direction choice index. The index illustrates the aggregated direction choice performance differences between empirical and simulation results. Theoretically, the pedestrian walking model describes the pedestrian movement in a two-dimensional space, and the direction choice basically plays a significant role. The unit vector of the velocity direction is obtained as follows.

$$\mathbf{e_i\ \ t} \qquad \frac{\mathbf{x}_i\ t\quad 1\ - \mathbf{x}_i\ t}{||\mathbf{x}_i\ t\quad 1\ - \mathbf{x}_i\ t\ ||} \tag{7}$$

while the unit vector of the direction to the destination is calculated as follows.

$$\mathbf{e_i^{\mathrm{dest}}\ \ t} \qquad \frac{\mathbf{x}_i^{\mathrm{dest}} - \mathbf{x}_i\ t}{\left|\left|\mathbf{x}_i^{\mathrm{dest}} - \mathbf{x}_i\ t\ \right|\right|} \tag{8}$$

Where $\mathbf{x}_i^{\mathrm{dest}}$ indicates the destination point of pedestrian i. The individual direction choice is determined according the direction vectors.

$$s_i\ t \qquad e_i\ t\ \cdot e_{i^{\mathrm{dest}}}\ t \tag{9}$$

Here, the direction choice set is obtained according to the trajectory sets as follows.

$$S_{\mathrm{DC}} \quad \left\{\ s_i\ t\ \ —\ \mathrm{i} \in I, t \in \left[T_i^{\mathrm{start}},\ T_i^{\mathrm{dest}}\right], t \in Z\right\} \tag{10}$$

(2) Tactical level.

In this level, the individual performance as well as the time related crowd performance is evaluated. The distribution indexes and the time-series indexes are introduced for evaluation, respectively. The distribution indexes mainly demonstrate the individual pedestrian choice and performance, and the base data are obtained through the separation of trajectory sets according to pedestrian individuals.

Route length distribution index. The index illustrates the individual route length choice differences between empirical and simulation results. The route length can be regarded as a significant indicator for the overall decision-making of pedestrian individuals, and it mainly reflects the spatial characteristics of pedestrian choice. The route choice sets are obtained as follows.

$$S_{\mathrm{RL}} \quad \left\{ \sum_{t \quad T_i^{\mathrm{start}}}^{T_i^{\mathrm{dest}}} \|x_i\ t \quad 1\ - x_i\ t\ \| \middle| i \in I \right\} \tag{11}$$

Travel time distribution index. The index demonstrates the individual travel time choice differences between empirical and simulation results. The travel time is also a critical indicator for the pedestrian individual decision-making choice, and it reflects the temporal characteristics of pedestrian choices. The travel time choice sets can be obtained as follows.

$$S_{\mathrm{TT}} \quad \left\{ T_i^{\mathrm{dest}} - T_i^{\mathrm{start}} \middle| i \in I \right\} \tag{12}$$

Starting position distance time-series index. The index calculates and compares the overall time-varying distance to the starting point during the crowd movement between empirical and simulation results. It can reflect the aggregated pedestrian behaviors on the timeline, and the time-series of the distance to starting point can be obtained as follows.

$$S_{\mathrm{TS}} \quad \left\{ \sum_{i \quad 1}^{N} \left\| x_i\ t\ \ - x_i\left(T_i^{\mathrm{start}}\right) \right\| / N \middle| t \in \left[T^{\mathrm{start}},\ T^{\mathrm{dest}}\right] \right\} \tag{13}$$

where N indicates the number of individuals in the set **I**. Note that

$$T^{\mathrm{start}} \quad min\left\{T_i^{\mathrm{start}} \middle| i \in I\right\},$$

and
$T^{\mathrm{dest}} \quad max\left\{T_i^{\mathrm{dest}} \middle| i \in I\right\}$, T^{start} and T_i^{start} respectively indicate that the start time of evacuation and pedestrian i.

Destination position distance time-series index. The index calculates and compares the overall time-varying distance to the destination point during the crowd movement between empirical and simulation results. It can reflect the aggregated pedestrian behaviors on the timeline, and the time-series of the distance to destination point can be obtained as follows.

$$S_{\mathrm{TD}} \quad \sum_{i \quad 1}^{N} \left\| x_i\ t\ \ - x_i\ \ T_i^{\mathrm{dest}}\ \ \right\| / N\ |t \in\ \ T^{\mathrm{start}},\ T^{\mathrm{dest}} \tag{14}$$

(3) Hybrid level.

In this level, the microscopic trajectory pattern index is illustrated to evaluate the individual movement pattern performance at both operational level and tactical level.

Trajectory pattern index. The index calculates the microscopic pattern differences between empirical and simulation trajectory patterns. Note that the index is significant for the similarity investigation but not a comprehensive one. The results might make a huge difference due to the previous minor disturbance from heterogenous or indeterminacy behaviors, and usually these models are actually not bad in reproducing pedestrian behaviors. The trajectory pattern sets can be obtained as follows.

$$S_{\mathrm{TP}} \quad x_i\ t\ \ |i \in I, t \in\ \ T_i^{\mathrm{start}},\ T_i^{\mathrm{dest}} \tag{15}$$

2.3 Processes

The overall technical route of the evaluation processes can be found in Fig.1 and Table. 1, and the source code can be found on `https://github.com/rickyspy/Pedestrian-Model-Evaluation`.

During the input procedure, both the empirical and the simulation trajectory sets shall be obtained and preprocessed. The common form of trajectory sets contains the individual id, the time step, and the corresponding position (i.e. x and y coordinate). The individual id is a unique symbol for each pedestrian, and it can connect the trajectory data in both empirical and simulation data. A critical point for the time step field is the unification of the time interval. Common frame rates for the video-based empirical trajectory data are 16 fps or 25 fps, which are usually different from the simulation. For a pedestrian walking model, the update time interval in simulation is generally 0.01 s (100 fps) or 0.001 s (1000 fps), which can basically agree with the realistic pedestrian reaction behaviors. To bridge the significant gap between the empirical trajectories and the simulation trajectories, a smooth approach is proposed for the unification of time interval, and the simulation trajectories of pedestrian i are adjusted as follows.

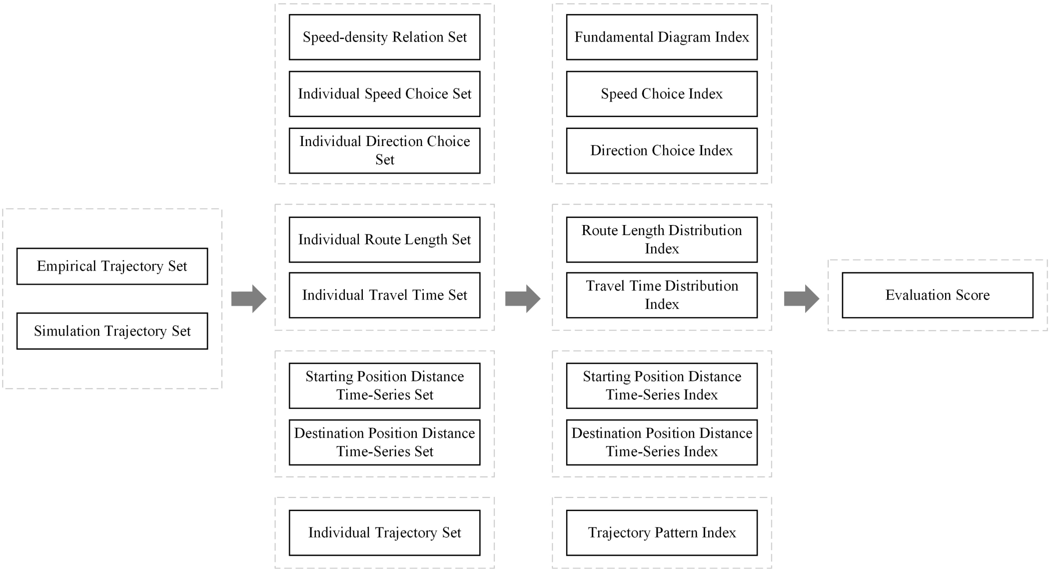

Figure 1. Sketch map of the evaluation procedures.

$$\widehat{\mathbf{x}}_{\mathbf{i}}\left(\widehat{t}\right) \quad \begin{cases} \left(t-\frac{k\widehat{t}}{\widehat{k}} \quad 1\right)\cdot \mathbf{x}_i \ t \quad \left(\frac{k\widehat{t}}{\widehat{k}}-t\right)\cdot \mathbf{x}_i \ t \quad 1 \\ x_i \ t \end{cases}, \qquad \frac{t>1}{t \quad 1} \tag{16}$$

where $\widehat{k}$ and k are respectively the fps of empirical and simulation trajectories, $\widehat{t}$ and t are respectively the time step of the original and adjusted trajectories, and $t \quad \left\lfloor \frac{k\widehat{t}}{\widehat{k}} \right\rfloor$. Besides, in order to ensure the normalization of indexes and enhance the reliability of results, the repeat times of the experimental results are required to be more than once in our approach.

Sketch map of the evaluation procedures

Trajectory-based Model Evaluation	
Inputs:	Empirical trajectory sets S^{emp} and simulation trajectory sets S^{sim}
Outputs:	Overall evaluation score u.
Step 1	Transformation of the empirical and simulation trajectory sets.
	According to Eq. (2), (5)–(15),
	the original empirical trajectory sets and the simulation trajectory
	sets are dimensionally transformed into different types of sets, respectively.
Step 2	Calculation of the indexes.
	Based on the similarity evaluation approaches
	introduced in Appendix A, the indexes are respectively evaluated.
Step 3	Calculation of the overall evaluation score.
	Based on the weights of different indexes, the overall evaluation score
	is calculated $u \quad \sum_{i \quad 1}^{N} \alpha_i u_i/N$.

Table 2. Evaluation Procedures.

Trajectory-based Model Evaluation **Inputs:** Empirical trajectory sets $\mathbf{S}^{\mathrm{emp}}$ and simulation trajectory sets $\mathbf{S}^{\mathrm{sim}}$
Outputs: Overall evaluation score u.
Step 1 Transformation of the empirical and simulation trajectory sets.

According to Eq. (2), (5) - (15), the original empirical trajectory sets $\mathbf{S}^{\mathrm{emp}}$ and the simulation trajectory sets $\mathbf{S}^{\mathrm{sim}}$ are dimensionally transformed into different types of sets, respectively.

Step 2 Calculation of the indexes.

Based on the similarity evaluation approaches introduced in Appendix A, the indexes are respectively evaluated.

Step 3 Calculation of the overall evaluation score.

Based on the weights of different indexes, the overall evaluation score is calculated. $u \quad \sum_{i \quad 1}^{N} \alpha_i u_i/N$.

At step 1, the trajectory sets are dimensionally transformed into different element sets. The different types of element sets are applied to describe the similarities between the simulation and empirical trajectory sets from different perspectives.

At step 2, two types of approaches (i.e., K-S test and DTW method) are proposed to evaluate the different element sets. Specifically, the speed choice index, the direction choice index, the route length distribution index and the travel time distribution index are evaluated with the K-S test method. The fundamental diagram index, the starting and destination position distance time-series indexes, and the trajectory pattern index are evaluated with the DTW method.

At step 3, the calculated indexes are integrated into an overall evaluation score considering the weights of different evaluation indexes. Here, the three operational level indexes share a weight of 0.25, so the weights of three indexes are 0.083. The two distribution indexes share a weight of 0.25, and the two time-series indexes also share a weight of 0.25. The trajectory pattern index owns a weight of 0.25.

The main output of the evaluation approach is an index in the range from 0 to 1, and the evaluation score can basically reflect the overall model capacity of reproducing pedestrian behaviors.

3. Evaluation and Analysis

In this section, the experimental trajectories of the circle antipode experiments are applied as the empirical results, and the SFM as well as the HM are introduced to formulate the simulation results. The trajectory-based evaluation approach proposed in the paper is attempted to find the evaluation results.

Trajectory data of experiment and simulation

Here, the circle antipode experiment (Xiao et al., 2019) with 64 participants and 10m radius (see 2-a) is applied for analysis. The specific experiment repeated 4 times, and each time of experiment corresponded to a different trajectory pattern. In the experiments, the pedestrians are uniformly initialized on the circle, and they are required to leave for their antipodal positions simultaneously. In the experiments, a conflicting area is naturally formulated as the shortest routes converged at the center region, and it is generally a challenging situation for most pedestrian walking models due to the combination of conflict avoidance behaviors and route choice behaviors during the experiment. The pedestrian behaviors during the experiments are recorded by cameras on the high-rise building, and the empirical trajectories are accordingly extracted by PeTrack (Boltes and Seyfried, 2013; Boltes et al., 2010). The empirical trajectories can be found in 2-b, and trajectories in the experiments correspond to a pattern of 25 frames per second.

The experiment is also simulated with the SFM (Helbing et al., 2000; Helbing and Molnar, 1995) and the HM (Moussaid et al., 2011), and the simulation results can be found in 2-c and 2-d, respectively. The two groups of simulation trajectories in the models correspond to the updated pattern of about 1000 frames per second. The gap between the updated pattern of simulation and experiment trajectories can be bridged according to Eq. (16).

Circle antipode experiment scenario and the empirical trajectories. (a) Realistic scenario. (b) Empirical trajectories. (c) Simulation trajectories of SFM. (d) Simulation trajectories of HM.

3.1 Evaluation results

The trajectories-based evaluation results for the SFM and the HM can be found in **??**. There are 8 different indexes for each model, and the overall model score is calculated on the radar figure. From an intuitive perspective, the HM performs better than the SFM. The detailed comparison results can be found in 3.

In the radar figure, the performance indexes are normalized according to the repeated empirical experiments, thereby all the performance indexes of the experiments are equal to 1. It is noted that the normalized value of experiments only represents the general performance differences between repeated experiments, but not indicates identical results. The heterogeneity behaviors and indeterminacy behaviors of pedestrians in practical cause the differences, thus the simulation may obtain a better performance than the repeated experiments.

For the fundamental diagram index, it generally reflects the dynamics reaction mechanism of pedestrian models. Both the SFM and the HM own a similar performance as the empirical experiment results. It means that the dynamics reaction mechanism of these two models basically agrees well with the empirical results.

For the speed choice index, the performances of the SFM and the HM are almost the same, but a significant gap is observed between the empirical results. Due to the lack of macroscopic detour mechanisms in the SFM and HM, the pedestrians in

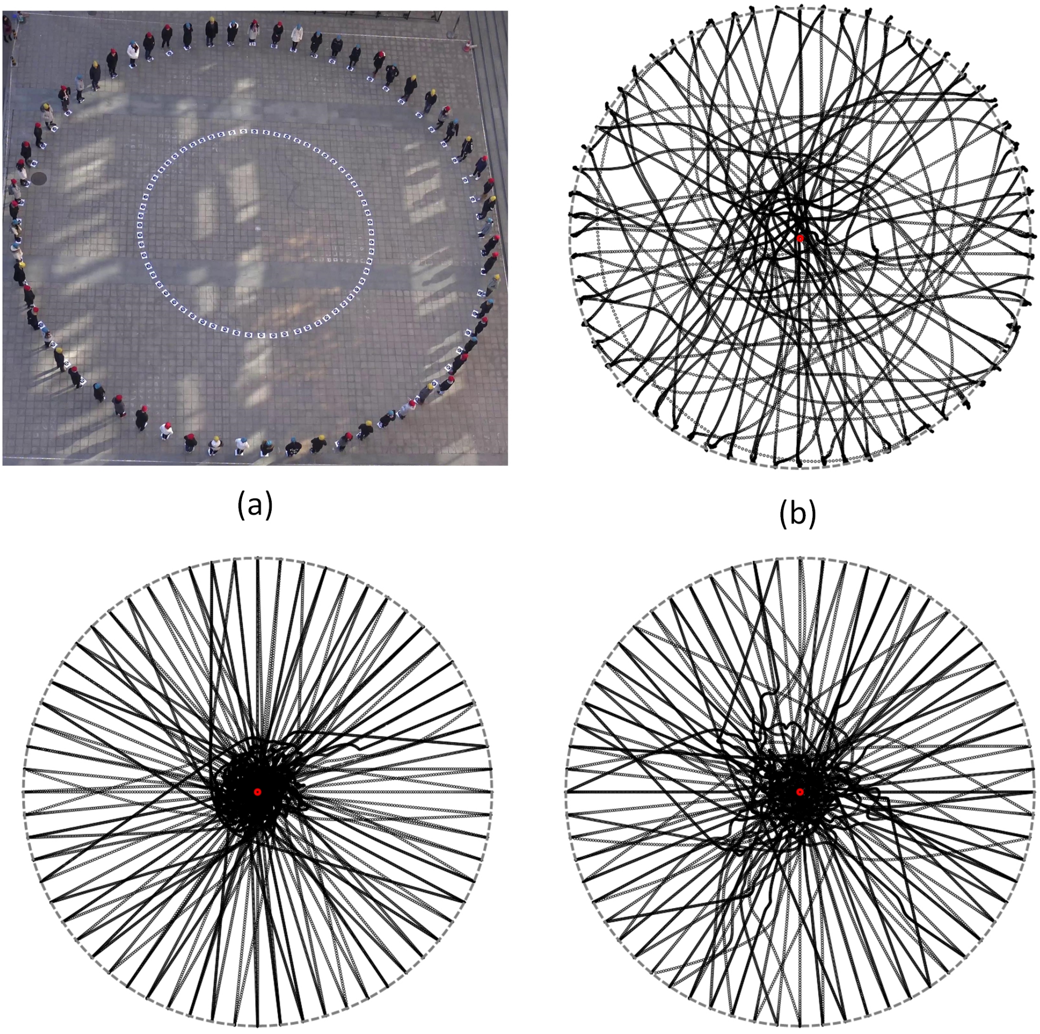

Figure 2. Circle antipode experiment scenario and the empirical trajectories. (a) Realistic scenario. (b) Empirical trajectories. (c) Simulation trajectories of SFM. (d) Simulation trajectories of HM.

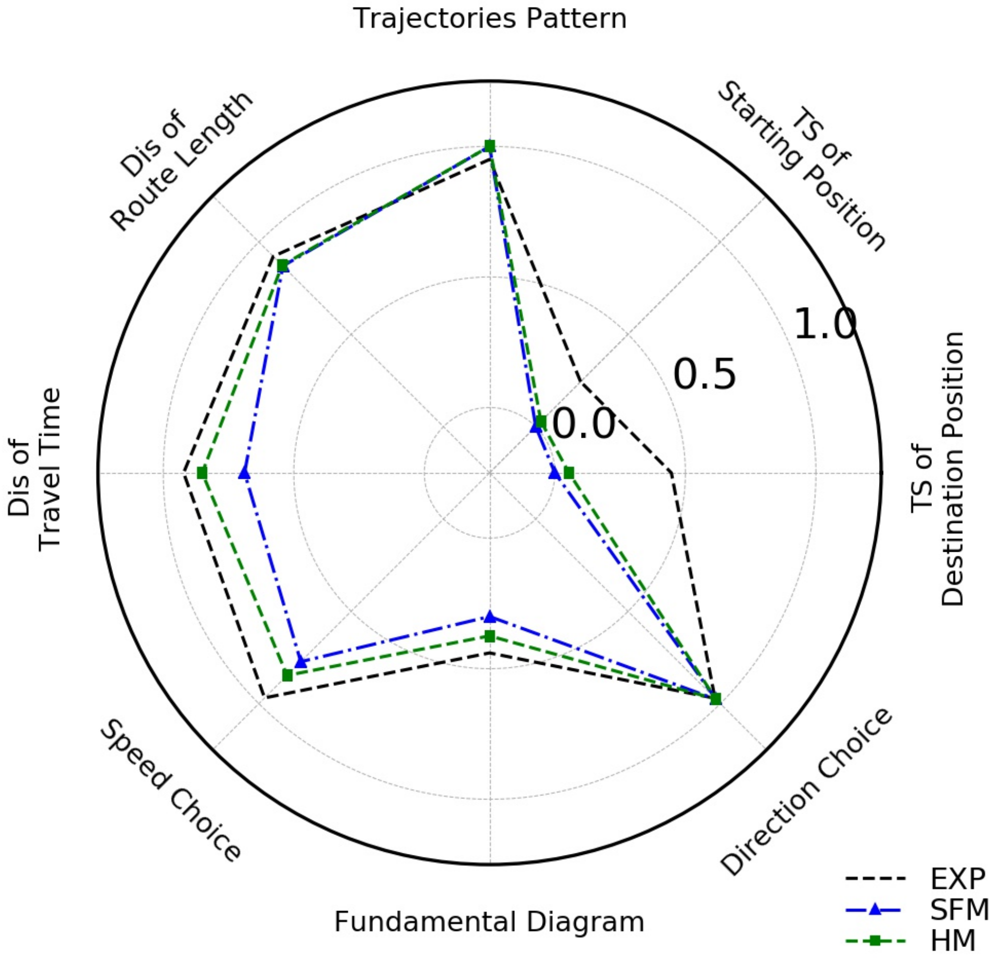

Figure 3. Model comparison results of the circle antipode experiments. Note that the similarity levels of the experiments, SFM and HM are compared, respectively.

simulations are likely to be blocked in the center of the region, and the overall speed distribution is different from the empirical results.

For the direction choice index, significant differences can be found between the models and the experimental performances. A critical reason is that the proposed models are not able to reproduce the pedestrian detour behaviors in empirical circle antipode experiments, and the index can quantitatively represent the differences.

For the travel time distribution index, the HM corresponds to a better performance than the SFM despite the apparent difference from the empirical experiments. The relatively efficient collision avoidance mechanism in the HM is believed to be the critical reason for the better model performance.

For the route length distribution index, the performances of the simulations are evidently different from the empirical experiments. The lack of consideration of detour routes in the models leads to significant differences between simulations and experiments.

For the starting and destination position distance time-series indexes, which can reflect the overall time-dependent trajectories performance. Here, the different performance indexes of the models reflect the different similarities with the empirical experiments. The delay of congestion resolution in the SFM leads to the distinguished performance indexes difference from the HM.

For the trajectories pattern index, it is found that the simulation results even perform more similar than the repeated experiments. The minor indeterminate pedestrian side choice in the circle antipode experiments (Xiao et al., 2021) would cause significant differences between trajectories, and it is considered to be a critical reason for the phenomenon. Even so, the trajectories pattern index shall be an important indicator for the model evaluation.

4. Conclusion and prospect

In this work, taking advantage of the K-S test and the DTW methods, a trajectories-based approach with 8 types of indexes is proposed to investigate and quantify the performance of pedestrian models. The practicability of the proposed approach is tested on the example of the empirical circle antipode experiments with two different models: the SFM and the HM. The results show that the overall performance of the HM is better than the SFM. Specifically, the travel time distribution and the time series indexes show obvious differences, but the rest indexes are more or less similar, which is understandable given that the HM is supposed to be an enhancement of the SFM. Moreover, this investigation indicates that both the SFM and HM are based on similar local velocity reaction mechanism, but the collision avoidance behaviors of the SFM is less practical than the HM. The results show that the approach is able to quantitatively catch differences between simulations and empirical data in different aspects.

On one hand, although eight indexes are proposed to analyze the performance of pedestrian models with trajectories, the completeness of the model is still hard to be assessed. First, some pedestrian behaviors, e.g., the heterogeneity, the indeterminacy, and side choice behavior might affect the evaluation of the models. However, these behaviors are still not considered in the analyses of current approaches. Second, the weights of the different indexes are not further adjusted, hence the final index might not reflect the practical capacity of the model. On the other hand, these different types of indexes can not only test the comprehensive abilities of simulation models at operational level, but also the abilities at tactical level. It is also a challenging task since most models usually focus on one side, and a model with only walking behavior module or route choice module can hardly act well with the indexes.

The evaluation approach can be applied as a capacity indicator in the calibration, validation and optimization for different types of pedestrian models. By comparing the simulation trajectories with the empirical trajectories, the corresponding model can be adjusted according to the specified evaluation index. For instance, we can pay more attention to the behavioral choice module of a pedestrian model if the fundamental diagram indexes perform worse than other indexes. For further application, the related source code as well as related instructions are open-sourced[1]. The approach can help to improve the accuracy of pedestrian models, and it contribute to ensuring the pedestrian safety in the activities of pedestrian crowds and the navigation of autonomous vehicles.

Acknowledgement

YX acknowledges the foundation support from the National Key R&D Program of China (Grant No. 2020YFB1600400) and the National Natural Science Foundation of China (Grant No. 72101276). MC acknowledges research support from the Deutsche Forschungsgemeinschaft (DFG, German Research Foundation) (Grant No. 446168800). Note: The appendix in the original publication is missing in this printed version.

---

[1] `https://github.com/rickyspy/Pedestrian-Model-Evaluation`

References

Abedi, N., Bhaskar, A., Chung, E., Miska, M., 2015. Assessment of antenna characteristic effects on pedestrian and cyclists travel-time estimation based on Bluetooth and WiFi MAC addresses. Transportation Research Part C-Emerging Technologies 60, 124-141.Alexandre, A., Kratarth, G., Vignesh, R., Alexandre, R., Li, F.-F., Silvio, S., 2016. Social lstm: Human trajectory prediction in crowded spaces, Proceedings of the IEEE Conference on Computer Vision and Pattern Recognition, pp. 961-971.Boltes, M., Seyfried, A., 2013. Collecting pedestrian trajectories. Neurocomputing 100(Supplement C), 127-133.Boltes, M., Seyfried, A., Steffen, B., Schadschneider, A., 2010. Automatic Extraction of Pedestrian Trajectories from Video Recordings. Pedestrian and Evacuation Dynamics 2008, 43-54.Burstedde, C., Klauck, K., Schadschneider, A., Zittartz, J., 2001. Simulation of pedestrian dynamics using a two-dimensional cellular automaton. Physica A 295(3), 507-525.Cao, S., Chen, M., Xu, L., Liang, J., Yao, M., Wang, P., 2020. Analysis of headway-velocity relation in one and two-dimensional pedestrian flows. Safety Science 129, 104804.Chraibi, M., Ensslen, T., Gottschalk, H., Saadi, M., Seyfried, A., 2016. Assessment of models for pedestrian dynamics with functional principal component analysis. Physica A 451, 475-489.Chraibi, M., Seyfried, A., Schadschneider, A., 2010. Generalized centrifugal-force model for pedestrian dynamics. Phys. Rev. E 82(4 Pt 2), 046111.Corbetta, A., Bruno, L., Muntean, A., Toschi, F., 2014. High Statistics Measurements of Pedestrian Dynamics. Transportation Research Procedia 2, 96-104.Do, T., Haghani, M., Sarvi, M., 2016. Group and Single Pedestrian Behavior in Crowd Dynamics. Transport Res Rec(2540), 13-19.Dong, H., Zhou, M., Wang, Q., Yang, X., Wang, F., 2020. State-of-the-Art Pedestrian and Evacuation Dynamics. IEEE Trans. Intell. Transp. Syst. 21(5), 1849-1866.Douthwaite, J.A., Zhao, S., Mihaylova, L.S., 2019. Velocity Obstacle Approaches for Multi-Agent Collision Avoidance. Unmanned Systems 7(01), 55-64.Galea, E.R., Deere, S.J., Brown, R., Filippidis, L., 2014. A validation data-set and suggested validation protocol for ship evacuation models. Fire Safety Science 11, 1115-1128.Gao, Z.Y., Qu, Y.C., Li, X.G., Long, J.C., Huang, H.J., 2014. Simulating the Dynamic Escape Process in Large Public Places. Oper Res 62(6), 1344-1357.Hanseler, F.S., Bierlaire, M., Farooq, B., Muhlematter, T., 2014. A macroscopic loading model for time-varying pedestrian flows in public walking areas. Transportation Research Part B-Methodological 69, 60-80.He, X., Aloi, D., Li, J., 2015. Probabilistic multi-sensor fusion based indoor positioning system on a mobile device. Sensors-Basel 15(12), 31464-31481.Helbing, D., Buzna, L., Johansson, A., Werner, T., 2005. Self-organized pedestrian crowd dynamics: Experiments, simulations, and design solutions. Transportation Science 39(1), 1-24.Helbing, D., Farkas, I., Vicsek, T., 2000. Simulating dynamical features of escape panic. Nature 407(6803), 487-490.Helbing, D., Molnar, P., 1995. Social force model for pedestrian dynamics. Phys. Rev. E 51(5), 4282-4286.Hidaka, K., Hayakawa, K., Nishi, T., Usui, T., Yamamoto, T., 2019. Generating pedestrian walking behavior considering detour and pause in the path under space-time constraints. Transportation Research Part C-Emerging Technologies 108, 115-129.Hoogendoorn, S.P., Bovy, P.H.L., 2004. Pedestrian route-choice and activity scheduling theory and models. Transportation Research Part B-Methodological 38(2), 169-190.Huang, Z., Chraibi, M., Cao, S., Huang, C., Fang, Z., Song, W., 2019. A microscopic method for the evaluating of continuous pedestrian dynamic models. Physica A 536, 122461.ISO, 2020. Fire safety engineering — Verification and validation protocol for building fire evacuation models. ISO, Switzerland.Johansson, A., Helbing, D., Shukla, P.K., 2007. Specification of the social force pedestrian model by evolutionary adjustment to video tracking data. Advances in complex systems 10(supp02), 271-288.Lü, Y.-X., Wu, Z.-X., Guan, J.-Y., 2020. Pedestrian dynamics with mechanisms of anticipation and attraction. Physical Review Research 2(4), 043250.Ma, Y., Lee, E.W., Hu, Z., Shi, M., Yuen, R.K., 2019. An Intelligence-Based Approach for Prediction of Microscopic Pedestrian Walking Behavior. IEEE Trans. Intell. Transp. Syst. , 1-17.Moussaid, M., Helbing, D., Theraulaz, G., 2011. How simple rules determine pedestrian behavior and crowd disasters. Proceedings of the National Academy of Sciences of the United States of America 108(17), 6884-6888.Porter, E., Hamdar, S.H., Daamen, W., 2018. Pedestrian dynamics at transit stations: an integrated pedestrian flow modeling approach. Transportmetrica A: Transport Science 14(5-6), 468-483.Poulos, A., Tocornal, F., de la Llera, J.C., Mitrani-Reiser, J., 2018. Validation of an agent-based building evacuation model with a school drill. Transportation Research Part C: Emerging Technologies 97, 82-95.Qu, Y.C., Gao, Z.Y., Xiao, Y., Li, X.G., 2014. Modeling the pedestrian's movement and simulating evacuation dynamics on stairs. Safety Science 70, 189-201.Ronchi, E., 2021. Developing and validating evacuation models for fire safety engineering. Fire Saf. J. 120, 103020.Ronchi, E., Kuligowski, E.D., Reneke, P.A., Peacock, R.D., Nilsson, D., 2013. The process of verification and validation of building fire evacuation models. US Department of Commerce, National Institute of Standards and Technology.Sadeghian, A., Kosaraju, V., Sadeghian, A., Hirose, N., Rezatofighi, H., Savarese, S., 2019. Sophie: An attentive gan for predicting paths compliant to social and physical constraints, Proceedings of the IEEE Conference on Computer Vision and Pattern Recognition, pp. 1349-1358.Schadschneider, A., Chraibi, M., Seyfried, A., Tordeux, A., Zhang, J., 2018. Pedestrian Dynamics: From Empirical Results to Modeling, in: Gibelli, L., Bellomo, N. (Eds.), Crowd Dynamics. Springer International Publishing, Cham, pp. 63-102.Seer, S., Brandle, N., Ratti, C., 2014. Kinects and human kinetics: A new approach for studying pedestrian behavior. Transportation Research Part C-Emerging Technologies 48, 212-228.Seyfried, A., Steffen, B., Klingsch, W., Boltes, M., 2005. The fundamental diagram of pedestrian movement revisited. J. Stat. Mech: Theory Exp. 2005(10), P10002.Sticco, I.M., Frank, G.A., Cornes, F.E., Dorso, C.O., 2020. A re-examination of the role of friction in the original Social Force Model. Safety Science 121, 42-53.Van den Berg, J., Lin, M., Manocha, D., 2008. Reciprocal velocity obstacles for real-time multi-agent navigation, Robotics and Automation, 2008. ICRA 2008. IEEE International Conference on. IEEE, pp. 1928-1935.Vanumu, L.D., Ramachandra Rao, K., Tiwari, G., 2017. Fundamental diagrams of pedestrian flow characteristics: A review. European Transport Research Review 9(4), 49.Weidmann, U., 1993. Transporttechnik der Fussgänger: Transporttechnische Eigenschaften des Fussgängerverkehrs (Literaturauswertung). ETH, IVT.Xiao, Y., Gao, Z., Jiang, R., Huang, Q., Yang, H., 2021. Exploration of pedestrian side preference behavior with circle antipode experiments: analysis, simulation and implication. Transportmetrica B: Transport Dynamics 9(1), 266-282.Xiao, Y., Gao, Z.Y., Jiang, R., Li, X.G., Qu, Y.C., Huang, Q.X., 2019. Investigation of pedestrian dynamics in circle antipode experiments: Analysis and model evaluation with macroscopic indexes. Transportation Research Part C-Emerging Technologies 103, 174-193.Xiao, Y., Gao, Z.Y., Qu, Y.C., Li, X.G., 2016. A pedestrian flow model considering the impact of local density: Voronoi diagram based heuristics approach. Transportation Research Part C-Emerging Technologies 68, 566-580.Xue, H., Huynh, D.Q., Reynolds, M., 2018. SS-LSTM: A hierarchical LSTM model for pedestrian trajectory prediction, 2018 IEEE Winter Conference on Applications of Computer Vision (WACV). IEEE, pp. 1186-1194.Zhang, J., Klingsch, W., Schadschneider, A., Seyfried, A., 2011. Transitions in pedestrian fundamental diagrams of straight corridors and T-junctions. J. Stat. Mech: Theory Exp. 2011(06), P06004.Zhang, J., Klingsch, W., Schadschneider, A., Seyfried, A., 2012. Ordering in bidirectional pedestrian flows and its influence on the fundamental diagram. J. Stat. Mech: Theory Exp. 2012(02), P02002.Zhang, P., Li, X.-Y., Deng, H.-Y., Lin, Z.-Y., Zhang, X.-N., Wong, S.C., 2020. Potential field cellular automata model for overcrowded pedestrian flow. Transportmetrica A: Transport Science 16(3), 749-775.Zhang, P., Ouyang, W., Zhang, P., Xue, J., Zheng, N., 2019. Sr-lstm: State refinement for lstm towards pedestrian trajectory prediction, Proceedings of the IEEE Conference on Computer Vision and Pattern Recognition, pp. 12085-12094.

A.14 Article XIII

Hybrid multi- and inter-modal transport simulation: A case study on large-scale evacuation planning

---

G. Lämmel, M. Chraibi, A. Kemloh, B. Steffeni

Transportation Research Record, 2561(1), 1–8. (**2016**)

Transportation Research Record, 2561(1), 1–8. 2016
https://doi.org/10.3141/2561-01

Hybrid multi- and inter-modal transport simulation: A case study on large-scale evacuation planning

Gregor Lämmel[1], Mohcine Chraibi[1], Armel Ulrich Kemloh Wagoum[1] Bernhard Steffen[1]

Abstract
Transport simulation models exist on multiple scales from evacuation simulations of nightclubs with a few hundred guests over the simulation of transport hubs such as large train stations up to evacuation simulations of megapolis in case of tsunamis. Depending on precision and complexity requirements, continuous (e.g. force-based, velocity obstacle based), spatiotemporal discrete (e.g. cellular automata), or queue models are applied. In general, the finer the spatiotemporal resolution the more precise the interactions between travelers (e.g. pedestrians or vehicles) are captured, but the computational burden increases. The obvious approach to achieve higher computational speeds is to reduce the physical complexity (e.g. by using a queue model), which in turn also reduces the precision. One way to increase the computational speed while staying precise enough to make reliable prognosis is to combine models of different scale in a hybrid manner, where a finer model is applied where needed and a coarser model where plausible. This contribution discusses an application of a hybrid simulation approach in the context of a large-scale multi- and inter-modal evacuation scenario. The presented case study investigates the feasibility of an evacuation of parts of the city of Hamburg in Germany in case of a storm surge.

Keywords
application; Multimodal simulations

[1] *Institute for Advanced Simulation, Forschungszentrum Jülich, Jülich, Germany*

Contents

Introduction

Transport simulation models exist on multiple scales from evacuation simulations of nightclubs with a few hundred guests over the simulation of transport hubs such as large train stations up to simulation of the commuter traffic of entire countries [1]. Vehicular traffic usually is confined to roads and vehicles drive in lanes, while pedestrians do not follow such strict rules and walk, in particular in open spaces, omnidirectional. Consequently, large-scale vehicular traffic can be adequately simulated with simplified models such as queue models [2]. Due do its more open nature the movement of pedestrians is more difficult to

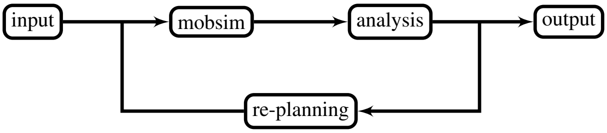

Figure 1. General workflow of the MATSim framework.

model. Depending on precision and complexity requirements continuous (e.g. force-based, [3] velocity-based [4, 5]), event based (e.g. event based cellular automata [6]), spatiotemporal discrete (e.g. cellular automata [7]), or queue based [8]) models are applied. The reader is referred to [9] for a comprehensive review of existing pedestrian models. In general, the finer the spatiotemporal resolution the more precise the interactions between pedestrians are captured, but at the price of a higher computational burden. In the past, pedestrian simulations were mainly applied for planning purposes where the computational burden played a minor part. Currently, the focus shifts towards real-time crowd management decisions support systems, where the simulation is used to make (short term) predictions on how a particular situations will evolve [10]. An integral requirement is that the simulation runs faster than real-time, without loosing accuracy of the models (by oversimplifying for instance). The obvious approach to achieve higher computational speeds is to reduce the physical complexity (e.g. by using a queue model), which in turn also reduces the precision. One way to increase the computational speed while staying precise enough to make reliable prognosis is to combine models of different scale in a hybrid manner, where a finer model is applied where needed and a coarser model where plausible [11, 12]. This raises two problems: (i) finding an assignment of different simulation models to different sub-areas in a way that maximizes computational efficiency while still getting feasible simulation results; (ii) the interface between the models must guaranty that fundamental properties like flow and density are preserved. According to [13] consistency in traffic performance and transparent communication and data exchange should be preserved when coupling models from different simulation frameworks.

In this work we present a prototype for combining two different open-source frameworks, in order to deal in an adequate manner with the aforementioned complexity-performance duality. On one hand MATSim[1] is used to perform large-scale traffic simulations. On the other hand, MATSim makes use of microscopic simulation results communicated by JuPedSim[2]. The agent's states are communicated between the two frameworks via GRPC[3].

The presented concept is tested on a real-world scenario, by investigating the multi- and inter-modal evacuation of Hamburg Wilhelmsburg (Germany) in case of a storm surge.

1. Simulation model

This work combines two simulation models in a hybrid model. Vehicular traffic, pedestrians in low-density conditions, and public transport are simulated by a simple queue model, while the movement of pedestrians under dense conditions is simulated by a force-based model. The hybrid coupling method guarantees that no traveller can exist in both simulation models at the same time. The queuing model is part of the MATSim framework and the force-based model is integrated into JuPedSim. MATSim is programmed in Java, while JuPedSim is programmed in C++. The fact that both frameworks are developed in different programming languages makes a hybrid coupling more challenging but also enables the development of a general interface that can be implemented by any simulation framework.

1.1 MATSim

MATSim is a simulation framework for large-scale transport problems. The general workflow of MATSim is depicted in Figure 1. The actual traffic flow simulation runs in the *mobsim* module. After the traffic flow simulation terminates the performance (e.g. in terms of travel-time) of all travelers is scored in the *analysis*. The *re-planning* modules enables travelers to revise their travel plans before *mobsim* is run again. Details on the functioning of this iterative best-response dynamics are discussed in [14, 15]. The construction and analysis of travel plans is discussed in [16]. Details about the queue model can be found in [2] and its adaptation to pedestrian traffic is discussed in [17]. In its current implementation travelers do not interact interact directly with each other, instead flow dynamics are determined by static attributes such as free speed, flow capacity, and space capacity. Newer approaches [18, 19] aim of introducing some kind of physical interaction between travelers for a more precise representation of the flow dynamics. Those approaches are, however, not adapted in the present study.

---

[1] MATSim stands for Multi-Agent Transport Simulation and is an opensource software designed to perform large-scale transport simulations (see, `www.matsim.org`)

[2] Jülich Pedestrian Simulator, `www.jupedsim.org`

[3] GRPC is a high performance framework for remote procedure calls (see, `grpc.io`) that make use of Google Protocol Buffers (`developers.google.com/protocol-buffers/`) to efficiently encode messages.

1.2 JuPedSim

JuPedSim is an open source framework for simulating pedestrian dynamics [20]. It is platform independent, released under the LGPL license. JuPedSim consists of different modules: *JPScore* is the core module computing the trajectories based on numerical simulations. The simulated or experimental trajectories can be visualized with *JPSvis*. Based on the gained trajectories different characteristic quantities e.g. density, flow and velocity can be measured and analyzed with *JPSreport*. Last, with *JPSedit* importing CAD-geometries or editing of needed geometries (for simulation or measurement of experiments) is possible.

All four aforementioned modules are loosely coupled. That means they can be used independently of each other. In this section we limit ourselves to describe the mathematical model implemented in *JPScore* and used to simulate microscopically the movement of pedestrians. The movement of pedestrians at each time step is defined by superposition of a driving force and repulsive forces. On an operational level, the implemented model is continuous in space and time. The model is based on a *continuous* physical force. Depending on the chosen parameter, the model simulates *social* as well as *physical* forces in a continuous manner. This is in contrast to other known physical forces which are defined as a step-function to hinder excessive overlapping of pedestrians. In *JPScore* pedestrians are modeled as two-dimensional ellipses with velocity-dependent semi-axes. While this form is more calculation intensive than simple circles or even points, it represents more adequately the projection of a moving human body on two-dimensional space.

Given the Gompertz function

$$\mathscr{G}(\beta_{ij}) = \exp\big(-b\exp(-c\beta_{ij})\big), \tag{1}$$

with b the displacement along the x-axis ($\equiv$ cut off radius) and c the growth rate (y scaling). The function (Equation 1) depends on the quantity

$$\beta_{ij} = 1 - \frac{d_{ij}}{r_i + r_j}, \tag{2}$$

with d_{ij} being the distance between the pedestrian i with polar radius r_i and the pedestrian j with polar radius r_j. See Figure Figure 2.

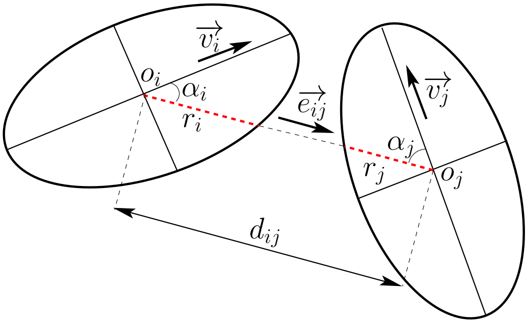

Figure 2. Distance between two pedestrians modeled as ellipses.

Considering the aforementioned quantities, the repulsive force is defined as

$$\overrightarrow{F_{ij}}^{\text{rep}} = -\eta \cdot \parallel \overrightarrow{v_i^0} \parallel \cdot \mathscr{G}(\beta_{ij}) \cdot \overrightarrow{e_{ij}}. \tag{3}$$

η is a parameter to calibrate the strength of the force and $\overrightarrow{v_i^0}$ is the desired velocity of pedestrian i.

In most known force-based models the repulsive force is whether algebraically decaying or exponential. Which means the forces do not vanish for high distances but are infinitely small. Therefor, imposing an explicit cutoff-radius is often used as a remedy to reduce the range of the repulsive forces. In the Gompertz model there is no need for such measure. The cutoff-radius is *implicitly* part of the model definition. For this purpose we choose a cutoff radius β_c such that, the distance (between centers) is equal to a multiple of the sum of radii, $\mathscr{G}(\beta < \beta_c) \ll 0$. Considering Equation 2 we set $\beta_c = -2$ as corresponding to $3\times$ the sum of radii.

$$\beta < \beta_c \text{ and } d - r_i - r_j = -(r_i + r_j)\beta \text{ imply}$$
$$d - r_i - r_j \geq \underbrace{-2\max(\mathrm{E_a}, \mathrm{E_b})\beta_\mathrm{c}}_{\text{cutoff}}. \tag{4}$$

E_a and E_b are resp. the semi-axes in the direction of motion and orthogonal to it.

We have per definition of the ellipses

$$\max(E_a) = a_{\min} + a_\tau v^0,$$

and

$$\max(E_b) = 0.5(b_{\min} + 0.49).$$

For more details about the modeling of the shape of pedestrians we refer to [3]. For $a_{\min} = 0.18$ m, $a_\tau = 0.23$ s and $v^0 = 1.34$ m/s we get $\max(E_a) = 0.488\ m$ and for $b_{\min} = 0.4\ m$ we get $\max(E_b) = 0.445\ m$. These values imply that the cutoff radius for (Equation 4) is effectively about 2 m (0.488· 2· 2 = 1.952 m).

We want to choose b and c such that the following inequalities are fulfilled

$$\mathscr{G}(\beta < \beta_c) < \varepsilon, \tag{5}$$

and

$$\mathscr{G}(\beta > \beta_m) > \Theta. \tag{6}$$

β_c being the cutoff radius and β_m the maximum allowed β_{ij} reducing the amount of possible overlapping between pedestrians i and j. Θ is a threshold and ε is a small constant[4].

Simple calculations yield $b = 0.034229, c = 2.450932$. Figure 3 shows the resulting shape of the repulsive force using the aforementioned calculations of b and c.

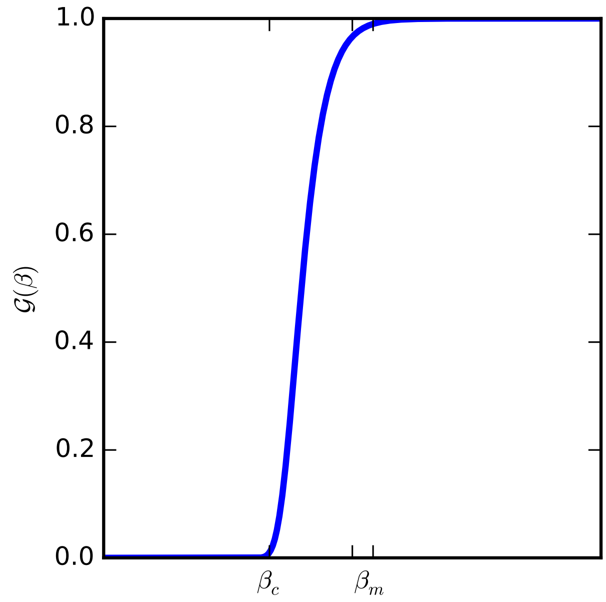

Figure 3. The repulsive force with respect to β for b=0.034229, c=2.450932.

---

[4] $\Theta = 0.99$ and $\varepsilon = 0.01$.

1.3 Hybrid coupling

In the hybrid coupling MATSim is the primary module that controls the program flow, which includes all JuPedSim operations. MATSim and JuPedSim are coupled by transition areas that guarantee a smooth transition between the models. The communication between both simulation frameworks is realized via the cross-platform remote procedure call framework GRPC. Thus, it is neither necessary that both simulation frameworks run on the same host, nor is it necessary that both hosts run the same operating system. This makes the usage of the proposed hybrid coupling approach very flexible and can be easily adapted by other simulation frameworks. The general iterative learning cycle (see Figure 1) remains unchanged. Changes in MATSim are confined to the *mobsim* module. Every time a traveller is about to leave the simulation area that is handled by the queue model, MATSim "asks" JuPedSim if there is space at the corresponding location to host one additional traveler. If this is the case the traveler is transferred to JuPedSim. Vice-versa, when a traveller reaches the boundary of the exchange area that is simulated by the force-based model, JuPedSim "asks" MATSim whether there is space at the corresponding queue link and if so, the traveller is transferred. Each side (MATSim and JuPedSim) implements the same send and receive procedures in a symmetric manner.

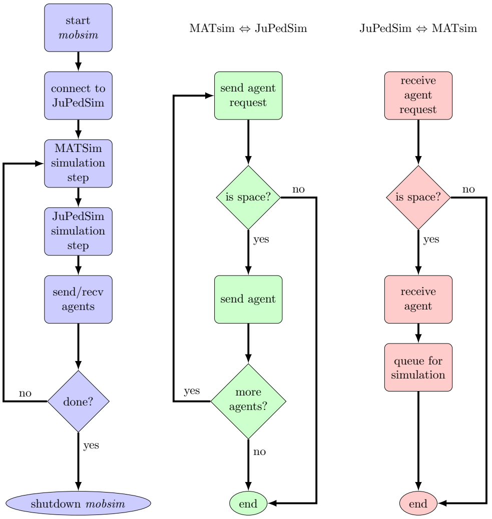

Figure 4. Workflow of the *mobsim* module and the hybrid coupling.

A schema of this workflow is depicted in Figure 4.

Note, a JuPedSim simulation step may consist of several micro simulation steps in the force-based model. Currently, MATSim has a time step resolution of one second, while the force-based model has a time resolution of at least 0.01 seconds. Thus, every time *JuPedSim simulation step* is called JuPedSim actually performs 100 micro-steps or more. In the current implementation *MATSim simulation step* is always executed before *JuPedSim simulation step*. The actual order does only play a minor role and in any case the temporal deviation between both models will never exceed 1 second. At the end of each *MATSim simulation step* both models are temporally synchronized. The main loop of *mobsim* repeats until the last traveller reaches its destination in which case the *done?*-condition is met and *mobsim* shuts down.

2. Scenario setup

The simulation requires two essential inputs: A simulation environment and the evacuation demand. The simulation environment describes the space in which the physical movement of the travelers takes place. For the queue simulation the physical environment is given by a graph consisting of links and nodes. For vehicular traffic links correspond to road segments, while nodes correspond to intersections. For pedestrians links might correspond to sidewalks, crosswalks, but also escalators and elevators are possible. Accordingly, nodes corresponds more to decision points than strictly to intersections. The links in the queue model have various attributes. Such as, free speed, flow capacity, or number of lanes. These attributes, might also be time-dependent in order to model dynamic aspects like time-dependent inundations [21]. In the underlying hybrid simulation approach, those time-dependent attributes are applied in order to emulate the opening and closing of doors of commuter trains. Time-dependent inundation is not modeled since it is assumed that the evacuation is finished before the storm surge arrives.

The force-based simulation model requires a much more detailed model of the physical environment. Herein, the space is decomposed in rooms connected with lineal transitions. Depending on the degree of granularity, rooms may also be subdivided in many walkable areas, which may be useful to simulate room specific aspects e.g. distribution of pedestrians in different neighboring sub-components of a certain areas.

The departure time distribution is perhaps the most tenuous parameter to set; the authors are not aware of any holistic research into this matter. In general, it seems reasonable to assume that many people start evacuating at the same time, or soon after the evacuation order has been issued and as time proceeds, fewer and fewer people are left to depart. This requires a departure time distribution that has a probability density function beginning with a steep positive gradient, leveling out slowly after a peak. The probability density function of a log-normal distribution produces this kind of curve; log-normal and normal distributions are closely related. If the random variable Y is normal distributed, then $X = \exp(Y)$ is log-normal distributed. The expected value $E[X]$ and the variance $Var[X]$ are

$$E[X] = \exp(\mu + \frac{\sigma^2}{2}), \tag{7}$$

and

$$Var[X] = \exp(2(\mu + \sigma^2)) - \exp(2\mu + \sigma^2). \tag{8}$$

Conversely, if the expected value and variance is given, μ and σ of the associated normal distribution can be obtained as follows:

$$\sigma = \sqrt{\log\Big(1 + \frac{Var[X]}{(E[X])^2}\Big)}, \tag{9}$$

and

$$\mu = \log(E[X] - \frac{1}{2}\sigma^2). \tag{10}$$

If users wish to generate a population with departure times following a log-normal distribution, it is hard to see how σ and μ will determine the outcome. It is much more convenient to consider expected value and variance. Given Equation (9) and Equation (10), a conversion from expected value and variance to σ and μ is straightforward.

After the initial demand with corresponding departure times has been created a safe location as destination has to be assigned to each individual evacuee. In the underlying domain, every node outside the evacuation area is a possible destination for an evacuee seeking an escape route. Thus, the evacuation problem is, in general, a multi-destination problem. To resolve this, the standard approach (e.g. [22, 23]) is to extend the network in the following way: All exit links (i.e. links that originate inside the evacuation area and terminate outside the evacuation area) are connected, using virtual links with very high (essentially infinite) flow capacity and equal length, to a super-node; all evacuation routes are routed to the super-node. This way, the problem is reduced to a multi-source single-destination problem. And thus, finding the shortest path from any node inside the evacuation area to this super-node and, in consequence, to safety, can efficiently be solved.

3. Case study Hamburg Wilhelmsburg

Hamburg-Wilhelmsburg is a district of the city of Hamburg in Germany with about 50,000 inhabitants. The district is situated on an island surrounded by the river of Elbe. The distinct location on an island in one of Central Europe's major rivers close to the outfall into the North Sea makes Hamburg-Wilhelmsburg prone to storm surge disasters. Hamburg-Wilhelmsburg was severely flooded by a storm surge in 1962. More than 300 people lost their lives and up to 6,000 homes were destroyed in the city of Hamburg. Today, Hamburg-Wilhelmsburg is much better prepared to such an event than it was in 1962. The island is now protected by stronger and higher dikes. What is more, back in 1962 many people still lived in makeshift shelters that had been build after World War II. Those makeshift shelters, that could not withstand the flooding have been replaced by modern concrete buildings over the years. Thus, even without evacuating the island people would be safe in most cases by going upstairs (e.g. to their neighbors) in case of a flooding. However, it might take long time for the water masses to retreat after a storm surge and this would let the people trapped in their houses. Thus, an orderly evacuation seems to be the best solution in case of a major event and with a sufficient long advance warning time. Todays early warning systems can predict a storm surge about 9 hours before the event and the civil protection authorities in Hamburg have a detailed evacuation plan in place. The first public announcement of the imminent evacuation will be issued 3 hours before the official evacuation order. The evacuation itself is assumed to take 3 hours. Thus, there is a time buffer of another 3 hours in case the event occurs earlier or the evacuation takes longer. A detailed description of the evacuation plan is discussed in [24]. The total evacuation time t_{evac} over the entire population P is:

$$t_{\text{evac}} = t_{\text{detect}} + t_{\text{decide}} + t_{\text{alarm}} + \max_{i \in P}(t^i_{\text{prepare}} + t^i_{\text{move}}), \tag{11}$$

with t_{detect} being the time it takes to detect the threat, t_{decide} the time after which the evacuation decision is made, t_{alarm} the time disseminating the evacuation order, t^i_{prepare} the time evacuee i needs to prepare her/his evacuation, and t^i_{move} her/his actual movement time. As t_{evac} depends on the performance/choices of the individual evacuees, t_{evac} is not a particular robust quantity (e.g. if only one single evacuee decides not to evacuate at all t_{evac} becomes infinity).

This case study focuses mainly on the movement times t^i_{move} under the assumption the preparation time t_{prepare} follows a log-normal distribution as discussed in the previous section. The expected value for the departure time X is set to $E[X] = 0.75$ h and the variance is set to $Var[X] = 0.5$. An interpretation of this is that most people start their evacuation around 45 minutes after the evacuation has been ordered. Taking the fact that people are getting informed up to 3 hours before the official evacuation order this is a rather conservative assumption.

The evacuation simulation comprises the simulation of vehicular traffic as well as the evacuation of pedestrians who walk to the next commuter rail station in order to evacuate by train. The evacuation demand for the vehicular traffic is based on previous studies (see, [24, 25]). The number of private owned vehicles in Hamburg Wilhelmsburg is about 11,200. The simulation network for vehicular traffic has been extracted from openstreetmap. It consists of 6,419 nodes and 11,470 links. The length of all links in the network is about 460 km (276 miles). Link attributes such as flow capacity and number of lanes are derived from openstreetmap by evaluating the link specific *highway*-tags. Details about simulation network extraction from openstreetmap are discussed in [26]. The expected bottlenecks for the vehicular traffic are the bridges connecting the island with the other districts of Hamburg. Besides some smaller bridges and a very low capacity tunnel in the north, there are 4 motorway or arterial road bridges. The combined capacity of those bridges is well beyond 11,200 vehicles per hour. Thus, the predominant factor is expected to be the preparation and not the actual movement time. A detailed simulation of evacuees without access to a motorized vehicle has thus far not been studied by a simulation approach. Without simulating, in [24], the evacuation of those evacuees is assumed to take about 4 hours, which would exceed the available evacuation time by one hour. In the following it is referred to evacuees without access to a motorized vehicle as pedestrians.

The present study investigates the evacuation process of those pedestrians that live in a distance of at most 2 km (1.24 miles) of the commuter rail station Hamburg Wilhelmsburg. Indeed, the chosen distance of 2 km covers only a fraction of the island. Still, it seem to be unrealistic for pedestrians to walk distances of more than 2 km. In fact, in the event of an evacuation bus companies will operate special bus lines to evacuate those pedestrians. Those bus lines are not considered in this case study.

An aerial image of Hamburg Wilhelmsburg indicating the area around the commuter rail station is depicted in Figure 5. Pedestrians who have reached the commuter rail station are not yet safe, but have to wait for the next train. Thus, the evacuation of pedestrians is an intermodal evacuation. Taking the number of people residing inside the 2 km radius (14,108), the average household size of Hamburg (1.81), the number of private vehicles inside the 2 km radius (3,389), and assuming that households that own a vehicle use it for the evacuation, a total of 7,974 pedestrians has to evacuate by foot and public transport. The commuter rail station in Hamburg Wilhelmsburg has two platforms. In case of an evacuation each of the platforms is served every 5 minutes. Thus, a train arrives every 2:30 min on average. The trains are not simulated physically. Instead, each of the two platforms has 18 doors on the side of the tracks. Those doors open and close according to the schedule of the trains. The

Figure 5. Aerial image of Hamburg Wilhelmsburg, the area from which pedestrian evacuated by foot to the train stations is indicated by the dashed orange circle (image source: Landsat ETM+ WRS-2 195/023, 05.11.2001, `www.landcover.org`).

ultimate goal for the pedestrians is to walk through one of those doors. Once a pedestrian has crossed a door she is taken out of the simulation. The travel time that each of the train needs to leave Hamburg Wilhelmsburg is thus neglected. In case of an evacuation the regular service of the commuter trains is ceased and instead an emergency schedule will be activated.

The capacity of the train network is high enough to serve this schedule. Thus, no delays are expected and the travel time of the trains can be assumed to be constant. This means, once an evacuee has boarded a train it will take her/him not longer than $\approx$ 10 min to leave the endangered area. While the simulation of the vehicular traffic is performed with queue model, for the pedestrian simulation a hybrid approach has been applied. The surrounding of the commuter rail station is also simulated with a queue model, but with different parameters. The commuter rail station itself, however, is simulated with a force-based model. The transition from the queue model to the force-based model is performed on an access ramp spanning from one side of the tracks to the other. An illustration of the commuter rail station is given in Figure 6.

4. Results

In the simulation vehicles and pedestrians do not interact with each other. Thus, both modes of transport are performed independently. In a first stage the evacuation simulation of the vehicular traffic has been performed on a standard laptop computer. As discussed, the simulation framework performs an iterative best-response dynamic approach to find a solution that is close to a Nash or dynamic user equilibrium. For the vehicular traffic the simulation has been performed for 100 learning iterations. It took about 12 minutes to simulate all the 100 iterations. Simulation results in terms of departures and arrivals are depicted in Figure 7(a). It is shown that given the assumed departure time distribution at most 2306 vehicles are concurrently on the network. Given the size of the network (¿ 11,000 links) and the combined bottleneck capacity (¿ 11,200 vehicles per hour), those numbers are rather moderate. Still, some minor congestions are observed in particular at on-ramps. An example is shown in Figure 8. Overall, the vehicular evacuation takes about 2 hours. This is well bellow the available 3 hours from the official evacuation plan.

The evacuation simulation for pedestrians has been performed in a similar way. The number of learning iterations is again 100. Since the hybrid approach couples the two simulation models (queue model and force-based model) via a tcp/ip connection it is not necessary that both simulation models run on the same physical hardware. The queue simulation model has been run on a standard desktop computer, while the force-based model has been run on a work station with 8 cores. The total simulation time for all 100 iterations was 46:36 hours. Departure and arrival curves are given in Figure 7(b). Similar to the vehicular evacuation, also for pedestrians the departure time distribution is a critical factor for overall evacuation performance. Still, compared to the vehicular evacuation the maximum number of pedestrians that are concurrently on the move is much higher. The maximum number of 5,337 has been observed 35 minutes after the start of the evacuation.

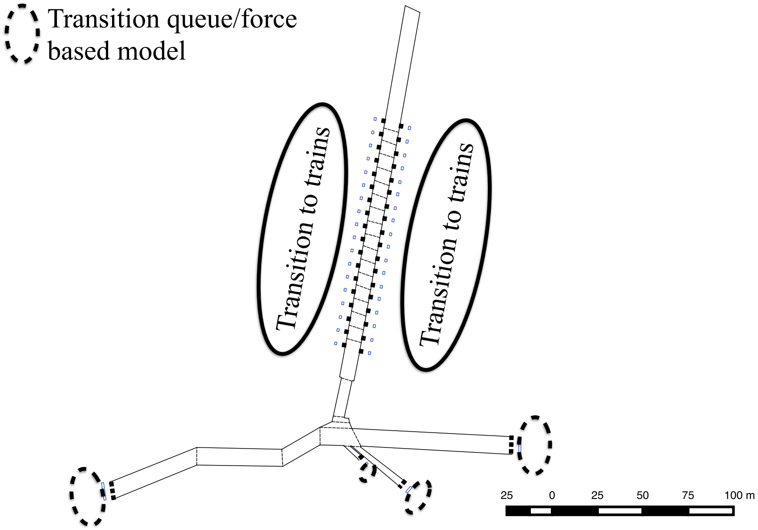

Figure 6. Illustration of the commuter rail station Hamburg Wilhelmsburg. The station itself is simulated using a force-based model. The transition to the queue model and to the trains are indicated by dashed and solid ellipses respectively.

The relatively high number of pedestrians that are concurrently on the move can lead to problems in particular at the commuter rail station Hamburg Wilhelmsburg. Figure 9 illustrates the situation after about 50 minutes. It is clearly shown that there are a high number of pedestrians inside the commuter rail station. This problem will intensify in case the departure time distribution is be narrow. In general, an active crowd management is recommended to limit the number of people inside the commuter rail station. Such a crowd management would require staging areas outside the commuter rail station, where evacuees can wait.

5. conclusion

This work present a new approach to couple different simulation models and different simulation frameworks seamless into a hybrid model. Through its platform independent design the hybrid coupling approach can easily adapted by other simulation frameworks. In fact, the GRPC library is compatible among others with C++, Java, C#, and Objective-C. Thus, an application on a variety of operation systems and computing platforms seems to be viable.

The hybrid coupling approach has been demonstrated on a case study for the city of Hamburg. The case study deals with an evacuation situation of the district of Hamburg Wilhelmsburg. In case of a storm surge up to 50,000 people need to evacuate. While many people will evacuate by car a considerable amount of people without access to a vehicle needs to evacuate by other means. The simulation supported the assumption of the local authorities that an evacuation within 3 hours is possible. The evacuation, independent of the mode of transport, took about 2 hours. As it turned out the dominant factor is the departure time distribution and not the amount of congestion in the network. In particular, the vehicular evacuation is expected to be smoothly and doable in time. For the evacuation of pedestrians who walk to the next train station one has to consider that depending on the departure-time distribution a high demand of passengers might stand on platforms of the train station. A recommendation is that the local authorities should establish staging areas next to the train station where people can be hold back if the platforms tend to overcrowd.

An important issue to be addressed is refining the interface between the simulation models. First steps in this direction have already been proposed in [12]. Furthermore, the current interface allows only for a static coupling of two different models. Further future work will investigate how multiple models can by dynamically coupled at arbitrary spatiotemporal coordinates.

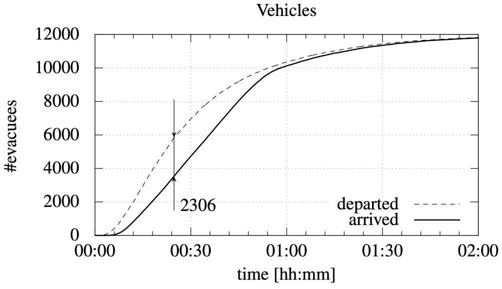

(a) Vehicles

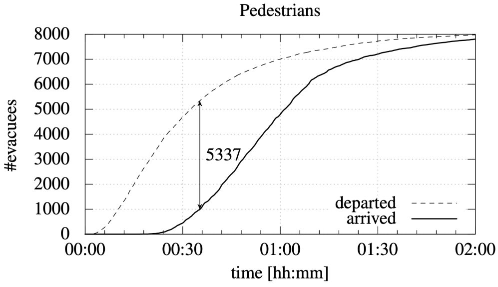

(b) Pedestrians

Figure 7. Departure and arrival curves.

Figure 8. Situation about 20 minutes into simulation showing vehicles in congestion (indicated by the nongreen triangles) at and around an on-ramp to the Wilhelmsburger Reichsstraße, one of the major evacuation routes.

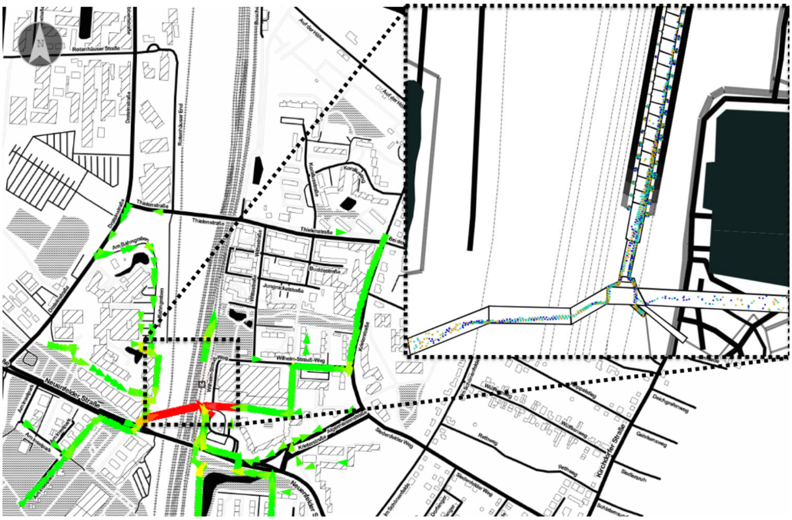

Figure 9. Snapshot of the pedestrian simulation. Major congestions occur inside the commuter rail station.

Acknowledgments

This project was Funded in part by the German Ministry for Education and Research (BMBF) under grant 13N11382 (“GRIPS”).

References

[1] M. Balmer, K. Nagel, and B. Raney. Large scale multi-agent simulations for transportation applications. *J. of Intelligent Transport Systems*, 8:205–223, 2004.

[2] P.M. Simon, J. Esser, and K. Nagel. Simple queueing model applied to the city of Portland. *International Journal of Modern Physics*, 10(5):941–960, 1999.

[3] Mohcine Chraibi, Armin Seyfried, and Andreas Schadschneider. Generalized centrifugal force model for pedestrian dynamics. *Physical Review E*, 82:046111, 2010.

[4] J. van den Berg, S.J. Guy, M. Lin, and D. Manocha. Reciprocal n-body collision avoidance. In *Robotics Research: The 14th International Symposium ISRR*, volume 70, pages 3–19. Springer, 2011.

[5] Christian Eilhardt and Andreas Schadschneider. Stochastic headway dependent velocity model for 1d pedestrian dynamics at high densities. *Transportation Research Procedia*, 2(0):400 – 405, October 2014. The Conference on Pedestrian and Evacuation Dynamics 2014 (PED 2014), 22-24 October 2014, Delft, The Netherlands.

[6] G. Lämmel and G. Flötteröd. A CA model for bidirectional pedestrian streams. *Procedia Computer Science*, 52:950–955, 2015.

[7] A. Schadschneider and A. Seyfried. Validation of ca models of pedestrian dynamics with fundamental diagrams. *Cybernetics and Systems*, 40(5):367–389, july 2009.

[8] G. Lämmel, H. Klüpfel, and K. Nagel. The MATSim network flow model for traffic simulation adapted to large-scale emergency egress and an application to the evacuation of the Indonesian city of Padang in case of a tsunami warning. In H. Timmermans, editor, *Pedestrian Behavior*, chapter 11, pages 245–265. Emerald Group Publishing Limited, 2009.

[9] A. Schadschneider, D. Chowdhury, and K. Nishinari. *Stochastic Transport in Complex Systems. From Molecules to Vehicles*. Elsevier Science Publishing Co Inc., 2010.

[10] Armel Ulrich Kemloh Wagoum, Bernhard Steffen, and Armin Seyfried. Runtime optimisation approaches for a real-time evacuation assistant. In R. Wyrzykowski, editor, 9^{th} *Conference on Parallel Processing and Applied Mathematics*, volume 7203 of *Lecture Notes in Computer Science*, pages 386–395. Springer Berlin/Heidelberg, 2012.

[11] Q. Yang and D. Morgan. A hybrid traffic simulation model. Annual Meeting Preprint 06-2582, Transportation Research Board, Washington D.C., 2006.

[12] G. Lämmel, A. Seyfried, and B. Steffen. Large-scale and microscopic: a fast simulation approach for urban areas. Annual Meeting Preprint 14-3890, Transportation Research Board, Washington, D.C., 2014.

[13] Wilco Burghout and Johan Wahlstedt. Hybrid traffic simulation with adaptive signal control. *Transportation Research Record*, 1999:191–197, 2007.

[14] C. Gawron. An iterative algorithm to determine the dynamic user equilibrium in a traffic simulation model. *International Journal of Modern Physics C*, 9(3):393–407, 1998.

[15] B. Raney and K. Nagel. Iterative route planning for large-scale modular transportation simulations. *Future Generation Computer Systems*, 20(7):1101–1118, 2004.

[16] D. Charypar and K. Nagel. Gernerating complete all-day activity plans with genetic algorithms. *Transportation*, 32(4):369–397, 2005.

[17] G. Lämmel and K. Nagel. Multi agent based large-scale evacuation simulation. Annual Meeting Preprint 09-2135, Transportation Research Board, Washington D.C., 2009. Also VSP WP 08-13, see www.vsp.tu-berlin.de/publications.

[18] A. Agarwal and G. Lämmel. Seepage of smaller vehicles under heterogeneous traffic conditions. *Procedia Computer Science*, 52(C):890–895, 2015.

[19] A. Agarwal, G. Lämmel, and K. Nagel. Modelling of backward travelling holes in mixed traffic conditions. In *Traffic and Granular Flow '15*, Delft, NL, accepted. Also VSP WP 15-15, see `http://www.vsp.tu-berlin.de/publications`.

[20] Armel Ulrich Kemloh Wagoum, Mohcine Chraibi, and Jun Zhang. JuPedSim: an open framework for simulating and analyzing the dynamics of pedestrians. In *3rd Conference of Transportation Research Group of India*, 2015 (To appear).

[21] G. Lämmel, D. Grether, and K. Nagel. The representation and implementation of time-dependent inundation in large-scale microscopic evacuation simulations. 18(1):84–98, February 2010.

[22] L.R. Ford and D.R. Fulkerson. *Flows in Networks*. Princeton University Press, 1962.

[23] Q. Lu, B. George, and S. Shekhar. Capacity constrained routing algorithms for evacuation planning: A summary of results. *LNCS*, 3633:291–307, 2005.

[24] D. Durst, G. Lämmel, and H. Klüpfel. Large-scale multi-modal evacuation analysis with an application to hamburg. In U. Weidmann, U. Kirsch, and M. Schreckenberg, editors, *Pedestrian and Evacuation Dynamics 2012*, pages 361–369. Springer International Publishing, 2014.

[25] G. Lämmel and H. Klüpfel. Slower is faster: the influence of departure time distribution on the overall evacuation performance. In *International Conference on Evacuation Modeling and Management*, Northwestern University, Evanston, Illinois, USA, 2012.

[26] D. Röder, I. Cabrita, and K. Nagel. Simulation-based sketch planning, part III: Calibration of a MATSim-model for the greater Brussels area and investigation of a cordon pricing for the highway ring. VSP working paper 13-16, TU Berlin, Berlin, Germany, 2013. See `http://www.vsp.tu-berlin.de/publications`.

A.15 ARTICLE XIV

On the Effectiveness of the Measures in Supermarkets for Reducing Contact among Customers during COVID-19 Period

Q. Xu and M. Chraibi

Sustainability (**2020**)

Sustainability 12(22), 9385, 2020
10.3390/su12229385

On the Effectiveness of the Measures in Supermarkets for Reducing Contact among Customers during COVID-19 Period

Qiancheng Xu[1], Mohcine Chraibi[1]

Abstract
The spread of the COVID-19 virus had a huge impact on human life on the global scale. Many control measures devoted to decrease contact among people have been adopted to slow down the transmission of the disease. A series of measures have been taken in supermarkets, which include restricting the number of customers, keeping social distance, and entering with a shopping cart. In this work, we investigate with numerical simulations the effectiveness of these measures in reducing the contact among customers. Several scenarios with different control measures are designed for numerical analysis. The movements of customers in a supermarket are simulated by a microscopic model for pedestrian dynamics. Moreover, an index based on the distance between customers is defined to measure the degree of contact and therefore evaluate it quantitatively. The effect of these measures on the average contact degree of each customer is explored, and the spatial distribution of the contact among customers in the supermarket is shown in a qualitative way. Simulation results show that except shopping cart measure, the other two measures are effective in reducing contact among customers.

Keywords
Application; COVID-19 virus disease; control measures; supermarket; numerical simulation

[1] *Institute for Advanced Simulation, Forschungszentrum Jülich, 52425 Jülich, Germany; m.chraibi@fz-juelich.de*

Contents

Introduction

The so-called Coronavirus (COVID-19) was first identified in December 2019 in Wuhan, Hubei, China and has became an infectious disease worldwide [1]. As of 29 June 2020, there have been more than 10 million confirmed cases of COVID-19, including nearly 500,000 deaths, as reported by the World Health Organization (WHO) [2]. The disease spreads primarily from person to person through small droplets produced by coughing, sneezing, or speaking of an infected person [3]. Therefore, as there is still no known vaccine against the virus, reducing close contact situations among people is one of the recommended measures to prevent infection [4]. Other measures taken by many countries to avoid or even prohibit situations leading to close contact among people, including travel restrictions, closing schools, and canceling large gatherings. The effectiveness of these control measures are investigated in some works [5, 6, 7].

The pandemic and these control measures also have a huge impact on pedestrian dynamics at different scales, e.g., touristic urban areas [8, 9] and university buildings [10, 11]. In this work, we focus on supermarkets, which are kept open during the outbreak. In order to keep the safety of customers, a series of measures have been adopted. These measures include setting a limitation on the number of customers in the supermarket, asking customers to keep a certain distance with each other (a minimum of 1.5 m), and requiring customers to enter the supermarket with a shopping cart, while wearing a face mask.

In this paper, we investigate the extent to which these measures are effective in reducing the contact among customers with the help of numerical simulations. Many simulations have been performed to predict the influence of this pandemic on the example of supermarket visitors, and to investigate the best measures to slow down its spread.

Existing models for COVID-19 transmission dynamics operate on different levels, which can be described as macroscopic and microscopic. On the macroscopic level, the investigated population is divided into different groups of individuals sharing the same status, and the interactions between groups are described by systems of differential equations. The most popular model in this category is the SEIR model (Susceptible–Exposed–Infected–Recovered). Many significant works about COVID-19 are based on this model and its extensions [12, 13, 14, 15, 16]. Macroscopic models are computationally cheap and can intuitively reflect the changing trend of groups of population with different infectious statuses. It can be used to predict the spread of the disease, and estimate the effectiveness of control measures in regions with large population, e.g., a city.

As opposed to macroscopic models, which divide population into several groups, microscopic models treat each person as an individual with different properties. The status of each people in the simulation is different, which can be healthy, infected or other. Microscopic models for COVID-19 are usually composed of a model for pedestrian dynamics and a model for disease transmission dynamics. The movement and interaction of individuals are simulated by a model for pedestrian dynamics, and the status transitions of individuals are simulated by a disease transmission model [17, 18, 19, 20]. Although microscopic models are computationally more expensive than macroscopic models, they can map more details in person level, therefore it is suitable to simulate the spread of virus in confined spaces during a short time period.

A supermarket is a relatively small scenario that can have a high population mobility. Therefore, in this work we use a microscopic model to investigate different scenarios in a supermarket and evaluate the effectiveness of measures taken in these scenarios. In the following, we focus on the contact among customers instead of the virus transmission among customers, as reducing contact is important to slow down the transmission of COVID-19. By measuring the contact degree, we can study the effectiveness of various measures more directly.

To simulate the movement of customers in the supermarket, the generalized collision-free velocity model (GCVM) for pedestrian dynamics is adopted [21]. First, we define a distance-based index to quantify the degree of contact among customers. Second, according to the different measures taken by the supermarket, corresponding simulation scenarios are designed and executed. Finally, the values of the contact index obtained from different scenarios are analyzed and compared to evaluate the effectiveness of these measures. This work is organized as follows. In Section 1.1, we briefly introduce the GCVM adopted in this work and give the definition of the index to quantify the contact among pedestrians. Section 1.2 presents the supermarket scenarios designed for the simulations and describes how customers move in the supermarket. Section 2 gives simulation results obtained in the scenarios with different control measures and the corresponding analysis. Finally, in Section 3 we finish with a discussion.

1. Research Methods

1.1 How to Quantify Contact among Pedestrians

The collision-free velocity model for pedestrian dynamics is used in this work to simulate the movement of customers in the supermarket. It is composed of a direction sub-model and a speed sub-model, and can be described as

$$\dot{X}_i(X_i, X_j, \dots) = \vec{e}_i(X_i, X_j, \dots) \cdot V_i(X_i, X_j, \dots), \tag{1}$$

where X_i, $\vec{e}_i$, and V_i are the position, moving direction, and moving speed, respectively.

The direction sub-model calculates the moving direction $\vec{e}_i$ for pedestrian i as

$$\vec{e}_i = u \cdot \left(\vec{e}_i^{\,0} + \sum_{j \in N_i} k \cdot \exp\left(\frac{-s_{i,j}}{D} \right) \cdot \vec{e}_{i,j} + \vec{w}_i \right), \tag{2}$$

where u is a normalization constant such that $\|\vec{e}_i\| = 1$. The new direction is decided by three different components. The first component is the $\vec{e}_i^{\,0}$, which is an unit vector representing the desired moving direction of the pedestrian i. The second component is the effect from other pedestrians belonging to N_i, which is the set that contains all the neighbors who affect the moving direction of pedestrian i. The magnitude of the effect from these neighbors is a function of $s_{i,j}$, which is the distance between the edges of pedestrian i and j along the line connecting their positions. Coefficients $k > 0$ and $D > 0$ are used to calibrate the function accordingly. The direction of the effect from pedestrian j to i is denoted by $\vec{e}_{i,j}$, which is a unit vector point from the position of pedestrian j to pedestrian i. The definitions of $s_{i,j}$ and $\vec{e}_{i,j}$ are shown in Figure 1. The last part is $\vec{w}_i$, which is the effect from walls and obstacles in the building.

The speed sub-model calculates the moving speed V_i for pedestrians i as

$$V_i = \min\left\{V_i^0, \max\left\{0, \frac{s_i}{T}\right\}\right\}, \tag{3}$$

where V_i^0 is the desired moving speed of pedestrian i, s_i is the collision-free moving spacing of pedestrian i in the moving direction $\vec{e}_i$, and coefficient $T > 0$ is used to adjust the speed according to the gap between two pedestrians. A more detailed definition of the model can be found in [21].

The distance among pedestrians changes with time while they are moving in space. We assume that small distances lead to a bigger contact index. Therefore, the index $C_i(t)$, representing the contact degree of pedestrian i with its neighbors at time t, is defined as

$$C_i(t) = \sum_{j \in N_i} \exp\left(-d_{i,j}(t)\right), \tag{4}$$

where $d_{i,j}$ is the distance between the position of pedestrians i and j, see Figure 1.

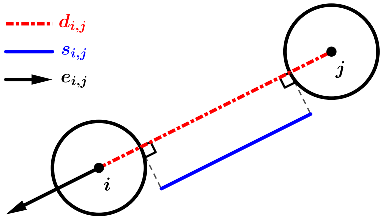

Figure 1. The definition of $s_{i,j}$, $d_{i,j}$ and $\vec{e}_{i,j}$. $s_{i,j}$ is the distance between the edges of pedestrian i and j along the line connecting their positions, $d_{i,j}$ is the distance between the position of pedestrians i and j, and $\vec{e}_{i,j}$ is a unit vector point from the position of pedestrian j to pedestrian i.

1.2 Simulation of Shopping Behavior in the Supermarket

A fictive supermarket scenario, as shown in Figure 2, is built based on a real supermarket nearby the city Jülich in Germany to simulate several scenarios. It represents the typical structure of a medium-sized supermarket in Germany. The supermarket is 34 m long and 18 m wide. It is composed of three different areas: a checkout, a shopping, and an outside area.

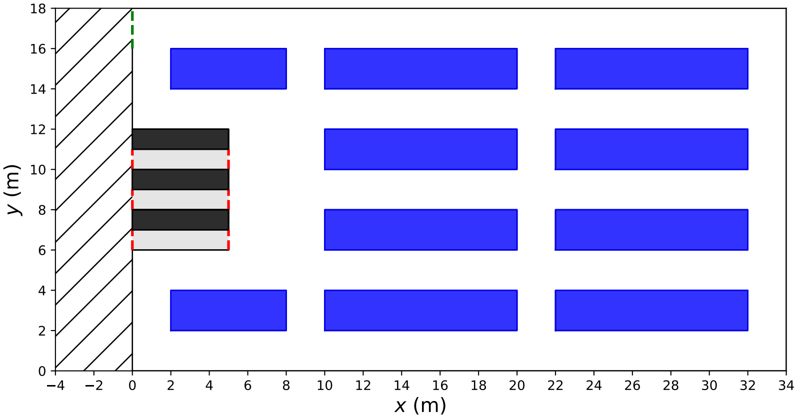

Figure 2. The geometrical structure of the supermarket used in the simulations, the outside area of the supermarket is filled with hatch lines.

The checkout area includes three counters 5×1 m^2 (in black) and three corridors (in gray), while the shopping area includes 10 goods shelves. The sizes of the far left two shelves are 6×2 m^2 and the sizes of other shelves are 10×2 m^2. Except the area in front of the checkout area, the widths of the walking paths are 2 m. The entrance is located in the upper left corner of the supermarket (green dashed segments). The exits from the shopping area to the checkout area and the exits from checkout area to outside are all marked with red dash segments.

We perform the simulations with a total of M customers. Hereby, P persons are generated outside the supermarket every minute until all the M customers are generated. The generated customers enter the supermarket from the entrance and move in the shopping area. Each customer is assigned a random goal within the supermarket after entering the supermarket. After reaching the goal, the customer is assigned another random goal until the time spent in the shopping area is longer than t_i^{shop}, the shopping time for customers.

As introduced before, there are three counters in the checkout area, which means customers have three choices after finishing the shopping. We assume customers prefer to check out at the counter with the fewest customers. Customers who choose the same counter check out one by one in the order of entering the corridor. The time spent for checking out t_i^{check} is proportional to the shopping time and is defined as

$$t_i^{\text{check}} = \alpha \cdot t_i^{\text{shop}}, \tag{5}$$

where $\alpha < 1$ is a parameter. Finally, after checking out, the customers leave the supermarket.

Besides the basic movement of customers, the behavior of customers is influenced by the measures adopted by the supermarket. Therefore, these measures are considered into the basic movement model. We introduce three main measures commonly used in supermarkets nowadays.

The first measure is setting a limitation for the maximal number of customers in the supermarket. This is realized by introducing a new parameter $L_{\max}$ in our model, which is the max allowable number of customers in the supermarket at the same time. Customers can only enter the supermarket when the number of persons inside the supermarket does not exceed the threshold $L_{\max}$. Otherwise, customers have to wait outside.

The second measure is asking customers to keep social distance to each other. From daily observations in supermarkets, the social distance rule is well maintained in the checkout area, but cannot be maintained in a strict manner in the shopping area. Therefore, compared with simulations without the social distance rule, a larger value of D in Equation (2) is adopted to enforce larger distances among pedestrians.

Besides, to simulate the queuing of customers, a modified speed sub-model as following is used when customers are in the checkout area.

$$V_i = \min\left\{V_i^0, \max\left\{0, \frac{d_i - d_i^{\text{wait}}}{T}\right\}\right\}. \tag{6}$$

In the modified speed sub-model, d_i is the distance between positions of customer i and the nearest front customer. d_i^{wait} is the distance that customer i wants to keep with the nearest front customer. The expression of d_i^{wait} is

$$d_i^{\mathrm{wait}} = \max\left\{d_{\mathrm{rule}}, \beta \cdot t_i^{\mathrm{shop}}\right\}, \tag{7}$$

where d_{rule} is the social distance adopted and β is a parameter.

When there is no social distance rule, the distance between the customers in the checkout area is decided by the shopping time, as we assume that longer shopping times correspond to more space for putting purchased good on the conveyor belt. When the social distance measure is taken, customers maintain at least d_{rule} distances with each other even when they purchase few items in the market.

The last measure is requiring customers to enter the supermarket with a shopping cart. In our simulations, customers are represented by circles with a radius r. Considering that shopping carts increase the space occupied by each customer in the supermarket, a bigger ellipse is used to represent the customers with shopping carts. The length of the semi-major axis in the moving direction is a, and the length of semi-minor axis is b.

2. Simulation Results

To explore if the measures taken by the supermarkets are efficient in reducing the contact among customers, the simulations are implemented in the geometry shown in Figure 2 with four different scenarios. For all cases, we use the following parameter values in Table 1. We assumed reasonable values for the desired moving speeds and the shopping times of customers, which are normally distributed for heterogeneity. The mean and standard deviation of the desired moving speeds refer to the free walking speed of pedestrians [22, 23]. The other values in Table 1 are kept constant to guarantee the justification of the comparisons between different scenarios.

Table 1. The same parameters in all four scenarios. k (Equation (2)) is the parameter to calibrate the strength of the impact from other pedestrians, T (Equations (3) and (6)) is the parameter to calibrate the speed according to the gap between two pedestrians, α (Equation (5)) is the parameter to calibrate the checkout time according to the shopping time, β (Equation (7) is the parameter to calibrate the distance between customers in checkout area according to the shopping time, M is the total number of customers generated in the simulation, P is the number of customers generated every minute, V_i^0 (Equations (3) and (6)) is the desired moving speed of customers, and t_i^{shop} is the shopping time of customers.

Parameters	Values
k	8
T (s)	1
α	0.1
β (m/s)	0.003
M (person)	100
P (person/minute)	10
V_i^0 (m/s)	$N \sim (1.34, 0.26^2)$
t_i^{shop} (s)	$N \sim (300, 50^2)$

The differences among the settings of these four scenarios are shown in Table 2. A complete list of all parameters choices in the four scenarios is given in Table 5.

Table 2. The setting of four scenarios in this work. $L_{\max}$ is the max allowable number of customers in the supermarket at the same time, d_{rule} is the social distance, and D (Equation (2)) is the parameter to calibrate the scale of the impact from other pedestrians.

Scenario ID	$L_{\max}$ (Person)	d_{rule} (m)	D (m)	Need Shopping Cart
1	50	0	0.1	No
2	30	0	0.1	No
3	30	1.5	0.3	No
4	30	1.5	0.3	Yes

The snapshots of each scenario are shown in Figure 3. The customers are represented by circles with $r = 0.2$ m in scenarios 1, 2, and 3, where customers can enter the supermarket without a shopping cart. In scenario 4, customers enter the supermarket with shopping carts, therefore they are represented by ellipses with semi-axes $a = 0.4$ m and $b = 0.25$ m. Customers inside the supermarket are in green whereas customers outside are in red.

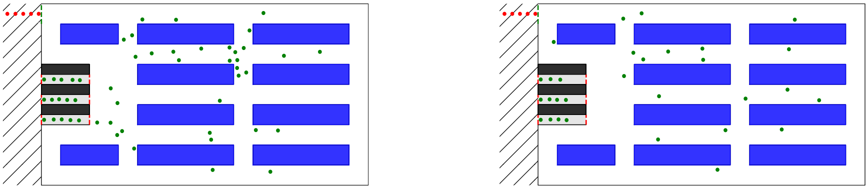

(**a**) (**b**)

Figure 3. *Cont.*

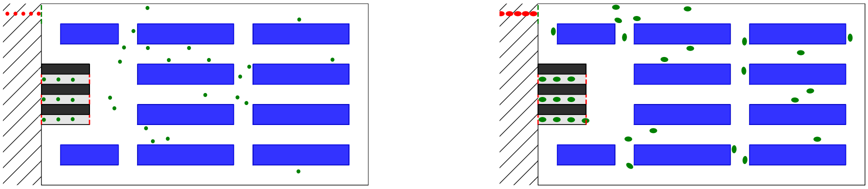

(**c**) (**d**)

Figure 3. The snapshots of four scenarios; customers inside the supermarket are in green, whereas customers outside are in red. (**a**) Scenario 1. (**b**) Scenario 2. (**c**) Scenario 3. (**d**) Scenario 4.

Supermarkets take measures to reduce the contact among customers, but these measures may result in a decrease in the service efficiency. Two quantities are chosen to study the trade-off between the efficiency of the supermarket and the effectiveness of the measures: The first one is t^{sim}, which is the time spent by all the M customers in the supermarket. t^{sim} reflects the efficiency of the supermarket. It can be represented by

$$t^{\text{sim}} = t^{\text{last}} - t^{\text{first}}, \tag{8}$$

where t^{first} is the time when the first customer enters the supermarket, and t^{last} is the time when the last customer leaves the supermarket. The second one is the average contact degree of all the M customers, which is defined as

$$\bar{C} = \frac{1}{M} \cdot \int_{t^{\text{first}}}^{t^{\text{last}}} \sum_{i=1}^{M} C_i(t) dt. \tag{9}$$

If customer i is outside the supermarket, C_i is equal to zero. A reasonable measure should reduce $\bar{C}$ as much as possible without increasing t^{sim} significantly.

The simulations of this work are performed using JuPedSim [24], which is an open framework for simulating and analyzing the dynamics of pedestrians. The simulations are executed on a standard computer (Inter(R) Core(TM) CPU of 2.50 GHZ) with Euler scheme using a time step $\Delta t = 0.05$ s. The update of the customers is parallel in each time-step. We run simulations in each scenario for 30 times. Then, we calculated the mean value and standard deviation of t^{sim} and $\bar{C}$, which are shown in Figure 4.

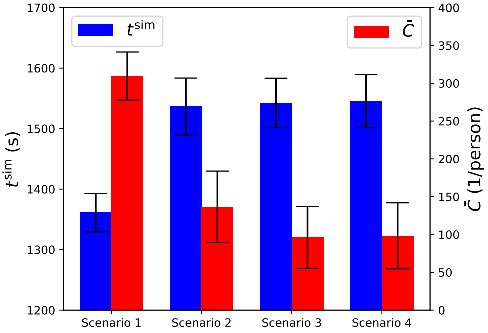

Figure 4. The comparison of t^{sim} (time spend by all customers) and $\bar{C}$ (average contact degree of all customers) for four scenarios, the error bars show the standard deviation.

Hypothesis testing is implemented before comparing the results of different scenarios. The null hypothesis is set as there is no significant difference between the results of two compared scenarios. The Shapiro–Wilks test is performed first to test the normality of the differences between the results of two scenarios. Since all the differences satisfy the condition of normality (p_1 is greater than 0.05), we can perform the Paired t-test for all the comparisons. The null hypothesis is accepted when p_2 is greater than 0.05. The results of Shapiro–Wilks test and Paired t-test are shown in Table 3.

Table 3. The result of Shapiro–Wilks test and Paired t-test. ($S1$ means the result from scenario 1.)

		Mean	Standard Deviation	Shapiro–Wilks Test		Paired t-Test	
				W	p_1	t	p_2
t_{sim}	$S1$–$S2$	−175.3000	26.8790	0.9798	0.8200	−35.1211	0.0000
	$S2$–$S3$	−6.1125	16.1472	0.9666	0.4497	−2.0385	0.0507
	$S3$–$S4$	−3.2083	18.0953	0.9709	0.5639	−0.9548	0.3476
$\bar{C}$	$S1$–$S2$	172.7929	11.7533	0.9828	0.8938	79.1711	0.0000
	$S2$–$S3$	40.5942	5.8819	0.9755	0.6980	37.1660	0.0000
	$S3$–$S4$	−2.1007	7.5094	0.9426	0.1070	−1.5065	0.1428

From scenario 1 to scenario 4, the protective measures adopted by the supermarket become stricter. Comparing scenario 1 and scenario 2, scenario 2 has smaller L_{max} than scenario 1. The values of p_2 for t_{sim} and $\bar{C}$ are both less than 0.05, showing a significant difference between the results of these two scenarios. From scenario 1 to scenario 2, the mean value of $\bar{C}$ decreases roughly 56%, and the mean value of t^{sim} increases roughly 13%. In conclusion, restricting the number of customers in the supermarket is an effective measure to reduce the contact among customers with a slightly reduced efficiency of the supermarket.

Scenario 2 and scenario 3 have the same L_{max}, but the social distance rule is adopted in scenario 3. Since the value of p_2 for t_{sim} is greater than 0.05, we can say there is no significant difference between t_{sim} of these two scenarios. For $\bar{C}$, the value of p_2 is less than 0.05. The mean value of $\bar{C}$ decreases nearly 29% from scenario 2 to scenario 3. Therefore, social distance rule is also effective to reduce the contact, and hardly affect the efficiency of the supermarket.

In scenario 4, the shopping cart is required for entering the supermarket. Compared with scenario 3, the values of p_2 for t_{sim} and $\bar{C}$ are both greater than 0.05. Therefore, it seems that the shopping cart rule has limited effect with respect to reducing the contact, although this rule can reduce the workload of counting customers, since the supermarket can limit the number of people in the supermarket by placing a shopping cart with a quantity of L_{max}.

In addition to the two quantities, the spatial distribution of the contact among customers in the supermarket is investigated. The steady state of each scenario is identified first, which is defined as the status that the number of customers in the supermarket reaches L_{max}. For each scenario, one run is picked out to show the steady states. The steady states of these four scenarios correspond to the flat regions of four lines in Figure 5. The steady areas of scenarios 2, 3, and 4 are almost overlapped, as the value of L_{max} are the same. The vertical axis represents the number of customers in the supermarket. The oscillation of the steady state is caused by the time gap between customers entering and leaving the supermarket. The start time and the end time of the steady state is defined as t^{start} and t^{end}, respectively.

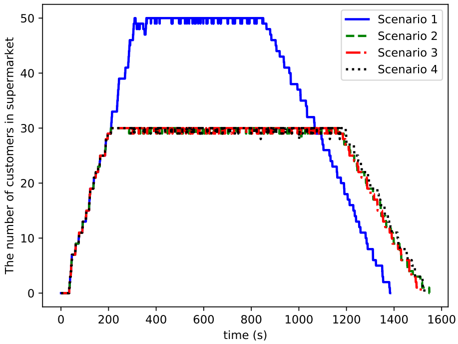

Figure 5. The steady states of the four scenarios.

The geometry of the supermarket is divided into regular grids of size 0.2×0.2 m^2, and an index C^{grid} is calculated for each grid according to

$$C^{\text{grid}} = \frac{\int_{t^{\text{start}}}^{t^{\text{end}}} \sum_{i \in G} C_i(t) dt}{\int_{t^{\text{start}}}^{t^{\text{end}}} \sum_{i \in G} dt}, \tag{10}$$

where G is the set containing all the customers in the grid. We calculate the mean value of C^{grid} in each grid with the 30 times simulations of each scenario. The distributions of C^{grid} in the supermarket for four scenarios are shown in Figure 6.

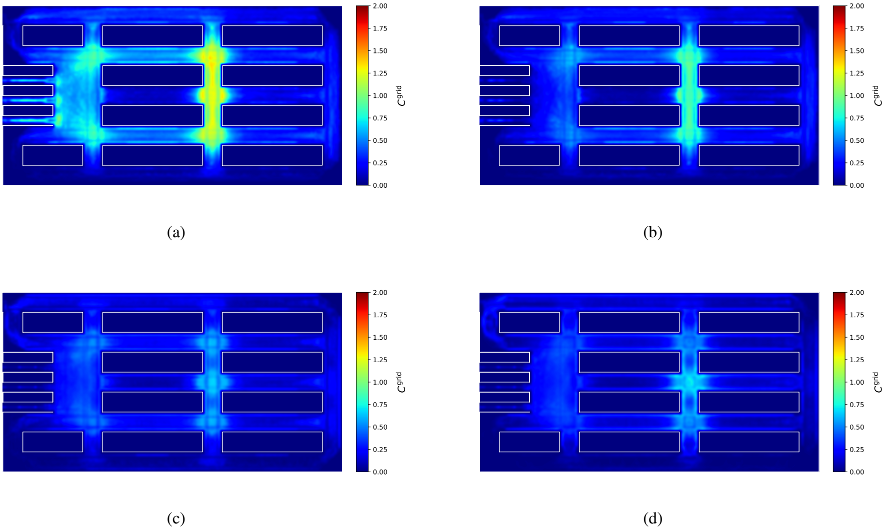

(a)

(b)

(c)

(d)

Figure 6. The distributions of C^{grid} in the supermarket for four scenarios. (**a**) Scenario 1. (**b**) Scenario 2. (**c**) Scenario 3. (**d**) Scenario 4.

A qualitative observation shows that the distribution of C^{grid} changes with the measures taken by the supermarket. The same conclusions as before can be obtained, for instance, restricting the number of customers and social distance rule are useful to reduce the contact among customers, and the shopping cart rule is not effective.

The four profiles in Figure 6 also show that the values of C^{grid} differ depending on different parts of the supermarket. Therefore, in Figure 7a four areas in the supermarket are specified, and the average values of C^{grid} in these areas are calculated. The grids which are located in the obstacles (e.g., counters and goods shelves) are ignored in the calculation, as the values of C^{grid} in the obstacle areas are always equal to zero. The mean values and standard deviations of 30 times simulations for four scenarios are compared in Figure 7b.

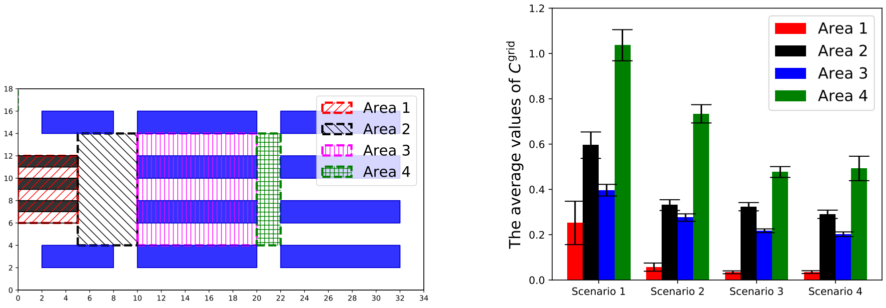

(a)

(b)

Figure 7. The average values of C^{grid} in specified areas. (**a**) The locations of these areas. (**b**) The comparison of average values; the error bars show the standard deviation.

The same hypothesis testing is implemented for following comparisons. Paired *t*-test is performed when the difference between two scenarios satisfy the condition of normality. Otherwise, Wilcoxon signed-rank test is used. The testing results are shown in Table 4.

Table 4. The testing result of comparisons for different areas in the supermarket. ($S1$ means the result from scenario 1.)

		Mean	Standard Deviation	Shapiro–Wilks Test		Paired *t*-Test (Wilcoxon)	
				W	p_1	t (W)	p_2
Area 1	$S1$–$S2$	0.1952	0.0907	0.6739	0.0000	0.0000	0.0000
	$S2$–$S3$	0.0229	0.0135	0.9247	0.0355	0.0000	0.0000
	$S3$–$S4$	−0.0009	0.0052	0.9837	0.9140	−0.8889	0.3814
Area 2	$S1$–$S2$	0.2646	0.0663	0.9414	0.0994	21.5000	0.0000
	$S2$–$S3$	0.0070	0.0285	0.9705	0.5527	1.3228	0.1962
	$S3$–$S4$	0.0336	0.0257	0.9638	0.3851	7.0483	0.0000
Area 3	$S1$–$S2$	0.1210	0.0316	0.9822	0.8799	20.5898	0.0000
	$S2$–$S3$	0.0582	0.0167	0.9939	0.9996	18.7725	0.0000
	$S3$–$S4$	0.0153	0.0133	0.9488	0.1566	6.1786	0.0000
Area 4	$S1$–$S2$	0.3027	0.0774	0.9711	0.5688	21.0676	0.0000
	$S2$–$S3$	0.2570	0.0520	0.9908	0.9946	26.6224	0.0000
	$S3$–$S4$	−0.0157	0.0587	0.9714	0.5795	−1.4439	0.1595

The common point of these four scenarios is the average values of C^{grid} in Area 2 and Area 4 are higher than in Area 1 and Area 3. The reason is that crossing structures are exist in Area 2 and Area 4. Customers in these crossing areas can move in more directions, thus increasing the likelihood of congestion, especially when the number of customers in the supermarket is high.

More information can be obtained by combining Figure 7b and Table 4. Restricting the number of customers decreases the value of C^{grid} in all four areas. The social distance rule also reduces the contact of customers in Area 1, Area 3 and Area 4, but has no effect in Area 2. As for the shopping cart rule, it has a little influence in Area 2 and Area 3, and no effect in Area 1 and Area 4.

3. Conclusions

Supermarkets are closely related to people's daily life. During the COVID-19 period, a series of measures are adopted in supermarkets to slow down the propagation of the disease. The effectiveness of these measures are investigated in this paper. The contact degree among customers is treated as the standard for comparing different measures. Simulations of several scenarios corresponding to different measures taken by supermarkets are performed.

We run simulations in each scenario for 30 times and implement hypothesis testing. Although the supermarket scenarios used in this work is simplified and the behavior of customers in our simulations are based on several assumptions, the following results can be obtained by comparing the accumulation of the time spent by all the customers in the supermarket and the average contact degree of these costumers. The limitation on the number of customers in the supermarket slightly reduces the efficiency of the supermarket, but significantly reduces the contact among customers. The social distance rule is also effective at reducing the contact among customers. However, the shopping cart rule has little effect in reducing the contact among customers.

Moreover, the spatial distribution of the contact between customers in the supermarket shows that the contact in the areas with crossing structure is obviously higher than in other areas. Therefore, reducing the crossing area in the supermarket may be an effective measure to reduce the contact among customers.

In summary, supermarkets should continue to limit the number of customers and require customers to maintain a minimum social distance. Besides, supermarkets can change the layout to reduce the crossing area.

The work in this paper only focus on the contact among people using on a velocity-based model, but has potential to be extended to an epidemiology model by combining the knowledge and data about the spread COVID-19 into the movement model.

The results of this work may change with the structure of the fictive supermarket scenario and the behavior of customers in simulations, but nonetheless we believe that the framework presented in this study can evaluate the effectiveness of control measures in indoors scenarios.

Future research will focus on the dependence of our results on the structure of scenarios (like the width of walking paths, the number of counters in the checkout area) and behavior of customers (i.e., the shopping time t^{shop} and the desired moving speed V_i^0). Besides, the validation of both movement and behavioral models in this work will be proceed.

Authors contribution

Conceptualization, Q.X. and M.C.; methodology, Q.X. and M.C.; software, Q.X.; writing—original draft preparation, Q.X.; writing—review and editing, Q.X. and M.C.; visualization, Q.X. All authors have read and agreed to the published version of the manuscript.

Acknowledgment

Qiancheng Xu thanks the funding support from the China Scholarship Council (Grant NO.201706060186).

List of parameters

List of parameters

Table 5. The complete list of all parameters choices in four scenarios with the explanation.

Parameters	Explanation	Values			
		Scenario 1	Scenario 2	Scenario 3	Scenario 4
k	The parameter to calibrate the strength of the impact from other pedestrians (Equation (2))	8			
D	The parameter to calibrate the scale of the impact from other pedestrians (Equation (2))	0.1	0.1	0.3	0.3
V_i^0 (m/s)	The desired moving speed of customers (Equations (3) and (6))	$N \sim (1.34, 0.26^2)$			
T (s)	The parameter to calibrate the speed according to the gap between two pedestrians (Equations (3) and (6))	1			
α	The parameter to calibrate the checkout time according to the shopping time (Equation (5))	0.1			
β (m/s)	The parameter to calibrate the distance between customers in checkout area according to the shopping time (Equation (7))	0.03			
M (person)	The total number of customers generated in the simulation	100			
P (person/minute)	The number of customers generated every minute	10			
t_i^{shop} (s)	The shopping time of customers	$N \sim (300, 50^2)$			
d_{rule} (m)	The social distance	0	0	1.5	1.5
$L_{\max}$ (person)	The max allowable number of customers in the supermarket at the same time	50	30	30	30
Need shopping cart	Decide the shape of customers in simulations (customers without shopping cart are represented by circles with $r = 0.2$ m, customers with shopping cart are represented by ellipses with semi-axes $a = 0.4$ m and $b = 0.25$ m.)	No	No	No	Yes
Δt (s)	The size of time-step in simulations	0.05			

References

[1] World Health Organization. WHO Timeline—COVID-19. Available online: `https://www.who.int/news-room/detail/27-04-2020-who-timeline---covid-19`, accessed on 29 June 2020.

[2] World Health Organization. WHO Coronavirus Disease (COVID-19) Dashboard. Available online: `https://covid19.who.int/`, accessed on 29 June 2020.

[3] World Health Organization. Q&A on Coronaviruses (COVID-19). Available online: `https://www.who.int/emergencies/diseases/novel-coronavirus-2019/question-and-answers-hub/q-a-detail/q-a-coronaviruses`, accessed on 29 June 2020.

[4] World Health Organization. Novel Coronavirus (2019-nCoV) Advice for the Public. Available online: `https://web.archive.org/web/20200126025750/https://www.who.int/emergencies/diseases/novel-coronavirus-2019/advice-for-public`, accessed on 29 June 2020.

[5] Prem, K.; Liu, Y.; Russell, T.W.; Kucharski, A.J.; Eggo, R.M.; Davies, N.; Flasche, S.; Clifford, S.; Pearson, C.A.; Munday, J.D.; et al. The effect of control strategies to reduce social mixing on outcomes of the COVID-19 epidemic in Wuhan, China: A modelling study. *Lancet Public Health* **2020**, *5*, e261–e270.

[6] Kraemer, M.U.; Yang, C.H.; Gutierrez, B.; Wu, C.H.; Klein, B.; Pigott, D.M.; Du Plessis, L.; Faria, N.R.; Li, R.; Hanage, W.P.; et al. The effect of human mobility and control measures on the COVID-19 epidemic in China. *Science* **2020**, *368*, 493–497.

[7] Tian, H.; Liu, Y.; Li, Y.; Wu, C.H.; Chen, B.; Kraemer, M.U.; Li, B.; Cai, J.; Xu, B.; Yang, Q.; et al. An investigation of transmission control measures during the first 50 days of the COVID-19 epidemic in China. *Science* **2020**, *368*, 638–642.

[8] D'Orazio, M.; Bernardini, G.; Quagliarini, E. Sustainable and resilient strategies for touristic cities against COVID-19: An agent-based approach. *arXiv* **2020**, arXiv:2005.12547.

[9] Szczepanek, R. Analysis of pedestrian activity before and during COVID-19 lockdown, using webcam time-lapse from Cracow and machine learning. *PeerJ* **2020**, *8*, e10132.

[10] Ronchi, E.; Lovreglio, R. EXPOSED: An occupant exposure model for confined spaces to retrofit crowd models during a pandemic. *arXiv* **2020**, arXiv:2005.04007.

[11] D'Orazio, M.; Bernardini, G.; Quagliarini, E. A Probabilistic Model to Evaluate the Effectiveness of Main Solutions to COVID-19 Spreading in University Buildings according to Proximity and Time-Based Consolidated Criteria. *Research Square* **2020**, doi:10.21203/rs.3.rs-82941/v1.

[12] Kucharski, A.J.; Russell, T.W.; Diamond, C.; Liu, Y.; Edmunds, J.; Funk, S.; Eggo, R.M.; Sun, F.; Jit, M.; Munday, J.D.; et al. Early dynamics of transmission and control of COVID-19: A mathematical modelling study. *Lancet Infect. Dis.* **2020**, *20*, 553–558.

[13] Berger, D.W.; Herkenhoff, K.F.; Mongey, S. *An Seir Infectious Disease Model with Testing and Conditional Quarantine*; Technical report; National Bureau of Economic Research: Cambridge, MA, USA, 2020.

[14] Barbarossa, M.V.; Fuhrmann, J.; Meinke, J.H.; Krieg, S.; Varma, H.V.; Castelletti, N.; Lippert, T. The impact of current and future control measures on the spread of COVID-19 in Germany. *medRxiv* **2020**, doi:10.1101/2020.04.18.20069955.

[15] Hou, C.; Chen, J.; Zhou, Y.; Hua, L.; Yuan, J.; He, S.; Guo, Y.; Zhang, S.; Jia, Q.; Zhao, C.; others. The effectiveness of quarantine of Wuhan city against the Corona Virus Disease 2019 (COVID-19): A well-mixed SEIR model analysis. *J. Med. Virol.* **2020**, doi:10.1002/jmv.25827.

[16] Iwata, K.; Miyakoshi, C. A Simulation on Potential Secondary Spread of Novel Coronavirus in an Exported Country Using a Stochastic Epidemic SEIR Model. *J. Clin. Med.* **2020**, *9*, 944.

[17] Fang, Z.; Huang, Z.; Li, X.; Zhang, J.; Lv, W.; Zhuang, L.; Xu, X.; Huang, N. How many infections of COVID-19 there will be in the "Diamond Princess"-Predicted by a virus transmission model based on the simulation of crowd flow. *arXiv* **2020**, arXiv:2002.10616.

[18] D'Orazio, M.; Bernardini, G.; Quagliarini, E. How to restart? An agent-based simulation model towards the definition of strategies for COVID-19 "second phase" in public buildings. *arXiv* **2020**, arXiv:2004.12927.

[19] Kai, D.; Goldstein, G.P.; Morgunov, A.; Nangalia, V.; Rotkirch, A. Universal masking is urgent in the covid-19 pandemic: Seir and agent based models, empirical validation, policy recommendations. *arXiv* **2020**, arXiv:2004.13553.

[20] Xiao, Y.; Yang, M.; Zhu, Z.; Yang, H.; Zhang, L.; Ghader, S. Modeling indoor-level non-pharmaceutical interventions during the COVID-19 pandemic: A pedestrian dynamics-based microscopic simulation approach. *arXiv* **2020**, arXiv:2006.10666.

[21] Xu, Q.; Chraibi, M.; Tordeux, A.; Zhang, J. Generalized collision-free velocity model for pedestrian dynamics. *Phys. A Stat. Mech. Appl.* **2019**, *535*, 122521.

[22] Bosina, E.; Weidmann, U. Estimating pedestrian speed using aggregated literature data. *Phys. A Stat. Mech. Appl.* **2017**, *468*, 1–29.

[23] Buchmueller, S.; Weidmann, U. Parameters of pedestrians, pedestrian traffic and walking facilities. *IVT Schriftenreihe* **2006**, *132*, 15, doi:10.3929/ethz-b-000047950.

[24] Wagoum, A.U.K.; Chraibi, M.; Zhang, J.; Lämmel, G. JuPedSim: An open framework for simulating and analyzing the dynamics of pedestrians. In Proceedings of the 3rd Conference of Transportation Research Group of India, West Bengal, India, 17–20 December 2015.

A.16 Article XV

Come together: A unified description of the escalator capacity

C. Gnendiger, M. Chraibi, A. Tordeux

PLOS, *under review* (2023)

PLOS ONE
under review

Come together: A unified description of the escalator capacity

Christoph Gnendiger[1], Mohcine Chraibi[1], Antoine Tordeux[2]

Abstract
We investigate a variety of aspects related to the simulation of passenger dynamics on escalators, mainly focusing on the discrepancy between the ‘theoretical’ and the ‘practical’ capacity that is observed for these facilities. The structure of the paper is twofold. In the first part, we introduce a space-continuous model to describe the transition of agents from walking on the plain to standing on the escalator. In the second part, we use numerical findings from simulations to study important measures like minimum distances between the standing agents and average occupancies of the escalator steps. One of the most important results obtained in this paper is a generalized analytical formula that describes the escalator capacity. We show that, apart from the conveyor speed, the capacity essentially depends on the time gap between entering passengers which we interpret as human reaction time. Comparing simulation results with corresponding empirical data from field studies and experiments, we deduce a minimum human reaction time in the range of $0.15\,\mathrm{s}-0.30\,\mathrm{s}$ which is in perfect agreement with results from social psychology. With these findings, it is now possible to determine accurately the relationship between the capacity and the speed of an escalator, allowing a science-based performance evaluation of buildings with escalators.

Keywords
application; escalators

[1] *Institute for Advanced Simulation, Forschungszentrum Jülich, Jülich, Germany*
[2] *School of Mechanical Engineering and Safety Engineering, University of Wuppertal, Wuppertal, Germany*

Contents

Introduction

With an ever-growing urbanization [1], the peak performance of pedestrian facilities in public buildings like shopping malls, entertainment centers, and sport stadiums, is gaining importance. Moreover, public transport via trains has become one of the most effective and climate-friendly transportation modes available. As a result, more multiple-level train and metro stations are being built and used on a regular basis. To increase comfort of the passengers as well as to satisfy in particular intermittent performance demands of buildings as a whole, escalators are being used ubiquitously as they generally transport large passenger groups much faster between different levels than stairs and elevators [2].

One important measure to assess and evaluate the performance of escalators is the maximum passenger flow that can be realized over a certain period of time. As with other pedestrian facilities, this handling capacity strongly depends on the geometrical dimensions which are usually fixed and typically known or easily accessible. More importantly (and in contrast to many other pedestrian facilities), however, escalators have an additional setting option that can be adjusted dynamically during operation: the conveyor speed. According to this, the escalator capacity is not a fixed number but depends on the mode in which the facility is operated [3, 4, 5].

The question that naturally arises is how the escalator speed should be selected. There are two main points to consider. First, it is obvious that the choice of a particular conveyor speed is always a trade-off between comfort, safety, and performance demands as not all these aspects can be maximized at the same time. For instance, while a larger conveyor speed may increase the capacity, it also complicates the adaptation process of the entering persons to match the fast-moving escalator which in turn may endanger the passenger safety. The importance of the safety aspect is underpinned by the fact that escalator-related injuries have increased in the past years [6].

Second, in order to strike a balance between the aforementioned aspects, the performance of an escalator has to be known exactly. Surprisingly, however, there exists a long-standing and persistent ambiguity regarding the relation between conveyor speed and capacity of escalators. Many guidelines, norms, and handbooks, for instance, propose a *linear* speed-dependence of the maximum possible passenger flow [7, 2, 8, 9, 10]. The corresponding quantity is often referred to as 'theoretical' capacity although the underlying theoretical assumptions are often not explained in detail. At the same time, however, it is known that the idealized situation of maximum escalator utilization is almost never observed in field studies and experiments, see for instance Table 1 which summarizes empirical findings on maximum observed flows at escalators.

Regarding the discrepancy between 'theory' and observation, Fruin already noticed in the 70s the so-called 'empty'- or 'vacant'-step phenomenon which states that a fully utilized escalator is never observed, even in peak travel times [20]. Therefore, usually a so-called 'practical' or 'nominal' capacity is introduced in (manufacturer) handbooks and in norms. This quantity is consistently and significantly smaller than the 'theoretical' one. What often remains unclear, however, is the actual size and speed-dependence of the deviation as well as the underlying reason for it. Even among escalator manufacturers [3, 4, 5], there is no consensus about these points and, accordingly, many values for the 'practical' capacity can be found in the literature, see Fig. 1 for a qualitative illustration. As a consequence, manufacturers and norms recommend speed-settings that might not be optimal.

reference	escalator speed $[\mathrm{m\,s^{-1}}]$	count interval [s]	maximum flow $[\mathrm{s^{-1}}]$
Bodendorf et al. (2014) [11]	0.50	10	1.73
Böhm-Franke (2015) [12]	0.50	10	1.80
Kinsey (2011) [13]	0.50	60	1.70
Nai et al. (2012) [14]	0.61	20	2.25
Kahali et al. (2021) [15]	0.65	30	2.57
Kahali et al. (2021) [16]	0.65	24	2.47
Davis et al. (2002) [17]	0.72	variable	1.98
Al-Sharif et al. (1996) [18]	0.75	30	2.03
Majo (1966) [19]	0.75	60	2.25

Table 1. References for maximum observed upward flows at escalators. The clear width of the escalator is one meter in all cases. The column 'count interval' indicates the length of the time span in which the maximum flow is measured.

In the following, we aim to contribute resolving this issue by putting the speed-capacity relation and therefore the performance analysis of escalators on a firmer basis. We do this by presenting an efficient space-continuous first-order model that describes the transition of agents from walking on the plain to standing on the escalator. We suggest solving the duality problem of the capacity by proposing a generalized formula that

- is able to explain the deviation between 'theoretical' and 'practical' capacities,
- is at the same time able to explain the existence of different 'practical' capacities that can be found in the literature, and
- is compatible with observed empirical values from field studies and experiments.

Based on purely numerical studies, we deduce and validate an analytical formula that quantifies the variation of the escalator capacity with respect to its speed. Our results show that assuming standing agents leads to reasonable predictions of the escalator performance. Moreover, it is found that the obtained capacity formula is a valid generalization of the linear approach often assumed and used in the literature.

1. Simulation of escalators

Usually, experimental and numerical studies of pedestrian dynamics serve as validation ground for mathematical models that aim to describe them. Concerning escalators, however, this approach is only partially practical as there is only little empirical

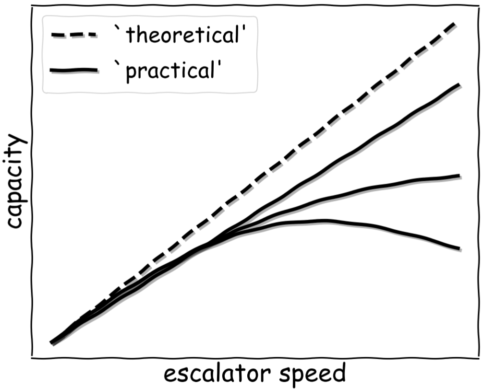

Figure 1. Qualitative difference between the ‘theoretical’ and the ‘practical’ escalator capacity in the range of typical conveyor speeds. Regarding the ‘practical’ capacity, linear, saturating, and even decreasing curve progressions can be found in the literature.

data to compare with and due to limited possibilities to perform experimental work under extreme conditions and over an extended period of time. In this work, we therefore follow a different approach by developing a space-continuous model that describes the entering behavior of pedestrians at escalators. We implement the model in the open-source software *JuPedSim* [21] and capitalize on the obtained numerical results to formulate a theoretical concept of the escalator capacity. For the simulations, we use the geometry shown in Fig. 2. In this setup, two floors with a height difference of $\Delta h = 5\,\mathrm{m}$ are connected by a single escalator with a projected horizontal length of $l_{\mathrm{esc}} = 10\,\mathrm{m}$ and an inclination angle of approximately 27°. As clear widths of the escalator, we consider the cases $w = 0.6\,\mathrm{m}$ and $w = 1.0\,\mathrm{m}$. For the upcoming capacity analysis, it is important to generate a constant density in front of the entrance to the escalator. Accordingly, we ensure that the relation $\alpha > \beta$ holds in all simulations, where α is the incoming agent flow and β is the flow on the escalator. Only with this condition it is guaranteed that the escalator is operated in a mode that corresponds to its capacity.

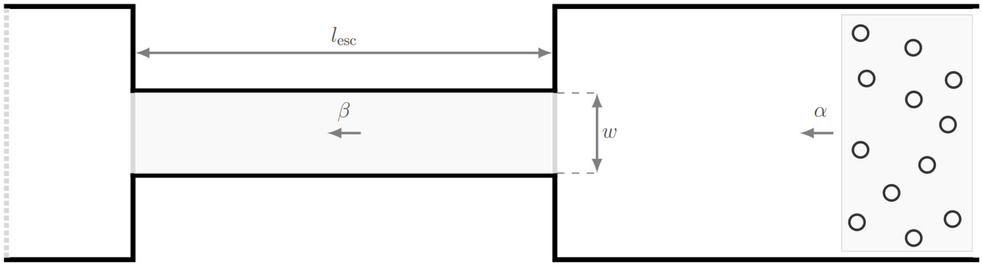

Figure 2. Geometry used for the simulations. The geometry consists of three parts: a lower floor including the agent sources (right), an escalator with a clear width of $w \in \{0.6, 1.0\}\mathrm{m}$, and a projected horizontal length of $l_{\mathrm{esc}} = 10\,\mathrm{m}$ (middle), as well as an upper floor which is located $\Delta h = 5\,\mathrm{m}$ above the lower one (left). The movement direction of the agents and of the escalator is from right to left. The incoming agent flow α can be freely adjusted whereas the flow β is typically measured.

Model of pedestrians

To account for dynamical factors of the passenger dynamics on escalators, several rule-based models have been developed in the past [22, 23, 24, 25]. In this contribution, we do not use one of the existing models but extend the collision-free speed model [26] which, compared to second-order models [27, 28], is characterized by a reduced computational effort and a faster run time of the simulations. The model is minimum in the sense that it is defined by only a small set of parameters. It is also particularly well suited for describing the passenger dynamics on escalators, as will be shown below.

In the simulations, we use circular-shaped agents with a projected diameter of $d = 0.4\,\mathrm{m}$ and a corresponding occupation area of $A \approx 0.13\,\mathrm{m}^2$.[1] In addition, each agent is assigned an individual desired velocity which it tries to reach on the plain. The absolute values of the velocities are provided in the form of a normal distribution for which we use $v_{0,\mathrm{horiz.}} = 1.3\,\mathrm{m\,s^{-1}}$ as expected value and $\sigma = 0.26\,\mathrm{m\,s^{-1}}$ as standard deviation which is in accordance with [9]. Moreover, we assume the actual speed of an agent to be proportional to the available free space [26]:

$$v(s,T) = \min\left\{v_{0,\mathrm{horiz.}}, \max\left\{0, \frac{s-d}{T}\right\}\right\}, \qquad T > 0, \tag{1}$$

where s is the smallest distance to the neighbors in the motion direction. The variable T corresponds to the time gap between successive pedestrians in single-file motion [26]. As with the desired velocities, individual T-values can be assigned to the agents in form of a normal distribution. In order to study the impact of T on the numerical results, however, in each of the simulations we use one T-value for all agents. This value is then (possibly) varied in successive simulations. A typical value is $T = 0.25\,\mathrm{s}$.

Finally, neighbors and walls not only influence the speed of an agent but also its movement direction. In this work, we use default values for the model parameters as suggested in [21, 29, 26]: $a_{\mathrm{agent}} = a_{\mathrm{wall}} = 5$, $D_{\mathrm{agent}} = 0.1\,\mathrm{m}$, and $D_{\mathrm{wall}} = 0.02\,\mathrm{m}$. Here, a_{agent} and a_{wall} are dimensionless repulsion coefficients while D_{agent} and D_{wall} are repulsion distance thresholds between pedestrians and with the geometry, respectively.

Model of escalators

So far, we have introduced rules that govern the movement of pedestrians in 2D space in general. However, unlike static geometrical components like corridors and bottlenecks, escalators have their own dynamics and move upwards or downwards with a specific conveyor speed. In *JuPedSim*, an upward or downward escalator is implemented by specifying an inclined area of the geometry in which agents mainly move at the escalator speed. As the desired speed of a walking agent on the plain, $v_{0,\mathrm{horiz.}}$, is typically different from the speed of the escalator, v_{esc}, it becomes necessary to moderate between the two quantities. In *JuPedSim* this is done by means of a smooth adaptation function that avoids any discontinuities [21]. The actual position-dependent speed of the agent is then given by

$$v_0(x) = v_{0,\mathrm{horiz.}}\big(1 - f(x)\big) + v_{\mathrm{esc}} \cdot f(x), \tag{2a}$$

$$\text{with} \quad f(x) = \tanh(cx^2) \cdot \tanh\big(c\,(x - l_{\mathrm{esc}})^2\big), \tag{2b}$$

where c is a parameter to adjust the adaptation function. To take the speed adaptation into account, the replacement $v_{0,\mathrm{horiz.}} \to v_0$ has to be made in Eq. (1).

Fig. 3 shows the development of the actual speed as one single agent passes the same escalator for two different values of the parameter c and three common escalator speeds, respectively. In each of the cases, the agent decelerates beginning at $x = 0\,\mathrm{m}$, adapts to the speed of the escalator, holds it, and accelerates at $x > 9\,\mathrm{m}$ to reach again the desired speed of free walking on the plain.

On a real-life escalator, the adaptation process is supposed to take place in the horizontal flights at the entrance and the exit areas. According to norm EN 115-1:2017 [7], the minimum length required in movement direction of these regions depends on the conveyor height, slope, and speed of the escalator, see e. g. Table 2.

escalator speed	minimum length
$v_{\mathrm{esc}} \leq 0.50\,\mathrm{m\,s^{-1}}$	0.8 m (≈ 2 steps)
$0.50\,\mathrm{m\,s^{-1}} < v_{\mathrm{esc}} \leq 0.65\,\mathrm{m\,s^{-1}}$	1.2 m (≈ 3 steps)
$0.65\,\mathrm{m\,s^{-1}} < v_{\mathrm{esc}} \leq 0.75\,\mathrm{m\,s^{-1}}$	1.6 m (≈ 4 steps)

Table 2. Required length of the horizontal flights at the entrance and exit of an escalator according to norm EN 115-1 [7]. The values are valid for heights $\Delta h \leq 6\,\mathrm{m}$.

Comparing the requirements with Fig. 3, it follows that the deceleration and acceleration of the agent can be adjusted such that it takes place fast enough. More precisely: for $c = 50$, the adaptation length is approximately 1.0 m which, according

---

[1] According to [10], this space requirement corresponds to the one of an adult wearing thick clothing. In principle, circular-shaped agents can cause gridlocks in the presence of narrow bottlenecks. In the considered simulations, however, all bottlenecks are considerably wider than $w = 0.4\,\mathrm{m}$ and the problem does not occur.

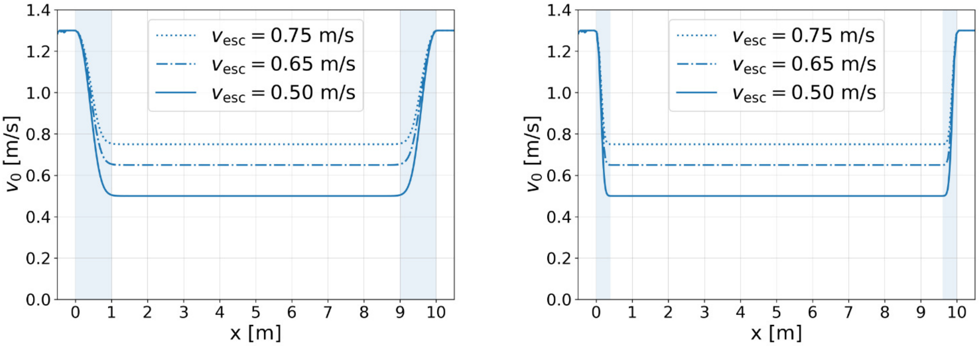

Figure 3. Speed of a single agent, depending on the position on the escalator. Shown are simulation results obtained for $c = 50$ (left) and $c = 500$ (right), and for the common escalator speeds $v_{\mathrm{esc}} \in \{0.50, 0.65, 0.75\}\,\mathrm{m\,s^{-1}}$, respectively. The desired speed of free walking on the plain is here $v_{0,\mathrm{horiz.}} = 1.3\,\mathrm{m\,s^{-1}}$. The shaded areas indicate regions where the agent speed is adapting to the one of the respective escalator. The corresponding adaptation lengths are approximately $1.0\,\mathrm{m}$ (left panel) and $0.4\,\mathrm{m}$ (right panel).

to Table 2, would be too long for escalator speeds $v_{\mathrm{esc}} \leq 0.5\,\mathrm{m\,s^{-1}}$. Setting $c = 500$, however, the adaptation length can be shortened to approximately $0.4\,\mathrm{m}$ which is in accordance with the requirements of norm EN 115-1.

Simulation of multiple agents

As mentioned before, in *JuPedSim* escalators are modeled such that each agent is assigned an individual *desired* speed which it tries to attain passing the facility. When considering a single agent, this method is definitely sufficient to obtain realistic results since a single agent can choose its speed almost completely freely. In crowded situations, however, interactions among the agents limit this freedom and, accordingly, the simulated speed is likely to be below the desired one. This is in contrast to the situation at an escalator since here the conveyor speed constitutes a lower bound for the speed of the agents located on it.

In order to estimate whether it is possible to model realistic behavior on escalators with the concept of a desired speed, we consider the following setup: We use the geometry of Fig. 2 and simulate 1.000 agents passing successively an escalator that is operated at a speed of $v_{\mathrm{esc}} = 0.5\,\mathrm{m\,s^{-1}}$. The continuous incoming agent flow of $\alpha = 3\,\mathrm{s^{-1}}$ is chosen such that it lies above the capacity of the escalator, as will be shown below. The corresponding simulation results are summarized in Fig. 4.

As expected, all agents are adapting their speed to match the speed of the escalator. Since α is larger than the escalator capacity, a congestion forms in front of the facility leading to stronger interactions among the agents and therefore to a reduction of the individual speeds in the region $x < 0\,\mathrm{m}$. As a consequence, most of the agents have to accelerate instead of decelerate when entering the escalator which is reflected by the fact that Fig. 4 is asymmetrical around $x = 5\,\mathrm{m}$ (downward shift of the l. h. s.). Compared to the right diagram in Fig. 3, also the adaptation length is slightly extended at the entrance of the escalator. However, it is, for the vast majority of the agents, still compatible with the requirements of Table 2. Outside the adaptation phases (in the region $1\,\mathrm{m} < x < 9\,\mathrm{m}$) all agents are moving with approximately the same speed which corresponds to the case of standing agents on the escalator.

Finally, the results in Fig. 4 show that it is indeed possible to model realistic behavior on escalators with the concept of a desired speed, even for the case that the incoming agent flow is significantly larger than the handling capacity of the facility. The agreement between simulation results and simulation goal is particularly striking for escalator speeds $v_{\mathrm{esc}} \leq 0.5\,\mathrm{m\,s^{-1}}$.

2. Passenger dynamics of escalators

In the following, we examine different quantities with simulations that are difficult to access through experiments and field studies. More precisely, we consider situations that involve the operation of escalators *above* their respective capacity, meaning that the incoming agent flow α is larger than the maximum flow β that can be transported away by the escalator. In real-life situations, these situation are either too dangerous for the involved people or the necessary boundary conditions can only be ensured for a short amount of time. In contrast, the following results (and underlying simulations) do not suffer from these restrictions. It is therefore possible to realize and investigate steady-states of almost any temporal extension.

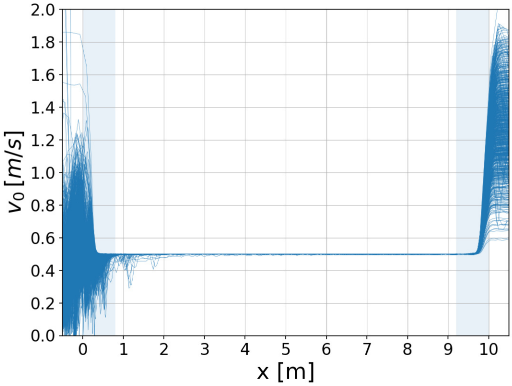

Figure 4. Individual speeds of 1.000 agents, depending on the position on the escalator. The results are obtained using $c = 500$, $v_{\mathrm{esc}} = 0.5\,\mathrm{m\,s^{-1}}$, and $w = 1.0\,\mathrm{m}$. The shaded areas indicated the minimum required length of the horizontal flights according to Table 2.

Spatial separation of agents on the escalator

One particular feature of an escalator with standing agents is that the distances between any agent and its direct neighbors do not change, even though the overall agent flow is non-vanishing. To verify if the model introduced in the previous section recovers this feature, in each simulation we label the n agents currently located on the escalator according to their position in movement direction (in our case x-direction) and consider all $(n-1)$ spatial distances between adjacent agents. The average along the x- and the y-axis is then given by

$$\Delta x(t_0) = \frac{1}{n(t_0)-1} \sum_{i=1}^{n(t_0)-1} \Big| x_{i+1}(t_0) - x_i(t_0) \Big| , \tag{3a}$$

$$\Delta y(t_0) = \frac{1}{n(t_0)-1} \sum_{i=1}^{n(t_0)-1} \Big| y_{i+1}(t_0) - y_i(t_0) \Big| , \tag{3b}$$

where x_j is the absolute x-position of agent j and similar for the y-direction. In a similar way, it is possible to determine the total distance s:

$$s(t_0) = \frac{1}{n(t_0)-1} \sum_{i=1}^{n(t_0)-1} \sqrt{\Big| x_{i+1}(t_0) - x_i(t_0) \Big|^2 + \Big| y_{i+1}(t_0) - y_i(t_0) \Big|^2} . \tag{3c}$$

Simulation results of the different distances are shown in Fig. 5.

As can be seen, after an initial phase where the first agents are arriving at the escalator, the average distance in movement direction is dropping and a steady-state with constant spatial separations establishes for each of the considered escalators. The only quantity in Fig. 5 that shows a significant speed dependence for *both* escalator widths is Δx, or more specifically, $\overline{\Delta x}$ which is the average of Δx over all considered frames in the steady-state (shaded areas). To further study this dependence, we consider a wider range of escalator speeds and determine the average of the *minimum* spatial separations in x-direction as before. The corresponding simulation results are summarized in the left diagram of Fig. 6.

For both escalator widths and over the entire considered speed range, $\overline{\Delta x}$ depends *linearly* on v_{esc}. The obtained simulation results can therefore be fitted by a linear regression for which we obtain

$$\text{fit for } w = 0.6\,\mathrm{m}: \quad \overline{\Delta x}(v_{\mathrm{esc}}) = 0.404\,\mathrm{m} + 0.248\,\mathrm{s} \cdot v_{\mathrm{esc}} , \quad T = 0.25\,\mathrm{s} , \tag{4a}$$

$$\text{fit for } w = 1.0\,\mathrm{m}: \quad \overline{\Delta x}(v_{\mathrm{esc}}) = 0.199\,\mathrm{m} + 0.127\,\mathrm{s} \cdot v_{\mathrm{esc}} , \quad T = 0.25\,\mathrm{s} . \tag{4b}$$

In order to check the impact of the model parameter T, we vary the T-value for the fixed escalator speed $v_{\mathrm{esc}} = 0.5\,\mathrm{m\,s^{-1}}$ with corresponding simulation results shown in the right diagram of Fig. 6. As before, the simulation results show a linear parameter

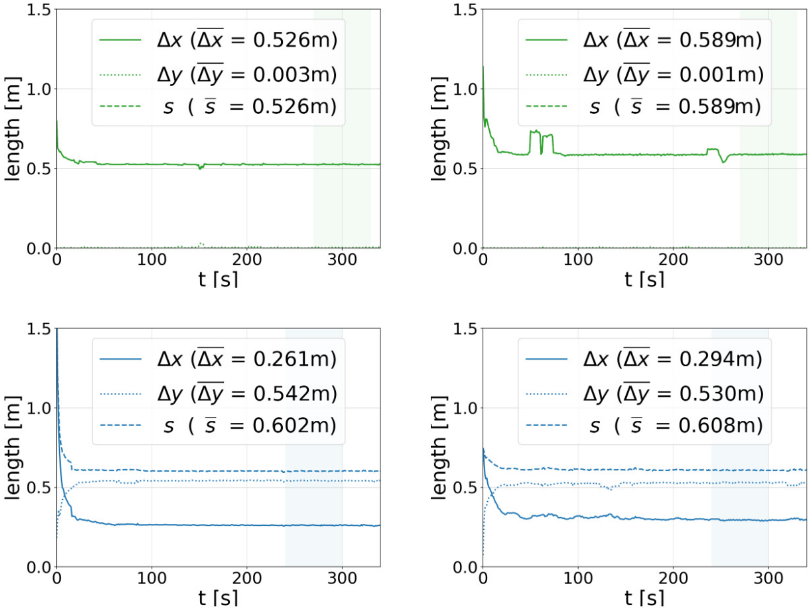

Figure 5. Simulation results for spatial distances between the agents. Shown are results for the clear widths $w = 0.6\,\mathrm{m}$ (first row) and $w = 1.0\,\mathrm{m}$ (second row), as well as for the escalator speeds $v_{\mathrm{esc}} = 0.5\,\mathrm{m\,s^{-1}}$ (left) and $v_{\mathrm{esc}} = 0.75\,\mathrm{m\,s^{-1}}$ (right), respectively. The average values of the distances are obtained from steady-state regions of 60 s length (shaded areas) and are indicated by a bar. Since Δy almost vanishes in the upper two diagrams, the total distance s is approximately the same as Δx.

dependence and can be fitted accordingly:

$$\text{fit for } w = 0.6\,\mathrm{m}: \qquad \overline{\Delta x}(T) = 0.405\,\mathrm{m} + 0.482\,\mathrm{m\,s^{-1}} \cdot T\,, \qquad v_{\mathrm{esc}} = 0.5\,\mathrm{m\,s^{-1}}\,, \tag{5a}$$

$$\text{fit for } w = 1.0\,\mathrm{m}: \qquad \overline{\Delta x}(T) = 0.203\,\mathrm{m} + 0.229\,\mathrm{m\,s^{-1}} \cdot T\,, \qquad v_{\mathrm{esc}} = 0.5\,\mathrm{m\,s^{-1}}\,. \tag{5b}$$

The results in Eqs. (4) and (5) can be explained as follows: The typical step depth of an escalator is $d_{\mathrm{step}} = 0.4\,\mathrm{m}$ [3, 4, 5]. On the narrow escalator with a clear width of $w = 0.6\,\mathrm{m}$, only one person can stand on each step simultaneously, resulting in a minimum possible x-distance between the agents of $\min(\overline{\Delta x}) = 0.4\,\mathrm{m}$. In contrast, for escalators with a width of $w = 1.0\,\mathrm{m}$, two persons can stand next to each other on each step, resulting in a minimum x-distance $\min(\overline{\Delta x}) \approx 0.2\,\mathrm{m}$.[2] Introducing the step depth of an escalator, d_{step}, as a new variable, Eqs. (4) and Eqs. (5) can therefore be approximated and rewritten in a unified form as

$$\overline{\Delta x}(w, v_{\mathrm{esc}}) \simeq \frac{1}{\mathscr{O}_0(w)} \left(d_{\mathrm{step}} + T \cdot v_{\mathrm{esc}}\right), \qquad T,\, v_{\mathrm{esc}} > 0\,. \tag{6}$$

In this expression, the whole width dependence is factored out in terms of the parameter $\mathscr{O}_0(w)$ which is given by $\mathscr{O}_0 = 1$ for $w = 0.6\,\mathrm{m}$ and $\mathscr{O}_0 = 2$ for $w = 1.0\,\mathrm{m}$. One particular feature of Eq. (6) is that it explicitly contains the model parameter T which governs the inverse slope of the speed function, see for instance Eq. (1). In the present case of an escalator with congestion upstream, T acts in the role of a time gap as most of the agents have to accelerate when entering the escalator which in turn is a consequence of the congestion in front of the facility.[3] The acceleration of each agent can only be initiated in case there is free space available at the entrance of the escalator. For non-vanishing values of T and v_{esc}, this fact causes additional spatial gaps in movement direction between the standing agents since the escalator is constantly moving on during the entering process. Conversely, in the (hypothetical) case that T vanishes, the spatial separation in movement direction coincides with the step

---

[2] The considered escalator has a projected length of $l_{\mathrm{esc}} = 10\,\mathrm{m}$, resulting in 25 steps with a depth of $d_{\mathrm{step}} = 0.4\,\mathrm{m}$. In the case that each step is occupied by two persons, Eq.(3b) yields $(25 \cdot 0\,\mathrm{m} + 24 \cdot 0.4\,\mathrm{m})/49 \approx 0.196\,\mathrm{m}$.

[3] A congestion in front of the escalator is caused by the fact, that the incoming agent flow α is larger than the escalator capacity, i. e. $C_{\mathrm{esc}} = \max(\beta) < \alpha$.

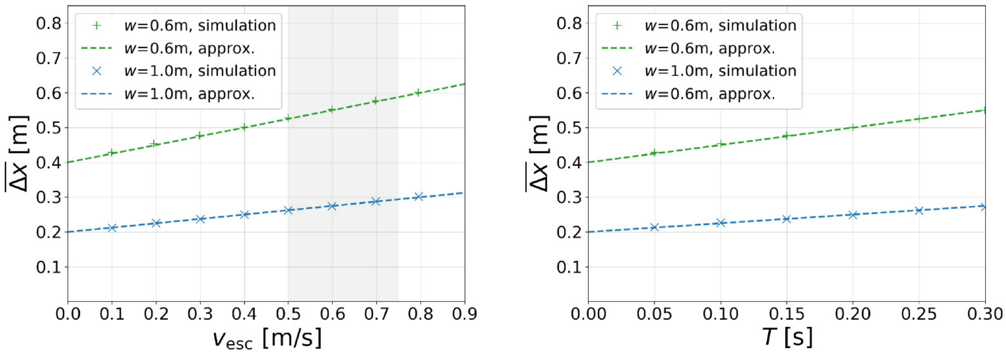

Figure 6. Minimum spatial separations in movement direction depending on the escalator speed (left) and the model parameter T (right). The simulation results are obtained by measuring $\overline{\Delta x}$ for the escalator widths $w = 0.6\,\text{m}$ and $w = 1.0\,\text{m}$, respectively. The model parameters are fixed by $T = 0.25\,\text{s}$ (left) and $v_\text{esc} = 0.5\,\text{m}\,\text{s}^{-1}$ (right). The approximations follow from Eq.(6) using $d_\text{step} = 0.4\,\text{m}$, $\mathcal{O}_0 = 2$ for $w = 1.0\,\text{m}$, and $\mathcal{O}_0 = 1$ for $w = 0.6\,\text{m}$. The shaded area indicates the range of typical escalator speeds.

depth d_step. Accordingly, the term $T \cdot v_\text{esc}$ can be regarded as a 'reaction distance' which is an inevitable consequence of the fact that T is non-vanishing. Moreover, apart from the global prefactor $\mathcal{O}_0$, the reaction distance appears without any non-trivial coefficient and exponent. In this way, the 'unphysical' model parameter T directly translates into a 'physical' observable that can be measured.

We would like to stress that, apart from T and v_esc, the simulation results have been obtained by using *identical* values for the other model parameters. Although individual escalator steps are not implemented in the simulations, reasonable results for the facility parameter d_step are obtained as a consequence of the used parameters, in particular the projected diameter of the agents. We have also checked explicitly that the obtained results are independent of the model parameter c, introduced in Eqs. (2) to govern the speed adaptation of the agents. Overall, the deviation between the different simulation results in Fig. 6 and the approximation in Eq. (6) and is less than one per cent in the considered parameter range.

Step occupancy and density on the escalator

In contrast to the previous considerations, the spatial distances in movement direction between standing agents are discretized on a real-life escalator due to the presence of individual (moving) steps. In other words, the horizontal length of an escalator, l_esc, is divided into n_steps steps of depth d_step:

$$l_\text{esc} = n_\text{steps} \cdot d_\text{step}\,. \tag{7}$$

As mentioned before, the actual number of persons that can simultaneously stand on the same step depends on the clear width w of the escalator. To quantify this fact, we introduce the so-called *step occupancy* $\mathcal{O}_i(t_0)$ which counts the absolute number of standing agents on step i at time t_0. Considering persons with a shoulder width of $d = 0.4\,\text{m}$ as before, it is obvious that the following step occupancies can be realized:

$$0.4\,\text{m} \le w < 0.8\,\text{m}: \qquad \mathcal{O}_i(t_0) \in \{0,1\}\ , \tag{8a}$$

$$0.8\,\text{m} \le w < 1.2\,\text{m}: \qquad \mathcal{O}_i(t_0) \in \{0,1,2\}\,. \tag{8b}$$

The *average* step occupancy of an escalator can then be computed by simply taking the average of all steps, i. e.

$$\overline{\mathcal{O}}_{n_{steps}}(t_0) = \frac{1}{n_\text{steps}} \sum_{i=1}^{n_\text{steps}} \mathcal{O}_i(t_0) \equiv \frac{1}{n_\text{steps}} n_\text{esc}(t_0) \overset{(7)}{=} \frac{d_\text{step}}{l_\text{esc}} n_\text{esc}(t_0)\,, \tag{9}$$

where n_esc is the number of standing agents on the escalator.

In Eq. (9), the step occupancy is defined in a *macroscopic* way by considering the whole escalator at a time and by measuring the absolute number of agents currently located on it. Apart from this global definition, it is also possible to consider only the *occupied* area of an escalator by using the results of the spatial distances from the previous section. For example, on an escalator with a step depth of $d_{\mathrm{step}} = 0.4\,\mathrm{m}$ the average distance between the agents in movement direction is $\overline{\Delta x} = 0.4\,\mathrm{m}$ if each step is occupied by one person. If only every second step is occupied, the average distance between the agents is $\overline{\Delta x} = 0.8\,\mathrm{m}$ etc. This relationship between the (macroscopic) occupancy and the (microscopic) spatial separation can be written as

$$\overline{\mathscr{O}}_{\Delta x}(t_0) = \frac{d_{\mathrm{step}}}{\overline{\Delta x}(t_0)}\,. \tag{10}$$

Since both quantities on the r. h. s. are known from Eq. (6), we can write the occupancy as

$$\overline{\mathscr{O}}_{\Delta x} \simeq \frac{\mathscr{O}_0(w)\cdot d_{\mathrm{step}}}{d_{\mathrm{step}} + T\cdot v_{\mathrm{esc}}}\,, \qquad T,\, v_{\mathrm{esc}} > 0\,. \tag{11}$$

Simulation results based on this definition of the step occupancy are shown in the left diagram of Fig. 7.

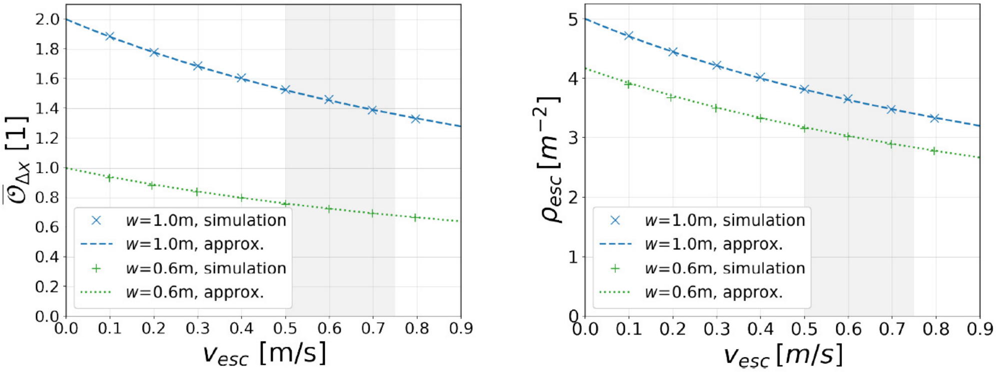

Figure 7. Speed dependence of the step occupancy. The simulation results are obtained from Eq. (10) by using results of the spatial separation in movement direction from the previous section. The respective approximations follow from Eq.(11) using $T = 0.25\,\mathrm{s}$, $d_{\mathrm{step}} = 0.4\,\mathrm{m}$, $\mathscr{O}_0 = 2$ for $w = 1.0\,\mathrm{m}$, and $\mathscr{O}_0 = 1$ for $w = 0.6\,\mathrm{m}$.

The simulation results show that the average step occupancy

- decreases with increasing escalator speed; the decrease is (slightly) non-linear,
- stays below $\mathscr{O}=1$ for the escalator width $w=0.6\,\text{m}$ which is compatible with the fact that at most one person can simultaneously occupy one step, see Eq. (8a),
- stays below $\mathscr{O}=2$ for the escalator width $w=1.0\,\text{m}$ which is compatible with the fact that at most two persons can simultaneously occupy one step, see Eq. (8b).

As mentioned before, at a real-life escalator distances between standing agents in movement direction are discretized due to the presence of individual steps. Larger spatial distances as a consequence of a finite time gap between entering passengers can therefore only be realized in the form of an under-occupation of individual steps. Even though individual steps are not explicitly considered in the presented space-continuous model, the obtained simulation results as well as Eq. (11) recover this feature. In this way, the left diagram in Fig. 7 also explains observations already formulated in [20]:

> ‘Numerous observations have shown that 100 per cent step utilization is never obtained, even with the heaviest traffic pressure and use by the most knowledgeable and agile pedestrians, including commuters.’

In addition, the meaning of the previously introduced parameter $\mathscr{O}_0$ becomes clear. It is the *maximum* occupancy that can only be realized in the hypothetical limits $T\to 0$ and $v_\text{esc}\to 0$:

$$\lim_{T\to 0}\overline{\mathscr{O}}_{\Delta x}=\lim_{v_\text{esc}\to 0}\overline{\mathscr{O}}_{\Delta x}=\mathscr{O}_0(w)\,. \tag{12}$$

In all considered simulations, the escalators are set up in an operational mode that is above their respective capacity. Eqs. (9) and (10) should therefore yield similar results for the steady-states since the escalators are continuously fully occupied. We have checked explicitly that the relation $\overline{\mathscr{O}}_{n_\text{steps}}\approx\overline{\mathscr{O}}_{\Delta x}$ indeed holds. Moreover, the maximum deviation between the individual simulation results and the approximation in Eq. (11) is at most one per cent.

Finally, we would like to mention that, for a given escalator, the quantities *occupancy* and *density* are closely related but not identical. For instance, the density on an escalator can be obtained by dividing the total number of agents located on the escalator, n_esc, by the projected area of the escalator, $A_\text{esc}=w\cdot l_\text{esc}$. Using Eqs. (9) and (10), we therefore write the relation between density and occupancy as

$$\rho_\text{esc}=\frac{n_\text{esc}}{A_\text{esc}}=\frac{n_\text{esc}}{w\cdot l_\text{esc}}\overset{(9)}{=}\frac{\overline{\mathscr{O}}_{n_{steps}}\cdot l_\text{esc}}{d_\text{step}\cdot w\cdot l_\text{esc}}=\frac{\overline{\mathscr{O}}_{n_{steps}}}{d_\text{step}\cdot w}\,, \tag{13a}$$

$$\approx\frac{\overline{\mathscr{O}}_{\Delta x}}{d_\text{step}\cdot w}\overset{(10)}{=}\frac{d_\text{step}}{d_\text{step}\cdot\overline{\Delta x}\cdot w}=\frac{1}{\overline{\Delta x}\cdot w}\,. \tag{13b}$$

In the second line, we made use of the relation $\overline{\mathscr{O}}_{n_\text{steps}}\approx\overline{\mathscr{O}}_{\Delta x}$ which is valid for the case that the escalator is fully occupied. Simulation results for the density on escalators are shown in the right diagram of Fig. 7.

Escalator capacity

One key measure of an escalator is its capacity which, for a given time interval $\Delta t=t_1-t_0$, is the maximum number of persons that can be transported away by the facility, i. e.

$$C_\text{esc}(w,v_\text{esc})=\max\Big\{\beta(w,v_\text{esc})\Big\}=\max\Big\{\frac{n(t_1)-n(t_0)}{\Delta t}\Big\}\,. \tag{14}$$

According to this definition, the determination of the capacity consists of two independent measurements as one has to determine the agent number (at least) at two different times t_1 and t_0. At an escalator, the situation is slightly different since here the conveyor speed is continuously constant. In order to obtain the capacity, it is therefore sufficient to measure only one quantity at a fixed time. In general, there are two options:

(a) **measurement of the agent number**:
The starting point of this approach is the hydro-dynamical equation $\beta=\rho_\text{esc}\cdot w\cdot v_\text{esc}$ together with the definition of the capacity in Eq. (14). Using Eq. (13a), the capacity is given by

$$C_\text{esc}(w,v_\text{esc})=\frac{\max\big\{n_\text{esc}(w,v_\text{esc})\big\}}{l_\text{esc}}\cdot v_\text{esc}\,,\qquad \alpha>C_\text{esc}\,. \tag{15a}$$

(b) **measurement of the spatial separation in movement direction**:
As in approach (a), the starting point is the hydro-dynamical equation. However, using Eq. (13b), the density is expressed in terms of the spatial separation in movement direction, i. e.

$$C_{\text{esc}}(w, v_{\text{esc}}) = \frac{1}{\min\{\overline{\Delta x}(w, v_{\text{esc}})\}} \cdot v_{\text{esc}}\,, \qquad \alpha > C_{\text{esc}}\,. \tag{15b}$$

Conceptually, approach (a) is based on the measurement of agent numbers which can be carried out comparatively easily. The obtained results are, however, very sensitive to small fluctuations of the agent numbers.[4] In contrast, the measurement of Δx in approach (b) is mainly limited by the spatial resolution of the simulations, resulting in overall smaller uncertainties.[5] In the following, we therefore use Eq. (15b) to measure the speed-dependent capacity of the escalators. In doing so, we check explicitly that the obtained results are compatible with the other approach within the measurement uncertainties.

In Eq. (15b), the capacity is expressed in terms of spatial separations in movement direction. Using Eq. (6), we can therefore write

$$C_{\text{esc}}(w, v_{\text{esc}}, T) \;\simeq\; \mathcal{O}_0(w) \cdot \frac{v_{\text{esc}}}{d_{\text{step}} + T \cdot v_{\text{esc}}}\,, \qquad T,\, v_{\text{esc}} > 0\,, \tag{16}$$

where again $\mathcal{O}_0 = 2$ for $w = 1.0\,\text{m}$ and $\mathcal{O}_0 = 1$ for $w = 0.6\,\text{m}$. This *non-linear* function for the speed-dependent capacity of an escalator is one of the most important findings in this contribution. To the knowledge of the authors, it is for the first time that such a formula is given in an explicit analytical form only including physical parameters. A graphical representation of the capacity formula is shown in Fig. 8.

Regarding large escalator speeds, i. e. $v_{\text{esc}} \to \infty$, Eq. (16) has no local maximum, but is bounded above by

$$\lim_{v_{\text{esc}} \to \infty} C_{\text{esc}}(w, v_{\text{esc}}, T) = \frac{\mathcal{O}_0(w)}{T}\,. \tag{17}$$

In other words, the capacity of an escalator is not only limited by the clear width of the facility, but also by the value of the parameter T. In the present case of an escalator with congestion upstream, the parameter can be regarded as a reaction time of the passengers entering the facility, see for instance Eq. (6) and the discussion below that formula. Only in the limit of a vanishing time gap T, the capacity can get in principle arbitrarily large. In Eq. (16), this hypothetical(!) case then corresponds to a linear rise of C_{esc} with increasing v_{esc}.

The fact that Eq. (16) explicitly contains the model parameter T is a strong indication that the underlying collision-free speed model [26] is very well suited for describing the passenger dynamics of escalators, at least for the considered escalator widths. Moreover, we would like to stress that T is the only 'free' parameter in Eq. (16) that can be used to adjust the simulations. All other parameters are properties of the escalator itself and are therefore fixed for a given scenario.[6] The T-dependence of the capacity in the range $0.15\,\text{s} \le T \le 0.3\,\text{s}$ is shown in Fig. 9.

To further verify the obtained results, we compare them with field studies summarized in Table 1 and with data provided by escalator manufacturers. When comparing Eq. (16) with the literature, the following points should be noted:

- Results of field studies are only available for the commonly used escalator width $w = 1.0\,\text{m}$. In Fig. 9, therefore only results for $w = 1.0\,\text{m}$ are shown. All following statements are, however, also valid for $w = 0.6\,\text{m}$.
- Eq. (16) describes the capacity of an escalator which is the *maximum* agent flow that can be realized over a certain period of time. Since the necessary boundary conditions are difficult to come across in real-life situations, observed results of field studies should lie *on or below* the respective curve in Fig. 9. Depending on which entries in Table 1 are considered valid, T can be chosen such that this is indeed the case.
- The minimum value of the time gap to explain *all* results in Table 1 is $T = 0.15\,\text{s}$. Using this value, Eq.(16) yields a (speed-dependent) escalator capacity that is slightly larger than all observed flows, including the ones obtained for escalator speeds $v_{\text{esc}} \ge 0.65\,\text{m}\,\text{s}^{-1}$, see Fig. 9.

---

[4] For example, for an escalator with a clear width of $w = 0.6\,\text{m}$ and a length of $l_{\text{esc}} = 10\,\text{m}$, a step depth of $d_{\text{step}} = 0.4\,\text{m}$ results in 25 steps, each with a maximum occupancy of $\max(\mathcal{O}_i) = 1$. A maximum of $n_{\text{esc}} = 25$ agents can therefore simultaneously be located on the escalator. In this case, each agent contributes at least 4 % to the result in Eq. (15a). For shorter escalators, the rate is even higher.

[5] On a commercial escalator, the smallest possible value of the spatial separation in movement direction is $\overline{\Delta x} \approx 0.2\,\text{m}$, see for instance Fig. 6. A spatial resolution of 0.001 m, as used in the simulations, then corresponds to a precision of 0.5 %.

[6] In this respect, we have checked explicitly that the obtained capacity values are independent of parameter c which is related to the speed adaptation of the agents, see Eqs. (2).

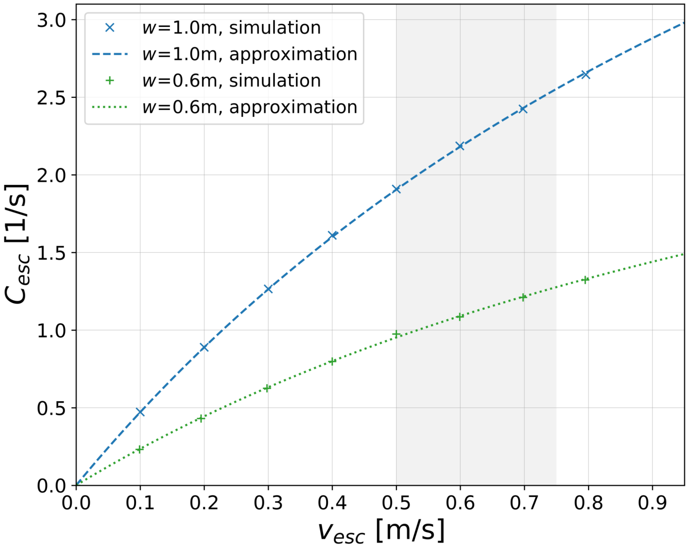

Figure 8. Non-linear speed-dependence of the escalator capacity. Shown are simulation results for the escalator widths $w = 1.0\,\mathrm{m}$ (blue markers) and $w = 0.6\,\mathrm{m}$ (green markers). The respective approximations are obtained by using Eq. (16) with $d_{\mathrm{step}} = 0.4\,\mathrm{m}$ and $T = 0.25\,\mathrm{s}$. The shaded area indicates the range of typical escalator speeds.

- Considering the most commonly used escalator speed, $v_{\mathrm{esc}} = 0.5\,\mathrm{m\,s^{-1}}$, a minimum time gap of $T = 0.2\,\mathrm{s}$ is sufficient to explain all results in Table 1 and data provided by the manufacturers.

- A time gap of $T = 0.35\,\mathrm{s}$ is too long to be compatible with observed flows of [12, 14, 15, 16] and data provided by [3, 4, 5]. In order to explain these experimental data with Eq. (16), therefore smaller T-values have to be used, see the above bullet points.

Summarizing, the comparison of Eq. (16) with available literature on escalator capacities shows that the applied setup as well as the introduced escalator model yield reliable and sound predictions. As one of the most important findings, we deduce a minimum additional time gap between entering passengers in the range of $T = (0.15 - 0.30)\mathrm{s}$ which is perfectly compatible with knowledge of social psychology on the minimum human reaction time, see e. g. [30, 31, 32, 33, 34].[7] This fact provides further evidence that, at least for the case at hand (escalator with congestion upstream), T can be interpreted as human reaction time. Moreover, the finite value of the additional time gap is the fundamental reason for a capacity reduction of the escalator. If the escalator is operated at the most commonly used speed $v_{\mathrm{esc}} = 0.5\,\mathrm{m\,s^{-1}}$, for instance, the capacity reduction amounts up to 27% compared to the (hypothetical) case $T = 0$.

3. Conclusions and outlook

The passenger dynamics of a pedestrian facility depends, in general, on properties of the facility (geometry, clear width, inclination angle, etc.) and on characteristics of the passengers (size, shape, desired speed, etc.). Typically, properties of the facility are known or can be assessed relatively easily. Agent characteristics, in contrast, are individual and can in general only be known approximately. Moreover, the multitude of the latter usually makes it difficult to identify structural dependences as the quantities are numerous and even interdependent. In this regard, escalators with standing agents located on it constitute an exception in the sense that many agents properties have no significant impact on the passenger dynamics of the facility.

---

[7] So far, in the simulations we consider a constant model parameter T which possibly may have an individual value for each simulated agent, but which is definitely independent of the escalator speed v_{esc}. The case that the time gap itself depends on the escalator speed is discussed in the appendix.

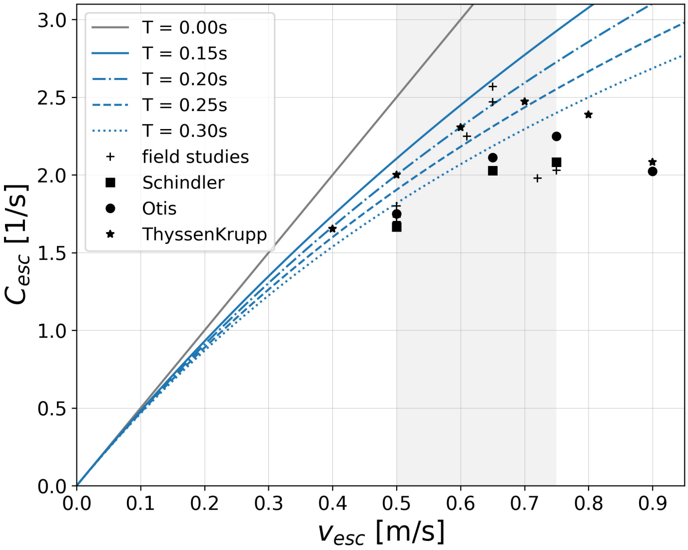

Figure 9. Speed-dependent capacity of an escalator for different values of the time gap T. The diagram compares Eq. (16) for different T-values with maximum observed flows summarized in Table 1 and 'practical' capacities provided by manufacturers [3, 4, 5]. The escalator parameters are fixed by $d_{\text{step}} = 0.4\,\text{m}$ and $w = 1\,\text{m}$ ($\mathscr{O}_0 = 2$). By definition, the capacity should be as big as or larger than all observed flows.

Using the model presented in this paper, we find in Eq. (16) that the only agent-related property that affects the escalator capacity is the parameter T of the underlying collision-free speed model. In the case at hand, this parameter is related to the entering process of the agents and quantifies an additional time gap between two entering passengers. Escalators are therefore a practical tool to study in particular this quantity. Regarding the T-dependence, two cases can be distinguished:

(I) The (hypothetical) case $T = 0$ (no passenger reaction time) results in a *linear* speed dependence of the capacity. In the literature, this case is often referred to as 'theoretical' capacity. Considering Eq. (16), it becomes clear that this case is an unrealistic simplification of the prevailing circumstances which therefore does not coincide with empirical observations.

(II) In contrast, the case $T > 0$ (positive passenger reaction time) results in a *non-linear* speed dependence of the capacity. The deviation from linearity is particularly evident in the range of large escalator speeds $v_{\text{esc}} > 0.5\,\text{m}\,\text{s}^{-1}$. The reason is that during each additional time gap, the escalator is constantly moving on, resulting in larger spatial gaps between the agents standing on the escalator. Of course, this effect is enhanced with larger v_{esc}. Even for the moderate and most commonly used escalator speed $v_{\text{esc}} = 0.5\,\text{m}\,\text{s}^{-1}$, a value of $T = 0.25\,\text{s}$ leads to a capacity reduction of approximately one fourth compared to the hypothetical case $T = 0$.

The capacity formula developed in this work is surprisingly simple but agrees remarkably well with available literature on escalator capacities for T-values in the range $T = (0.15 - 0.30)\,\text{s}$. Furthermore, obtained results of the additional time gap are in perfect agreement with knowledge of social psychology on the human reaction time. This fact serves as an independent consistency check of both the introduced escalator model and of the applied setup as a whole. In this way, the deduced capacity formula delivers a solid basis for the performance analysis of escalators and contributes to the decision-making of operators to find the optimal conveyor speed. It should be noted that complex passenger behavior like walking on escalators as well as other 'escalator etiquette' is beyond the scope of this work. Also regarding the speed-dependence of the time gap, only first considerations have been conducted in the present contribution, see for instance the appendix. These aspects as well as their impact on the escalator capacity should be carefully integrated into future work.

Appendix: Possible speed dependence of the time gap

In case we interpret T as reaction time of entering passengers, it can be assumed that the T-value increases if the escalator is operated at higher speeds. The reason is that the adaptation process of the walking agent to adapt to the fast-moving escalator is more complicated and, therefore, it is likely that passengers will hesitate longer when entering a faster escalator than a slower one. Unfortunately, and to our best knowledge, reliable empirical data regarding an individual and speed-dependent hesitation time of passengers entering escalators are lacking. Regardless, however, in the obtained capacity formula (16), a speed-dependent hesitation time can be taken into account by adding terms to the finite time gap T, e. g. in form of a power series[8]:

$$T \rightarrow \underbrace{T}_{\text{reaction time}} + \underbrace{A_1 \cdot v_{\text{esc}}^1 + A_2 \cdot v_{\text{esc}}^2 + \dots}_{\text{hesitation time}} . \tag{18}$$

The exact values of the introduced coefficients A_i are (of course) unknown and have to be determined e. g. through dedicated experiments or field studies. Regarding in particular capacity values stated in [3, 5, 19], however, good agreement is achieved by using $A_5 = 0.6\,\text{s}^6\text{m}^{-5}$ and $A_j = 0$ for the other coefficients, see Fig. 10.

As can be seen, introducing a finite hesitation time, it is even possible to model the case that the capacity of an escalator *decreases* for larger conveyor speeds as stated e. g. by [3, 5, 19]. Using Eq. (16) together with replacement (18), the decrease can be implemented such that it does not significantly affect the range at which escalators are most commonly operated, namely $v_{\text{esc}} \leq 0.5\,\text{m}\,\text{s}^{-1}$. Further statements regarding a speed-dependent hesitation time related to the entering process at escalator are difficult to make due to missing comparison possibilities. Both the collection of corresponding empirical data, e. g. through dedicated experiments and field studies, as well as the modelling of the latter therefore remain tasks for future work.

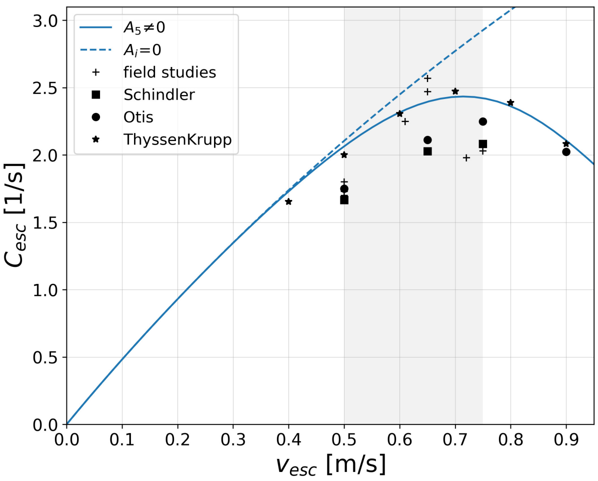

Figure 10. Speed-dependent capacity of an escalator in case of a speed-dependent hesitation time. The capacity function is obtained replacing $T \rightarrow 0.15\,\text{s} + 0.6\,\text{s}^6\text{m}^{-5} \cdot v_{\text{esc}}^5$ in Eq. (16). The escalator parameters are fixed by $d_{\text{step}} = 0.4\,\text{m}$ and $w = 1\,\text{m}$ ($\mathcal{O}_0 = 2$).

References

[1] Ritchie H, Roser M. Urbanization. Our World in Data. 2018;.

[2] Barney G, Al-Sharif L. Elevator Traffic Handbook - Theory and Practice (2nd ed.). Taylor and Francis Group; 2015.

---

[8] The implementation of speed-dependent terms in Eq. (18) is by no means unique since the underlying velocity-dependence is (so far) unknown. Using a power series is only *one possible* realization.

[3] OTIS. Planungshandbuch - Projektierung von Fahrtreppen und Fahrsteigen; 2022.

[4] Schindler Aufzüge und Fahrtreppen GmbH. Planungsleitfaden für Fahrtreppen und Fahrsteige; 2022.

[5] ThyssenKrupp Elevator Americas. Escalators & Moving Walks planning guide; 2013.

[6] Xing Y, Dissanayake S, Lu J, Long S, Lou Y. An Analysis of Escalator-Related Injuries in Metro Stations in China, 2013–2015. Accident Analysis & Prevention. 2019;122:332–341. doi:https://doi.org/10.1016/j.aap.2017.10.007.

[7] Deutsches Institut für Normierung e V . Safety of escalators and moving walks - Part 1: Construction and installation; German version EN 115-1:2017; 2017.

[8] BSI British Standards. Safety rules for the construction and installation of escalators and moving walks; German version EN BS 5656-2:2004; 2004.

[9] Weidmann U. Der Fahrgastwechsel im öffentlichen Personenverkehr; 1994.

[10] Predtetschenski VM, Milinski AI. Personenströme in Gebäuden - Berechnungsverfahren für die Projektierung. Verlagsgesellschaft Rudolf Müller, Köln; 1971.

[11] Bodendorf H, Osterkamp M, Seyfried A, Holl S. Field Studies on the Capacity of Escalators. Transportation Research Procedia. 2014;2:213–218. doi:https://doi.org/10.1016/j.trpro.2014.09.037.

[12] Böhm-Franke T. Empirische Untersuchungen zur Kapazität von Fahrtreppen, Bachelor's thesis; 2015.

[13] Kinsey M. Vertical Transport Evacuation Modelling, PhD thesis; 2011.

[14] Nai W, Dong D, Chen S, Zheng W, Yang W. Optimizing the Usage of Walking Facilities between Platform and Concourse Layer in L-Shaped Interchange Metro Station. Procedia - Social and Behavioral Sciences. 2012;43:748–757. doi:https://doi.org/10.1016/j.sbspro.2012.04.148.

[15] Kahali D, Rastogi R. Analysis of Flow Characteristics and Step Size of Escalators at Metro Stations. Ksce Journal of Civil Engineering. 2021;25:1043–1055.

[16] Kahali D, Rastogi R. Passenger Flows at Escalators – Arriving at Count Interval for Design Flow Estimation. European Journal of Transport and Infrastructure Research. 2021;21(4):62–80. doi:https://doi.org/10.18757/ejtir.2021.21.4.5703.

[17] Devis P, Dutta G. Estimating of Capacity of Escalators in London Underground. Indian Institute of Management Ahmedabad, Research and Publication Department; 2002. WP2002-11-01.

[18] Al-Sharif L. Escalator Handling Capacity: Standards versus Practice. Elevator World. 1996;44.

[19] Majo AJ. A study of escalators and associated flow systems. MSc Degree Report; 1966.

[20] Fruin JJ. Pedestrian planning and design; 1971.

[21] Development Core Team. JuPedSim; 2022. Available from: `https://doi.org/10.5281/zenodo.6144559`.

[22] Kinsey M, Galea ER, Lawrence P. Extended Model of Pedestrian Escalator Behaviour Based on Data Collected within a Chinese Underground Station; 2009.

[23] Kauffmann PD. Traffic Flow on Escalators and Moving Walkways: Quantifying and Modeling Pedestrian Behavior in a Continuously Moving System, thesis; 2011.

[24] Li W, Gong J, Yu P, Shen S, Li R, Duan Q. Simulation and Analysis of Congestion Risk during Escalator Transfers Using a Modified Social Force Model. Physica A: Statistical Mechanics and its Applications. 2015;420:28–40. doi:https://doi.org/10.1016/j.physa.2014.10.044.

[25] Yue FR, Chen J, Ma J, Song WG, Lo SM. Cellular automaton modeling of pedestrian movement behavior on an escalator. Chinese Physics B. 2018;27:124501. doi:https://doi.org/10.1088/1674-1056/27/12/124501.

[26] Tordeux A, Chraibi M, Seyfried A. Collision-free speed model for pedestrian dynamics. arXiv: Physics and Society. 2015;.

[27] Helbing D, Molnár P. Social force model for pedestrian dynamics. Phys Rev E. 1995;51:4282–4286. doi:https://doi.org/10.1103/PhysRevE.51.4282.

[28] Chraibi M, Seyfried A, Schadschneider A. Generalized centrifugal-force model for pedestrian dynamics. Phys Rev E. 2010;82:046111. doi:https://doi.org/10.1103/PhysRevE.82.046111.

[29] Development Core Team. JuPedSim online manual; 2022. `https://www.jupedsim.org/jpscore_inifile.html#model-parameters-tordeux2015`.

[30] Malhotra V, Goel N, Ushadhar U, Tripathi Y, Garg R. Exercise and reaction times. Journal of Evolution of Medical and Dental Sciences. 2015;4:4277–4281. doi:https://doi.org/10.14260/jemds/2015/618.

[31] Kosinski RJ. A Literature Review on Reaction Time Kinds of Reaction Time Experiments; 2012.

[32] Ashoke B, Shikha D, Sudarsan B. Reaction time with respect to the nature of stimulus and age of male subjects.; 2010. Available from: `http://www.journalshr.com/papers/Vol%202_N%201/V02_1_5.pdf`.

[33] Niemi P, Näätänen R. Foreperiod and reaction time. Psychological Bulletin. 1981;89:133. doi:https://doi.org/10.1037/0033-2909.89.1.133.

[34] Niemi P. Stimulus intensity effects on auditory and visual reaction process. Acta psychologica. 1979;43:299–312. doi:https://doi.org/10.1016/0001-6918(79)90038-6.

References

[1] Erik Andresen, Mohcine Chraibi, and Armin Seyfried. A representation of partial spatial knowledge: A cognitive map approach for evacuation simulations. *Transportmetrica A: Transport Science*, 14(5-6):433–467, 2018-07-03. URL: `https://www.tandfonline.com/doi/full/10.1080/23249935.2018.1432717`, `doi:10.1080/23249935.2018.1432717`.

[2] Michael Behrisch, Laura Bieker, Jakob Erdmann, and Daniel Krajzewicz. SUMO – Simulation of Urban MObility: An Overview. In SINTEF & University of Oslo Aida Omerovic, RTI International-Research Triangle Park Diglio A. Simoni, and RTI International-Research Triangle Park Georgiy Bobashev, editors, *Proceedings of SIMUL 2011, The Third International Conference on Advances in System Simulation*. ThinkMind, 2011.

[3] Anna Braun, Mohcine Chraibi, and Lukas Arnold. Investigation of the capacity of train stations in case of a large-scale emergency evacuation. In *EPiC Series in Computing*, volume 62, pages 68–77, 2019. URL: `https://easychair.org/publications/paper/j2Dq`, `doi:10.29007/j32s`.

[4] M. Chraibi. Oscillating behavior within the social force model. *arXiv:1412.1133*, 2014. URL: `http://arxiv.org/abs/1412.1133`.

[5] Mohcine Chraibi. *Validated Force-Based Modeling of Pedestrian Dynamics*. phdthesis, University of Cologne, 2012. URL: `http://www.uni-koeln.de/`.

[6] Mohcine Chraibi and David Haensel. Cognitive Map Routing. In *Cellular Automata / El Yacoubi, Samira (Editor)*, volume 9863 of *Lecture Notes in Computer Science*, pages 210–218. 12th International conference on Cellular Automata for Research and Industry, Springer International Publishing, 2016. `doi:10.1007/978-3-319-44365-2_21`.

[7] Mohcine Chraibi, Armin Seyfried, and Andreas Schadschneider. Generalized centrifugal-force model for pedestrian dynamics. *Physical Review E*, 82(4):046111, 2010. `doi:10.1103/PhysRevE.82.046111`.

[8] Development Core Team. *JuPedSim*, version 0.9.4. URL: `https://github.com/JuPedSim/jpscore`.

[9] I. Echeverría-Huarte, I. Zuriguel, and R. C. Hidalgo. Pedestrian evacuation simulation in the presence of an obstacle using self-propelled spherocylinders. *Physical Review E*, 102(1):012907, 2020. URL: `https://link.aps.org/doi/10.1103/PhysRevE.102.012907`, `doi:10.1103/PhysRevE.102.012907`.

[10] Ingo A. Hansen. Review of planning and capacity analysis for stations with multiple platforms – Case Stuttgart 21. *Journal of Rail Transport Planning & Management*, 6(4):313–330, 2017. URL: `https://linkinghub.elsevier.com/retrieve/pii/S2210970616300427`, `doi:10/gpxgm6`.

[11] K. Hirai and K. Tarui. A simulation of the behavior of a crowd in panic. In *Proc. of the 1975 International Conference on Cybernetics and Society*, pages 409–411, 1975.

[12] McGrattan Kevin, Hostikka Simo, Floyd Jason, McDermott Randall, and Vanella Marcos. *Fire Dynamics Simulator*, 2022. URL: `https://pages.nist.gov/fds-smv/`.

[13] Raphael Korbmacher and Antoine Tordeux. Review of Pedestrian Trajectory Prediction Methods: Comparing Deep Learning and Knowledge-Based Approaches. *IEEE Transactions on Intelligent Transportation Systems*, pages 1–19, 2022. `doi:10.1109/TITS.2022.3205676`.

[14] Gerta Köster, Franz Treml, and Marion Gödel. Avoiding numerical pitfalls in social force models. *Physical Review E*, 87(6):063305, 2013. URL: `https://link.aps.org/doi/10.1103/PhysRevE.87.063305`, `doi:10.1103/PhysRevE.87.063305`.

[15] T. Kretz. On oscillations in the social force model. *Physica A*, 438:272, 2015. URL: `http://arxiv.org/abs/1507.02566`, `doi:http://dx.doi.org/10.1016/j.physa.2015.07.002`.

[16] Taras I. Lakoba, D. J. Kaup, and Neal M. Finkelstein. Modifications of the Helbing-Molnár-Farkas-Vicsek Social Force Model for Pedestrian Evolution. *SIMULATION*, 81(5):339–352, 2005-05. URL: `http://journals.sagepub.com/doi/10.1177/0037549705052772`, `doi:10.1177/0037549705052772`.

[17] Peter Molnar. *Modellierung und Simulation der Dynamik von Fußgängerströmen*. Berichte aus der Physik. Shaker, als ms. gedr edition, 1996.

[18] Louis A. Pipes. An Operational Analysis of Traffic Dynamics. *Journal of Applied Physics*, 24(3):274–281, 1953. URL: `http://aip.scitation.org/doi/10.1063/1.1721265`, `doi:10.1063/1.1721265`.

[19] Jonas Rzezonka, Mohcine Chraibi, Armin Seyfried, Ben Hein, and Andreas Schadschneider. An attempt to distinguish physical and socio-psychological influences on pedestrian bottleneck. *Royal Society Open Science*, 9(6):211822, 2022. URL: `https://royalsocietypublishing.org/doi/10.1098/rsos.211822`, `doi:10/gqbv9j`.

[20] Andreas Schadschneider, Mohcine Chraibi, Armin Seyfried, Antoine Tordeux, and Jun Zhang. Pedestrian Dynamics: From Empirical Results to Modeling. In Livio Gibelli, editor, *Crowd Dynamics, Volume 1*, Modeling and Simulation in Science, Engineering and Technology, pages 63–102. Springer International Publishing, 2018. URL: `https://juser.fz-juelich.de/record/860643`, `doi:10.1007/978-3-030-05129-7_4`.

[21] Benjamin Schröder, David Haensel, Mohcine Chraibi, Lukas Arnold, and Armin Seyfried. Knowledge- and Perception-based Route Choice Modelling in Case of Fire. In *Human Behaviour in Fire Symposium*, pages 327–338. Interscience Communications Limited, 2015. URL: `https://juser.fz-juelich.de/record/255941`.

[22] A. Seyfried. Intentions and superposition of forces in pedestrian models. *presentation at PED 2018, Lund, Sweden*, 2018.

[23] Antoine Tordeux, Mohcine Chraibi, Armin Seyfried, and Andreas Schadschneider. Artificial Neural Networks Predicting Pedestrian Dynamics in Complex Buildings. In Ansgar Steland, Ewaryst Rafajł owicz, and Ostap Okhrin, editors, *Stochastic Models, Statistics and Their Applications*, volume 294 of *Springer Proceedings in Mathematics & Statistics*, pages 363–372. Springer International Publishing, 2019. URL: `http://link.springer.com/10.1007/978-3-030-28665-1_27`, `doi:10.1007/978-3-030-28665-1_27`.

[24] Weichen Liao, Mohcine Chraibi, Armin Seyfried, Jun Zhang, Xiaoping Zheng, and Ying Zhao. Validation of FDS+Evac for pedestrian simulations in wide bottlenecks. In *17th International IEEE Conference on Intelligent Transportation Systems (ITSC)*, pages 554–559. The 17th International IEEE Conference on Intelligent Transportation Systems, Qingdao (China), 8 Oct 2014 - 11 Oct 2014, IEEE, 2014. URL: `http://ieeexplore.ieee.org/document/6957748/`, `doi:10.1109/ITSC.2014.6957748`.

[25] J. Zhang, D. Britto, M. Chraibi, R. Löhner, E. Haug, and B. Gawenat. Quantitative Validation of PEDFLOW for Description of Unidirectional Pedestrian Dynamics. *Transportation Research Procedia*, 2:733–738, 2014. The Conference on Pedestrian and Evacuation Dynamics 2014 (PED 2014), 22-24 October 2014, Delft, The Netherlands. URL: `https://linkinghub.elsevier.com/retrieve/pii/S2352146514001173`, `doi:10.1016/j.trpro.2014.09.081`.

The pictures used in the beginning of the chapters were produced using Midjourney and DALL·E.

Schriften des Forschungszentrums Jülich
IAS Series

Band / Volume 45
Supercomputer simulations of transmon quantum computers
D. Willsch (2020), IX, 237 pp
ISBN: 978-3-95806-505-5

Band / Volume 46
The Influence of Individual Characteristics on Crowd Dynamics
P. Geoerg (2021), xiv, 212 pp
ISBN: 978-3-95806-561-1

Band / Volume 47
Structural plasticity as a connectivity generation and optimization algorithm in neural networks
S. Diaz Pier (2021), 167 pp
ISBN: 978-3-95806-577-2

Band / Volume 48
Porting applications to a Modular Supercomputer
Experiences from the DEEP-EST project
A. Kreuzer, E. Suarez, N. Eicker, Th. Lippert (Eds.) (2021), 209 pp
ISBN: 978-3-95806-590-1

Band / Volume 49
Operational Navigation of Agents and Self-organization Phenomena in Velocity-based Models for Pedestrian Dynamics
Q. Xu (2022), xii, 112 pp
ISBN: 978-3-95806-620-5

Band / Volume 50
Utilizing Inertial Sensors as an Extension of a Camera Tracking System for Gathering Movement Data in Dense Crowds
J. Schumann (2022), xii, 155 pp
ISBN: 978-3-95806-624-3

Band / Volume 51
Final report of the DeepRain project
Abschlußbericht des DeepRain Projektes
(2022), ca. 70 pp
ISBN: 978-3-95806-675-5

Band / Volume 52
JSC Guest Student Programme Proceedings 2021
I. Kabadshow (Ed.) (2023), ii, 82 pp
ISBN: 978-3-95806-684-7

Schriften des Forschungszentrums Jülich
IAS Series

Band / Volume 53
Applications of variational methods for quantum computers
M. S. Jattana (2023), vii, 160 pp
ISBN: 978-3-95806-700-4

Band / Volume 54
Crowd Management at Train Stations in Case of Large-Scale Emergency Events
A. L. Braun (2023), vii, 120 pp
ISBN: 978-3-95806-706-6

Band / Volume 55
Gradient-Free Optimization of Artificial and Biological Networks using Learning to Learn
A. Yeğenoğlu (2023), II, 136 pp
ISBN: 978-3-95806-719-6

Band / Volume 56
Real-time simulations of transmon systems with time-dependent Hamiltonian models
H. A. Lagemann (2023), iii, 166, XXX pp
ISBN: 978-3-95806-720-2

Band / Volume 57
Plasma Breakdown and Runaway Modelling in ITER-scale Tokamaks
J. Chew (2023), xv, 172 pp
ISBN: 978-3-95806-730-1

Band / Volume 58
Space Usage and Waiting Pedestrians at Train Station Platforms
M. Küpper (2023), ix, 95 pp
ISBN: 978-3-95806-733-2

Band / Volume 59
Quantum annealing and its variants: Application to quadratic unconstrained binary optimization
V. Mehta (2024), iii, 152 pp
ISBN: 978-3-95806-755-4

Band / Volume 60
Elements for modeling pedestrian movement from theory to application and back
M. Chraibi (2024), vi, 279 pp
ISBN: 978-3-95806-757-8

Weitere ***Schriften des Verlags im Forschungszentrum Jülich*** unter
http://wwwzb1.fz-juelich.de/verlagextern1/index.asp

IAS Series
Band / Volume 60
ISBN 978-3-95806-757-8

Mitglied der Helmholtz-Gemeinschaft

JÜLICH
Forschungszentrum